SINGLE CRYSTAL GROWTH AND CHARACTERIZATION OF ZINTL PHASE THERMOELECTRIC COMPOUNDS

By

David M. Smiadak

A DISSERTATION

Submitted to
Michigan State University
in partial fulfillment of the requirements
for the degree of

Materials Science and Engineering – Doctor of Philosophy

2020

ABSTRACT

SINGLE CRYSTAL GROWTH AND CHARACTERIZATION OF ZINTL PHASE THERMOELECTRIC COMPOUNDS

By

David M. Smiadak

Zintl phases have been the focus of recent thermoelectric research due to their complex crystal structures, which include covalently bonded anionic sub-structures in a lattice of electropositive cations. The covalent bonds lead to high mobility, while strict electron-counting rules contribute to the formation of complex structures, which in turn lead to low thermal conductivity. In this manner, these compounds can fit the ideal phonon-glass and electron-crystal model for thermoelectric materials. Although Zintl phases are a promising class of thermoelectric materials that have been studied intensively since 2005, there are still several important fundamental questions that remain unanswered. These include questions related to anisotropic transport and how it relates to the crystal structure, and the role played by intrinsic defects in determining carrier concentration. Additionally, the field of Zintl compounds is ever expanding; through the use of exploratory single crystal growths and the careful selection of starting composition, novel compounds and structure types can be discovered that may be promising thermoelectric candidates.

Zintls with the $Ca_5M_2Sb_6$ (M = Al, Ga, In) structure type, characterized by one-dimensional, ladder-like polyanions, were previously predicted to have highly anisotropic electrical conductivity. To investigate this anisotropic behavior, single crystals of $Ca_5M_2Sb_6$ (M = Al, Ga, In) were grown in the current work via the self-flux method. These crystals grew preferentially along the polyanionic "ladders" of the structure, but only measured a few millimeters long by tens of microns thick. Characterizing the transport properties of these crystals both parallel and perpendicular to the growth direction demanded a novel characterization technique, as placing contacts by hand was infeasible in the perpendicular direction. Micro-fabrication techniques will be utilized whereby micro-ribbons are extracted from crystals both perpendicular and parallel to the preferred growth direction using a focused ion beam milling technique. Photolithography was then utilized to create

a circuit of sensors for transport measurements. The resistivity, carrier concentration, and mobility of a micro-ribbon of $Ca_5In_2Sb_6$ perpendicular to the preferred growth direction was successfully characterized using this approach. Resistivity measured in the parallel direction using a four-probe resistivity setup was found to be nearly 20 times higher than the perpendicular direction, confirming theoretical predictions.

Experimental investigation of intrinsic defects in single crystals is also explored in the promising Mg_3Sb_2 system, accomplished using single crystal X-ray diffraction. The defect chemistry of this system for both Mg- and Sb-rich single crystal synthesis is investigated, where vacancies and interstitial sites are identified and quantified in collaboration with researchers at the Max Planck Institute for Chemical Physics of Solids in Dresden, Germany.

Lastly, the discovery of a new quaternary Zintl phase, $Ca_9Zn_{3.1}In_{0.9}Sb_9$ is reported, which was discovered as a by-product during the attempted growth of Zn-doped $Ca_5In_2Sb_6$. The new $Ca_9Zn_{3.1}In_{0.9}Sb_9$ structure was solved with the help of collaborators at the University of Delaware. Measurements of the electrical resistivity of the $Ca_9Zn_{3.1}In_{0.9}Sb_9$ crystals performed at Michigan State University showed results similar to that of already-optimized $Ca_9Zn_{4.5}Sb_9$ compounds, pointing to promising thermoelectric performance.

I dedicate this work to my wife Saeeda,
my daughter Sofia, and all my friends and family.

Without you, none of this would be possible.
I love you with all my heart.

ACKNOWLEDGMENTS

I would like to first acknowledge my advisor, Dr. Alex Zevalkink. Thank you very much for your guidance, assistance, knowledge, and good humor. Secondly I would like to thank my doctoral committee Dr. Carl Boehlert, Dr. Tim Hogan, and Dr. Jason D. Nicholas for their advice and probing questions that helped shape this work for the better. I would also like to thank my friend and colleague Mario Calderón for his help in the laboratory and on the soccer pitch. Special thanks to Mack Marshall and Megan Rylko for their assistance with single crystal growth synthesis. Also to Dr. W. Adam Phelan, Research Scientist and Associate Director of the PARADIM Crystal Growth Facility at Johns Hopkins University for his advise and assistance.

Single crystal growth projects would not be possible without proper characterization and for that I would like to express my gratitude to Dr. Richard J. Staples, Manager of the Center for Crystallographic Research in Michigan State University's Department of Chemistry and Chemical Biology, for his assistance with single crystal X-ray diffraction across all of our compositions and projects. I would also like to thank Dr. Svilen Bobev and his post-doc Dr. Sviatoslav Baranets at the University of Delaware for their assistance in resolving the $Ca_9Zn_3InSb_9$ single crystal structure, their expertise was invaluable.

I would like to thank Dr. Don Morelli and his group for providing assistance with electronic transport characterization. This work would not have been a success if it were not for the assistance of Dr. Vijay Ponnambalam and Corey Cooling.

I would also like to thank my colleagues at both the IFW and Max Planck Institute in Dresden, Germany. I had the pleasure of working at the IFW Dresden as a Guest Scientist for three months, across two research trips, and had a wonderful learning experience. I would like to thank Almut Pöhl for her invaluable work FIB cutting our crystal samples, Cindy Kupka for providing assistance and training in the Microstructuring Lab, and to Lauritz Ule Schnatmann, Constantin Wolf, Sepideh Izadi, and Vida Barati for providing day-to-day assistance. I would like to thank Dr. Guodong Li for his helpful advice on photoresists and sample recovery techniques. I am grateful to Dr. Heiko Reith

for allowing me into his laboratory and using his equipment to complete my project. Special thanks to Dr. Nicolás Perez Rodriguez, who was my main contact at the institute and helped in a number of ways outside of his responsibilities of providing low temperature characterization assistance. Lastly, I would like to thank Dr. habil. Gabi Schierning, Head of Department Thermoelectric Materials and Devices for making everything possible and providing assistance in achieving our project goals. This project was a success due to the wonderful team at the IFW and I am very grateful for my experience there. I would also like to acknowledge the financial support provided by the National Science Foundation, IFW Dresden, and Michigan State University.

My success would also not be possible without the love and support of my wife, Saeeda and my young daughter Sofia. We have faced a number of challenges but we have done it together. I am a stronger and better person because of their influence. I would like to thank my close friends David and Lauren Luc, Benjamin and Stacey Crowgey, Sam and Simone Kauffold, Brett and Rachel Justice, and Steve and Lila Hughey all for their continued love and support over the years, you've made this experience so much better with your friendship. I would also like to thank my family, especially my father Matt Smiadak, who as of this writing is continuing to work and provide essentials to the community during the pandemic and to my mother Pamela Smiadak who continues to shower love on us and our daughter. They have been pillars of support for me since I was born and I can not thank them enough. I would like to thank my brother-in-law Sammy Usman Jr. and his girlfriend Tiffany Savoie, my sister-in-law Carmel Scott-Emuakpor and her husband Onome all for their loving support as well.

I would also like to thank John Brandenburg and John Plough from my East Lansing High School days for instilling a love of math and science. And special thanks to Dr. Mehmet Sözen for providing me with an independent study during my undergraduate at Grand Valley State University and conference opportunities even after I had graduated. Reaching out to me, was motivation to take a leap back into research and graduate school.

Lastly, thank you also to all of the front line worker and essential employees that are currently risking their lives, many out of financial necessity, to provide for others during this time. I hope that

we learn from this experience and create a more fair and equitable society as a result.

TABLE OF CONTENTS

LIST OF TABLES

LIST OF FIGURES

CHAPTER 1

INTRODUCTION: THERMOELECTRICS

1.1 Thermoelectrics

As the energy needs of the United States and the world continue to increase, thermoelectrics have come into focus as a possible environmentally friendly alternative. The estimated energy consumption of the United States for 2017 was 97.7 Quads (1.03×10^{20} J) with 66.7% of this consumption lost as rejected energy [8]. Thermoelectrics offer a solution for waste heat recovery and have far-ranging applications in industry and space exploration. Applications include but are not limited to thermal cycles for DNA synthesizers, car seat cooler/heaters, laser diode coolers, low-wattage power generators, and military applications such as heat-seeking missiles and night-vision systems [9]. Additionally, thermoelectrics can provide a clean energy alternative, replacing more environmentally costly sources such as fossil fuels. Thermoelectrics are appealing for their small size, robustness in difficult environments (solid-state devices), and rapid response times [10, 11].

A thermoelectric generator is capable of converting heat to electricity as shown in Figure 1.1. This device consists of thermoelectric junctions that are electrically in series and thermally in parallel. Each junction consists of a *p*- and *n*-type material connected by shunts made of an electrical conductor such as copper. In a *p*-type material, holes diffuse to the cold side while in an *n*-type material, electrons diffuse to the cold side. This carrier motion generates a voltage that drives a current through each junction, producing electricity [12]. The maximum thermoelectric efficiency of a device can be expressed as

$$\eta_{\max} = \frac{T_{\text{hot}} - T_{\text{cold}}}{T_{\text{hot}}} \frac{\sqrt{1+ZT}-1}{\sqrt{1+ZT}+\frac{T_{\text{cold}}}{T_{\text{hot}}}}, \tag{1.1}$$

where T_{hot} is the hot side temperature, T_{cold} is the cold side temperature, and ZT is the thermoelectric device figure-of-merit. The first term on the right side of this expression is the Carnot

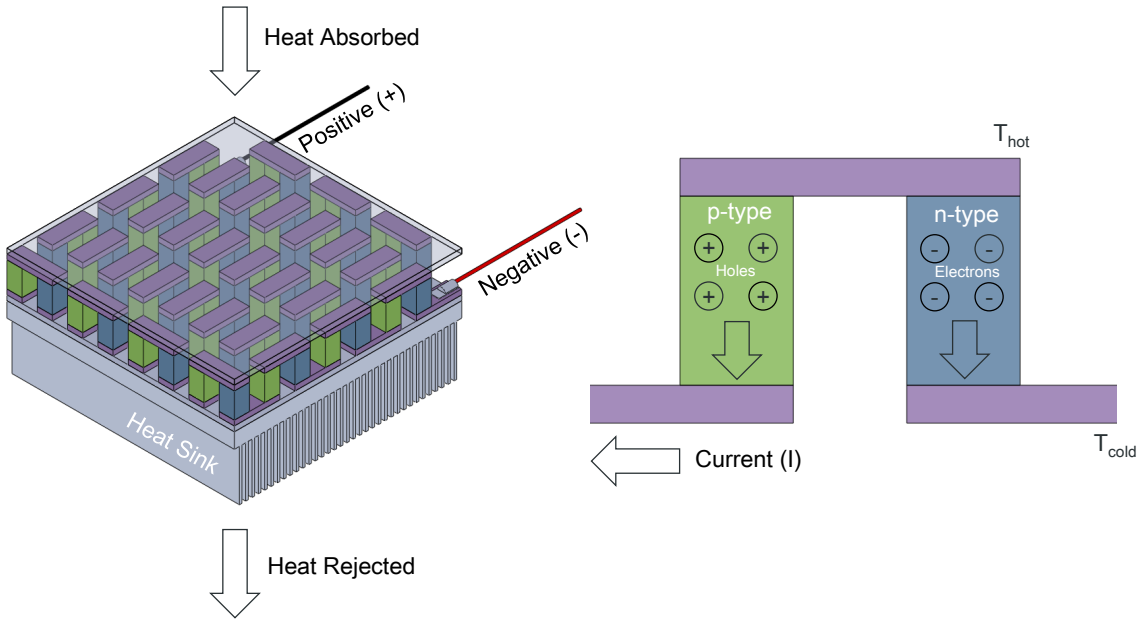

Figure 1.1: Thermoelectric module (left) with detail of single junction (right). Charge carriers diffuse to the cold side (T_{cold}) for a given temperature gradient.

efficiency ($\eta_{\text{Carnot}} = (T_{\text{hot}} - T_{\text{cold}})/T_{\text{hot}}$), which is the theoretical maximum efficiency of a heat engine equivalent to $zT = \infty$. The largest challenge facing the expansion of modern thermoelectric utilization is performance; most commonly represented by the dimensionless figure-of-merit, zT, for a specific compound,

$$zT = \frac{\alpha^2 \sigma T}{\kappa_e + \kappa_l}, \tag{1.2}$$

where α is the Seebeck coefficient, σ is the electrical conductivity, T is the operating temperature, κ_e is the thermal conductivity contribution from electrons and holes transporting heat, and κ_l is the thermal conductivity contribution from phonons traveling through the lattice. From Equation 1.2, it can be observed that an optimal thermoelectric material would simultaneously possess a large Seebeck coefficient, high electrical conductivity, high operating temperature, and minimal thermal conductivity.

While every material possesses thermoelectric effects in some capacity, many are not well suited to serve as a thermoelectric due to their prohibitively low zT. For metals, α is usually prohibitively

small, with thermal conductivities are too large. Insulators, on the other hand, suffer from resistivity ($\rho = 1/\sigma$) values that are too significant to overcome. This narrows the field of thermoelectric candidates to semiconductor-like materials.

The highest thermoelectric performance typically comes from heavily doped semiconductors with peak performance across a variety of temperature ranges [13]. Near room temperature applications (300-500 K) utilize promising Bi_2Te_3-based [14–16] and MgAgSb alloys [17, 18]. Medium-temperature range (500-900 K) thermoelectrics are numerous, including Pb(Te,Se,S) [19–22], PbTe-$AgSbTe_2$ [23], GeTe-$AgSbTe_2$ [24], $AgSbTe_2$ [25], and SnSe [26]. More recent additions to this temperature range include tetrahedrites [27], Zn_4Sb_3 [28, 29], In_4Se_3 [30], Cu_2(S,Se,Te) [31, 32], and a number of Zintl phases discussed in greater detail in subsequent sections [29, 33–37]. High temperature applications (> 900 K) include half-Heuslers [38–40], SiGe [41–43], and Zintl phases [44, 45] among others.

1.2 Thermoelectric Effects

The thermoelectric effects of a material can either create an electrical potential from a temperature difference or produce a temperature difference given an electrical potential. These effects manifest in three different ways: the Seebeck, Peltier, and Thomson effects.

The Seebeck effect was discovered by Thomas Seebeck in 1821 [46] when two electrically conducting materials (A and B) were connected across a temperature gradient. A magnetic needle was deflected when placed near the apparatus, the result of an electrical current flowing in the closed loop rather than a magnetic polarization. The magnitude of this voltage difference, ΔV, was found to be proportional to the temperature difference, ΔT,

$$\alpha_{\mathrm{AB}} = \frac{\Delta V}{\Delta T}, \tag{1.3}$$

where the proportionality coefficient, α_{AB}, is the Seebeck coefficient for the material couple. A positive Seebeck represents a electromotive force driving an electrical current through material A from the hot to cold junction. This loop can be separated, as shown in Figure 1.2(left), and the open

circuit voltage, ΔV, can be expressed as

$$\Delta V = \int_{T_1}^{T_2} \alpha_{AB} dT, \tag{1.4}$$

where

$$\alpha_{\mathrm{AB}} = \alpha_{\mathrm{B}} - \alpha_{\mathrm{A}} = \frac{\Delta V_{\mathrm{B}}}{\Delta T} - \frac{\Delta V_{\mathrm{A}}}{\Delta T}. \tag{1.5}$$

In this manner, α_{AB} can be decoupled into individual material Seebeck coefficients. The Seebeck coefficient is commonly reported in $\mu V/K$ and is evaluated at open circuit conditions. A voltage difference is required, necessitating a coupling of two unlike materials.

Intrinsically, the Seebeck coefficient describes the response of electrons to a temperature gradient. Materials that are *n*-type create a negative Seebeck coefficient in open circuit conditions where the electric field points in the direction of the cold side when exposed to a temperature gradient. A *p*-type material, in contrast, possesses a positive Seebeck coefficient with the opposite field effect. A practical way to take advantage of this effect is in the construction of thermocouples. In the traditional metal/metal-alloy thermocouple, two different electrical conductors are welded together to form an electrical junction where the two conductors are electrically in series but thermally in parallel as shown in Figure 1.2(left).

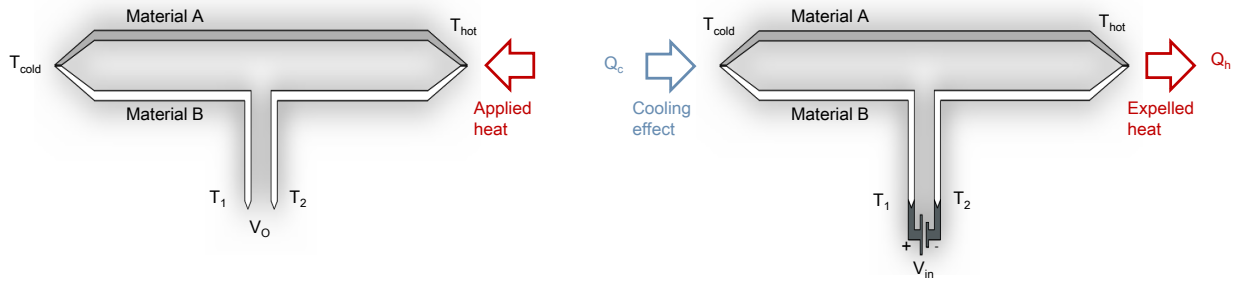

Figure 1.2: Thermocouple circuit illustrating the Seebeck effect where a voltage difference, ΔV, appears across the terminal at T_1 and T_2 (left). Modified circuit illustrating the Peltier effect whereby an applied voltage produces a current, I, creating a cooling effect at T_c, while expelling heat at T_h (right).

The Peltier effect describes the reverse case of the Seebeck effect and was discovered by Jean Charles Athanase Peltier in 1834 [47]. It is the fundamental effect governing thermoelectric refrigeration. Peltier discovered that when a current was passed through two dissimilar but physically connected materials, a heating or cooling effect occurs at their mating surface as shown in Figure 1.2(right). The cooling effect, Q_c, can be expressed as

$$Q_c = \Pi_{AB} I, \tag{1.6}$$

where Π_{AB} is the differential Peltier coefficient between material A and B, and I is the applied electrical current. Alternatively, the applied current flow can be reversed producing a heating effect at T_{cold}. The Peltier coefficient is also related to the Seebeck coefficient,

$$\alpha_{AB} = \frac{\Pi_{AB}}{T}. \tag{1.7}$$

The third thermoelectric effect is the Thomson effect, discovered by William Thomson, later known as Lord Kelvin, in 1857 [48]. The Thomson coefficient, K, described the heating or cooling of a conductor in a temperature gradient given an externally applied current and is related to the Seebeck coefficient,

$$\alpha_{AB} = \int \frac{K_{AB}}{T} dT \tag{1.8}$$

where the difference between the Thomson coefficients of the two materials is the rate of heating per unit length that is the result of the applied current [49].

For thermoelectric power generation, the Seebeck effect is critically important as described in Equation 1.3, which describes how well a material transforms thermal energy to electrical power due to the electrical bias generated in a material under a temperature gradient. The Seebeck coefficient is a quadratic term in the zT equation, illustrating its large influence on thermoelectric performance.

1.3 Electronic Transport

Electrical conductivity, σ, is the reciprocal of resistivity, ρ, and is a measure of how well a specific material conducts electricity. For semiconductors it can be expressed as,

$$\sigma = ne\mu_d, \tag{1.9}$$

where n is the carrier concentration, e is the electron charge, and μ_d is the drift velocity. This drift velocity is the average velocity of the electrons divided by the applied field in the direction of travel, which relates to the effective mass of the electron itself. Drift velocity can be expressed as,

$$\mu_d = \frac{e\tau}{m_e^*}, \tag{1.10}$$

where τ is the mean free time between collisions (*i.e.*, mean scattering time, relaxation time) and m_e^* is the effective mass of the electron. The mean free time multiplied by the mean speed of the electrons, v, yields the mean free path, l. The mean free time is of critical importance in thermoelectrics as it relates directly to the processes that scatter electrons. These scattering mechanisms include thermal lattice vibrations (*i.e.*, phonons), τ_T, and impurities, τ_I, among others. The overall frequency of scattering can be expressed as,

$$\frac{1}{\tau} = \frac{1}{\tau_T} + \frac{1}{\tau_I} + \dots . \tag{1.11}$$

It is desired that electrons be highly mobile in the structure, with long times between collisions generating a high τ which in turn increases electrical conductivity.

In semiconductors, m_e^* is considered to incorporate the effect of the periodic potential of the atoms and reflects the band curvature and doping of the material. The effective mass determines both the electronic structure and transport when parabolic band modeling is utilized [50].

1.4 Thermal Transport

Thermal conductivity, κ, in an isotropic material relates to the heat flux expressed as Fourier's law [51],

$$q = -\kappa \nabla T, \tag{1.12}$$

where q is the heat flux vector, κ is the thermal conductivity and ∇T is the temperature gradient. For thermoelectric materials that have multiple carriers, the total thermal conductivity consists primarily of an electronic and lattice component,

$$\kappa = \kappa_e + \kappa_l, \tag{1.13}$$

where κ_e is the thermal conductivity contribution from electrons and holes transporting heat and κ_l is the contribution from phonons traveling through the lattice.

1.4.1 Electronic Thermal Conductivity

The free electrons and holes that contribute to σ also carry heat with κ_e relating to σ according to the Weidemann-Franz Law [52],

$$\kappa_e = L\sigma T = ne\mu LT, \tag{1.14}$$

where L is the Lorenz number, defined as $L = \pi^2 k_B^2 / 3e^2 = 2.44 \times 10^{-8}$ WΩK^{-2} for a free electron gas with parabolic dispersion near the Fermi energy level. This value applies to most metals and degenerate semiconductors. For non-degenerate semiconductors, $L = 1.5 \times 10^{-8}$ WΩK^{-2}. The κ_e component of thermal conductivity thus scales linearly with σ and T. While all heat conduction should be minimized for high zT, in practice, κ_e is rarely targeted because of the need for high σ.

1.4.2 Lattice Thermal Conductivity

The lattice component of thermal conductivity describes the contribution of phonons traveling through the lattice, and it is often the focus in thermoelectric applications as it is independent of electrical conductivity. This lattice contribution is the product of heat capacity, C_V, phonon velocity, v, and the phonon mean free path, l [53],

$$\kappa_l = \frac{1}{3} C_V v l = \frac{1}{3} C_V v^2 \tau_{\text{ph}} \tag{1.15}$$

where τ_{ph} represents the mean free time between phonon interactions. The phonon velocity is often approximated by the low frequency speed of sound, $v_{sound} \propto \sqrt{\frac{E}{d}}$, where E is the elastic modulus and d is the density. Strategies for selecting materials with low lattice thermal conductivities include identifying materials with low phonon velocities, which arise in dense materials with soft bond or through the reduction of τ by introducing point defects or nanostructuring to scatter phonons [54]. These scattering mechanisms, i, obey Matthiessen's rule,

$$\frac{1}{l} = \sum \frac{1}{l_i}. \tag{1.16}$$

The dominant scattering mechanism in pure materials transitions from boundary scattering effects to phonon-phonon Umklapp scattering with increasing temperature. Umklapp scattering is due to anharmonic wave interactions from which thermal resistance is produced. This contribution was first described by Debye [55], whereby thermal motion was defined as the accumulation of all possible vibrations in a lattice. From the Debye model it has been experimentally proven that when $T > \theta_D$, where θ_D is the Debye temperature, lattice thermal conductivity proportional to T^{-1} is indicative of Umklapp scattering [56].

For thermoelectric applications, materials that have inherently low lattice thermal conductivity are preferred where τ_{ph} is reduced by decreasing phonon velocity and/or mean free path. This means complex crystal structures that can be further doped and/or further complicated with point defects. Differences in bond character and strength are also pathways to reducing κ_L.

1.5 Optimization of zT

Thermoelectric materials are optimized by maximizing zT, which expresses the efficiency of the *p*- and *n*-type couple materials. From Equation 1.2, it is observed that zT is maximized through increasing the power factor ($\alpha^2\sigma$) and operating temperature while minimizing κ [57–59]. The power factor is a descriptive metric of carrier concentration effects as both the Seebeck coefficient and electrical conductivity are strongly dependent on it. Unfortunately α and σ have opposing dependence on n. For degenerate semiconductors with a single carrier, the Seebeck coefficient can be expressed as,

$$\alpha = \frac{8\pi^2 k_b^2}{3eh^2} m^*_{DOS} T \left(\frac{\pi}{3n}\right)^{2/3} \tag{1.17}$$

where k_b is the Boltzmann constant, h is the Planck constant, m^*_{DOS} is the density-of-states effective mass of the carrier [59]. This expression is valid for large carrier concentrations and/or low temperature. From this expression it is observed that α is inversely proportional to n. Conductivity on the other hand, is proportional,

$$\sigma = ne\mu_d. \tag{1.18}$$

Large α is produced when a single type of carrier is dominant, either electrons (dominant in *n*-type) or holes (dominant in *p*-type). When a temperature gradient is applied to a material, these charge carriers move to the cold side and in the case of mixed carriers, they effectively cancel out portions of the induced Seebeck voltage through recombination, reducing efficiency. Therefore low n and insulating material behavior is desired for high α. Alternatively, high σ is achieved in materials possessing high n, often the case in metals. For a given thermoelectric material, its zT value is maximized through carrier concentration optimization. Usually a compromise of these requirements leaves a material optimized as a heavily doped semiconductor with n in the range of 10^{19}–10^{21} cm^{-3}. Both intrinsic and extrinsic defects control the tunability of n with many

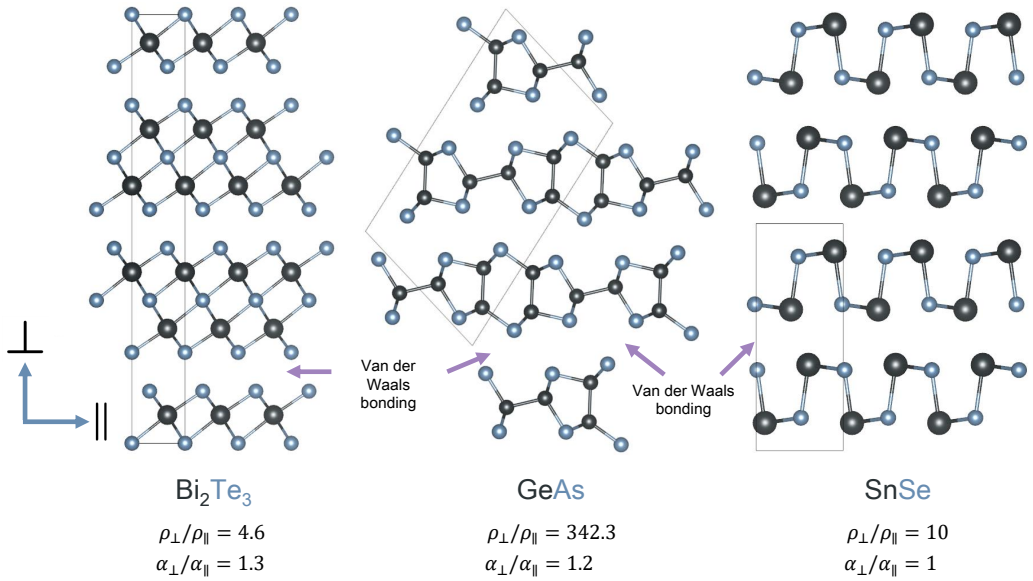

Figure 1.3: Layered thermoelectrics Bi_2Te_3 (left), GeAs (center), and SnSe (right) with low in-plane and high out-of-plane resistivity with more anisotropic behavior observed for Seebeck coefficient.

thermoelectric materials having defect concentrations that are too large, or prevent doping *n*- or *p*-type.

Assuming that n can be optimized independently by doping, the material quality factor, B, is designed to remove the n-dependence from the zT equation. It is particularly useful in the exploration of new thermoelectric candidate materials, which may not yet have optimized n. The material quality factor under the assumption of acoustic phonon scattering is given by [60],

$$B = \frac{2k_B^2\hbar}{3\pi}\frac{C_l N_V}{m_I^* \Xi^2 \kappa_l}T, \tag{1.19}$$

where $\hbar$ is the reduced Planck constant ($h/2\pi$), C_l is the average longitudinal elastic modulus, N_V is the valley degeneracy, m_I^* is the inertial effective mass, and Ξ is the deformation potential. In Equation 1.19, it is observed that κ_l is generally independent of the electronic band structure, emphasizing that a selected material must possess an inherently small κ_l. Valley degeneracy refers to the number of valleys/bands that contribute to the carrier transport. For a constant α, a greater band degeneracy, N_v, will result in a larger carrier concentration. Additionally, N_v increases both

electrical conductivity and zT [61]. High band curvature reflects decreases in effective mass, which increase conductivity, while shallow bands reflect increases in effective mass and Seebeck.

Among the material properties in B, the m_I^*, Ξ, and κ, are dependent on crystallographic direction (x,y,z). The anisotropy of κ_l is a function of the anisotropy of the speed of sound (and therefore the elastic moduli) and phonon scattering mechanisms. The anisotropy of the latter is not yet well understood. The averaged inertial effective mass, m_I^* (*i.e.*, conductivity effective mass or the susceptibility effective mass), is a tensor property which describes particle motion in a specific direction in response to a force. It can be expressed anisotropically as,

$$m_I^* = 3\left(\frac{1}{m_x}+\frac{1}{m_y}+\frac{1}{m_z}\right)^{-1}. \tag{1.20}$$

Estimates of m_x, m_y, and m_z, can be obtained from the curvature of the band structures obtained from DFT calculations. This is different from m_{DOS}^* in Equation 1.17 which is a scalar proportional to the density-of-states near the Fermi level which needs to be maximized to increase α. While m_{DOS}^* and m_I^* are equivalent for a single isotropic band, they diverge for anisotropic cases. Because m_{DOS}^* is by definition isotropic, $m_{I,\text{avg}}^*$ can be highly anisotropic, it is possible to achieve high σ in the m_I^* direction while simultaneously maintaining a high m_{DOS}^* to achieve high α. Finally, the factors controlling the deformation potential, Ξ, which determines the electron-phonon scattering rate, τ_T, are not well understood at this point. Thus, its is difficult to pinpoint its anisotropy.

In a given material, κ_l, m_I^*, and Ξ usually have different degrees of anisotropy. This means that a potential way to circumvent the inherent contradictions in the optimization of B (and thus zT) is the use of anisotropic single crystals. From this framework, an ideal anisotropic thermoelectric candidate material can be theorized. The material would possess a complex structure with intrinsically low, but isotropic lattice thermal conductivity and would possess a crystallographic direction with high mobility that minimizes m_I^* and Ξ. Along the high mobility direction, such a material would be an ideal phonon-glass, electron-crystal [58].

Because anisotropic properties are difficult to study, there are only a handful of anisotropic thermoelectric materials that have been proven experimentally to possess a preferred crystallographic

orientation for thermoelectric applications. Because electrical conductivity is more dependent on crystallographic orientation than α, materials with highly anisotropic crystal structures allow for thermoelectric optimization along the high mobility (low m_I^* and Ξ) crystallographic axis. Usually σ can vary significantly while α remains relatively constant, as is the case with layered Bi_2Te_3 [62, 63], GeAs [64], $CsBi_4Te_6$ [65, 66], and SnSe [26, 67] thermoelectric compounds, illustrated in Figure 1.3. Recently, $zT > 2$ was achieved by exploiting the high σ direction of SnSe single crystals [67, 68]. Through proper material investigation and carrier concentration optimization, new thermoelectric candidate materials can be discovered and subsequently optimized with anisotropy playing an important role in resolving seemingly contradictory material property demands.

CHAPTER 2

ZINTL THERMOELECTRICS

2.1 Zintl Phase Overview

Zintl phases have been the focus of recent thermoelectric research, due to their complex bonding, which includes covalently bonded anionic sub-structures in a lattice of electropositive cations. These structures adhere to a valence electron counting system known as the Zintl-Klemm concept. This research space is promising for thermoelectrics as the polyanions in these phases may create very anisotropic networks, which in some cases act as conductive pathways. These polyanions can be found to crystallize in a diverse set of complex structures from isolated zero-dimensional moieties to three-dimensional networks. Due to the requirement of being valence precise, Zintl phases have well-defined relationships between their physical and electronic structures, leading to a semiconductor-like energy gap. Unlike metals, Zintl phases show increasing electronic conductivity with increasing temperature [69]. Further, a significant amount of the Zintl phase space is still unexplored [70].

Broadly speaking, Zintl phases include an alkali metal (group 1), alkaline earth (group 2), or rare earth metal reacted with any post-transition metal or metalloid (group 13-16). The term Zintl phase came into use in 1941 [71], originating from the work of Eduard Zintl [72–76] who focused on intermetallic compounds that possessed salt-like structures [76]. Salt-like compounds are characterized by both cation and anions achieving a full octet of electrons, but make for poor thermoelectric materials due to their insulating behavior (*i.e.,* large band gaps). Alternatively, numerous other classes of intermetallics do not possess a band gap, and exhibit metallic behavior that make them poor thermoelectric materials. Zintl phases have been found to be a compromise between these two extremes as useful semiconductors in many cases [77].

From a synthesis standpoint, Zintl phases are characteristically brittle, possess high melting temperatures, and are typically line compounds, possessing very narrow homogeneity width [78, 79].

Zintl materials also offer inexpensive and non-toxic alternatives to current thermoelectric materials [80, 81] such as PbTe, which is both toxic and expensive [9].

2.1.1 Zintl-Klemm Concept

The Zintl-Klemm concept (ZKC) is a formalism first developed by Edward Zintl and expanded by Wilhelm Klemm in which a combination of valence electron counting rules and structure-based chemical considerations are used to explain bonding behavior [69, 82]. Here, electopositive metals (A) such as alkali, alkline earth and rare earth metals are combined with main group elements (X) in the general form A_aX_x, where the X atoms form X_y^{n-} polyanion structures and are bonded with covalent $X-X$ bonds. These structures can be rationalized by accounting for all of the valence electrons, including those donated by the A atoms [83]. The $A-X$ interactions are assumed to be almost entirely ionic. In this manner, the ZKC obeys the $(8-N)$ rule pioneered by Lewis [84], which describes the inclination of main group elements to possess a full octet shell within compound formation [85]. Here N is the number of valence electrons of the X atoms. This octet rule was a milestone in the field of chemistry, helping to explain chemical bonding and stabilities across an immense stretch of compounds, giving rise to what would later be termed Lewis notation.

Klemm's work applied Lewis's $(8-N)$ framework to Zintl phases. Here, the *VEC* is used to determine the number of total electrons available to each anion, including those donated by cations. Advances in DFT calculations have explained the role of the cations for specific compounds [86], with Zintl phases providing a rich field for theoretical electron localization function (ELF) calculations into this combined ionic and covalent bonding.

One of the simplest examples of these anionic-substructures is exhibited in the Zintl phase NaSi (Na^+Si^-) shown in Figure 2.1(left) where Na atoms act as the ionically bonded cation while covalently bonded Si anions form $[Si_4]^{4-}$ tetrahedra substructures. Each Na atom donates one valence electron to a Si atom, satisfying charge balancing according to ZKC rules. The number of bonds, N, is equal to 8-(*VEC*/anion). Thus, for NaSi, each Si has five valence electrons, so $VEC = 5$ and $N = 8-5 = 3$, which is the number of covalent Si-Si bonds.

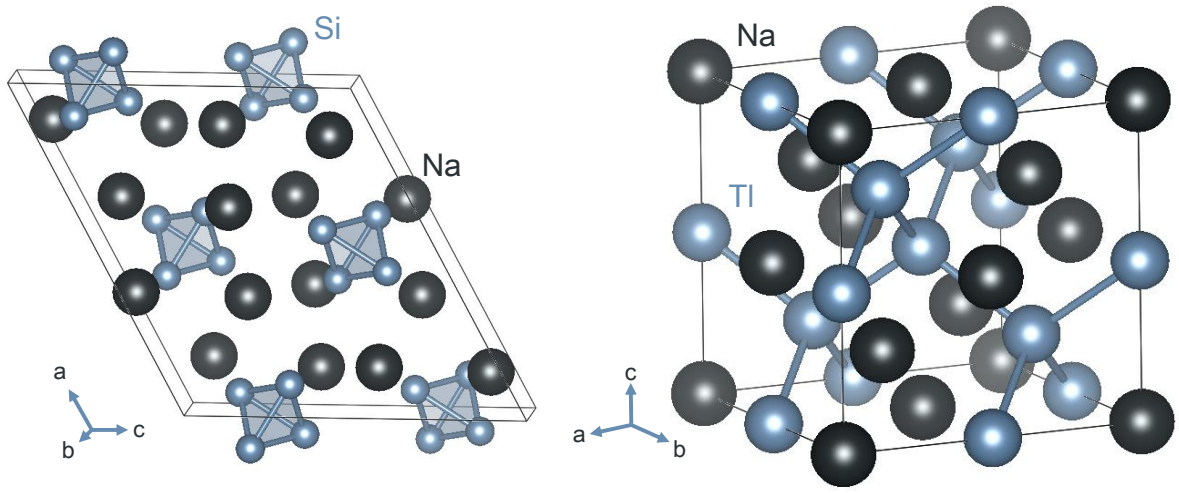

Figure 2.1: The NaSi unit cell with ionically bonded Na cations and covalently bonded anionic Si tetrahedra ($[Si_4]^{4-}$) (left). NaTl unit cell with diamond network of Tl atoms (right).

The ZKC also applies to the NaTl binary shown in Figure 2.1(right) that is not resolved by the traditional (8-*N*) formulation or the Hume-Rothery rules [87, 88] that formulated electron number relations based on specific crystal types. Here ZKC yields a $VEC = 4$, and $N = 8 - 4 = 4$. This explains why each Tl forms four Tl-Tl covalent bonds.

The ZKC explains that the Tl atoms form a diamond network whereby each Na atom donates its valence electron to a Tl atom, resolving the observed arrangement of Na and Tl, and satisfying the spatial requirements of the Na atoms within the Tl framework. This is due to the Tl^- anions having the same number of valence electrons as group 14 elements, creating a network of four-bonded Tl atoms [89, 90]. This NaTl-type structure is rare [91, 92], with only six other known binaries: LiZn [93], LiCd [94], LiAl [95], LiGa [96], LiIn, and NaIn. Most other alloys order to maximize neighbors of the opposite element while these binaries form interpenetrating diamond substructures [97]. This structure-type also extends to select ternary systems [98, 99]. NaTl does not possess a band gap and behaves metallically, making it a poor choice for thermoelectrics [100], but other Zintl phases have shown promise in both their semiconductor behavior and unique complexity of formation.

2.1.2 Thermoelectric Performance of Zintl Phases

The covalent regions of some Zintl phases are thought to provide electron crystal properties and crystallographic directions of high mobility. The ionic regions contribute to the formation of complex structures which in turn lead to phonon-glass properties that can create disorder and be doped to optimize carrier concentration. In this manner these compounds can fit the ideal phonon-glass and electron-crystal model. The classical view of Zintl phases describe valence precise semiconductors, however, degenerate behavior is a product of vacancies and interstitials which can be explained through electron counting schemes. For this reason, metallic behaving compounds are also referred to as Zintl phases. Generally speaking, thermoelectric performance is found in heavily-doped semi-conductors with carrier concentrations in the range of 10^{19} to 10^{21} carriers/cm^3, numbers that can be achieved for Zintl phases [59]. Good Zintl thermoelectrics include Zn_4Sb_3 [29], Mg_3Sb_2 [33] $Ca_xYb_{1-x}Zn_2Sb_2$ [34], $Ca_9Zn_{4+x}Sb_9$ [35], $Yb_{14}Mn_{1-x}Zn_xSb_{11}$ [36, 44, 45], and $YbCd_{2-x}Zn_xSb_2$ [37] with zT values greater than unity.

The potential anisotropic properties of the $Ca_5M_2Sb_6$ (M = Al, Ga, In) system are of particular interest despite their modest doped zT values below unity. This compound family can be *p*-type optimized through doping as is shown in the case of $Ca_5In_2Sb_6$ in Figure 2.2(left). Doped figure-of-merit values for the $Ca_5M_2Sb_6$ (M = Al, Ga, In) compounds are compared to other material systems of interest in Figure 2.2(right). Here, both *p*- and *n*-type Mg_3Sb_2 are listed with the superior *n*-type performance of $zT = 1.51$ [33]. The $Ca_9Zn_{4+x}Sb_9$ compounds possess some of the highest *p*-type performance values for thermoelectrics as well [35].

2.1.3 $A_5M_2Pn_6$ Zintl Phases

The $A_5M_2Pn_6$-type (A = Ca, Sr, Ba; M = Al, Ga, In; Pn = As, Sb) Zintl family of compounds crystallize in the structure shown in Figure 2.3(right), consisting of MSb_4 polyanionic tetrahedra sub-structures that are connected by covalent Sb-Sb bonds. The MSb_4 tetrahedra form one-dimensional chains that are surrounded by ionically bonded Ca^{2+} cations [80]. Transport properties of compounds in this family have yielded semiconducting behavior [60, 101–107].

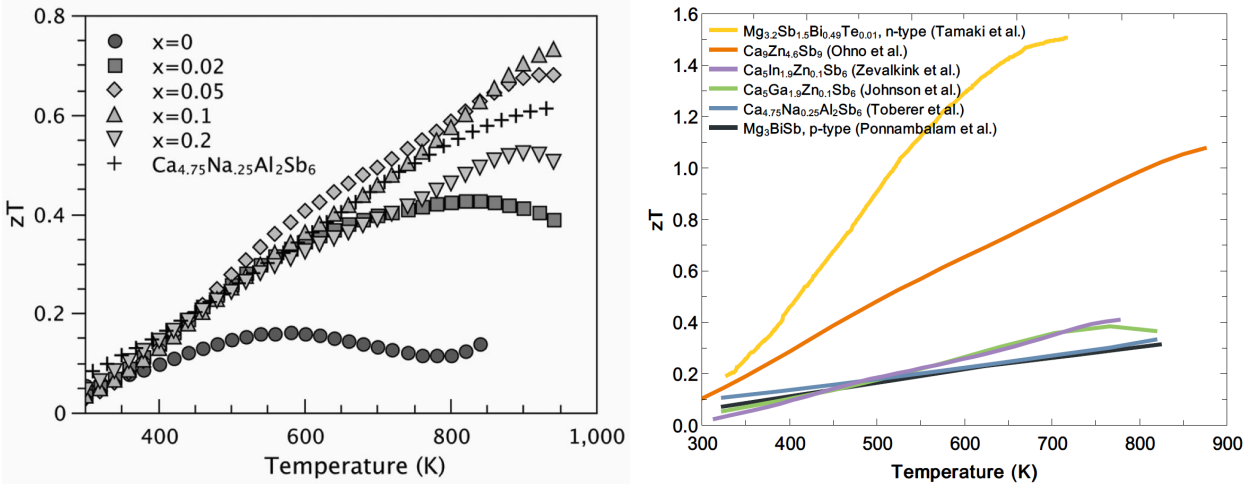

Figure 2.2: The figure-of-merit of $Ca_5In_{2-x}Zn_xSb_6$ samples, compared against Na-doped $Ca_5Al_2Sb_6$ [1] (left). The figure-of-merit for select Zintl phase compounds with respect to temperature after doping optimization (right).

The $Ca_5M_2Sb_6$ (M = Al, Ga, In) [108, 109] compounds exhibit semiconducting behavior and have been investigated extensively as potential thermoelectric materials. While doped zT values have remained under unity, $Ca_5In_2Sb_5$ experiences nearly a five-fold increase in performance due to Zn doping on the In site [1] while $Ca_5Ga_2Sb_5$ experiences a nearly nine-fold increase [110]. $Ca_5Al_2Sb_6$ was optimally doped with Na on the Ca site, producing a six-fold increase in performance [111]. The potential anisotropic properties of $Ca_5M_2Sb_6$ system are of particular interest.

2.1.4 AM_2X_2 Zintl Phases

The AM_2X_2 family of compounds [112, 113] offers a staggering number of compositions that crystallize in the $CaAl_2Si_2$ structure-type [114–122]. This structure takes the form of a trigonal bi-layer with two-dimensional slabs of $[Al_2Si_2]^{2-}$ comprised of $AlSi_4$ tetrahedra, which are edge sharing with three additional tetrahedra. These slabs alternate with trigonally arranged cations in the a-b plane as shown in Figure 2.3(left).

Thermoelectric interest in this compound family began in 2005 with the characterization of $Ca_xYb_{1-x}Zn_2Sb_2$ ($0 \leq x \leq 1$) solid solutions with a peak $zT \approx 0.55$ [34]. Other solid solution

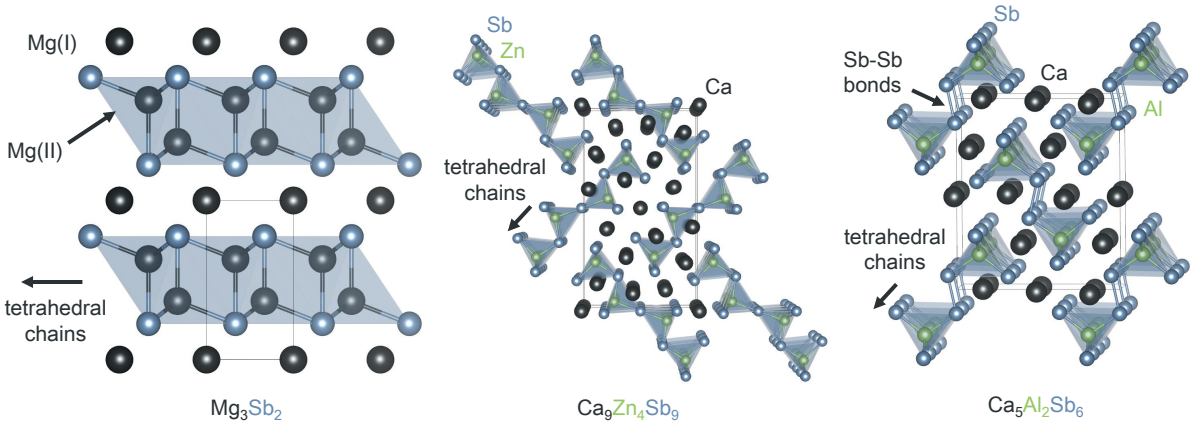

Figure 2.3: The Mg_3Sb_2 structure (left), $Ca_9Zn_{4+x}Sb_9$ structure (center), and the $Ca_5Al_2Sb_6$ structures (right).

studies followed [37, 123–126] producing a peak $zT \approx 1.3$ at 873 K [126]. High zT has also been characterized with $EuZn_2Sb_2$ (0.9 at 700 K) [127], and *n*-type Mg_3Sb_2 (1.51 at 716 K) [33] where Mg occupies both the Ca and Al sites.

Thermoelectric performance of this material family is generally strong due to light effective mass which translates to high electronic mobility [111]. Also the large substitution capacity of this family makes it an appealing area to discover and characterize novel thermoelectric compounds.

2.1.5 $A_9M_4Pn_9$ Zintl Phases

This family of Zintl phases, often referred to as the 9-4-9 system has been known since the late 1970s [128] and has steadily expanded to include a variety of elements [129–131]. More recent developments discovered partially occupied Zn interstitials sites in the $Yb_9Zn_{4+x}Sb_9$ and $Ca_9Zn_{4+x}Sb_9$ compositions [132], later expanding to other M-site elements across different 9-4-9 compounds [130, 131, 133–137]. These occupied interstitial sites result in compounds that are not valence-precise but allow carrier concentrations to be optimized. Thermoelectric tuning of the $Ca_9Zn_{4+x}Sb_9$ system has resulted in $zT > 1$ [138, 139] with a peak $zT = 1.1$ at 875 K [35]. These interstitially stabilized compounds make up a sizeable group $A_9M_{4+x}Pn_9$ (A = Yb, Eu, Ca, Sr; M = Mn, Zn, Cd; Pn = As, Sb, Bi), and in most cases, share a like structure type (*Pbam*). Exceptions do exist, however, as is the case with $Ca_9Zn_{4+x}As_9$ and $Ca_9Mn_{4+x}Sb_9$ (*Pnma*) [131].

These partially occupied sites decrease lattice thermal conductivity by adding complexity through additional disorder. Cation substitution has also been explored in the case of Eu in $Ca_9Zn_{4+x}Sb_9$ where the Eu atoms preferentially replaced Ca sites far away from the Zn-Sb structures. This substitution reduces lattice thermal conductivity by introducing point defects for the composition $Ca_{6.75}Eu_{2.25}Zn_{4.7}Sb_9$, highlighting the tunability of this material system and Zintl phases as a whole.

2.2 Summary of Research Direction

While Zintl phases are a promising class of thermoelectric materials that have been studied intensively since 2005, there are still several important fundamental questions that remain unanswered. These include questions related to anisotropic transport and how it relates to the crystal structure, and the role played by intrinsic defects in determining carrier concentration. Additionally, the field of Zintl compounds is ever expanding and through the use of exploratory single crystal growths and the careful selection of starting compounds, novel compounds and structure types can be discovered that may be promising thermoelectric candidates.

2.2.1 Anisotropic Transport

Anisotropic materials have the potential to possess exploitable high conductivity in strongly bonded directions, yielding a preferred crystallographic orientation for thermoelectric applications [16, 26, 64, 65, 67]. In general, electrical conductivity has been found to vary more significantly than the Seebeck coefficient, which remains relatively constant as a function of direction. This is because electrical conductivity is related to inertial effective mass, which is a tensor property, while the Seebeck coefficient is determined primarily by the DOS effective mass, which is a scalar.

Many Zintl structure types are highly anisotropic, often containing features such as covalent chains, layers, or even tunnels. This suggests, according to DFT studies [140–142], that their electronic and thermal properties might be highly anisotropic as well. Unfortunately, all of the previous studies of thermoelectric transport properties in Zintl phases discussed above involved

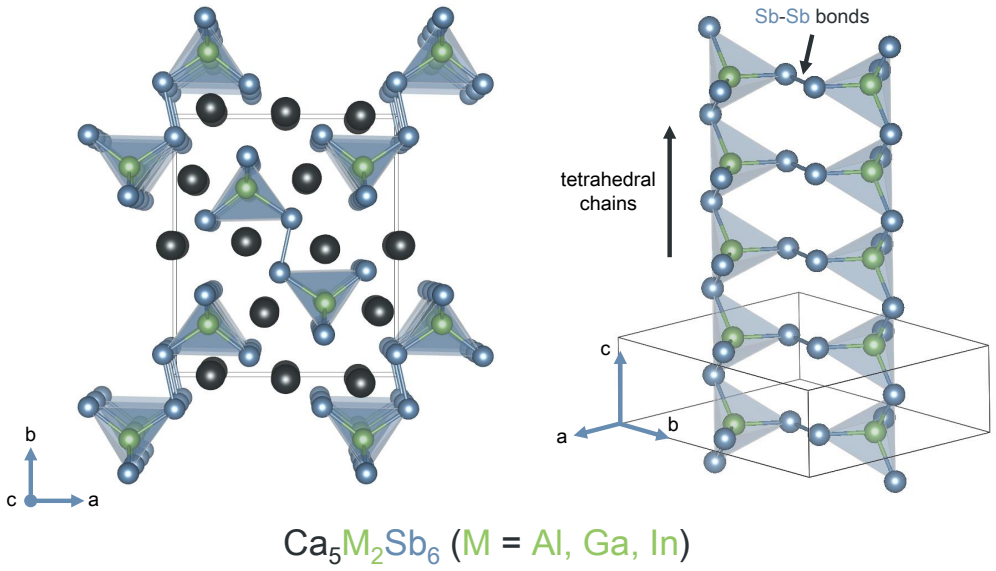

Figure 2.4: The orthorhombic unit cell of Zintl phases $Ca_5M_2Sb_6$ (M = Al, Ga, In) (left) with isolated one-dimensional polyanionic chains connected by Sb-Sb bonds (right).

polycrystalline samples, meaning that the reported transport properties were averaged over all crystallographic directions.

The $Ca_5M_2Sb_6$ (M = Al, Ga, Sb) Zintl system is an example of a structure predicted to exhibit extreme anisotropy in the inertial effective mass. The $Ca_5M_2Sb_6$ structure, shown in Figure 2.4, possesses complex bonding that adheres to the octet rule under the assumption that each bond is either purely ionic or covalent. Valence balance is achieved between five Ca^{2+} atoms and the anionic $(M_2Sb_6)^{10-}$ sub-structure. The anionic sub-structures consist of parallel tetrahedral chains formed from polar covalent M-Sb bonds, which are connected to neighboring chains by covalent Sb-Sb bonds. The bridging atoms are given a valence of Sb^{1-}, with two Sb^{1-} shared between two tetrahedra, and two Sb^{2-} that are only bonded to a single M atom. According to DFT calculations $Ca_5M_2Sb_6$ Zintl phases exhibit particularly anisotropic behavior due to these one-dimensional polyanionic chains [2]. These calculations have shown a high degree of inertial band mass anisotropy, which is evident in the electronic band structures shown in Figure 2.5. The band structures of all three compounds (M = Al, Ga, In) reveal significantly lighter effective mass in the c-direction ($m_c^* < m_a^*, m_b^*$).

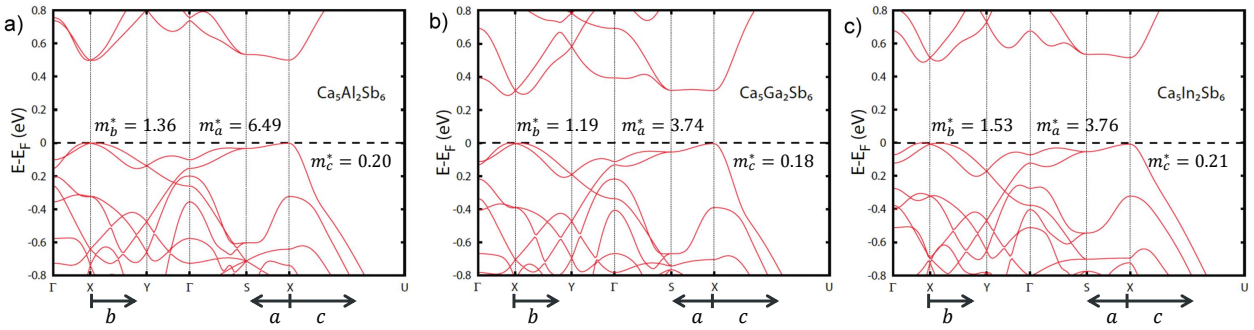

Figure 2.5: Previously reported band structures of $Ca_5M_2Sb_6$ (M = Al, Ga, In) compounds, illustrating a high degree of anisotropy in the valence band. The band mass (m^*_{X-U}) parallel to the anionic structures is lighter than the other perpendicular directions (m^*_{X-S} and $m^*_{X-\Gamma}$) [2].

By using the band structure from DFT and the Boltzmann transport model, Thunis et al. [3], showed that the anisotropy in the $Ca_5M_2Sb_6$ (M = Al, Ga, In) system leads to enhanced thermoelectric properties in the c-direction, parallel to the tetrahedral chains. Highly anisotropic electrical conductivity is predicted as shown in Figure 2.6(left), with a significantly higher conductivity in the c-direction than the a- and b-direction. The dashed curves show the average of the three directions, which is equivalent to the conductivity of polycrystalline samples ($n = 7 \times 10^{19}$ cm^{-3}). In contrast, the predicted Seebeck coefficients remain relatively isotropic, as shown in Figure 2.6(center). Overall, the preferential c-direction results in a superior power factor ($\alpha^2\sigma$), shown in Figure 2.6(right).

The calculations shown in Figure 2.6 make several assumptions about the single crystal properties that require more detailed investigations: First, the mean free time of electrons between collisions (τ) was set empirically so the "average" conductivity value would agree with the experimental polycrystalline conductivity reported in ref. [2]. Since τ for electrons is a challenging portion to calculated from first principles (it remains unclear if τ is anisotropic), experimental characterization is needed. One approach to experimentally estimate τ is to use measured mobility coupled with the effective mass predicted from DFT to extract a better estimate for τ for electrons. Another gap in literature on this system is lack of phonon calculations. Therefore detailed calculations of the anisotropy of the lattice thermal conductivity in this family of Zintl compounds does not yet exist. However, while DFT can be used to readily predict phonon velocities, accurate predictions

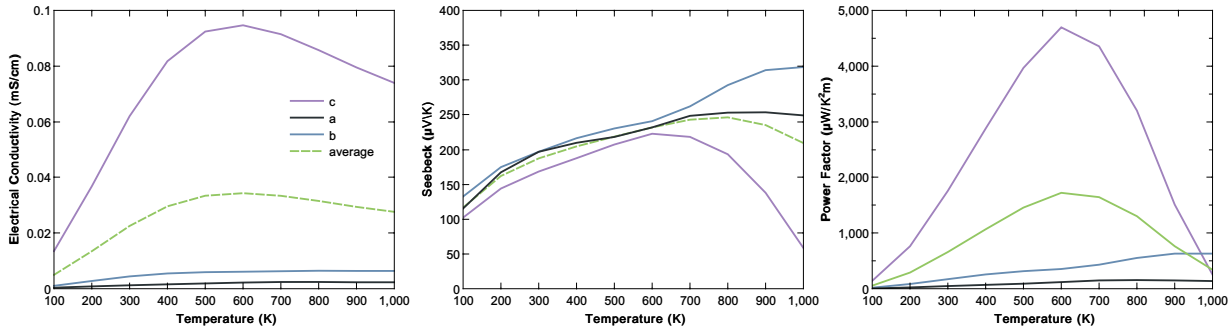

Figure 2.6: DFT calculations for electrical conductivity (left), Seebeck coefficient (center) and power factor (right) in different crystallographic directions along with the polycrystalline average [3].

of scattering rates (phonon τ) in complex materials remain challenging, and should be investigated experimentally.

Nearly all past studies of Zintl phases have focused on polycrystalline samples for characterization, overlooking how the crystallographic dependence of σ, α, and κ_L affects thermoelectric properties. While layered structures such as Bi_2Te_3, and GeAs have been studied extensively, these are layered van der Waals gap materials with weak out-of-plane bonding, in stark contrast to the ionic and covalent bonds found in the $Ca_5M_2Sb_6$ (M = Al, Ga, In) system. The difference between these potentially anisotropic compounds and that of the van der Wall gap materials is important. While the van der Waal gap materials have a relatively anisotropic elastic tensor due to the weak inter-layer bonding, the $Ca_5M_2Sb_6$ compounds possess relatively isotropic behavior. Figure 2.7 compares the Young's modulus tensor along different crystallographic planes for Bi_2Te_3 (top) and $Ca_5In_2Sb_6$ (bottom). Additionally, the Fermi surface of $Ca_5In_2Sb_6$ is illustrated in Figure 2.7(right) where it behaves as a pseudo one-dimensional electrical conductor. The isotropic elastic behavior of $Ca_5M_2Sb_6$ compounds translates into a mostly isotropic speed of sound which is a factor in defining κ_l in Equation 1.15 by the phonon velocity. From this, it is surmised that nominally low κ_l found in the $Ca_5M_2Sb_6$ compositions can be retained.

In order to investigate this anisotropic behavior, single crystals must be first grown. Single crystal $Yb_5Ga_2Sb_6$ has been grown from a Ga flux [106], offering a potential synthesis route for the $Ca_5M_2Sb_6$ (M = Al, Ga, Sb) system given its similar structure, but characterization of the crystals

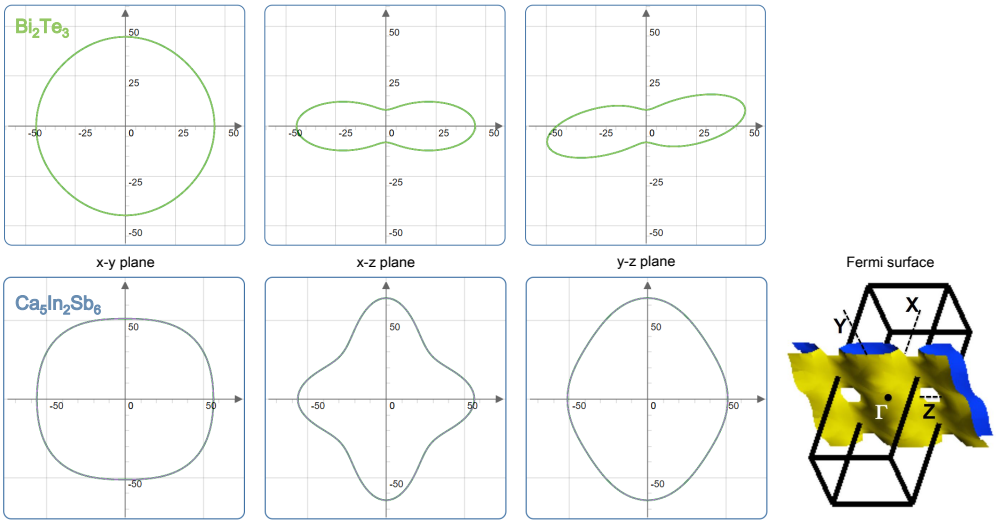

Figure 2.7: Young's modulus tensor with respect to crystallographic orientation for anisotropic Bi_2Te_3 (top) and approximately isotropic $Ca_5In_2Sb_6$ (bottom) [4]. Fermi surface of $Ca_5In_2Sb_6$, a pseudo one-dimensional electrical conductor [3] (right).

in different crystallographic directions was not accomplished, as the flux grown crystals were small and measurements perpendicular to the growth direction cannot be accomplished by hand.

In this work, $Ca_5M_2Pn_6$ (M = Al, Ga, In; Pn = Sb, Bi) Zintl phase crystal growth from a flux is detailed (Chapter 3), and electronic conductivity measurements of selected crystals in two crystallographic directions are discussed (Chapter 4).

2.2.2 Characterization of Defects

Intrinsic point defects play an important role in thermoelectric optimization of materials, because they impact charge carrier concentration. Intrinsic defects are present at all temperatures above absolute zero, since their formation increases configurational entropy, leading to a decrease in free energy [143]. Point defects can be both beneficial and harmful in thermoelectrics. On one hand, they may scatter short-wavelength phonons by adding complexity to a structure. However, some types of defects pin the Fermi level, limiting the carrier concentrations that can be obtained by doping. The presence of defect types in a material is governed by the corresponding defect formation energy with extrinsic defects incorporated deliberately as dopants. This defect energy can be influenced by growth conditions, allowing for defect engineering of thermoelectric candidate

materials. Identifying and understanding the conditions that foster useful defects can lead to a better understanding of a material and further optimization.

While Zintl compounds are generally considered to be line compounds, the reality is that each composition has a certain line width due to the presence of intrinsic point defects. Intrinsic defect concentrations are determined by their formation energies, which change based on growth conditions (*e.g.*, which phase the compound is in equilibrium with during growth). DFT has been used extensively to predict defect concentrations in Zintl phases [140–142], but few systems have been characterized experimentally. Such calculations of defects have been applied to compounds such as Mg_3Sb_2 where changing the growth environment has been predicted to influence the defect chemistry to change the dominant charge carrier type. This compound, grown under stoichiometric mixtures is persistently *p*-type, where holes are the dominant carrier due to Mg vacancies. However, with changes to the growth environment, electrons can become the dominant carrier as is evidenced by the recent success of *n*-type Mg_3Sb_2 ($zT = 1.51$ at 716 K) [33] grown in Mg-rich conditions. Defect formation energies are compared for both Sb- and Mg-rich growth conditions in Figure 2.8. Experimental investigation of intrinsic defects is most easily accomplished using single crystal X-ray diffraction, either with a laboratory or synchrotron source. Both require high quality single crystals produced from different growth conditions. The defect chemistry of this system is further investigated in Chapter 5 for both Sb- and Mg-rich single crystal synthesis where vacancies and interstitial sites are identified and quantified in collaboration with researchers at the Max Planck Institute for the Physics of Complex Systems in Dresden, Germany.

2.2.3 Unexplored Phase Space

The Zintl phase space is immense, with new phases still being discovered [44, 127, 134, 144]. These new phases are typically discovered using exploratory flux growths, where elements are melted together into a molten mixture before solidifying into single crystals. Small single crystals can then be picked out and characterized structurally using SC-XRD.

While a great deal of effort has been focused on the discovery and characterization of new

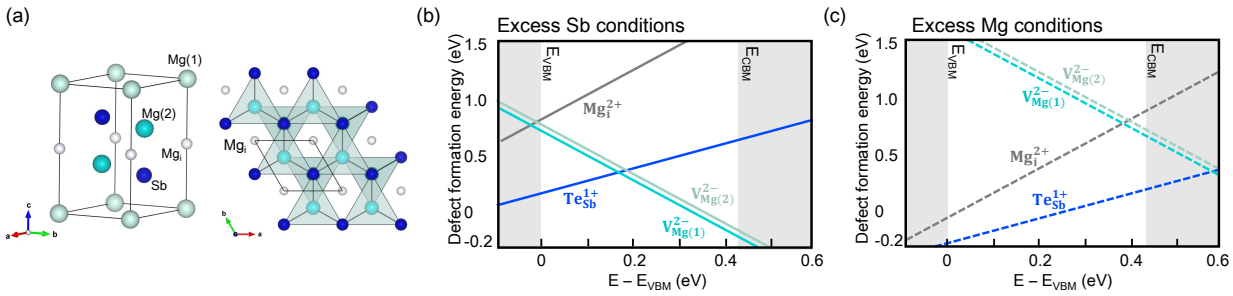

Figure 2.8: (a) Crystal structure of Mg_3Sb_2 with proposed interstitial sites. (b) Defect formation energy for Sb-excess Mg_3Sb_2 with Fermi level at 900 K. (c) Defect formation energy for Mg-rich Mg_3Sb_2 with undoped Fermi level at 900 K [5].

ternary Zintl phases, the vast quaternary phase space is relatively unexplored due to its inherent complexity. However, with increased complexity comes the opportunity to further suppress κ_l and additional routes to tuning properties.

The Ca-In-Zn-Sb composition space is a promising area to search for thermoelectric materials. This space includes the promising thermoelectric candidates Zn_4Sb_3 [29], $CaZn_2Sb_2$ [145], and $Ca_9Zn_{4.5}Sb_9$ [35]. In Chapter 6, the discovery of a new quaternary Zintl phase $Ca_9Zn_{3.1}In_{0.9}Sb_9$, which was discovered as a by-product during the attempted growth of Zn-doped $Ca_5In_2Sb_6$ is detailed. The new $Ca_9Zn_{3.1}In_{0.9}Sb_9$ structure was solved with assistance from collaborators at the University of Delaware. Measurements of the electrical resistivity of the $Ca_9Zn_{3.1}In_{0.9}Sb_9$ crystals were performed at Michigan State University and showed results similar to that of $Ca_9Zn_{4.5}Sb_9$ compounds [35].

CHAPTER 3

CRYSTAL GROWTH FROM MOLTEN METAL FLUX

3.1 Introduction

$Ca_5M_2Sb_6$ (M = Al, Ga, In) Zintl phases have been reported to be promising thermoelectric materials with zT values ranging from 0.35 – 0.7 when optimally doped with either Na [111], Zn [1, 110, 146] or Mn [147]. However, all of these studies focused on polycrystalline samples. Calculations of transport behavior in $Ca_5Al_2Sb_6$ have predicted enhanced thermoelectric performance in the poly-anionic chain direction with a maximum $zT = 1.37$ at 800 K [142] for crystals with an optimal carrier concentration of $\sim 6 \times 10^{19}$ cm^{-3} [141]. To experimentally characterize anisotropic properties of $Ca_5M_2Pn_6$ (M = Al, Ga, In; Pn = Sb, Bi) Zintl phases, it is necessary to grow high quality, macroscopic single crystals. Typically, large single crystals of semiconducting materials are grown using the Czochralski or floating zone techniques. In the case of the $Ca_5M_2Pn_6$ (M = Al, Ga, In; Pn = Sb, Bi) compounds, these methods are impractical as the melting behavior of these compounds is incongruent, the melt is highly reactive with containers, and the elements possess high vapor pressures. For these reasons, macroscopic (> 1 mm) single crystals of this structure-type have not been previously reported. In this work single crystal growth of $Ca_5M_2Pn_6$ (M = Al, Ga, In; Pn = Sb, Bi) Zintl phases from a molten metal flux is reported, along with single crystal structural characterization.

3.1.1 $Ca_5Al_2Sb_6$

The $Ca_5Al_2Sb_6$ composition [108] possesses an undoped peak $zT \approx 0.10$ at 725 K but is a promising thermoelectric candidate due to its inherently low lattice thermal conductivity ($\kappa_{min} = 0.53$ W/mK) and ability to be optimally doped. Optimizations to carrier concentration can be achieved with Na^{1+} doping on the Ca^{2+} site for $Ca_{4.75}Na_{0.25}Al_2Sb_6$ which produces a maximum $zT > 0.6$ at 1000 K [111]. Follow up studies have also investigated Zn^{2+} [146] and Mn^{2+} [147] *p*-type doping on the

Al^{3+} site with maximum $zT \approx 0.4$ in both cases.

The *n*-type compound has not been produced as the addition of electrons through doping will preferentially fill the Sb-Sb antibonding states. This destabilizing force could lead to the formation of Ca_3AlSb_3 [2].

3.1.2 $Ca_5Ga_2Sb_6$

From literature it is known that $Ca_5Ga_2Sb_6$ behaves as an intrinsic semiconductor possessing a smaller band gap (E_g = 0.43 eV) than either the Al (E_g = 0.65 eV) or In (E_g = 0.64 eV) analog with this difference explained in part due to relative electronegativities [2]. It also has the highest bipolar contribution to thermal conductivity due to its smaller band gap. Room temperature measurements where this effect is minimal place its thermal conductivity between that of the Al and In analogs [2]. $Ca_5Ga_2Sb_6$ possesses reduced phonon velocities and improved carrier mobility when compared to its $Ca_5Al_2Sb_6$ counterpart and *p*-type doping of Zn^{2+} on the Ga^{3+} site has shown to be effective in modestly increasing performance with $zT \approx 0.35$ at 750 K for $Ca_5Ga_{1.9}Zn_{0.1}Sb_6$ [110]. This peak zT value, however, is smaller than its counterparts due to the smaller band gap.

3.1.3 $Ca_5In_2Sb_6$

Like its counterparts, $Ca_5In_2Sb_6$ behaves as an intrinsic semiconductor with low *p*-type carrier concentration. This carrier concentration can be optimized with *p*-type doping of the In^{3+} site with Zn^{2+}. While the undoped $Ca_5In_2Sb_6$ composition has a peak $zT \approx 0.15$, doped $Ca_5In_{1.9}Zn_{0.1}Sb_6$ has a peak $zT \approx 0.7$ at 1000 K [1]. $Ca_5In_2Sb_6$ also possess a band gap greater than the Ga composition, allowing for more effective doping than that determined by Zn-doping of $Ca_5Ga_2Sb_6$ [140]. $Ca_5In_2Sb_6$ possesses the greatest density of the $Ca_5M_2Sb_6$ (M = Al, Ga, In) compounds with lattice stiffness decreasing with heavier M atoms. This translates to a lower bond strength and a softer crystal structure, leading to lower thermal conductivity.

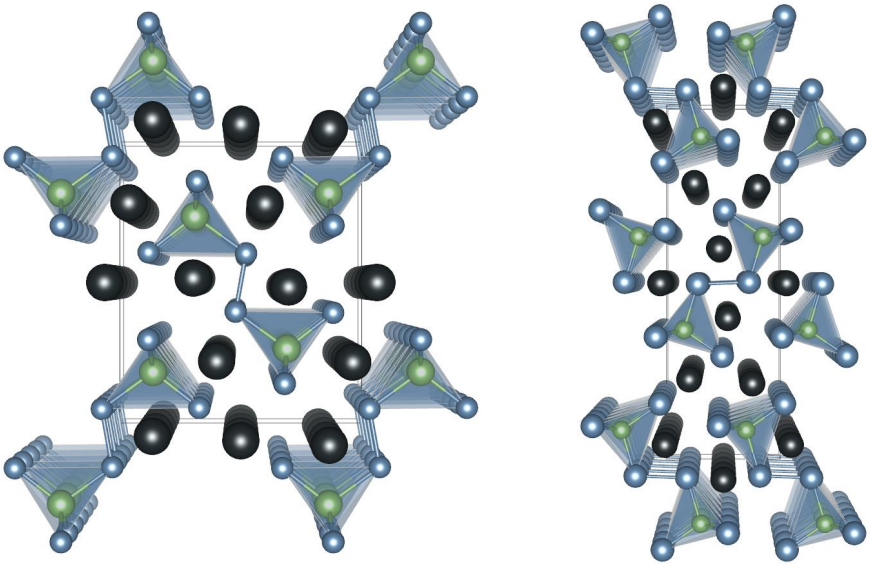

Figure 3.1: Comparison of the chain packing between the $Ca_5Ga_2As_6$ (left) and $Ca_5Al_2Bi_6$ (right) structure-types. The $Ca_5M_2Sb_6$ (M = Al, Ga, In) compounds belong to the $Ca_5Ga_2As_6$ structure-type with the difference being how the polyanionic chains are packed into the unit cell.

3.1.4 $Ca_5Al_2Bi_6$

The $Ca_5M_2Sb_6$ (M = Al, Ga, In) compounds all share a like structure-type, while $Ca_5Al_2Bi_6$ [148] takes on a different structure-type. The $Ca_5Al_2Bi_6$ structure-type compounds have a mix of metallic and semiconducting behavior. Both $Ca_5Al_2Bi_6$ and $Yb_5M_2Sb_6$ (M = Al [104, 105], Ga [106], In [107]) systems possess either no band gap, yielding poor thermoelectric performance with $zT < 0.15$ [149]. The $Sr_5In_2Bi_6$ [102] composition exhibits semiconductor behavior (E_g = 1.5 eV) according to initial band structure calculations, providing some hope for additional studies into the compound as a potential thermoelectric. These two structure-types are compared in Figure 3.1 with with the difference being how the polyanionic chains are packed into the unit cell.

3.2 Background - Single Crystal Growth

Single crystals can be produced by a variety of methods that utilize either a gas, liquid or solid state material to atomically arrange a quantity of compound into a single crystal. Growth from vapor can be accomplished by epitaxial processes, sublimation-condensation and sputtering among others [143]. Vapor transport methods are occasionally used in this work to remove undesirable flux

from single crystal samples. This method was not used to grow single crystals due to complexities arising from the selection of a proper transporting agent and unfavorable partial pressures of the crystalline elements.

Solid-state growth methods are primarily driven by atomic diffusion. Strain annealing, sintering, heat treatment, devitrification, polymorphic phase changes, precipitation from solid solution, and quenching are some examples of solid growth methods [143]. These techniques are more associated with grain growth than single crystal production as their atomic diffusion mechanisms are extremely slow making single crystal production, even in a laboratory environment, prohibitively time consuming. Many of the $Ca_5M_2Pn_6$ (M = Al, Ga, In; Pn = Sb, Bi) compounds discussed in this work were originally discovered using solid state growth, in which the reactants were simply annealed to allow grains of the target phase to form. By crushing and separating the resulting small grains (perhaps 10-50 microns), sufficiently large crystals for structure determination using SC-XRD could be obtained [108, 109, 148, 150, 151]. These crystals would not be large enough for transport measurements, however. In this work, sintering was used as an intermediate processing step to condense polycrystalline samples but stopped short of producing single crystals.

The liquid-to-solid crystallization process is most often used to obtain large bulk single crystals. Major methods include the floating zone, Bridgman, Czochralski, micro-pulling down, Verneuil, and flux growth [152], the latter of which is leveraged in this work. The atomic level processes in all of these methods can be broken into three parts, beginning from a disordered liquid phase:

i. *Supersaturation* is achieved in the system allowing crystal growth to propagate as long as supersaturation/supercooling of the liquid melt is maintained. Supersaturation is the driving force for nucleation and can be expressed as the difference in chemical potential of an atom/molecule in the solution, μ_s, and in the single crystal, μ_c,

$$\Delta\mu = \mu_s - \mu_c. \tag{3.1}$$

When $\Delta\mu > 0$ then the solution is defined as supersaturated while a negative value implies

decomposition of the solid [153]. In turn, this quantity can be related thermodynamically to the temperature,

$$\Delta\mu = kT \ln S_r, \tag{3.2}$$

where k is the Boltzmann constant, T is the temperature, and S_r is the supersaturation ratio. Supersaturation is the driving force behind crystal growth and relates to the decrease in free energy making crystal growth favorable [154]. Temperature is the experimental knob used to control the degree of supersaturation.

ii. *Nucleation* can be expressed generally as an atomic level process whereby atoms or molecules arrange themselves in ordered clusters. The work required to form these clusters is the difference in Gibb's free energy of the initial and final arrangements. For single crystal growth, nucleation of a single crystallite is desired, but in practice, many crystallites might compete.

iii. *Crystal growth* is the process by which atoms or molecules are incorporated into the surface of a crystal. This arrangement is governed by surface energy theory where the shape of the surface is driven by minimizing the surface energy. This energy determines the most appropriate placements for an atom to incorporate itself by minimizing the number of high energy dangling bonds [143]. Surface energy is a function of crystallographic orientation, and large differences in surface energy can lead to highly anisotropic crystal morphology.

3.2.1 Flux Growth

The flux technique is the general process by which crystallization occurs from a high temperature molten solution, known as a flux. This method has had success for a far ranging number of materials including metals, semiconductors, and oxides [143]. Here the elements of the desired crystal are dissolved in a flux that acts as a solvent. Due to the presence of the flux, crystals can precipitate well below their melting temperature. This characteristic is critical in the processing of incongruently melting compounds and for compounds that have ultra-high melting temperatures. Additionally,

phase transitions in congruently melting compounds can be avoided if the volume change associated with the transition leads to damage of the single crystal. The flux method also has the benefit of reducing thermal strain due to relatively cooler growth temperatures and a more gradual temperature gradient during cooling when compared to the floating zone technique.

One drawback of traditional flux growth is uncontrolled multi-nucleation. Nucleation can occur anywhere in the crucible, but typically initiates against the crucible walls. Extremely slow cooling rates are used to try to encourage fewer nucleation sites. Interference between competing facets can lead to intergrowth of crystallites. Because interference limits the maximum size of individual crystals, the typical crystal size is significantly smaller than that of other melt techniques. The selection of an appropriate flux can also be challenging, particularly in ternary and quaternary compounds with unknown phase diagrams, and the removal of flux post crystal growth is often problematic. The selection of an appropriate flux is elaborated on below in Section 3.2.2.1. Despite these drawbacks, traditional flux growths are still widely utilized because they do not require expensive specialized equipment, and the growth conditions are relatively repeatable. Small scale growths can also be completed quickly for exploratory studies, making it a cost- and time-effective solution for compounds with unknown melting behavior. The floating zone and Czochralski methods typically require a ten-fold increase in the amount of starting compound.

The flux growth setup is illustrated in Figure 3.2 where the desired phase, which in this case is portions of a pre-synthesized polycrystalline pellet is loaded into the growth crucible along with elements used as the flux. Here two crucibles are loaded with open ends facing each other, separated by a sieve [155]. The growth is then heated until the entire mixture is liquid and slow cooled past the point where crystallization of the desired phase occurs, still surrounded by the liquid flux. The flux growth is then removed at this elevated temperature, flipped upside down and centrifuged, to separate the grown crystals from the flux. These crucibles are contained in a sealed quartz ampule. Quartz makes an appropriate thin-walled container for many crystal growths due to its excellent thermal shock resistance, low coefficient of thermal expansion, and good chemical resistance. The sealing of a quartz ampule also ensures control over the growth atmosphere, pressure

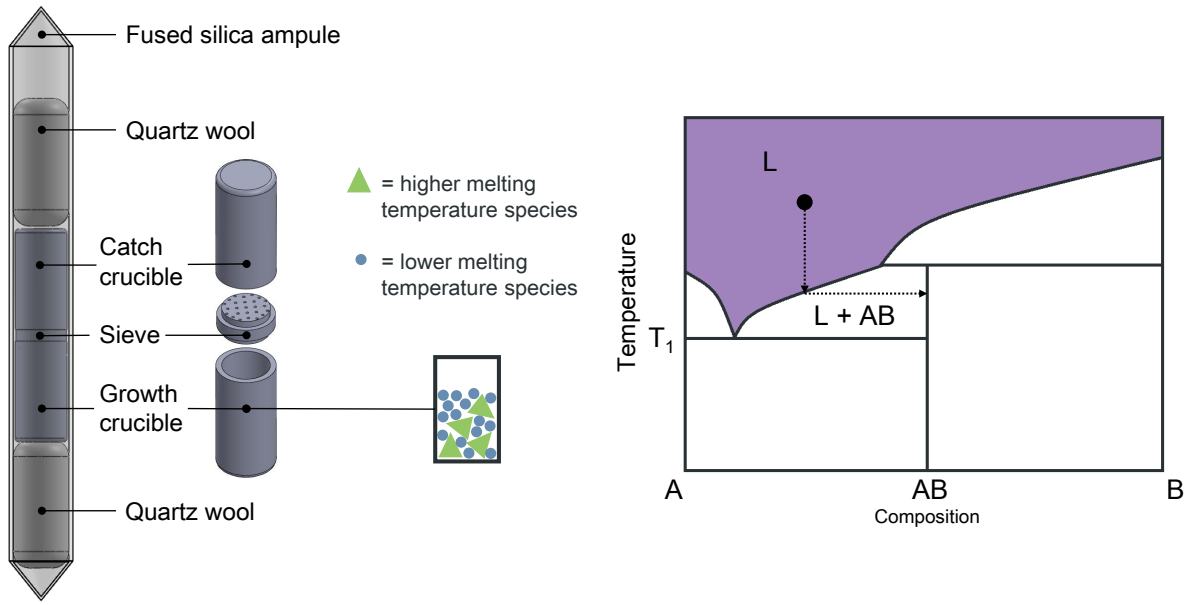

Figure 3.2: Schematic diagram of a flux growth ampule (left), containing quartz wool for cushioning during transport and centrifuging, growth crucible containing the compound and flux while the catch crucible is empty. The two crucibles are separated by a alumina sieve to catch crystals and drain liquid flux. Flux growth can be used off stoichiometry to grow incongruent melting compounds (right).

and vaporization and provides a protective environment for volatile material containing samples [156]. Additionally quartz is compatible with standard Al_2O_3 crucibles up to temperatures in excess of our expected experimental range [157].

3.2.2 Flux Growth of Zintl Phases

Many Zintl phases are incongruently melting compounds and/or highly reactive as a melt. If an incogruently-melting compound is cooled from the liquid phase of the target stoichiometry, the result will never be a phase pure sample. There is always a neighboring high-melting temperature compound that will crystallize first. The flux growth method is appropriate for incongruently melting compounds, as illustrated in Figure 3.2(right), because the melt can have an off stoichiometry composition. If AB is the target phase, then one uses an A-rich flux. When the melt is cooled in to L+AB region, the AB compound will begin to solidify. The remaining liquid can be removed by centrifugation as long as the temperature is above T_1. This is critical in systems where the melting

behavior of a system is unknown, as is the case of the $Ca_5M_2Pn_6$ (M = Al, Ga, In; Pn = Sb, Bi) phase compounds. Subsequent testing revealed incongruent melting behavior that makes crystal growth by other methods difficult.

Flux growths are very widespread for Zintl compounds [33, 132, 158], including several 5-2-6 family compounds [144]. Single crystals of Zintl phase $Yb_5Ga_2Sb_6$ have been successfully grown from a Ga-flux with its resistivity successfully characterized in the preferred growth direction [106]. This compound takes on the same structure as the $Ca_5Al_2Bi_6$ structure and acts as a proof of concept for our $Ca_5M_2Pn_6$ (M = Al, Ga, In; Pn = Sb, Bi) growths.

This method also provides flexibility with a number of experimental parameters that can be adjusted including crucible size, temperature, heating rate, holding times, cooling rate, extraction temperature, and flux composition among others. These parameters can be optimized and tracked to produce larger crystals in repeatable growth conditions [159].

3.2.2.1 Metallic Flux Selection

The selection of an appropriate flux for growth of Zintl phases can also be challenging, in particular in ternary and quaternary compounds with unknown phase diagrams. Appropriate flux candidates are selected based of a number of factors, including low melting temperature, a significant discrepancy between its melting temperature and boiling point, likelihood to separate from grown crystals by either physical or chemical means, and, most importantly, an inability to form stable binary or ternary compounds with any of the reactants [160]. Selected flux elements are listed in Table 3.1 along with their melting temperatures (T_m), viscosity at their melting temperature ($\eta(T_m)$), and solid and liquid (at T_m) densities. A low viscosity makes the centrifuging process more effective, while similar density to the target phase prevents large composition gradients in the melt. Chemical etching can remove excess flux but the etching process can also potentially attack the grown crystals.

Aluminum flux

Aluminum is a common flux [161–165] due to its low vapor pressure (2327°C, 1 atm.), and low viscosity as shown in Table 3.1. If centrifuging is not completely successful, aluminum flux can

Table 3.1: Viscosity data for selected flux elements along with density information for single crystal target compounds.

			Density (g/cm^3)	
	T_m (°C)	$\eta(T_m)$ (mPa s)	Solid	Liquid (T_m)
Al	660	1.30	2.70	2.38
Bi	272	1.80	9.78	10.05
Ga	30	2.04	5.91	6.10
In	157	1.89	7.31	7.02
Pb	328	2.65	11.34	10.66
Sb	631	1.22	6.70	6.53
Sn	232	1.85	7.27	6.99
Zn	420	3.85	7.14	6.57
$Ca_5Al_2Sb_6$	–	–	4.26	–
$Ca_5Al_2Bi_6$	–	–	6.25	–
$Ca_5Ga_2Sb_6$	–	–	4.70	–
$Ca_5In_2Sb_6$	–	–	5.00	–

also be removed chemically by NaOH [166] or HCl [165] solutions. Aluminum vapor, however, reacts with quartz ampules, compromising the internal inert vacuum atmosphere sealed inside, $4Al + 3SiO_2 \rightarrow 2\alpha\text{-}Al_2O_3 + 3Si$ [167, 168].

In order to diminish the severity of this reaction, growths can be performed more quickly or quartz tubes can be carbon coated. Another drawback of using an Al flux is that it possesses a higher melting temperature than most of the fluxes listed in Table 3.1. This is not an issue provided that the removal and centrifuge temperature are higher. For the prospective $Ca_5Al_2Sb_6$ growth, this was not an issue due to the high extraction temperature.

Bismuth flux

Bismuth is a common flux [169–172] that has also proven effective as a self-flux [173, 174], possessing a low melting temperature and vapor pressure (1627°C, 1 atm.). In this work, Bi was used as a self-flux for the growths of $Ca_5Al_2Bi_6$ and single crystal solubility study for the $Ca_5Al_2Pn_6$ (Pn = Sb, Bi) system. Bismuth flux can also be removed with dilute hydrochloric acid.

Gallium flux

Gallium is a popular flux [175–177] due to its extremely low melting temperature and vapor pressure (2427°C, 1 atm.). A drawback of this element is that it tends to wet to the surfaces of grown crystals even after thorough centrifuging [166], possessing a higher viscosity when compared

to Al, In, and Sb as shown in Table 3.1. Excess Ga can be removed by soaking crystals in a 5 M I_2 dimethylformamide (DMF) solution where it is able to form soluble GaI_3 [178].

Indium flux

Indium is another popular [179–181] low melting point flux that has a propensity not to wet to crystal surfaces [166]. It also has a low vapor pressure (2167 °C, 1 atm.) and viscosity as shown in Table 3.1. Excess In flux can also be removed with diluted HCl solutions if centrifuging proves insufficient [181]. This makes for an ideal flux candidate for the $Ca_5In_2Sb_6$ single crystal growth.

Lead flux

Lead is another common flux choice [182–185] with low melting temperature and vapor pressure (1737°C, 1 atm.). Pb does not form binary phases with Sb [186], Ga [187], or Al [188, 189], and binary phases are only formed with In at temperatures much lower than the extraction temperature for this work [190]. This flux choice suffers from wetting issues similar to that of Ga, and Sn, making it difficult to separate from grown crystals [166]. Secondly, it is highly toxic, complicating synthesis. Lastly, Pb is extremely dense and the homogeneity of the melt composition may suffer.

Tin flux

Tin is a promising flux due to its low melting temperature, low vapor pressure (2727°C, 1 atm.), and its general aversion to forming binary compounds [191, 192], making it a common choice for crystal growth [182, 193–195]. Sn unfortunately wets to grown crystals more readily than most fluxes. In order to remove flux from crystal surfaces, a Hg bath can be used that can be distilled away through evaporation. A non-toxic alternative is soaking in Ga, but a process to remove the Ga is then needed [196]. This flux is appealing in the growth of $Ca_5Al_2Sb_6$ as the Al-Sn system is a simple eutectic that forms no binaries [197].

Antimony flux

While antimony has a higher melting temperature than most of the fluxes listed here, it possess a sufficiently low vapor pressure (1617°C, 1 atm.), and very low viscosity listed in Table 3.1. While examples of it being used as a flux exist [198], it is not commonly used as it forms stable phases with rare-earth elements that are preferentially grown in place of the desired phase [166]. This work

utilizes at least an Sb partial flux for all of the $Ca_5M_2Pn_6$ (M = Al, Ga, In; Pn = Sb, Bi) compounds.

3.2.2.2 Crucible Selection

Alumina (Al_2O_3) crucibles were used for all flux growth trials as it is a cost effective option that is stable up to high temperatures and chemically resistant to common low melting temperature flux elements such as Al, Bi, Cu, Ga, Ge, In, Pb, Sb, and Sn. High purity alumina crucibles are also widely available in many geometries and even specific crucible sets for flux growth that include compatible sieves [199]. Cleaning these crucibles is difficult if not impossible due to the molten elements penetrating into the grain boundaries of the crucible, making them a single use item [154].

3.2.3 Energy-dispersive X-ray Spectroscopy

Energy-dispersive X-ray spectroscopy (EDS) was used to perform elemental analysis of single crystals. This process uses accelerated electrons generated from an electron gun to irradiate a sample with the kinetic energy of these electrons. This electron kinetic energy is dissipated within the sample and generates characteristic X-rays of the atom struck by the electron by generating an electron hole that is then filled by an electron from an outer shell as shown in Figure 3.3(left). This process, a form of the photoelectric effect, emits X-rays that are collected and used to identify elements within a compound, based on the characteristic emission of the elements. Electron transitions of major lines, are illustrated in Figure 3.3(right) which are characteristic of the emitting atom. This analysis detects elements that are present in the outer most 10 nm of the sample making it heavily influenced by any flux elements that may remain.

An energy sweep on the order of keV is performed and a spectrum is collected with the area underneath the curve relating to the amount of each element present. Quantification of each element is typically calculated with the expression,

$$I_{ij} = KT(KE)L_{ij}\sigma_{ij}\int n_i(z)e^{-z/\lambda(KE)\cos\theta}dz, \tag{3.3}$$

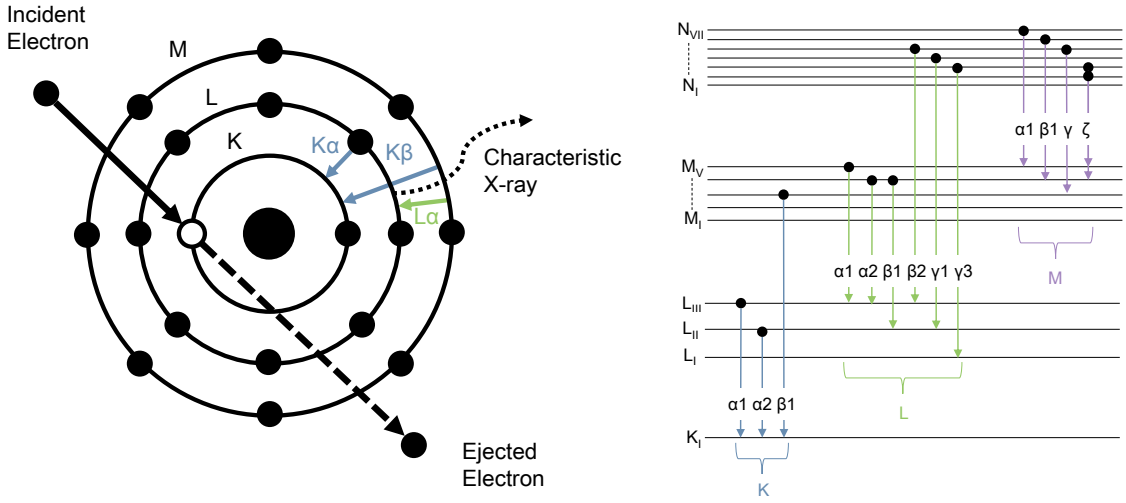

Figure 3.3: Characteristic X-ray production from incident electrons for EDS analysis (left). Electron transitions of major lines, characteristic of the emitting atom (right).

where I_{ij} is the area of peak j from element i, K is the instrument constant, $T(E_K)$ the transmission function of the analyzer, $L_{ij}(\gamma)$ the angular asymmetry factor for orbital j of element i, σ_{ij} the photoionization cross-section of peak j from element i, $n_i(z)$ the concentration of element i at a distance z below the surface, $\lambda(E_K)$ the inelastic mean free path length, and θ is the take-off angle of the photoelectrons. X-ray flux, area of the irradiated sample and the solid angle of the photoelectrons accepted by the apparatus are contained with the instrument constant K [200]. This expression assumes an amorphous sample structure while single crystals can generate peak intensities that deviate from expected values due to their ordered structure and orientation to the beam and detector.

3.2.4 Single Crystal X-ray Diffraction

SC-XRD is a non-destructive analytical technique that provides information on the structure of the crystal lattice including unit cell dimensions, atomic positions, site-ordering, bond-lengths and bond-angles [201]. A diffraction pattern is collected as the crystal is rotated through the X-ray beam. The spots generated in a diffraction pattern are termed reflections as they are reflected off of ordered parallel planes in the atomic structure, satisfying Bragg's law. From this diffraction pattern the unit cell can be determined (*a, b, c* and α, β, and γ). The $Ca_5M_2Pn_6$ (M = Al, Ga, In; Pn = Sb,

Bi) system of interest in this work forms the orthorhombic crystal structure where $a \neq b \neq c$ and $\alpha = \beta = \gamma = 90°$. The faces of this unit cell are typically the most apparent sets of planes and act as sources of diffraction that are designated by lattice indices, also known as Miller indices [202].

The X-ray source is created by bombarding a metal target, in our case Mo, with electrons produced by a heated filament and subsequently accelerated by an electric field. These high-energy electrons strike and displace an electron from a low orbital, like the process described for EDS but in the target rather than the sample. An electron from a higher orbital drops into the vacancy, emitting the excess energy of this transition as an X-ray photon as illustrated in Figure 3.3(left). The target material produces narrow characteristic lines of specific wavelengths [203]. In order to produce a monochromatic output from a Mo source, a secondary Zr filter is used to remove $K\beta$ radiation. Bragg reflections from the sample are measured on a scintillation counter that contains a phosphorescent material that produces a flash of light when an X-ray is absorbed [204].

This technique requires small (≈ 0.1 mm in longest diagonal direction), but excellent quality single crystals. The crystals must not possess significant imperfections (cracks, twinning, multi-crystals). Samples with well-defined twins can be analyzed, however any further disorder makes this method prohibitively difficult. As a general rule, the longest diagonal through the single crystal must not exceed the beam size.

Once data collection is complete the raw intensities are processed. Scaling is completed whereby reflections of the same index that were measured in multiple frames are given identical intensities. Next post-refinement is completed where usable data from partial reflection is recovered and spurious data removed through the process of data reduction [205].

3.3 Experimental Methods

3.3.1 Flux Growth

Flux growth experiments were carried out in a Thermo Fisher Scientific 1100°C box furnace with temperature maintained through a UP150 programmable controller and monitored with type K thermocouples. Al_2O_3 Canfield crucible sets were loaded into sealed quartz ampules at a vacuum

of less than 4×10^{-6} torr.

High purity elements were used in the synthesis of the various $Ca_5M_2Pn_6$ (M = Al, Ga, In; Pn = Sb, Bi) compounds, including: Al (Alfa Aesar: shot, approx. 4-8mm, 99.999%), Bi (Sigma-Aldrich: granular, 99.99+%), Ca (Sigma-Aldrich: dendritic pieces, 99.9%), Ga (Sigma-Aldrich: solid, 99.99%), In (Alfa Aesar: shot, 5mm & down, 99.9995%), Pb (Alfa Aesar: shot, 3mm, 99.999%), Sb (Alfa Aesar: shot, 6mm & down, 99.999%), and Sn (Alfa Aesar: shot, 3mm, 99.9999%). The overall melt compositions for the various growths are shown in Figures 3.7-3.10. The $Ca_5M_2Sb_6$ (M = Al, Ga, In) single crystals were all successfully grown from a temperature profile of room temperature to 900°C in 12 hours, followed by a soak for 2 hours then slow cooling to 730°C at a rate of 3°C/hr. The $Ca_5Al_2Bi_6$ single crystals only differed in their extraction temperature, which was 470°C.

3.3.2 Vapor Transport

Vapor transport was used in some cases to remove excess flux from single crystals growths. Samples were sealed inside a quartz ampule and placed horizontally in a MTI Corporation GSL-1100X tube furnace. The end with the sample was placed in the furnace, while the other end of the ampule was at room temperature, external to the furnace. Figure 3.4 shows a pair of samples being processed with $T_{\text{hot}} = 500$°C.

3.3.3 Material Characterization Techniques

3.3.3.1 Microscopy

Optical microscope images were taken with a Keyence VHX-600 up to 1000x magnification. Scanning electron microscope (SEM) was performed on a Zeiss Evo LS25, and a Tescan Mira 3XMH.

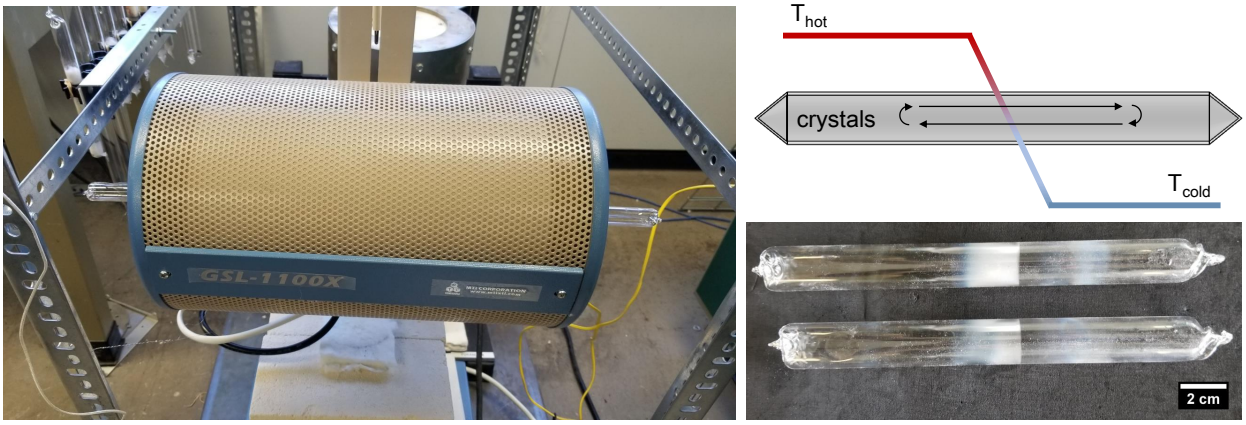

Figure 3.4: Horizontal tube furnace with two ampules positioned opposite each other (left). Illustrated temperature profile and vapor motion (top right) with deposited flux elements visible on ampules surface after processing (bottom right).

3.3.3.2 Energy-dispersive X-ray Spectroscopy

EDS was performed using an EDAX Apollo X module with an active area of 10 mm^2. Images were collected and processed with the Texture and Elemental Analytical Microscopy (TEAM) software suite to determine the approximate chemical composition of crystal and flux components. Single crystals were placed on conducting carbon tape to eliminate any potential charge build up. All samples evaluated were semiconducting or metallic in character.

3.3.3.3 Single Crystal X-ray Diffraction

Single crystal X-ray diffraction was performed using a Bruker-AXS Apex II CCD instrument shown in Figure 3.5 at 173 K, with reflection data acquired using a graphite-monochromated Mo Kα radiation source ($\lambda = 0.71073$Å) producing a 0.5 mm beam diameter. Data was integrated with SAINT [206]. Single crystals were cut down to an appropriate size with a surgical scalpel and mounted to a goniometer head. Samples were then held in a cold nitrogen stream to reduce thermal motion of the atoms and improves crystal scattering power, leading to a better quality structure.

Structures were solved using direct methods and refined on F^2 using SHELX [207] subroutines within the Olex2-1.2 crystallographic suite [208]. Reflections were merged using SHELXL with respect to the crystal class for the calculation of refinement. A preliminary rotation image was

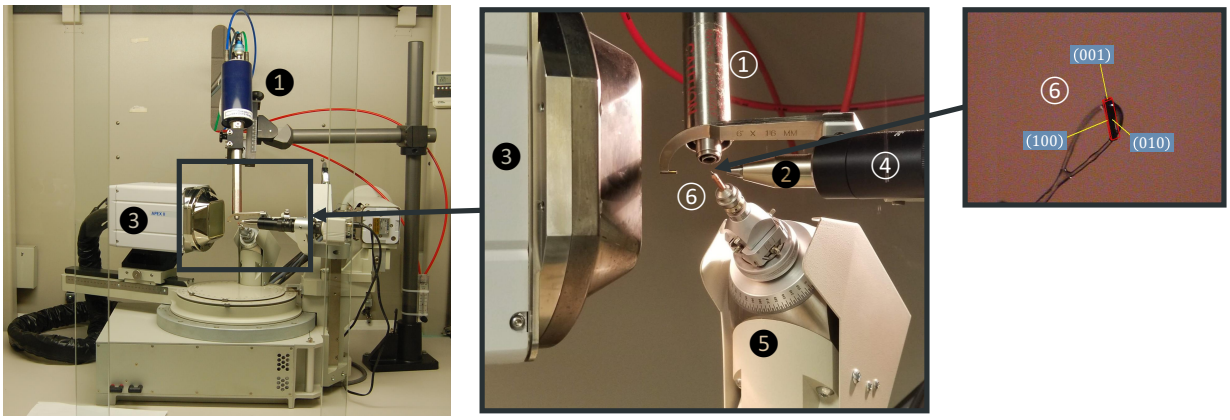

Figure 3.5: (1) Oxford 600 low temperature device, (2) X-ray emitter, (3) Charge-Integrating Pixel Array Detector (CPAD), (4) Camera for viewing crystal, (5) three-axis goniometer, and (6) sample mounted on nylon loop.

collected to perform an initial quality check and determination of unit cell dimensions.

3.3.3.4 Differential Scanning Calorimetry and Thermogravimetric Analysis

Differential scanning calorimetry (DSC) is a thermal analysis technique where the difference in the amount of heat required to increase the temperature of the sample and reference is recorded as a function of temperature [209]. While DSC is a thermal analysis technique focused on heat, thermogravimetric analysis (TGA) is focused on the mass of a substance in response to heat. TGA is useful for identifying phase transitions, absorption, adsorption and desorption [210]. Simultaneous DSC/TGA experiments were conducted on a TA Instruments SDT Q600 system and carried out at the Platform for the Accelerated Realization, Analysis, and Discovery of Interface Materials (PARADIM) at Johns Hopkins University.

3.4 Results & Discussion

3.4.1 Phase Diagram Determination and Crystal Growth Optimization

In this study, single crystals were grown in four different ternary systems ($Ca_5M_2Sb_6$ with M=Al, Ga, In, and $Ca_5Al_2Bi_6$). In each case, little initial knowledge of the ternary phase diagrams exists. Starting with only the binary phase diagrams, it was necessary to carry out exploratory synthesis to

identify selected tie lines, eutectic points, and liquidus surfaces in the regions of the phase diagram used for flux growth using powder and single crystal X-ray diffraction.

3.4.1.1 $Ca_5Ga_2Sb_6$

Single crystal growth began with the $Ca_5Ga_2Sb_6$ composition in part due to its chemical similarity with $Yb_5Ga_2Sb_6$, which has previously been reported to grow from a Ga flux. The Ca-Ga-Sb ternary phase diagram, shown in Figure 3.7, is constructed from the known binary phase diagrams [211–213] and includes the two ternary phases that are currently known to exist: fellow Zintl phase $Ca_{11}GaSb_9$ [214], and target phase $Ca_5Ga_2Sb_6$ [109]. Nothing was known about the solidification of the ternary compositions in this phase space. Our first aim was to determine the approximate melting temperature and whether or not $Ca_5Ga_2Sb_6$ melts congruently.

Both DSC and TGA analysis were performed using a polycrystalline $Ca_5Ga_2Sb_6$ sample (synthesis described in ref. [2]) from room temperature to 1000°C. From the data in Figure 3.6, significant heat flow into the sample at temperatures approaching 760°C is observed, which subsequent X-ray diffraction (XRD) analysis would confirm as incongruent melting. Rietveld analysis was performed to determine that, upon melting and re-solidification, the compound had partly decomposed into $Ca_{11}Sb_{10}$, Sb, and Ga. From the presence of decomposition products, it can be concluded that this compound is incongruently melting, making flux growth an appropriate growth method. Further, the Ca-rich melt was found to react severely with the Al_2O_3 crucible, presumably forming calcium oxide with the alumina crucible, $Al_2O_3 + 3Ca \rightarrow 3CaO + 2Al$. This suggests that crystal growth of this compound in Al_2O_3 crucibles (one of the most cost-effective options) requires a flux to dilute the reactive Ca.

The Ca-Ga-Sb ternary phase diagram contains several high melting-temperature binary Ca-Sb and Ca-Ga phases. For this reason, initial focus is on fluxes rich in Ga and/or Sb, moving the total melt composition on the ternary phase diagram further away from Ca and the undesired ternary $Ca_{11}GaSb_9$. The only binary between Ga and Sb is GaSb (T_m = 712°C), which can be avoided entirely if the extraction temperature is sufficiently high. The $Ca_5Ga_2Sb_6$ melting temperature is

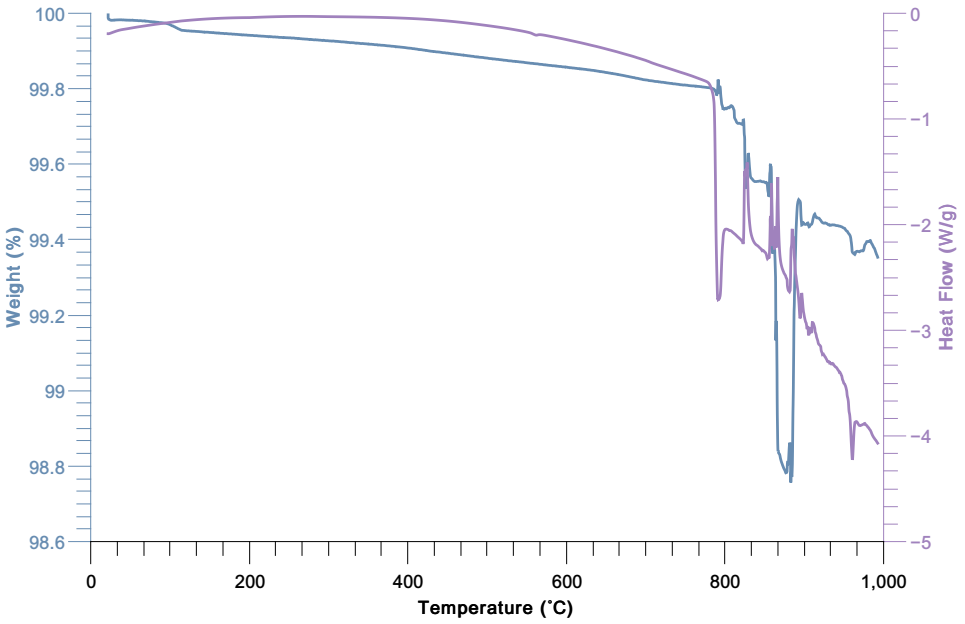

Figure 3.6: DSC and TGA data for $Ca_5Ga_2Sb_6$ from room temperature to 1000°C shows incongruent melting beginning above 760°C.

approximated from the DSC/TGA results as $T_m \approx 780$°C, which led to the selection of an extraction window of approximately 720-750 degrees.

Several growths using self-flux of different compositions were attempted, including Ga, Ga+Sb, and Sb. Self-fluxing elements were typically targeting a 9:1 ratio of flux to polycrystalline $Ca_5Ga_2Sb_6$ precursor as a precaution against reactivity. The overall compositions of the melt for each growth are shown as the square symbols in Figure 3.7, with green and red squares representing successful and unsuccessful crystal growths, respectively.

A Sb_{20} flux was attempted but failed to produce single crystals of the desired phase, producing polycrystalline $Ca_5Ga_2Sb_6$, Sb, and very small amounts of GaSb and $CaSb_2$. From these XRD results a tie line connecting $Ca_5Ga_2Sb_6$ and Sb on the phase diagram can be inferred, with Ca-rich portions of the melt forming $CaSb_2$ and more Ga-rich portions forming GaSb. A $Ga_{34}Sb_{34}$ flux produced polycrystalline $Ca_5Ga_2Sb_6$, Sb and GaSb, while pure Ga fluxes produced polycrystalline $Ca_5Ga_2Sb_6$, $CaGa_4$, and elemental Ga. From these phase triangles a number of useful tie lines for this phase diagram are determined.

Non self-fluxes were also attempted with a Bi_{20} flux decomposing to $Ca_{11}Sb_{10}$, Ca_2Sb, Ga, and Bi. Sn fluxes (Sn_{81}, Sn_{115}, Sn_{130}, Sn_{288}) were also attempted but did not produce crystals. A smaller amount of Sn (Sn_{15-20}) was shown to produce crystals in the $Ca_5Al_2Sb_6$ trials but severe wetting issues made this an impractical choice even if lower amounts of Sn were found to be successful.

Ultimately, it was determined that $Ca_5Ga_2Sb_6$ crystals could be grown optimally in a $Ga_{73}Sb_{42}$ self-flux. Successful crystal growth yields crystals large enough to remain in the growth crucible side of the sieve after centrifuging. An optical image of these crystals is shown in Figure 3.7. A high temperature soak of 900°C for two hours was selected to ensure that elemental Ca was completely dissolve in the melt and that the elements were mixed homogeneously. An appropriately slow cooling rate of 3°C/hr was selected and remained unchanged while the flux composition was adjusted. Crystal growth size could potentially be improved by a slower cooling rate. These flux parameters in both temperature and flux composition ($M_{73}Sb_{42}$) translated directly to the $Ca_5In_2Sb_6$ and $Ca_5Al_2Sb_6$ compositions.

3.4.1.2 $Ca_5In_2Sb_6$

The ternary Ca-In-Sb phase diagram in Figure 3.8 is constructed from the known binary phase diagrams [212, 215, 216] along with the two ternary phases known to exist: fellow Zintl phase $Ca_{11}InSb_9$ [214, 217] and desired phase $Ca_5In_2Sb_6$ [109]. It is very similar to that of the Ca-Ga-Sb phase diagram, and it is also presumed that $Ca_5In_2Sb_6$ also melts incongruently. Similar to the Ga-analogue, In- and Sb-rich fluxes were favored as to better avoid growing the Ca-rich $Ca_{11}InSb_9$. This system benefits from only possessing a single lower melting point In-Sb binary, InSb ($T_m = 527$°C). This could potentially allow for a lower extraction temperature if needed. A pure Sb flux (Sb_{20}) was attempted but did not produce crystals mainly due to the existence of Ca_8In_3, with the polycrystalline $Ca_5In_2Sb_6$ decomposing to Ca_8In_3, $CaSb_2$ and elemental Sb. As evidenced by the phase diagram in Figure 3.8this flux narrowly misses the target phase. A useful phase triangle can be deduced from this however, concluding that a mixed Sb-In flux that is more

In-rich would have better results, by shifting the overall melt composition into the three-phase region bound by $Ca_5In_2Sb_6$, Sb, and InSb.

Single crystals of $Ca_5In_2Sb_6$ were successfully grown from an $In_{73}Sb_{42}$ flux with approximately 0.25 grams of polycrystalline $Ca_5In_2Sb_6$ used. This amount was enough to generate hundred to thousands of crystals per growth, largely dependent on the success of the spontaneous nucleation. An SEM image of the grown $Ca_5In_2Sb_6$ single crystals are shown in Figure 3.8. The surfaces of these crystals appeared cleaner than their $Ca_5Ga_2Sb_6$ counterparts, largely due to the poor wetting properties of Ga, which resulted in it adhering to crystal surfaces more readily than either In or Sb.

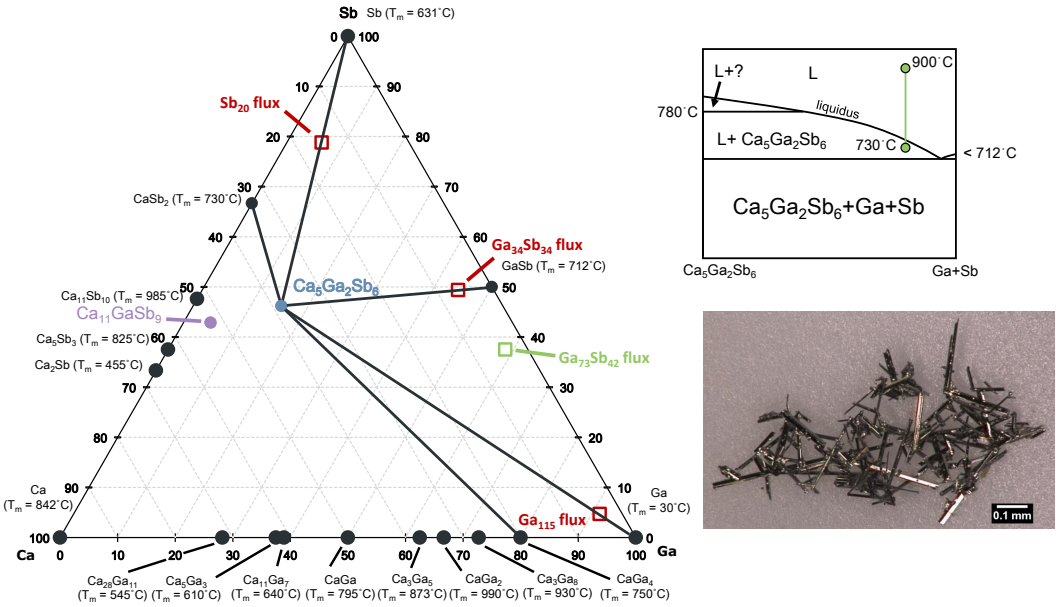

Figure 3.7: The Ca-Ga-Sb ternary phase diagram with known binaries (black), desired $Ca_5Ga_2Sb_6$ (blue), and other ternary phases (purple). Unsuccessful (red squares) and successful (green square) flux growths were used to determine the black tie lines. (upper right) A plausible pseudo-binary phase diagram was developed based on the successful flux growth. (lower right) optical image of grown crystals.

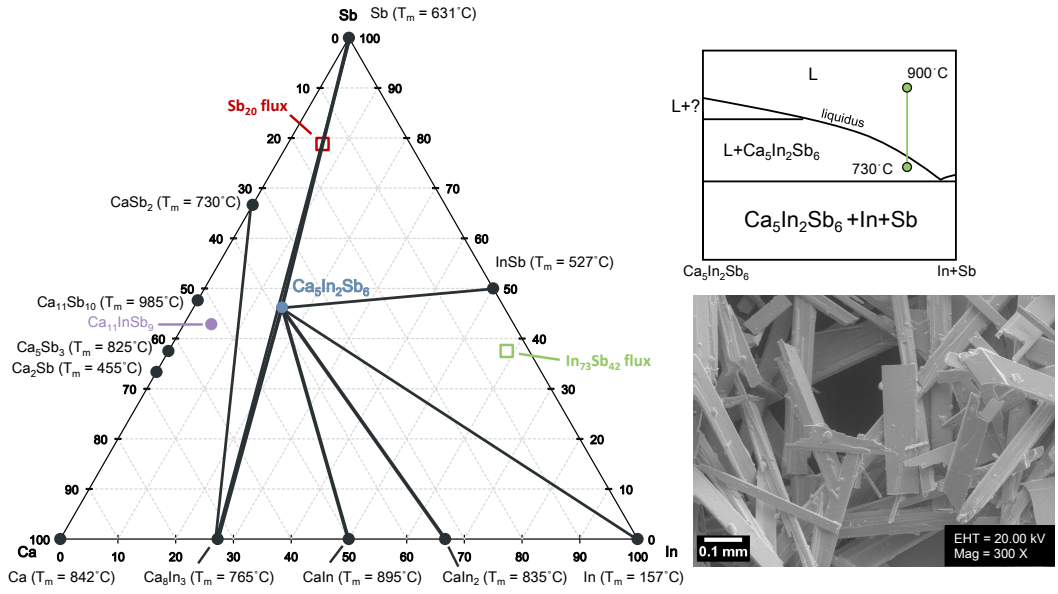

Figure 3.8: The Ca-In-Sb ternary phase diagram with known binaries (black), desired $Ca_5In_2Sb_6$ (blue), and other ternary phases (purple). Unsuccessful (red squares) and successful (green square) flux growths were used to determine the black tie lines. A plausible pseudo-binary phase diagram for the successful flux growth (upper right) and SEM image of grown crystals (lower right).

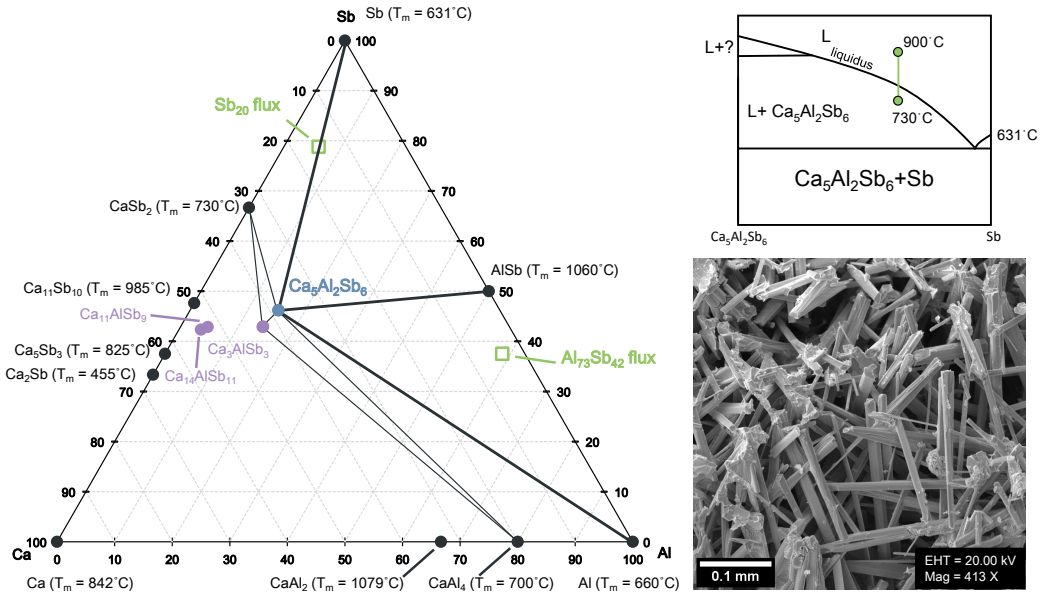

Figure 3.9: The Ca-Al-Sb ternary phase diagram with known binaries (black), desired ternary phase $Ca_5Al_2Sb_6$ (blue), and undesirable ternary phases (purple). Unsuccessful (red squares) and successful (green square) flux growths developed black tie lines between compounds. A plausible pseudo- binary phase diagram for the successful Sb_{20} flux (upper right) and SEM image of grown crystals (lower right).

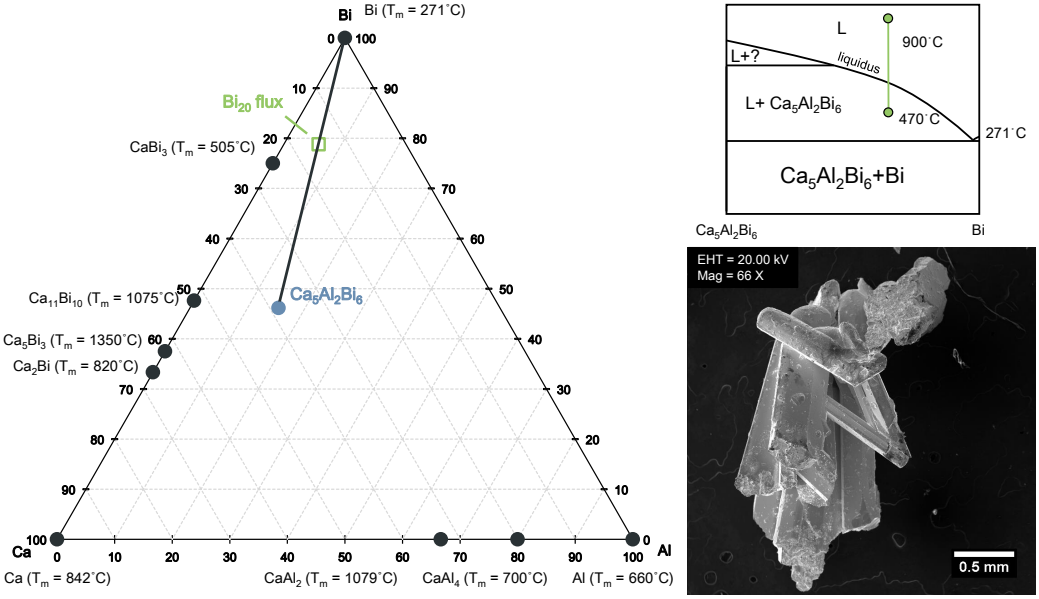

Figure 3.10: The Ca-Al-Bi ternary phase diagram with known binaries (black), desired ternary phase $Ca_5Al_2Bi_6$ (blue). Successful (green square) flux growth developed black tie line between compounds. A plausible pseudo-binary phase diagram for the successful Bi_{20} flux (upper right) and SEM image of grown crystals (lower right).

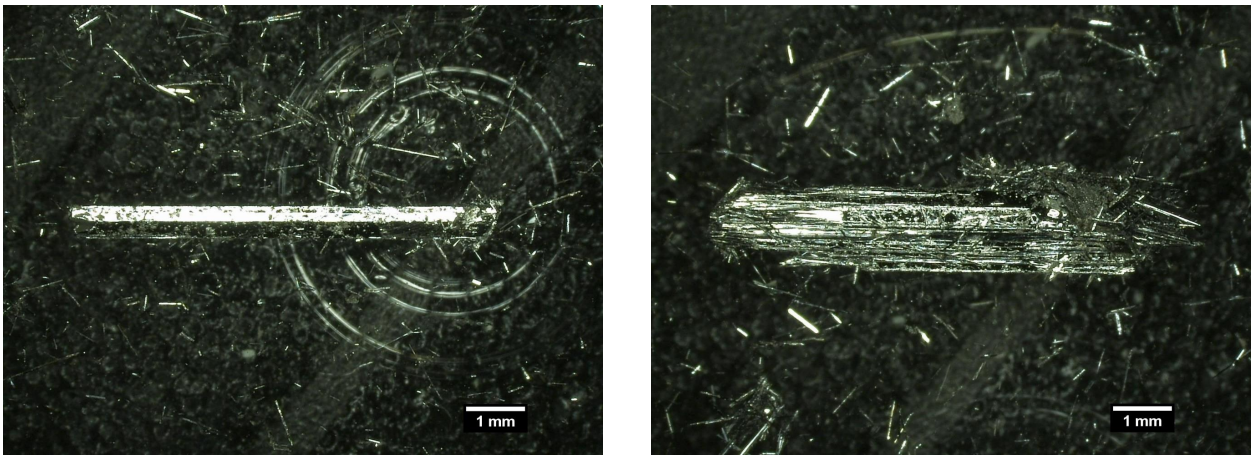

Figure 3.11: Large $Ca_5Ga_{2-x}In_xSb_6$ single crystal with well defined facets (left). Similarly large crystal but constructed of a large number of smaller $Ca_5Ga_{2-x}In_xSb_6$ single crystals grown in parallel (right).

3.4.1.3 $Ca_5Ga_{2-x}In_xSb_6$

The elements Ga and In are isoelectronic, so it is expected that $Ca_5Ga_2Sb_6$ and $Ca_5In_2Sb_6$ would exhibit either partial or complete solubility. Further, the electron and phonon scattering mechanisms in alloys are dominated by point defect scattering, meaning that the anisotropy of electronic and thermal conductivity in alloyed crystals might be different than in the pure compounds. For these reasons, growth of alloyed $Ca_5Ga_{2-x}In_xSb_6$ crystals were pursued.

We report the first single crystal alloy $Ca_5Ga_{2-x}In_xSb_6$, successfully grown from a five part mixture of $Ca_5Ga_2Sb_6$ (polycrystalline) + $Ca_5In_2Sb_6$ (polycrystalline) + $Ga_{37.5}$ + $In_{37.5}$ + Sb_{42} flux elements. The same temperature and time parameters described for $Ca_5Ga_2Sb_6$ were used for the alloyed samples. As discussed below, the EDS and SC-XRD analysis confirms that the crystals contain mixed occupancy of Ga and In on the metal site. From this crystal growth, two large crystalline masses were grown along with a thick array of smaller crystals, shown in Figure 3.11. The crystal shown in Figure 3.11(left) measures 7.34 mm in length and 0.57 mm in width with well-defined facets that run the length of the crystal, implying the crystalline mass is almost entirely a single crystal. In contrast, the crystalline mass shown in 3.11(right) has no large well defined facets and appears to a build up of smaller crystals that all grew parallel to one another in the growth environment. This mass measures 8.39 mm in length and 1.40 mm in width.

3.4.1.4 $Ca_5Al_2Sb_6$

The Ca-Al-Sb ternary phase diagram in Figure 3.9 is constructed from the known binary phase diagrams [212, 218–220]. In contrast to the Ga and In phase diagrams, the Ca-Al-Sb phase diagram has four ternary phases known to exist: Zintl phases Ca_3AlSb_3 [148], $Ca_{14}AlSb_{11}$ [150], $Ca_{11}AlSb_9$ [214], and desired phase $Ca_5Al_2Sb_6$ [108].

The Zintl phase Ca_3AlSb_3 is another thermoelectric candidate compound forming the Ca_3InP_3 structure-type, and composed of infinite chains of corner-sharing $AlSb_4$ tetrahedra. This composition has been successfully doped with Na^{+1} on the Ca^{+2} site for polycrystalline samples, producing a maximum figure-of-merit of $zT = 0.8$ at 777°C for $Ca_{3-x}Na_xAlSb_3$ (x = 0.03, 0.06) [221]. This compound will be difficult to discern from our intended $Ca_5Al_2Sb_6$ single crystal synthesis as EDS will most likely not be sensitive enough to identify the excess Ca of Ca_3AlSb_3. Fortunately, SC-XRD can be used instead to readily distinguish between the two structures. The Zintl phase $Ca_{14}AlSb_{11}$ has also been studied for potential thermoelectric applications [222] as it offers unusual Sb-Sb bonding manifesting in linear Sb_3^{7-} chains and isolated $AlSb_4$ tetrahedra [223, 224]. This composition will be easily distinguishable from our intended $Ca_5Al_2Sb_6$ at EDS due to its relative Al deficiency and at SC-XRD due to its larger unit cell.

The $Ca_{14}AlSb_{11}$ composition has been studied for potential thermoelectric application [222] as it offers unusual Sb-Sb bonding manifesting in linear Sb_3^{7-} chains and isolated $AlSb_4$ tetrahedra [223]. [224]. This composition will be easily distinguishable from our intended $Ca_5Al_2Sb_6$ at EDS due to its relative Al deficiency and at SC-XRD due to the larger unit cell ($Ca_5Al_2Sb_6$/$Ca_{14}AlSb_{11}$: a = 14.07/16.68, b = 12.09/16.68, c = 4.46/22.42).

In addition to the challenge of avoiding formation of the competing ternary phases described above, growth of $Ca_5Al_2Sb_6$ crystals is further complicated by the fact that aluminum vapor attacks the quartz ampules, as shown in Figure 3.12(left). In rare cases, this reaction caused the ampules to shatter during centrifuging. This problem was eliminated by carbon coating the interior of the quartz tubes by burning off acetone and rotating the quartz tube under a methane-rich flame, with results shown in Figure 3.12(right).

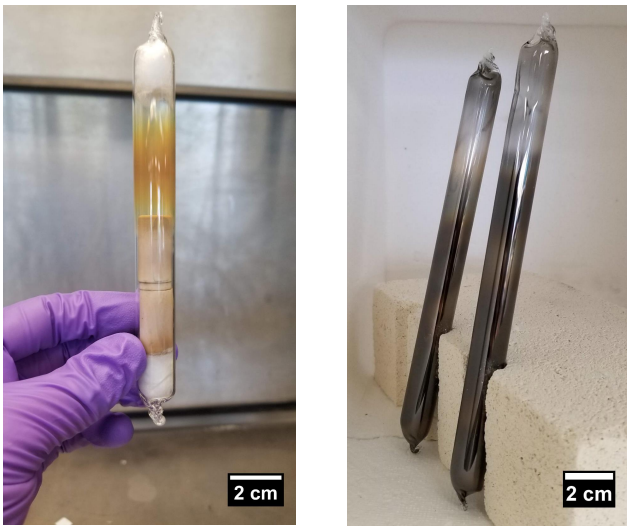

Figure 3.12: Aluminum vapor damage to the quartz ampule, concentrated at the gap between the crucibles and sieve prior to flipping (left). Carbon-coated quartz ampules formed a protective barrier (right).

Flux growths were successful in producing $Ca_5Al_2Sb_6$ single crystals using three different flux compositions: $Al_{73}Sb_{42}$, Sb_{20} and Sn_{15}, shown in Figure 3.16. The Al and Sb flux utilized was the same as those used in the other successful $Ca_5M_2Sb_6$ (M = Ga, In) single crystal growths. These Sb fluxes were successful mainly because overall melt composition fell inside of the three phase triangle containing Sb, $Ca_5Al_2Sb_6$, and $CaSb_2$. This was in contrast to the $Ca_5In_2Sb_6$ system, which contains a different three-phase region including Ca_8In_3.

The flux amount was reduced in the Sb_{20} flux (compared to $Al_{73}Sb_{42}$) trial but no Ca reaction with the container was observed. The Sb_{20} flux produced crystals in large numbers with little flux adhered to the crystal surfaces, with results comparable to the $Al_{73}Sb_{42}$ flux. While Sb has not shown to wet to crystal surfaces there appears to be a base level of flux that remains after centrifuging due to the liquid flux getting caught between the hundreds to thousands of the grown crystals per run. Smaller quantities of starting material may reduce this issue but may risk additional reaction of Ca with the crucible.

Single crystal growth of $Ca_5Al_2Sb_6$ was also attempted from a Sn_{20} and Sn_{15} flux with a representative crystal shown in Figure 3.16(c-d). The yields for these growths were extremely low and the crystals were heavily coated in flux, to such an extent that SC-XRD was not possible without

a secondary process to remove the Sn flux. A Pb flux was also attempted (Pb_{94}) but did not produce crystals. Similar to the $Ca_5In_2Sb_6$ attempt, a smaller amount of Pb flux may improve intermixing, but toxicity and wetting concerns make this an unfavorable choice when other options have shown success.

3.4.1.5 $Ca_5Al_2Bi_6$

The Ca-Al-Bi ternary phase diagram in Figure 3.10 is constructed from the known binary phase diagrams. In contrast to the Sb-containing phase diagrams, there is no binary compound along the Bi-Al edge. The first flux growth attempt of the $Ca_5Al_2Bi_6$ replicated the successful $Ca_5Al_2Sb_6$ + Sb_{20} growth using a Bi_{20} flux and an extraction temperature of 730°C. This temperature was too high, with the entire melt drained into the catch crucible, indicating that nothing had yet solidified. Successful crystal growth occurred with an extraction temperature of 470°C with elemental composition confirmed by EDS and structural confirmation by SC-XRD. Crystals are shown in Figure 3.10(right) and 3.15(e-f). The temperature profile still soaked at 900°C for two hours before cooling at a rate of 10°C/hr until 620°C where it was then cooled by 3°C/hr to the 470°C extraction temperature. This slower rate was to account for the likely crystal formation during this time. Growths could be further optimized to potentially have a lower soak temperature thereby reducing experiment time.

3.4.1.6 Crystal growth summary

Single crystals of $Ca_5M_2Sb_6$ (M = Al, Ga, In) were successfully grown using a $M_{73}Sb_{42}$ flux, and a temperature profile of room temperature to 900 °C in 12 hours, a two hour soak at 900°C and then slow cooled to 730°C at 3°C/hr. $Ca_5Al_2Sb_6$ was also successfully grown in a Sb_{20} flux and Sn_{15} flux using the same temperature profile. Single crystal $Ca_5Al_2Bi_6$ was grown from a Bi_{20} flux with a slow cool at 3°C/hr from 620°C to the 470°C extraction temperature.

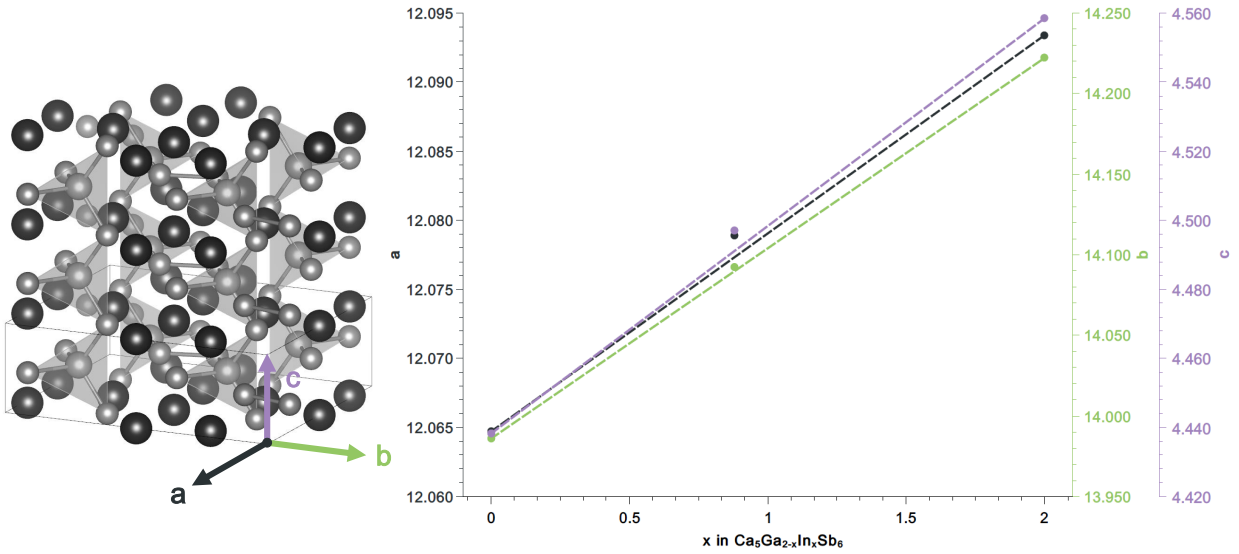

Figure 3.13: Alloyed reference structure (left). Linear relationship between unit cell parameter dimensions between alloy phase $Ca_5Ga_{1.12}In_{0.88}Sb_6$ and unalloyed ternary phases $Ca_5Ga_2Sb_6$ and $Ca_5In_2Sb_6$ (right).

3.4.2 Crystal Structure and Composition

SC-XRD was performed to confirm the crystal structure and composition of the single crystals and to identify the orientation of the needle-like crystals with respect to the orthorhombic unit cell. Crystallographic data is summarized in Table 3.2. All compositions were confirmed to be orthorhombic and in the *Pbam* space group. The lattice parameters and atomic positions are all in excellent agreement with published values with all unit cell dimensions showing a discrepancy of less than 0.50%. Single crystal results were encouraging when it came to the alloyed composition, confirming that both Ga and In were incorporated into the same lattice as opposed to simply producing a mixture of $Ca_5Ga_2Sb_6$ and $Ca_5In_2Sb_6$ crystals which reflected the starting spark plasma sintering (SPS) pellet compositions. Using SC-XRD the M site occupancy was refined using a mixture of Ga and In, resulting in a resolved composition of $Ca_5Ga_{1.12}In_{0.88}Sb_6$. The alloyed composition maintains the *Pbam* space group within the orthorhombic crystal structure with the In and Ga atoms both partially occupying the center of the anionic polyhedral structures as illustrated in Figure 3.13(left).

The lattice parameters of an alloyed composition can be predicted according to Vegard's Law

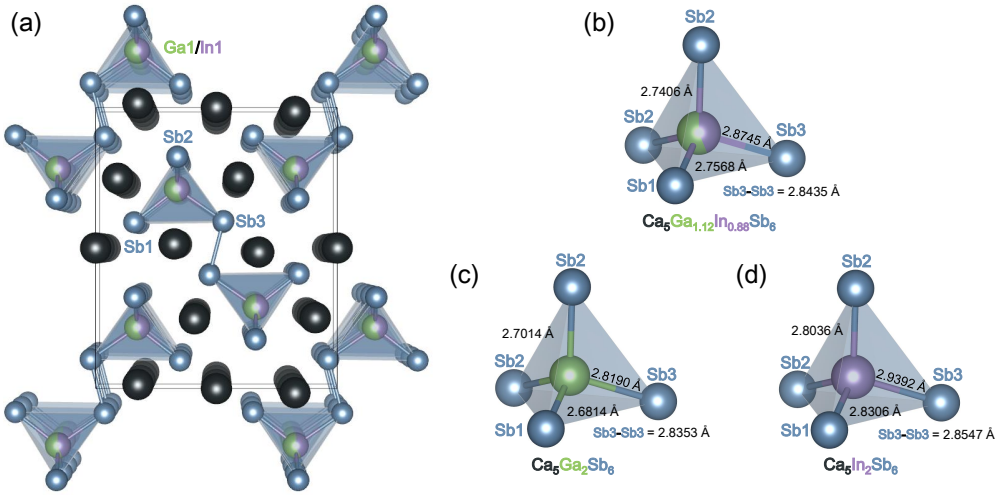

Figure 3.14: (a) The $Ca_5Ga_{1.12}In_{0.88}Sb_6$ crystal structure with select atom labels. Polyhedra bond length comparison between (b) $Ca_5Ga_{1.12}In_{0.88}Sb_6$ (c) $Ca_5Ga_2Sb_6$, and (d) $Ca_5In_2Sb_6$.

[225, 226], which is an empirical rule stating that a linear relationship exists between the crystal lattice parameters of an alloy and the concentrations of the constituent elements at a constant temperature. For an alloyed composition,

$$a_{A(1-x)B_x} = a_{A(1-x)} + a_B x, \tag{3.4}$$

where $a_{A(1-x)B_x}$ is the lattice parameter for the alloyed composition, a_A and a_B are the lattice parameter for the two unmixed compositions, and x is the molar fraction of B in the solid solution.

The lattice parameters of the alloyed composition are compared to the lattice parameters of the $Ca_5Ga_2Sb_6$ and $Ca_5In_2Sb_6$ in Figure 3.13(right), where the linear relationship can be observed. The tetrahedra bond lengths of the alloyed structure also fall in between that of $Ca_5Ga_2Sb_6$ and $Ca_5In_2Sb_6$ as detailed in Figure 3.14. The increase in lattice parameter with increasing In content is due to In being a larger atom than Ga with the crystal structure expanding to accommodate. This may also be the reason for the slight preference of Ga to occupy this site in the compound.

Table 3.2: Crystal data collected from single crystal X-ray diffraction for the $Ca_5Ga_{2-x}In_xSb_6$ compositions. Programs used: APEX2, SAINT, SHELXS97, SHELXL97, and OLEX2. Unit cell dimensions are in good agreement with published data.

Crystal data					
Empirical formula	$Ca_5Al_2Sb_6$	$Ca_5Al_2Bi_6$	$Ca_5Ga_2Sb_6$	$Ca_5Ga_{1.12}In_{0.88}Sb_6$	$Ca_5In_2Sb_6$
Formula weight	984.86	1,508.24	1,070.34	1,109.80	1,160.54
Crystal system	orthorhombic	orthorhombic	orthorhombic	orthorhombic	orthorhombic
Space group	Pbam	Pbam	Pbam	Pbam	Pbam
Unit cell dimensions					
a (Å)	12.0486(4) [-0.34%]	7.5569(4)[-0.33%]	12.0647(5) [-0.34%]	12.0789(4)	12.0934(12) [-0.33%]
b (Å)	14.0356(4) [-0.24%]	23.2361(13)[-0.42%]	13.9859(5) [-0.25%]	14.0924(4)	14.2222(15) [-0.24%]
c (Å)	4.45290(10) [-0.16%]	4.5175(3)[-0.25%]	4.4382(2) [-0.28%]	4.49710(10)	4.5585(5) [-0.30%]
α (°)	90	90	90	90	90
β (°)	90	90	90	90	90
γ (°)	90	90	90	90	90
Volume *($Å^3$)*	753.03(4)	793.24(8)	748.88(5)	765.50(4)	784.04(14)
Z	2	2	2	2	2
Density, calc. (g/cm^3)	4.344	6.315	4.747	4.815	4.916
Absorption coefficient	12.384	68.002	15.856	15.290	14.650
F(000)	864	1248	936	968	1008
Crystal size (mm)	$0.110 \times 0.047 \times 0.034$	$0.141 \times 0.087 \times 0.034$	$0.041 \times 0.027 \times 0.026$	$0.167 \times 0.059 \times 0.032$	$0.308 \times 0.065 \times 0.043$
θ range	2.228°to 26.391°	3.506°to 65.166°	2.229°to 24.986°	2.89°to 30.39°	2.211°to 28.772°
Index ranges	$-14 \leq h \leq 15$	$-11 \leq h \leq 10$	$-14 \leq h \leq 14$	$-16 \leq h \leq 17$	$-16 \leq h \leq 16$
	$-17 \leq k \leq 17$	$-35 \leq k \leq 35$	$-16 \leq k \leq 16$	$-20 \leq k \leq 20$	$-19 \leq k \leq 18$
	$-5 \leq l \leq 5$	$-6 \leq l \leq 6$	$-5 \leq l \leq 5$	$-6 \leq l \leq 5$	$-6 \leq l \leq 5$
Reflections collected	10,271	14,616	14,913	13,178	7,752
Independent reflections	883	1,604	564	892	957
Largest diff. peak and hole	2.973/-1.270	2.92/-5.74	2.78/-2.02	4.975/-2.164	6.68/-2.54

EDS was used to quickly evaluate the approximate chemical composition of many individual crystals, as well as to identify impurity phases present either on the surface, or as inclusions. This analysis technique suffers from potential peak overlap which makes resolving exact quantities of individual elements difficult. For this reason, tie lines for the ternary phase space were constructed from powder and single crystal X-ray diffraction results only. To shed light on potential pitfalls, EDS patterns were simulated using a Monte Carlo model in NIST DTSA II [227, 228] for the $Ca_5M_2Sb_6$ (M = Al, Ga, In) compositions and can be found in the Appendix. For this system, the Ca and Sb peaks were found to overlap in the 3-5 keV energy range but have enough separation to confirm the presence of the elements in approximate quantities. Ga possesses an isolated energy peak at approximately 1.09 keV which represents L orbital transitions with contributions from the α, β, and γ transitions, highlighting how this peak is amplified in magnitude with increasing Ga content. The presence or absence of Ga in the EDS scan is readily apparent giving further experimental confirmation of the consistency of these crystal growths. The Ca/Sb ratios deviate significantly from the expected 5:6 ratio, which was common to every crystal composition tested. However, this is almost certainly due to the overlap of the EDS peaks, as opposed to true deviation in stoichiometry. The excellent agreement of the SC-XRD results with prior work confirms this assumption. On the $Ca_5Ga_2Sb_6$ crystals, homogeneous spherical droplets on the surface were identified as pure Ga from the Ga flux. Regions devoid of any crystalline facets were a combination of excess Ga and Sb flux elements. Sb tended not to wet directly to the surface of the crystal but would accumulate between crystals in the centrifuging process.

Monte Carlo simulations were also run for the Ca-In-Sb known ternary phases $Ca_5In_2Sb_6$ and $Ca_{11}InSb_9$. The In L$\alpha 1+2$ peak at approximately 3.29 keV was identifiable and separate from the Ca and Sb peaks. Additionally, the relatively In-deficient $Ca_{11}InSb_9$ composition could be confidently separated from the more In-rich $Ca_5In_2Sb_6$. Further details of this analysis can be found in the Appendix.

The alloyed composition $Ca_5Ga_{2-x}In_xSb_6$ underwent extensive EDS analysis to better evaluate the consistency of the Ga:In ratio across many individual crystals. Due to the unique Ga peak

at approximately 1.09 keV and the unique In peak at approximately 3.29 keV this technique can reliably detect the presence/absence of the minority element. Results were very consistent with all measured crystals containing both Ga and In. Ga was slightly preferred, consistent with the results of SC-XRD.

$Ca_5Al_2Sb_6$ single crystals from an $Al_{73}Sb_{42}$ flux are shown in Figure 3.16(a), from a Sb_{15} flux in Figure 3.16(b), and Sn_{15} flux in Figure 3.16(c-d). For these crystals, SC-XRD was invaluable to confirm the composition and structure type, due to the existence of several nearby ternary phases with similar stoichiometry. In particular, the Monte Carlo model in NIST DTSA II [227, 228] showed that that the $Ca_5Al_2Sb_6$ and Ca_3AlSb_3 patterns are nearly indistinguishable due to their similar stoichiometry. However, by comparison, the $Ca_{14}AlSb_{11}$ and $Ca_{11}AlSb_9$ ternaries are distinguishable due to a significantly smaller Al Kα1+2/Al Kβ1 peak centered at 1.48 keV.

The EDS analysis conducted in Figure 3.16 displays heterogeneity in the compositions, more specifically to the Al content. This variation was not detected in subsequent SC-XRD but could be contributed to some crystals possessing a Al-rich surface. In some cases this could be contributed to Al-rich fluxes but this variation was also detected in non Al fluxes such as Sb_{20} in Figure 3.16(b). This variation was limited to the $Ca_5Al_2Sb_6$ composition while $Ca_5Al_2Bi_6$ produced more consistent Al amounts. This highlights how EDS analysis can not be used exclusively in the identification of compound compositions.

Finally, EDS analysis for the $Ca_5Al_2Bi_6$ composition is shown in Figure 3.15(e-f). In this case, there are no competing ternary phases in the Ca-Al-Bi system, so EDS could readily differentiate the target phase. Additionally Bi produces unique energy peaks distanced from any potential Al and Ca peaks. These peaks are at approximately 10.85 keV representing L$\alpha 1+2$ emissions, and approximately 13.01 keV representing $L\beta 1+2$ emissions, making results even easier to resolve. A detailed summary of EDS across all compositions and fluxes is conducted in the Appendix.

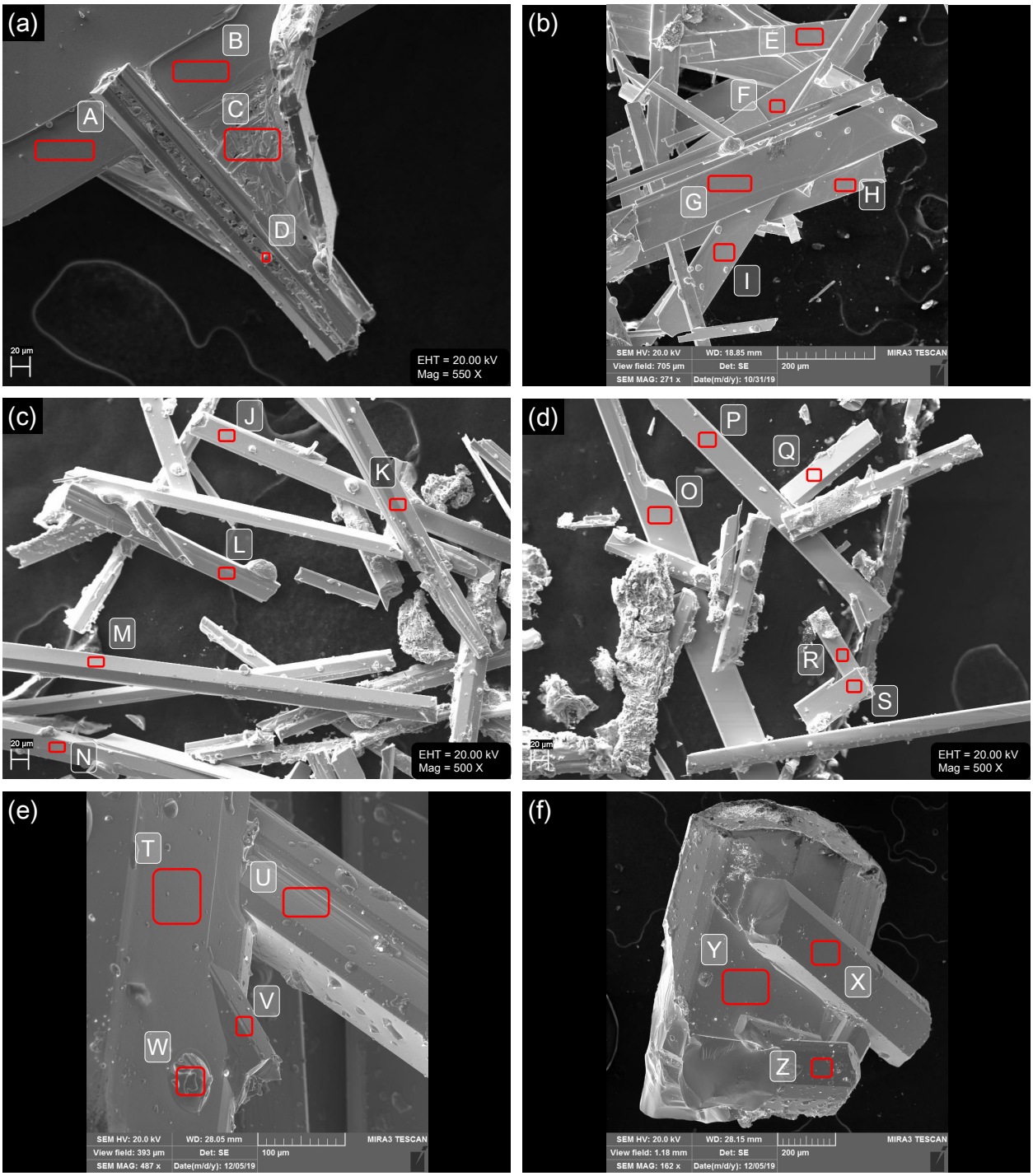

Figure 3.15: EDS analysis of (a) $Ca_5Ga_2Sb_6$ crystal and flux elements, (b) $Ca_5In_2Sb_6$ crystals, (c-d) $Ca_5Ga_{2-x}In_xSb_6$ single crystals, and (e-f) $Ca_5Al_2Bi_6$ single crystals.

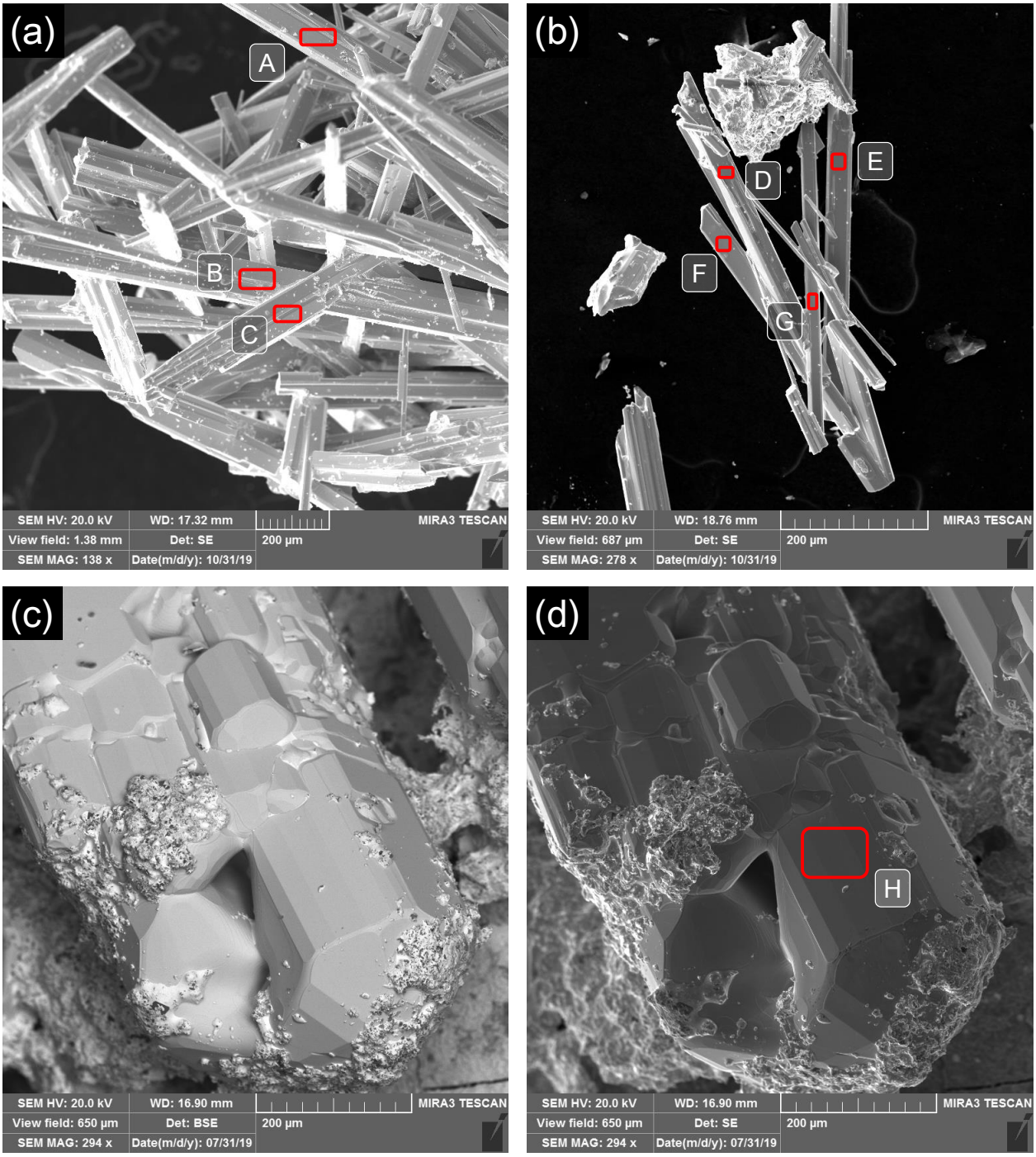

Figure 3.16: EDS analysis of $Ca_5Al_2Sb_6$ crystals grown from a (a) $Al_{73}Sb_{42}$ flux, (b) Sb_{20} flux, (c) Sn_{15} flux, back-scattered electron image to highlight flux, and (d) Sn_{15} flux, standard SEM.

3.4.3 Crystal Morphology

Crystal shape is influenced by both the intrinsic properties of the crystallographic structure and extrinsic factors such as the growth environment. In this study, single crystals were grown from a flux that acted as a solvent, influencing the growth environment. The crystal morphology is influenced by the surface energies associated with the exposed surfaces. This surface energy attempts to minimize itself with the fastest growth occurring on surfaces that expose the lowest energy. The grown crystal shape is determined by the minimization of total surface free energy of the crystal. This surface energy is dependent on several factors including chemical composition, atomic scale roughness, surface reconstruction and crystallographic orientation [143]. The $Ca_5M_2Pn_6$ (M = Al, Ga, In; Pn = Sb, Bi) crystals have a preferred growth direction, [001], making the (001) surface the highest surface energy plane.

Subsequent surface energy studies have begun on the $Ca_5M_2Sb_6$ (M = Al, Ga, In) crystal system to explain specifically how the intrinsic properties of the crystal and extrinsic properties of the flux drive crystal growth. Here a brief overview is provided, limiting the scope to geometric considerations by utilizing the Bravais-Friedel-Donnay-Harker (BFDH) law [229].

While a significant number of crystals adhered together with amorphous flux, many crystals were isolated, allowing for a detailed morphology study to take place where the dimensions of the crystals were measured. Crystal separation was further improved with the use of vapor transport methods previously described. Some crystals tested at SC-XRD were large enough to successfully identify planes, as shown in Figure 3.17, based off unit cell refinements. This analysis substitutes for more reliable EBSD methods which are exceedingly difficult to perform on small, brittle, single crystals due to the requirement of a highly polished surface.

Crystals grown in a $M_{73}Sb_{42}$ flux took on rectangular geometries that had a preferred growth direction as shown in Figure 3.17(a) for the $Ca_5Ga_2Sb_6$ composition and Figure 3.17(b) for the $Ca_5In_2Sb_6$ composition. While the majority of crystals appeared to have chamfered long edges as shown in Figure 3.18(c-d). Preliminary measurements of these angled facets lead us to believe these are the {110} family of planes. Interestingly enough, growths were primarily a mixture of

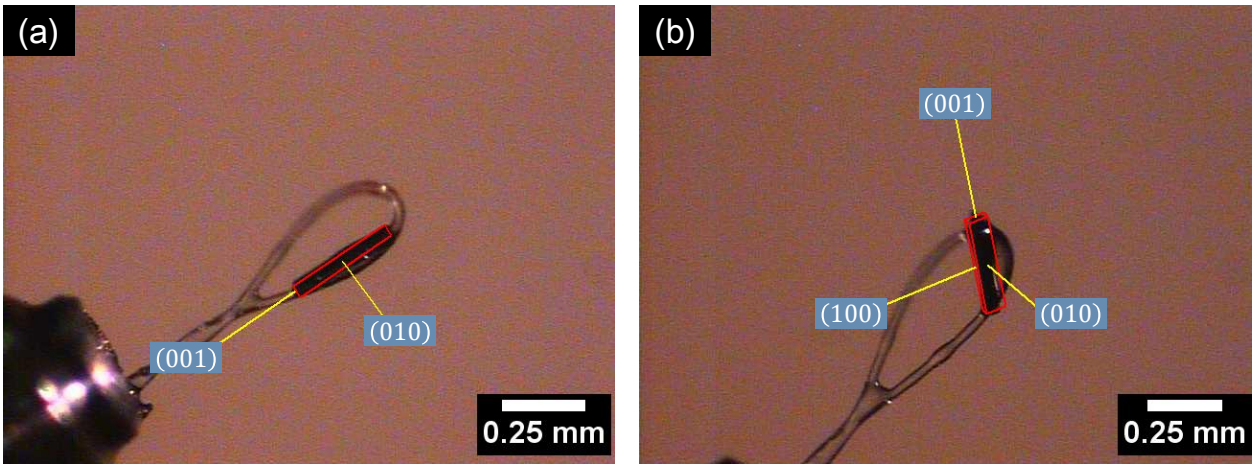

Figure 3.17: Single crystals mounted at SC-XRD for (a) $Ca_5Ga_2Sb_6$ from a $Ga_{73}Sb_{42}$ flux and (b) $Ca_5In_2Sb_6$ from a $In_{73}Sb_{42}$ flux.

these two geometries with Figure 3.18(b-c) coming from the same $Ca_5In_2Sb_6$ growth, even though they exhibit different morphologies. This is likely due to a composition gradient within the flux. Figure 3.18(d) illustrates a single crystal of $Ca_5Al_2Sb_6$ grown from a Sb_{20} flux that exhibits more prominent {110} growth planes.

These planes are in good agreement with preliminary BFDH calculations. The BFDH law reveals a correlation between the morphological importance of a crystal face and its interplanar distance d_{hkl}, where d_{hkl} is the distance that separates physically identical surfaces. The morphological importance of a crystal face is understood as its relative size in a given crystal habit [230] such as those displayed in Figure 3.17. Using the Mercury software package [231], relative BFDH areas are calculated for the $Ca_5M_2Sb_6$ (M = Al, Ga, In) which find (110), $(1\bar{1}0)$, $(\bar{1}\bar{1}0)$, $(\bar{1}10)$ the most favorable for growth followed by (001)/$(00\bar{1})$, and lastly $(0\bar{2}0)$/(020). These are the faces that should appear in the crystal morphology which is in agreement with observed geometries from SEM images. For the $Ca_5In_2Sb_6$ composition a portion of the single crystals grown took on distinct right angles such as the crystal observed in Figure 3.15(b) with the long axis belonging to the <001> direction family and the other growth axes <100> and <010>.

The BFDH is a practical geometric method that is based off the intrinsic properties of a crystal but does not take into account growth environment and has no energy considerations [230]. For this

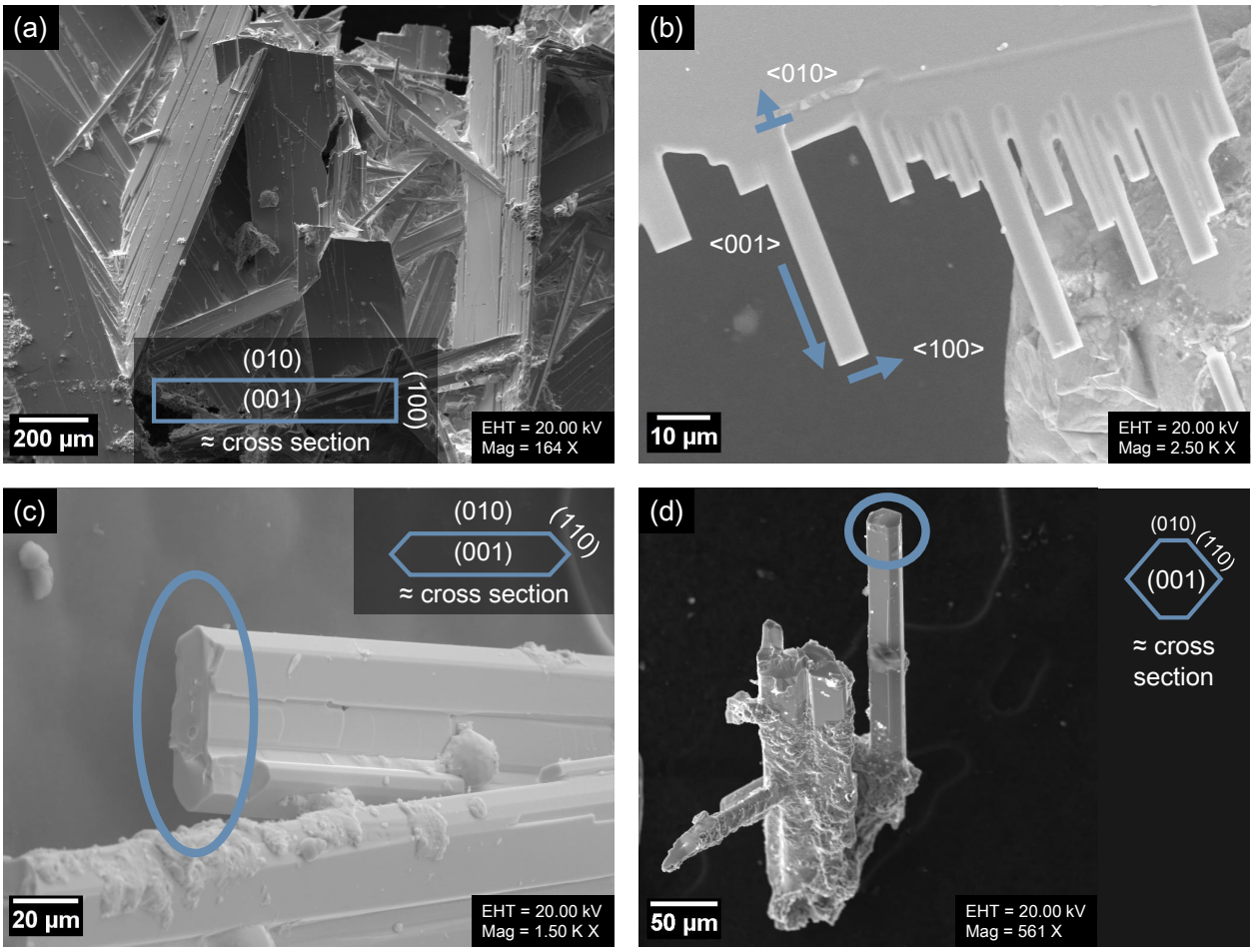

Figure 3.18: Single crystals of (a) $Ca_5Ga_2Sb_6$ from $Ga_{73}Sb_{42}$ flux with rectangular cross sections, (b-c) $Ca_5In_2Sb_6$ from same $Ga_{73}Sb_{42}$ flux, and (d) $Ca_5Al_2Sb_6$ from Sb_{20} flux.

reason the predicted planes and their relative prominence remains unchanged among the $Ca_5M_2Sb_6$ (M = Al, Ga, In) crystals. This methodology also introduces confusion between the lattice and the structure, leading to an unnecessary multiplication of Miller indices which may be the case for the (020) planes [232]. The ordering of the planes from the BFDH does not match the order of prominence in our growths with our (010)/(020) planes having the most surface area.

Single crystals from a $Al_{73}Sb_{42}$ flux are shown in Figure 3.16(a), from a Sb_{20} flux in Figure 3.16(b), and Sn_{15} flux in Figure 3.16(c-d). The crystal geometry appeared to change for the Sn_{15} flux, displaying more competing facets along the crystal length but some ribbon-like geometries were still present.

The $Ca_5Al_2Bi_6$ composition possesses a different structure-type and produces a unique list

of BFDH areas. Here $(00\bar{1})/(001)$ are the most favorable for growth, followed by $(0\bar{1}0)/(010)$ then $(\bar{1}00)/(100)$. This deviates from the crystal structure observed more substantially as these crystals had a preferred growth direction along [001] but were generally thicker with a number of competing facets along the length of the fibers, never appearing rectangular as their orthorhombic crystal system might suggest. This shows how significantly the growth environment can influence crystal growth and why a more detailed surface energy study would be required to understand these interactions.

3.5 Concluding Remarks

In this work single crystal $Ca_5M_2Pn_6$ (M = Al, Ga, In; Pn = Sb, Bi) compounds have been grown from a molten metal flux. The $Ca_5M_2Sb_6$ compounds were all successfully grown from a $M_{73}Sb_{42}$ flux, with $Ca_5Al_2Sb_6$ also being successfully grown from an Sb_{20} and Sn_{15} flux. $Ca_5Al_2Bi_6$ was grown from a Bi_{20} flux, a simpler option than the mixed self-flux. The first single crystal alloy $Ca_5Ga_{2-x}In_xSb_6$ was successfully grown from a five part mixture of $Ca_5Ga_2Sb_6$ (polycrystalline) + $Ca_5In_2Sb_6$ (polycrystalline) + $Ga_{37.5}$ + $In_{37.5}$ + Sb_{42} flux elements. In addition, several tie lines have been added to the $Ca_5M_2Pn_6$ (M = Al, Ga, In; Pn = Sb, Bi) ternary phase diagrams where none existed before, providing guidance to future crystal growth and synthesis studies. Single crystals in excess of 7 mm were grown but the average crystal size was significantly smaller. These single crystals, however, are sufficiently large for characterization using a modern photolithography process where normal application of contacts by hand are impractical.

The $Ca_5M_2Pn_6$ (M = Al, Ga, In; Pn = Sb, Bi) crystals have a preferred growth direction, [001], with the (001) surface the highest surface energy plane. Other morphological habits observed were dependent on the growth environment and composition gradients within the melt, with different crystal shapes produced from the same crystal growth experiment.

CHAPTER 4

ELECTRONIC CHARACTERIZATION OF $Ca_5In_2Sb_6$ SINGLE CRYSTALS

4.1 Introduction

Single crystals of $Ca_5M_2Sb_6$ (M = Al, Ga, In) were grown via the flux method. These crystals possessed a preferred growth direction along the covalent chains of the structure but only measured a few millimeters and tens of microns in the perpendicular direction. Our desire to characterize the transport properties of these crystals both parallel and perpendicular to the growth direction demanded a novel characterization technique, as placing contacts by hand is infeasible in the perpendicular direction. Micro-fabrication techniques were utilized with micro-ribbons of $Ca_5Ga_2Sb_6$ and $Ca_5In_2Sb_6$ extracted both perpendicular and parallel to the preferred growth using a focused ion beam milling technique. Photolithography was then utilized to create a circuit of sensors for low temperature characterization of Hall effect, and simultaneous measurement of sample thermal conductivity, Seebeck coefficient, and electrical resistivity. Here, a temporary coat of photoresist was applied, transferring a designed micro-circuit onto the substrate surrounding and covering portions of the micro-ribbon. The micro-circuit fabrication was accomplished using a laser photolithography process. After the exposure and subsequent development, a layer of chromium and gold was applied and selectively removed to form the characterization circuit. This method shows great potential in eliminating the need for large single crystal samples to perform characterization, allowing samples to be evaluated for their thermoelectric potential before more resources are invested in scaling up crystal growth. The resistivity, carrier concentration, and mobility of a micro-ribbon of $Ca_5In_2Sb_6$, perpendicular to the preferred growth direction, was successfully characterized using this approach. Resistivity was measured in the parallel direction using a four-probe resistivity setup and was accomplished by manually contacting the sample with silver paste. In this manner, the anisotropy of resistivity in $Ca_5In_2Sb_6$ was determined and compared to other classes of materials.

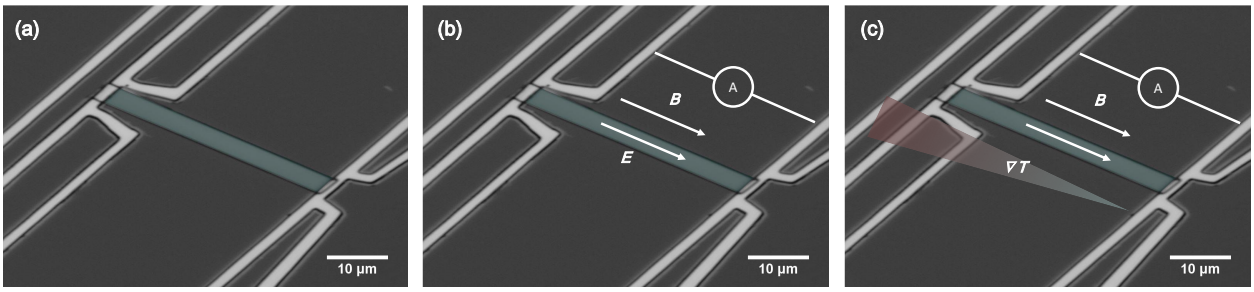

Figure 4.1: (a) False color image of the NbP micro-ribbon (green) with sputtered heater line (upper left) and a pair of thermometers. (b) Configuration used to measure the electrical conductance G = J/E. (c) Configuration used to measure thermoelectric conductance GT = J/$|\nabla T|$ with the red and green ends of the color gradient representing hot and cold sides of the circuit [6].

4.2 Background

4.2.1 Photolithography for Material Characterization

Photolithography is widely used in the production of commercial grade integrated circuits (ICs) but has only recently begun to make an impact as a pathway to characterizing material properties in research. The benefit of this method is that samples can be precisely cut in different crystallographic directions to isolate their properties. Additionally, micro-ribbons of material are used, extracted from larger crystals so only small samples are required. The application of sensors over the top of these micro-ribbons has been successfully performed by Gooth et al. [6]. Two thermocouples and a resistive heater line were used to measure conductance and are shown in Figure 4.1. Each micro-ribbon measured approximately 50 μm $\times$ 2.5 μm $\times$ 0.5 μm in size [6]. In principle, all of the thermoelectric transport properties (Seebeck coefficient, electrical and thermal conductivity) can be measured on samples as small as 25 μm.

In this study, focused ion beam milling, photolithography, and the subsequent electrical transport characterization were carried out at the Leibniz Institute for Solid State and Materials Research (IFW) in Dresden, Germany which was accomplished over two research stays at the institute.

4.2.2 Focused Ion Beam Milling

Removing material by ion milling (*i.e.*, source sputtering) is the most widely used application for a focused ion beam (FIB) system. This method is capable of extracting micro-ribbons of material from larger single crystals with micrometer scaled lengths and nanometer scaled features and thicknesses. The process is limited by removal rate, resolution, and crystal quality [233]. Removal rates need to be carefully adjusted based on each crystal composition, with heavier elements slowing the rate of milling. Semiconductor-type materials are favorable for this method as more insulating ceramics can accumulate charge and deflect the ion beam if given an insufficient path to ground, which is limited during the cutting and extraction of material [234]. For conducting materials, milled material is removed from the bulk by a combination of system vacuum and redeposition elsewhere in the chamber [235].

4.2.3 Selection and Treatment of Photoresists

In this study, a photolithography process was optimized, beginning with the selection of photoresists. A photoresist is a photoactive polymer suspended in a solvent. This polymeric structure protects a substrate from chemical or physical attack during the photolithography process. While photoresists can work for a variety of processes, most resins are optimized to specific applications. A photoresist chemically changes when exposed to specific wavelengths which creates a difference in the dissolution rate of the photoresist when exposed to a developer solution. This discrepancy in dissolution rate allows for the creation of micro-structures where a circuit of conducting material can selectively be placed.

Photoresists can be characterized as either positive or negative. Positive resists are soluble in the developer after exposure while negative resists by comparison are cross-linked within the exposed areas and remain, while non-exposed areas are removed in the development process [236]. This cross-linking process is not a driving force in positive resists. Some positive photoresists are also capable of image reversal whereby the tone of the photoresist is reversed similar to negative photoresists. Image reversal can be applied using a hard bake and flood exposure after the main

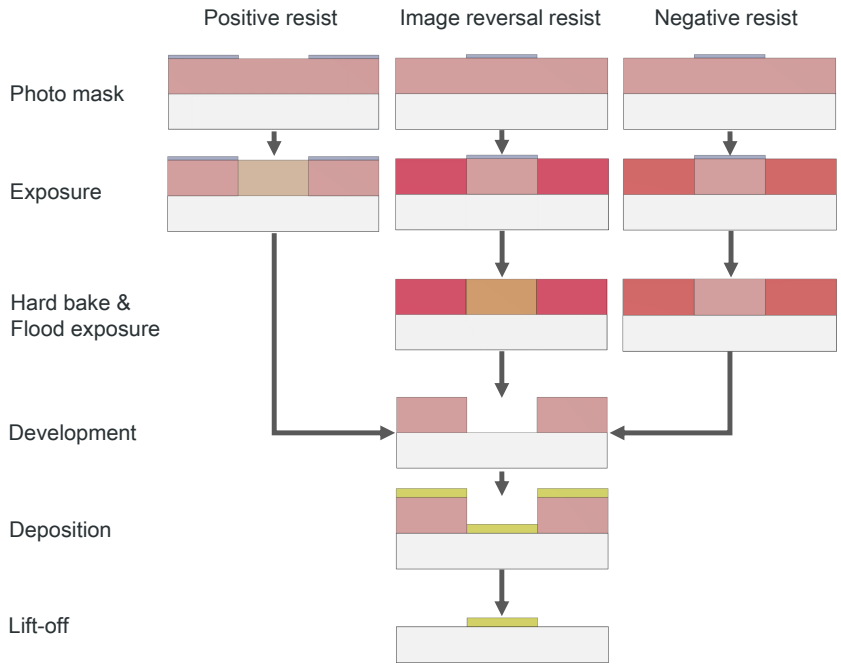

Figure 4.2: The photoresist process sequence for positive, image reversal, and negative resists. While chemically different through the development, deposition, and lift-off phases they are structurally equivalent for low resolution structures, combined here for simplicity. Resist profiles are based off large dose exposures.

exposure. The primary benefit of negative photoresists is that they are generally cheaper while positive photoresists offer better resolution. These photoresist types are compared in Figure 4.2 where the process flows from top to bottom.

Properties of a given photoresist are largely driven by the photoactive polymer chain length. Increasing the average chain length increases the softening temperature and as a consequence, the stability against thermal rounding which can impede subsequent lift-off operations. Decreasing the average chain length improves adhesion to the substrate so a compromise must be struck.

Positive photoresists have been used exclusively in this study and belong to either the diazonaphthoquinone (DNQ)/Novolak or polymethylglutarimide (PMGI) groups. These types of photoresists are applied as a liquid to the substrate and spin coated to uniform thickness. DNQ is an inhibitor which reduces the development rate (*i.e.*, alkaline solubility) in the unexposed state relative to pure phenolic resin, in this case Novolak, a polymerized phenolic made of formaldehyde and phenol

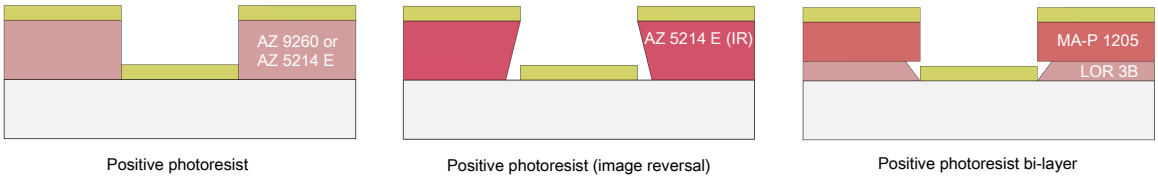

Figure 4.3: Selected photoresists and their types: positive photoresist (left), image reversal (center), and bi-layer (right). The gold layer represents the sputter deposition prior to the lift-off process.

[237]. Exposure wavelengths for DNQ typically range between 320-440 nm. The mechanism behind the DNQ-Novolak interaction has been an area of extensive study [238–244]. While efforts continue to understand the fundamental mechanism behind the unexposed DNQ inhibiting the dissolution of Novolak it is largely assumed to be changes in the hydrogen bonding [245].

The PMGI positive photoresist bi-layer describes a PMGI bottom planarization layer and a top imaging layer photoresist such as a DNQ-Novolak blend. The application and soft bake of the PMGI layer prior to the application of the imaging resist prevents intermixing of the two layers. During exposure the PMGI layer produces an undercut profile relative to the imaging resist above. PMGI resists also benefit from possessing a narrow range of sensitivity and do not require a solvent for development [246]. This narrow range allows for the potential development of the PMGI while the imaging resist maintains its structure. This photoresist stack was patented for the use in the manufacturing of metal-semiconductor field-effect transistors (MESFETS), modulation-doped field-effect transistors (MODFETS), metal-oxide-semiconductor field-effect transistor (MOSFETS), and other structures with gate metal usage [246]. A number of photoresists were attempted in this study to find the most accurate and repeatable process. These included positive, positive bi-layer and positive image reversal photoresists.

4.2.3.1 Positive photoresists

The AZ 9260 positive photoresist, manufactured by Microchemicals [247], was designed for thick resist structure patterning up to 24 μm. This photoresist was appealing for its thickness, ensuring that any micro-ribbon processed would be completely submerged in the resist where thicknesses

of only 0.2-0.5 μm are anticipated. The thick photoresist can also minimize texture effects that could negatively impact spin coating consistency. Like many thick photoresists, AZ 9260 offers excellent adhesion characteristics so no adhesion promoter is required [248]. This photoresist is illustrated in Figure 4.3(left). The sidewalls of the AZ 9260 will be significantly higher, due to its higher viscosity than the AZ 5214 E positive photoresist but are shown as equivalent for simplicity.

4.2.3.2 Image reversal photoresist

The AZ 5214 E photoresist, manufactured by Microchemicals [249], can be utilized in either the positive or image reversal configuration. This photoresist was designed and has proven effective for lift-off applications [250]. The image reversal state is capable of producing a negative sidewall profile which is ideal for our lift-off application. It is noted that the film thickness is less than that of the AZ 9260 and optimization is required for generating a repeatable and effective negative sidewall. This photoresist in the image reversal configuration is illustrated in Figure 4.3(center). The undercut, when sufficiently optimized can provide additional clearance for our lift-off process.

4.2.3.3 Positive bi-layer photoresist

A positive photoresist bi-layer is also a viable option and has proven effective for lift-off applications [251] with ribbon characterization being successfully completed using a LOR 3B and ma-P 1205 photoresist stack by Gooth et al. [6].

LOR 3B is based off the PMGI platform and manufactured by Kayaku Advanced Materials, Inc. [252]. It is used in conjunction with positive resists and acts as an underlayer in the bi-layer lift-off process. The ma-P 1205 positive photoresist, also manufactured by Kayaku Advanced Materials, Inc. [253], is used in conjunction with LOR 3B. This photoresist stack is illustrated in Figure 4.3(right) where the LOR 3B provides an undercut, allowing for easier separation during the lift-off process.

4.2.4 Spin Coating

Spin coating is a technique where a photoresist is dispensed onto a substrate which is then spun at a rate of several thousand RPM. The centrifugal force generated by this rotation produces an evenly dispensed photoresist layer across the substrate surface, while excess photoresist is spun off the perimeter [254]. The resist is further settled in this process as a portion of the solvent within the photoresist evaporates. This highly reproducible technique also benefits from a simple application and short cycle times [255]. Additionally, process repeatability is not severely temperature dependent. While higher temperatures lead to increased solvent evaporation they also increase resist viscosity, with these phenomena counteracting each other it provides the user a few °C range in which to apply and spin coat the photoresist for consistent results [256].

The spin coating operation requires at least a 100 or better cleanroom environment with excellent air filtration. This is largely due to the photoresist being tacky for a significant period of time, making it susceptible to airborne particulate during and after the spinning operation. Laboratory humidity should also be tightly controlled ($< 30\% \pm 2\%$) as solvent evaporation during the spinning operation will cool the substrate, creating potential water vapor condensation [255].

A disadvantage of this method is that air turbulence over the edges of the substrate can result in accelerated drying which can limit the spin-off of excess photoresist from the center due to accumulation along the perimeter. This edge bead issue is exasperated with the use of more viscous resists, and substrate geometries with sharp edges such as rectangles or squares. For non-circular substrates the edges can be broken off entirely but risks contamination from the breaking process [257].

Another characteristic of this technique to consider is that any substrate texture reduces the homogeneity of the resist coating, so the micro-ribbon used in this process must be thin enough not to produce a significant texture effect in the photoresist and must be submerged uniformly in the resist.

Resist discontinuities can also result if contamination or air bubbles are present in the resist, emphasizing the need for clean room conditions and careful application. For DNQ-based positive

and image reversal photoresists, nitrogen bubbles can occur due to the gradual thermal decomposition of the photoactive compound. Ultrasonic baths can be employed to outgas these nitrogen bubbles if necessary [237]. Discontinuities can be reduced or eliminated with high spin coating accelerations (1,000s of RPM/s) leading up to the primary spin speed. Multistage spin coating profiles can be used to compensate for textured substrates as well, where a slower rotational speed is held for several seconds before accelerating to the primary spin coating speed [255].

Spin speed correlates directly to the final resist thickness. For liquid photoresists the final resist thickness can be approximated by the inverse square root of the spin speed [255]. Therefore one can adjust resist thickness by simply adjusting the spin speed, provided that the photoresist is spun until dry. This drying effect is also dependent on the residual solvent content of the photoresist, with the remaining solvent being removed during the soft bake immediately to follow.

4.2.5 Soft and Hard Bakes

In general a soft bake (*i.e.*, pre-bake) is any baking process step that heats the sample prior to exposure. The photoresists in this study required a soft bake to reduce the residual solvent concentration still present in the photoresist after spin coating. The soft bake also anneals stress in the applied film [255]. This process of residual solvent reduction is beneficial for DNQ-based resists to avoid the bubbling of nitrogen, which is a by-product of the exposure process. An optimized soft bake, both in temperature and duration ensures a more uniform surface quality and improved repeatability. While solvents assist in the thinning of a photoresist they absorb radiation applied in the exposure process and also negatively affect adhesion. Over-baking a substrate increasingly polymerizes the photoresist and reduces its photo-sensitivity while under-baking affects adhesion and exposure. Resist absorption rates relative to soft bake time and temperature can be done experimentally or computational to assist in the optimization of soft bake parameters [258].

A hard bake or more specifically, a post-exposure bake, is a baking step which immediately follows the exposure for image reversal and negative photoresists. For image reversal photoresists a post-exposure bake is used to invert areas of the resist that were exposed during the photolithography

process, rendering them insoluble in the developer. Typical post-exposure bake hot plate parameters are 100-130°C for a few minutes.

4.2.6 Exposure

The exposure in a photolithography process is typically carried out in one of three methods: using mask aligners, a stepper, or laser direct writing. Laser direct writing, was used in this study and is achieved with a focused rastering laser. There is no physical photomask, rather the circuit design is programmed into the laser and selectively exposed into the photoresist. The absence of a photomask is a significant advantage of this technique, allowing for quick modifications of the design but suffers from longer cycle times. Generally speaking, the photoreaction for positive and image reversal resists is a one-photon process with the required exposure dose a function of both intensity and time [259]. A laser application applies a high intensity of photons but is limited to a pixel-by-pixel approach, in contrast to the blanket of light employed in the mask aligner and stepper methods previously mentioned.

4.2.7 Flood Exposure

A flood exposure, also referred to as an open frame exposure, exposes the entire substrate to blanket radiation. Here no mask is present, with the flood exposure following both the main exposure and hard bake. For image reversal photoresists a flood exposure is utilized to completely convert the photoinitiator. For negative photoresists, a flood exposure completes the cross-linking process that was initiated in the main exposure.

4.2.8 Developer

The developers used in this study include metal ion-free (MIF) organic tetramethylammonium hydroxide which is preferred to diluted sodium hydroxide as sodium contamination of a circuit can degrade its properties [260–262]. Care needs to be taken to isolate the developers from open air as much as possible because CO_2 exposure reduces the activity of the developer.

4.2.9 Sputter Deposition and Lift-off

After development samples have their metal conductive layers sputtered onto the surface, adhering to the substrate and photoresist. The lift-off process removes the remaining photoresist, taking the sputtered metals with it. While all organic solvents can act as a suitable lift-off medium, low boiling temperature solvents are not recommended as this evaporation can cause re-deposition of removed metal. In order for repeatable lift-off to be achieved, the sputtered layers can only be a few hundred nanometers thick. It is only desirable for the lift-off medium to attack the photoresist but an important consideration in this study is that the micro-ribbon will be partially exposed and can be potentially etched or even damaged if it must remain submerged in the remover for extended periods of time.

4.3 Experimental Methods

The FIB milling and photolithography processes required a number of experimental methods that collectively produce a desired circuit design. Each process was optimized for select photoresists using blank substrates, with the best results determining which photoresist would be used for the processing of the single crystal micro-ribbons. The FIB milling was accomplished by technicians at the Leibniz Institute for Solid State and Materials Research (IFW) in Dresden, Germany.

4.3.1 Focused Ion Beam Milling

A FEI Helios NanoLab 600i SEM instrument integrated with a FIB was used to cut small oriented micro-ribbons from grown single crystals. These systems are capable of *in situ* specimen modification through ion milling or deposition with precision material removal occurring with nano-scale resolution [263]. While several types of FIB systems exist, the system herein discussed and utilized is a Ga liquid metal ion source, which is the most common source type. The Ga source is very stable with both a low vapor pressure and melting point while being relatively heavy which offers favorable sputtering rates [234, 264]. Crystal composition was also confirmed prior to cutting a

region by EDS using an EDAX SDD Apollo X detector at 30.00 kV, 0.00 tilt, and a take off angle of 36.49°.

The nominal processing time for FIB milling of a $Ca_5M_2Sb_6$ (M = Ga, In) micro-ribbon from a larger single crystal was 16 hours with the micro-ribbon extraction taking an additional 1 to 1.5 hours. Milling voltage and current were above normal at 30 kV and 65 nA respectively as deep cuts through flux regions were sometimes required. Samples were thinned beginning at 30 kV/21 nA with current decreasing to 80 pA. The cutting of the edges which support the micro-ribbon began at 0.79 nA and decreased to 80 pA.

4.3.2 Substrate Preparation

Optical quality borosilicate glass wafers measuring 10×10 mm with a thickness of 300 μm were used as the circuit substrate. Optimization experiments were conducted on coverslips produced by Menzel, measuring 18 x 18 mm.

Substrate cleaning is a critical aspect of the photolithography process. All substrates were cleaned sequentially with an acetone (C_3H_6O) bath, isopropanol (C_3H_8O) bath, and a deionized water rinse. Substrates were then dried with a nitrogen pistol and dehydration bake on a hotplate at 120°C for 10 minutes to remove any trace moisture. For substrates with a micro-ribbon present, the nitrogen blow-off step was bypassed due to concerns that the micro-ribbon position would shift or be lost completely. It was important that all moisture was removed from the surface as many photoresists are hydrophobic, leading to application and adhesion issues if not properly baked.

4.3.3 Circuit Design

The micro-structure applied across the single crystal micro-ribbons was detailed in a digital photomask. This mask was designed in LASI7 (LAyout System for Individuals), a layout and design program for integrated circuits [265]. Here complex micro-structure designs are made from simpler hierarchical objects that are assembled and applied in subsequent design layers to produce a top

layer structure that can be exposed at a laser lithographer. This construction substitutes for the more traditional physical masks that are placed above the photoresist during exposure.

The main sensor components were drawn and then connected to a surrounding padframe. These pads are the interface between the circuit and wired connections of the external characterization equipment. While commonly made from aluminum or copper in industrial applications [266], our low temperature application utilized gold because it is a noble metal that resists oxidation in the absence of industry standard passivation techniques.

4.3.4 Photoresist Application

All photoresists were applied using a manual static spin coating process using spin coaters manufactured by Polos, whereby resist was applied to the substrate using a pipette prior to initiating the spin profile. Special care was made to not transfer bubbles to the applied photoresist as these can lead to inhomogeneities or voids in the spun resist. Baking on a hot plate immediately after spin coating was implemented to minimize the chances of introducing particulate contamination, which can result in opaque spots or pinholes after exposure and development.

4.3.5 Soft and Hard Bakes

Soft and hard bakes were accomplished using hot plates, manufactured by Präzitherm. Hot plates were selected over ovens due to their faster applied temperature gradient which leads to more precise, repeatable results. After either a soft or hard bake was completed the substrate was cooled at ambient for two minutes prior to the next processing step.

4.3.6 Laser Lithography

The exposure process was performed using a μ-PG 101 micro pattern generator, manufactured by Heidelberg Instruments. The system was equipped with a laser diode which emits 375 nm wavelength radiation, allowing it to expose both standard and UV resists. Substrates could be as large as 100×100 mm with exposed structures down to 0.6 μm. Laser settings were set to

40 address grid, 0.9 μm minimum structure, and a write speed of 5 mm^2/minute. Both manual and pneumatic focusing methods were used to focus on the micro-ribbons and substrate. Micro-structures were rotated and aligned with the observed micro-ribbon by marking the opposite corners of the ribbon. These corners correspond to geometric coordinates in the designed mask. The first coordinate represents the photomask origin while the other required a precise measurement of the length and width of the micro-ribbon using either a Leica DM 2700M or Olympus BX53M optical microscope.

All samples were processed uni-directionally whereby the laser was only emitted during forward movement. This led to better stability but increased processing time compared to a standard bi-directional exposure. Batch exposures were processed, incrementing laser power for optimization in energy series. Grids of features were created in this manner and compared to one another for optimization purposes. Samples were also run in standard 1×1, and 1×2 energy modes with the first number referring to the number of exposures conducted while the second is a reduction in exposure speed. A 1×2 energy mode executes one exposure with double write energy, accomplished by reducing the stage speed by a factor of two. Reductions in speed led to longer processing times but in some instances improved marking quality.

4.3.7 Flood Exposure

This photolithography study utilized a hard bake, two minute cool down, and flood exposure for the AZ 5214 E image reversal photoresist. Flood exposure under 375 nm light occurred for 30 seconds. The flood exposure apparatus is shown in Figure 4.4.

4.3.8 Photoresist Development and Evaluation

The photoresists utilized in this study were developed by submerging the substrate in a glass petri dish filled with the recommended developer. Substrates were then rinsed in purified deionized water and dried with nitrogen blow-offs. Photoresist thickness was evaluated with a Bruker DektakXT

Figure 4.4: Flood exposure apparatus ($\lambda = 375$ nm).

stylus profiler after development. Here a stylus is dragged across the surface of either the developed photoresist or sputtered circuit elements, producing feedback on the topology of the structure.

4.3.9 Sputter Deposition

Sputter deposition was conducted in a Compact Research Coater (CRC-622-2G2-RF-DC) manufactured by Torr International. This manual planar magnetron system utilizes DC current to sputter material from two inch diameter targets, shown in Figure 4.5. The chamber was evacuated with a turbo molecular vacuum pump with matching dual stage rotary vane pump, pulling a vacuum of $1-2\times10^{-5}$ Torr with flowing argon used to sputter. Due to the targets being angled relative to the substrate, the platform was rotated to produce a more uniform coating during the sputter operation. An adhesion layer of chromium was sputtered on top of the developed photoresist, substrate, and micro-ribbon, followed by a thicker conductive layer of gold. The parameters for sputtering were independent of the photoresists used. The Cr target was energized for 5 minutes prior to exposing the substrate to the sputtering, this is done to remove any oxide layer formed on the surface. Once sufficiently clean, the Cr target is sputtered onto the substrate surface for four minutes ($\approx$ 50 nm thickness) as it rotates on the platen. This deposition is then stopped and the substrate is sputtered with Au to a thickness of 120-200 nm.

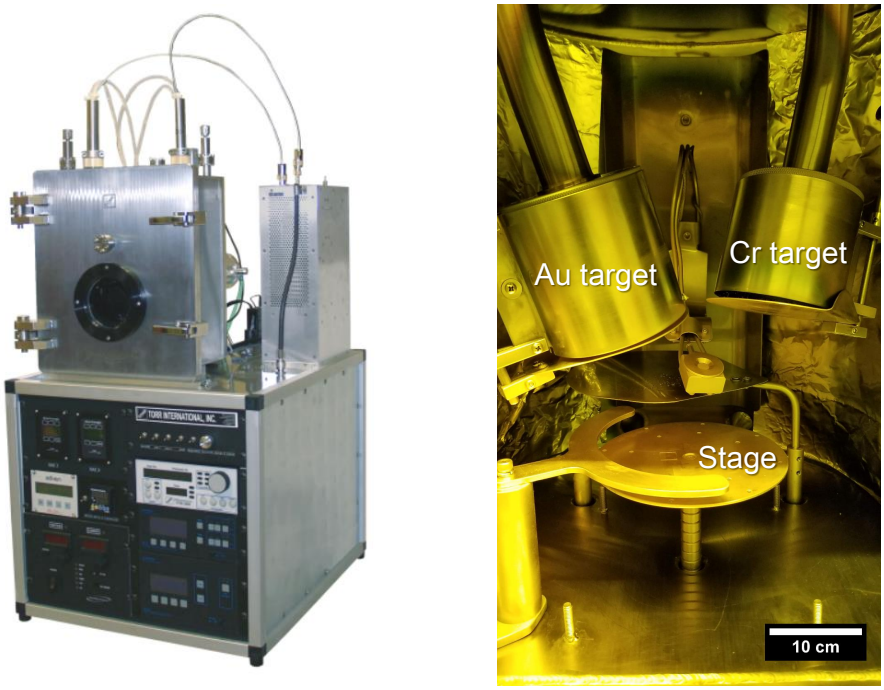

Figure 4.5: Sputter deposition device (left). Inside the chamber, with labeled Au and Cr targets angled over the stage. Note the shutters over each, used to keep each component isolated from each other (right).

4.3.10 Lift-off

Each remover was poured into a quartz Petri dish with a lid and heated on a hot plate inside a fume hood to reduce processing time. A plastic pipette was used to flush remover across the surface of the substrate and to pick at the edges in order to expedite lift-off. Decreasing processing time is important when a single crystal micro-ribbon is present because some portions of the micro-ribbon are in direct contact with the remover which can undesirably etch the sample.

4.3.11 Transport Characterization

The glass substrates in which circuits were successfully printed on were mounted to PPMS pucks with GE varnish and bonded to external contact pads with either 25 μm Au or 33 μm Al wire using a TPT HB16 semi-automatic bonder. Electrical transport characterization was carried out on a Dynacool cryostat with 14 T magnet manufactured by Quantum Design. Resistance was characterized using a sourcemeter Keithley 2400 and a nanovoltmeter Keithley 2182A.

4.4 Results & Discussion

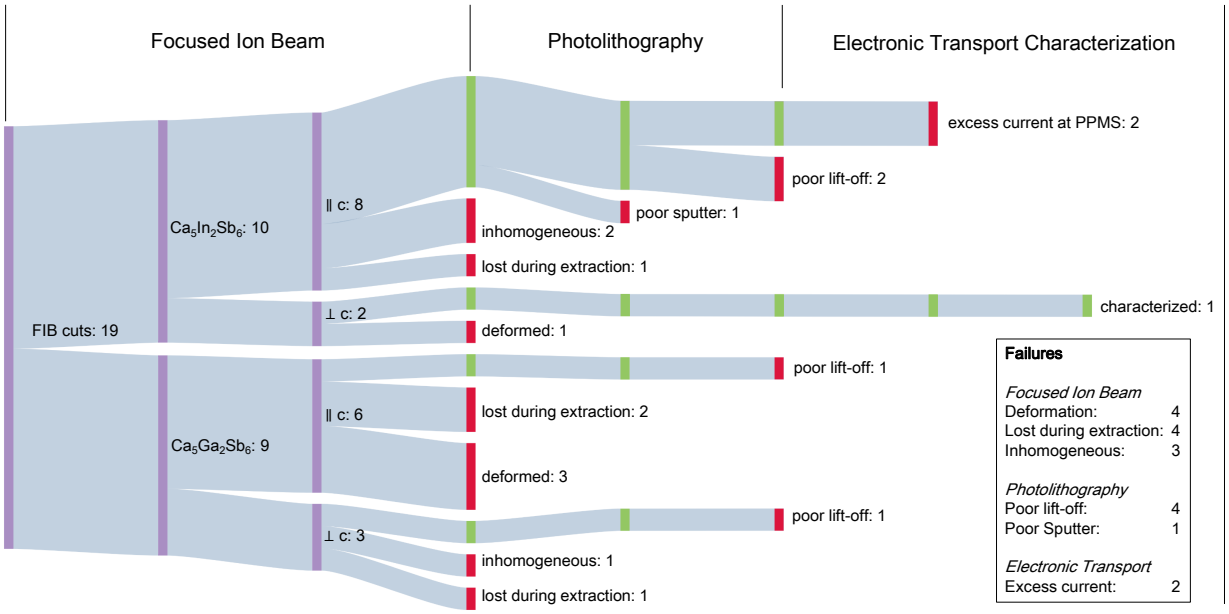

Figure 4.6: Summary of processed micro-ribbons through stages of development.

A summary of the processing results is shown in Figure 4.6. This process flow was broken into three regions: FIB processing, photolithography, and electronic transport characterization. FIB processing was completed by technicians at the IFW Dresden, while the photolithography and electronic transport characterization was conducted during research visits with a group of supporting scientists at the IFW Dresden. The majority of process losses occurred in the time consuming FIB milling process, with only eight sample being viable going into photolithography. Of these eight, three made it to the electronic transport characterization with a partial data set completed on a $Ca_5In_2Sb_6$ ribbon cut perpendicular to the c-direction.

4.4.1 Ribbon Processing

Single crystals of $Ca_5Ga_2Sb_6$ and $Ca_5In_2Sb_6$ were cut into micro-ribbons measuring 18-80 $\times$ 3-7 $\times$ 0.2-0.5 μm using FIB milling as illustrated in Figure 4.7. The Ga containing $Ca_5Ga_2Sb_6$ crystals proved difficult to cut. When the ion beam struck any latent Ga flux on the surface or a Ga-rich inclusion in the crystal the Ga would immediately liquify and burst, ruining the partially cut

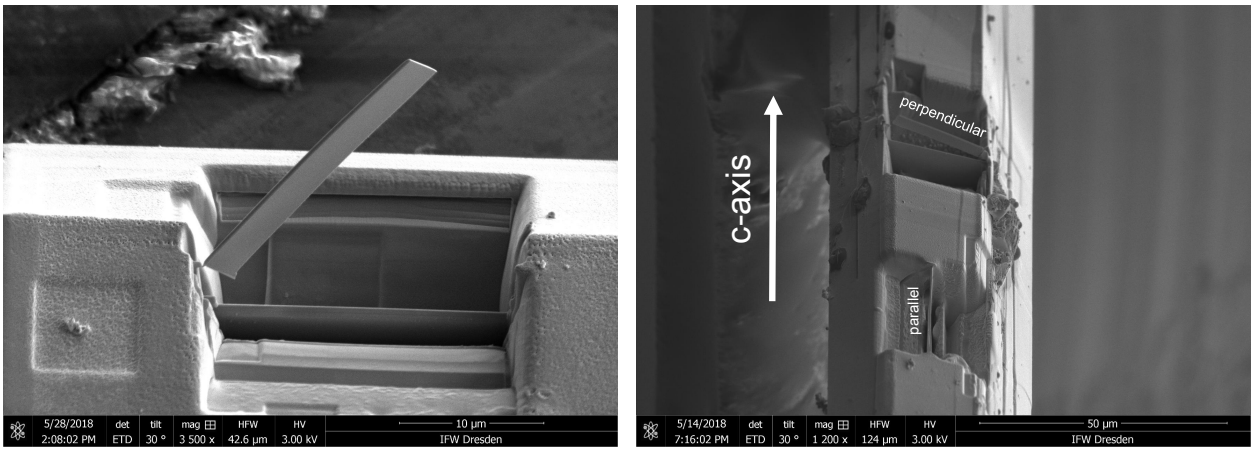

Figure 4.7: Successfully FIB milled micro-ribbon ready for extraction (left). Successfully FIB milled micro-ribbons ready for extraction both perpendicular and parallel to growth direction (right).

micro-ribbon. These $Ca_5Ga_2Sb_6$ crystals had been grown in a Ga- and Sb-rich flux with excess Ga collecting on the surface of crystals due to its unfavorable wetting behavior. Once mounted, several cuts were attempted from each sample as shown in Figure 4.7(right). Some of these micro-ribbons would spring loose prior to transfer. While the FIB system was capable of tilting, all cuts were made perpendicular to the beam, utilizing sample rotation instead.

The $Ca_5In_2Sb_6$ samples were grown in an In- and Sb-rich flux and appeared to have cleaner surfaces as In does not wet to the surface of the grown crystals as readily as Ga. These crystals however did suffer from inhomogeneous regions as excess In and Sb formed the InSb binary when trapped between grown crystals. Distinct phase contrast was observed in some instances with the milling operation well underway, resulting in that region of the single crystal being abandoned. Other micro-ribbons bent as a result of the milling process. Successfully cut samples were transferred to a glass substrate using a micromanipulator to begin the photolithography process. Due to air sensitivity concerns, both single crystals and cut micro-ribbons were stored under vacuum in a desiccator before and after FIB milling the eight successfully extracted micro-ribbons.

4.4.2 Circuit Design

The goal of this circuit design is to fully characterize micro-ribbons of our compounds both parallel and perpendicular to the c-axis. This is accomplished by developing a number of sensors that will

measure Hall, Seebeck, resistivity, and thermal conductivity.

In order to optimize individual photoresist combinations a prototype Hall circuit was generated shown in Figure 4.8. This design was limited to six sensors compared to the full characterization circuit which would have 16, shown in Figure 4.9. This reduced Hall circuit cut down on cycle time at the laser and allowed for the creation of 2×2 grids of this circuit at different power levels on a single substrate. Profiler measurements were taken over the larger circuit contact pads to determine photoresist depth and uniformity. These contact pads are where the circuit is externally bonded to characterization equipment. Due to the semi-manual nature of placing these contacts, larger pads are made to make the process easier. These larger areas are also useful for profiler measurements as the fine features in proximity to the micro-ribbon are below the tolerances in which the profiler can reliably detect. Resistivity measurements were conducted using a four probe method where a current is passed through two outer contacts while the voltage is measured between two inner contacts. Hall effect is measured using a four probe configuration in the presence of a magnetic field. The Hall sensors used to measure voltage are positioned opposite each other at the micro-ribbon center. A prototype Hall circuit is shown in Figure 4.8.

The Seebeck coefficient is measured by running a current through a sensor in close proximity to the end of the ribbon, referred to hereafter as a heater, with a pair of thermometers measuring the difference in induced voltage across the micro-ribbon. Thermal conductivity is determined by measuring the thermal conductance of the micro-ribbon by taking into account the voltage drop between sensors and the temperature difference between the thermocouples.

A unique digital mask was created for each micro-ribbon based off its dimensions. This was especially critical because it was beneficial to maximize the allowed space between sensors and also to determine the correct spacing between the Hall contacts which were required to contact opposite edges of a sample but not contact each other. All of these sensors are integrated into a single design as shown in Figure 4.9.

Both circuit designs in Figure 4.8 and 4.9 are made with sensors that have a width of 4 μm. Through optimizations it was determined that 3 μm and in some instances 2 μm are also possible

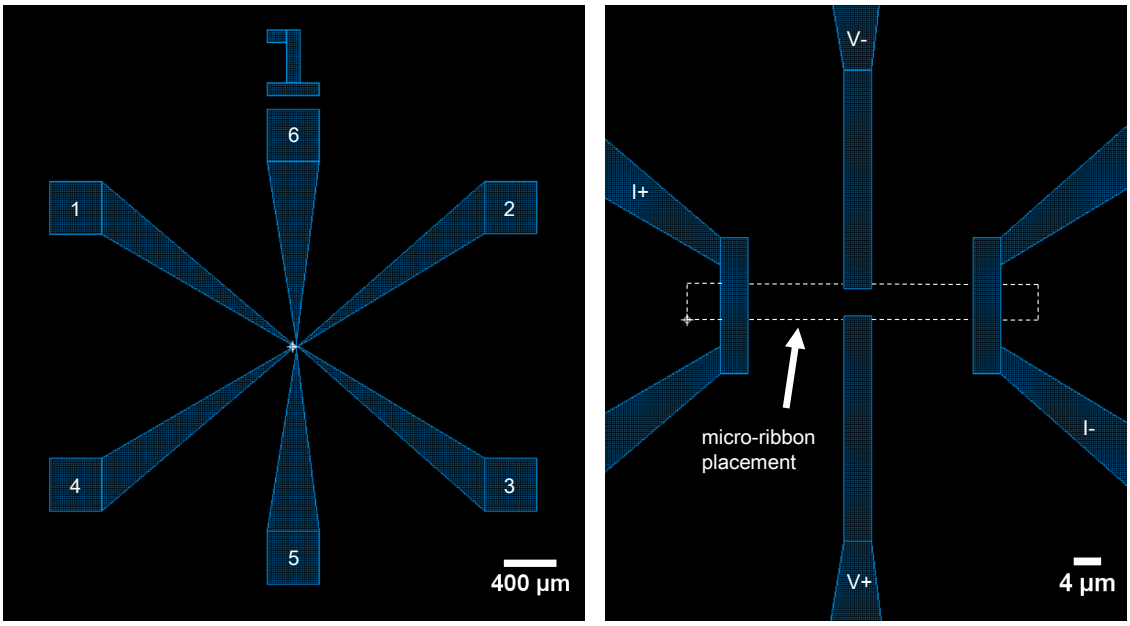

Figure 4.8: Prototype Hall circuit (left), and magnified view of sensors over the micro-ribbon at center (right).

but 4 μm was used because it provides more tolerance in the process. These wider contacts proved useful in alleviating some contact issues as the sputter deposition was not thick enough in some instances to consistently coat substrate and micro-ribbon interface.

4.4.3 Photoresist Optimization and Selection

A number of photoresists were utilized with their spin coating profiles compared in Figure 4.10. Ti Prime and AZ 5214 E (purple), LOR 3B and ma-P 1205 (blue), and AZ 9260 10 μm and AZ 9260 24 μm (black) constitute the different photoresist stacks. These optimized parameters were within the recommended manufacturer's range for both speed and duration but were adjusted slightly to our specific spin coater and laboratory conditions.

The low viscosity Ti Prime adhesion layer is spun at high speed and soft baked to the substrate prior to the application of the AZ 5214 E photoresist for both the standard positive and image reversal configurations. LOR 3B is spin coated and soft baked prior to the application of ma-P 1205 and used as a positive photoresist bi-layer where the LOR 3B is undercut in the development proces to improve the subsequent lift-off. The AZ 9260 10 μm can be used on its own or as the

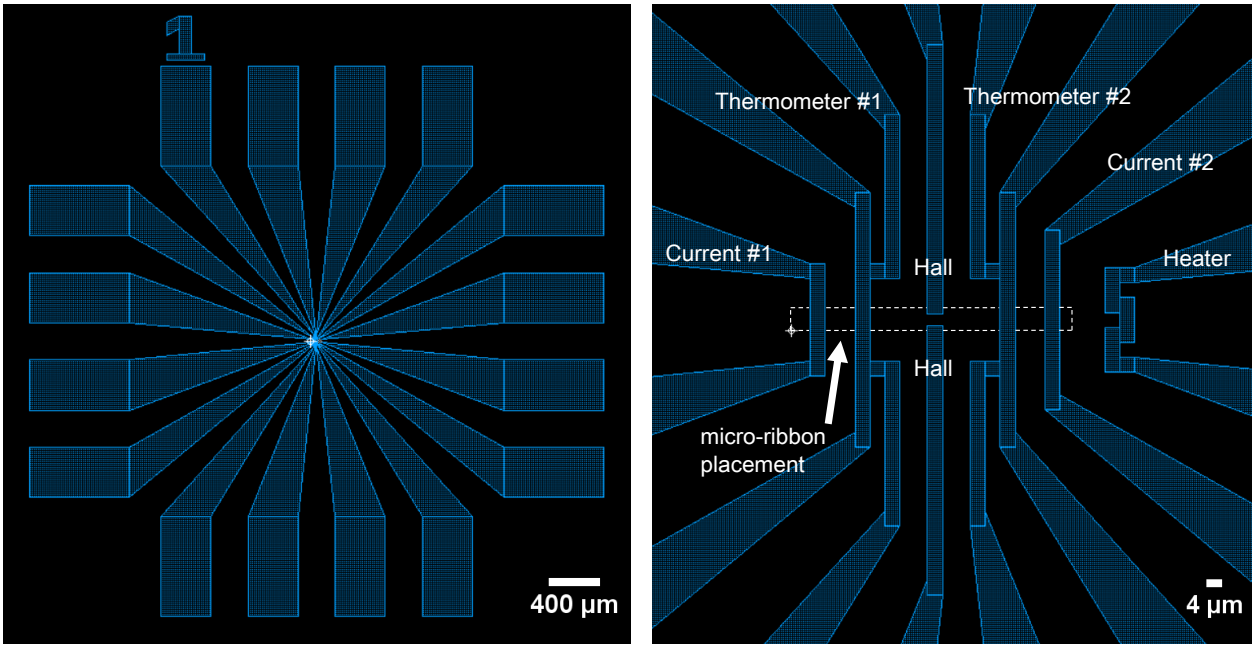

Figure 4.9: Full characterization circuit design (left), and magnified view of sensors over the micro-ribbon at center (right).

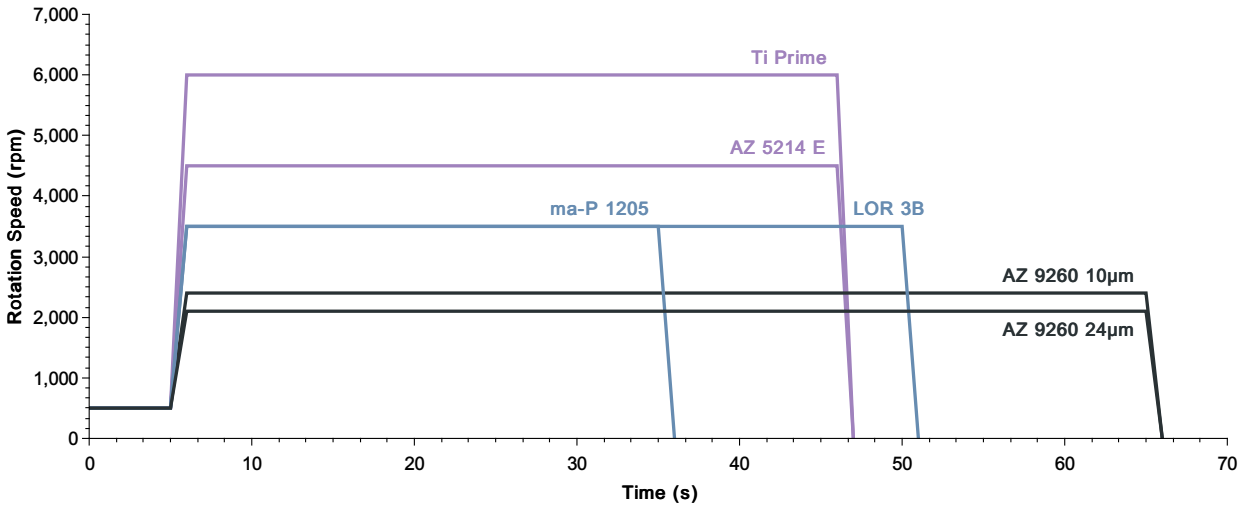

Figure 4.10: Optimized spin coating profiles for select photoresists grouped by color. Ti Prime is applied prior to AZ5214 E (purple). LOR 3B is applied prior to ma-P 1205 (blue). AZ 9260 10 μm can be used singularly or preceding the AZ 9260 24 μm profile that is a second application of the photoresist (black).

Table 4.1: Optimized temperature and duration of soft bake for selected photoresists. AZ 9260 24 μm is a two step application starting with AZ 9260 10 μm layer. AZ 5214 E was optimized as a positive photoresist and in the image reversal state.

	Temperature (°C)	Time (s)
Ti Prime	120	120
AZ 5214 E	110	50
AZ 5214 E (IR)	90	240
LOR 3B	180	250
ma-P 1205	100	30
AZ 9260 (10 μm)	110	80
AZ 9260 (24 μm)	110	160

base layer for the AZ 9260 24 μm thickness whereby the photoresist is applied a second time after the first application is spin coated and soft baked. The AZ 9260 photoresist was highly viscous and when coupled with the small, difficult square geometry produced a noticeable edge bead along the substrate perimeter which worsened at the corners. This non-uniform application of photoresist was later confirmed by profiler data once the photoresist had been developed.

Soft bake temperatures and durations are listed in Table 4.1. While the Ti Prime parameters remained the same for both configurations of the AZ 5214 E photoresist, the photoresist itself required different optimizations depending on its state. This photoresist was less viscous than the AZ 9260 photoresist and had a significantly lessened edge bead at the substrate perimeter once the soft bake was complete. The LOR 3B photoresist required the longest and hottest soft bake and was coupled with ma-P 1205 to produce a bi-layer undercut profile post-development. Both of these photoresists showed a small, non-detrimental edge bead, similar to that of the AZ 5214 E. While the laboratory environment was humidity controlled, significant temperature increases were experienced in the laboratory due to hot summer weather resulting in sometimes sporadic and unreliable results. Special care was used to process these samples quickly and preferably during the cooler morning hours.

Table 4.2: Development times for select photoresists.

Photoresist		Developer	Time (s)
LOR 3B + ma-P 1205		ma-D 331	20
AZ 9260			
	10 μm	AZ 400K 1:4	420-660
	24 μm	AZ 400K 1:4	660-1200
Ti Prime + AZ 5214 E			
	Standard	AZ MIF 726	50
	Image Reversal	AZ MIF 726	40

4.4.4 Development Optimization

The laser lithography process required extensive optimization, as different power settings would produce different line thicknesses in the photoresist despite implementing a common digital mask. Challenges also arose in the development stage as one had to be cautious not to over-develop the pattern in the photoresist. These processes directly impacted the effectiveness of the subsequent lift-off which was also found to be heavily circuit geometry dependent. Some of the lift-off issues were resolved with circuit design optimization, whereby sensors were separated as much as possible and the angles in which they exited the micro-ribbon staging area were staggered.

Prior to the critical task of line thickness optimization, appropriate developer times needed to be established. Development followed the laser lithography process, immediately after in the case of the positive photoresists, and after a hard bake, cool down, and flood exposure for image reversal photoresists. The development process submerged the substrate in the manufacturer's recommended developer for a specific amount of time before it was rinsed clean with purified deionized water and dried with nitrogen blow-offs. Initial times were dictated by manufacturer recommendation but deviated significantly in the case of the AZ 9260. Final development durations are listed in Table 4.2 for each photoresist. Samples were observed under an optical microscope to evaluate the developer progress, re-submerging substrates in instances of under-development. When over-developed, the substrate was simply scrapped in optimization trials but could be recovered by submerging the substrate in an appropriate remover to begin the process again if a micro-ribbon needed to be recovered.

The ma-D 331 alkaline aqueous based developer solution was used to develop the LOR 3B and ma-P 1205 photoresists. This bi-layer developed the circuit area repeatably in only 20 seconds, but more variability was observed in the undercut layer of LOR 3B, which is critical for the subsequent lift-off process. These consistent circuit development results are shown in Figure 4.11(left) for the six sensor Hall circuit design, shown previously in Figure 4.8 with nominal pad widths of 0.4 mm. Here a profiler needle was dragged across the surface of the photoresist and glass substrate. The exposed circuit design was developed, with the photoresist being removed completely as indicated by the flat bottoms that the profiler recorded. The target depth of this trough, which is a measurement of photoresist thickness, was expected to be in the 0.8 to 1.0 μ range as dictated by the spin coating profile. These measurements fail to capture the amount of undercut that the base layer of LOR 3B experiences, so while these results are encouraging, more optimization was required once the effectiveness of the lift-off could be evaluated.

The Ti Prime and AZ 5214 E photoresist performed repeatably for both the standard and image reversal configurations using AZ MIF 726 as a developer solution. Profiler results for the standard application are shown in Figure 4.11(right) with a repeatable depth of approximately 1.4 μm. As was the case with the bi-layer photoresist additional tests with lift-off are necessary as the undercut geometry of the developed photoresist sidewall can not be directly evaluated.

The AZ 400K developer solution was used in a 1:4 ratio with purified distilled water for the development of the AZ 9260 photoresist. As shown in Table 4.2, the development times for the AZ 9260 photoresist were extremely long and variable with several optimization studies failing to produce satisfactory results, whereby a portion of the circuit remained under-developed while the intricate sensors near the micro-ribbon were severely over-developed. Significant resist thickness variation was observed for the AZ 9260 photoresist as shown in Figure 4.12(right). Here the profiler was run across two contact pads as shown in Figure 4.12(left) with the contours normalized to the glass substrate. Despite a photoresist target depth of 24 μm based off the spin coating speed, the remaining photoresist varied widely between approximately 6 and 23 μm. This was largely due to the high viscosity of this photoresist coupled with the very small substrate size. This size is

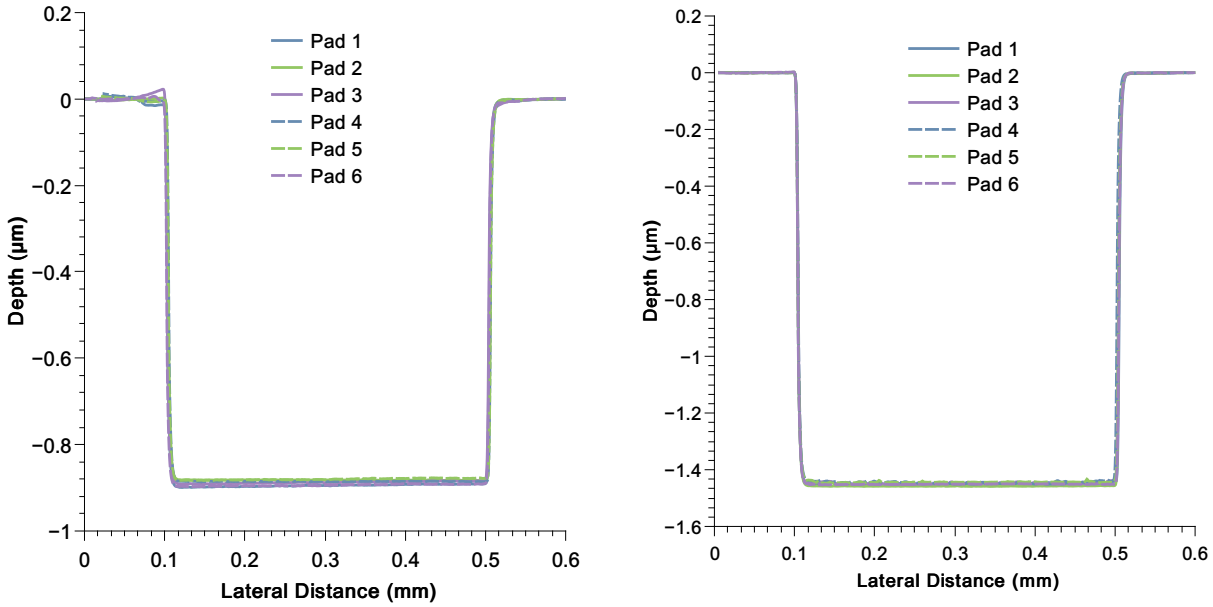

Figure 4.11: Profiler paths across the photoresist surface for the LOR 3B and ma-P 1205 photoresists (left), and Ti Prime + AZ 5214 E photoresist (right). Pad numbers correspond to Hall circuit labels in Figure 4.8.

constrained by the mounting requirements for a standard PPMS sample puck used for electronic characterization. The edge bead for this photoresist is larger, making the photoresist thickness widely variable across the center of the substrate due to poor removal. Additionally any tilt in the spin coater station can be a source of photoresist thickness variability. While large differences in the height of the remaining photoresist can potential cause slight sputtering differences the variable topology is detrimental to the lift-off process, causing some areas to progress more quickly, with other areas being unable to lift-off, as shown in Figure 4.17(left).

Another issue highlighted by profiler measurements is the under-development of some of the large contact pads while the more intricate features in close proximity to the micro-ribbon would over-develop and lose dimensional control. A properly developed AZ 9260 photoresist with a target depth of 10 μm is shown in Figure 4.13(left). Despite not achieved the target depth, the development was successful with each pad showing a flat surface against the glass substrate. An under-developed case is shown in Figure 4.13(center) with development issues being exacerbated when a second photoresist layer is applied for an intended target depth of 24 μm shown in Figure

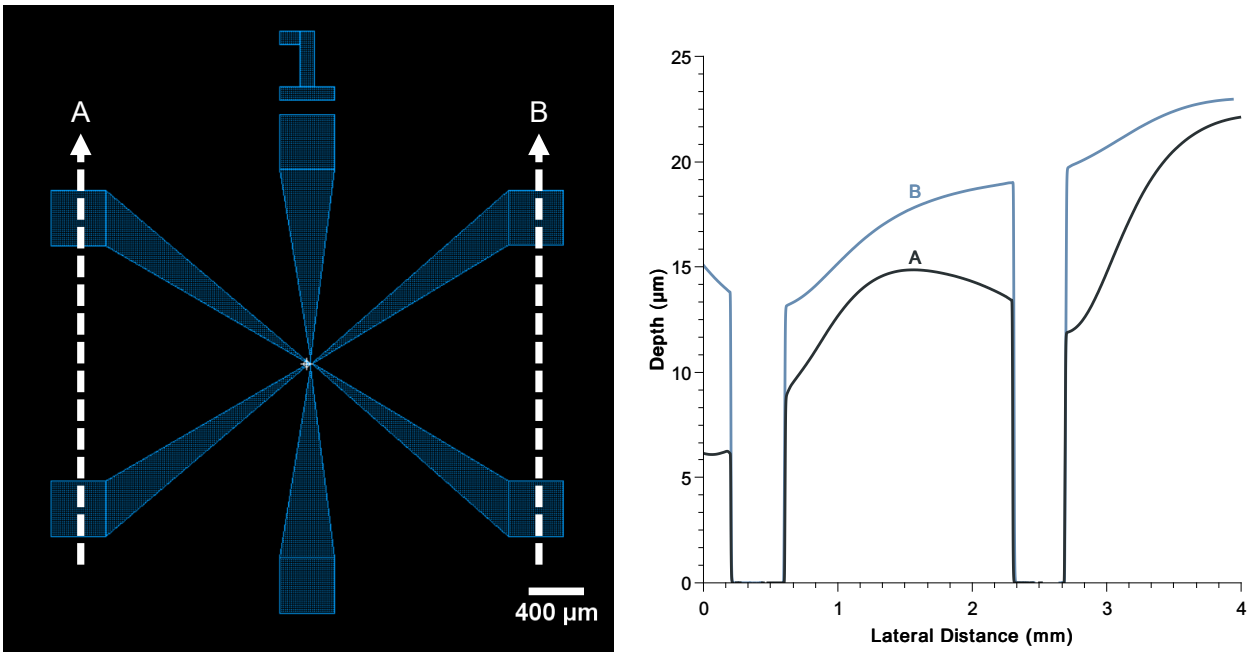

Figure 4.12: Profiler paths illustrated across a LASI7 designed Hall circuit (left). Each contact pad is 0.4 mm square. Profiler data on AZ 9260, 24 μm target photoresist thickness shows significant thickness variability (right).

4.13(right). Here photoresist is still present on the glass surface, creating texture in what should be a flat surface. This resist could potentially be improved given better spin coating optimization via faster accelerations or by increasing the laser exposure power, but the over-development of fine features at the circuit center is more difficult to simultaneously resolve. The repeatable results from the AZ 5214 E and LOR-3B + ma-P 1205 are preferred.

4.4.5 Line Width Repeatability

With a consistent development process in place, power optimization studies began whereby laser power in the exposure process was adjusted incrementally. These studies were conducted with the selected photoresists in order to determine accuracy and repeatability specific to circuit feature dimensions. A power optimization study was conducted for the AZ 5214 E image reversal photoresist shown in Figure 4.14(left) with measured dimensions for each power averaged and compared in Figure 4.14(right). Here the heater element from the circuit design was isolated and repeated with a target thickness of 2, 3, and 4 μm. This heater pathway has a number of bends which were

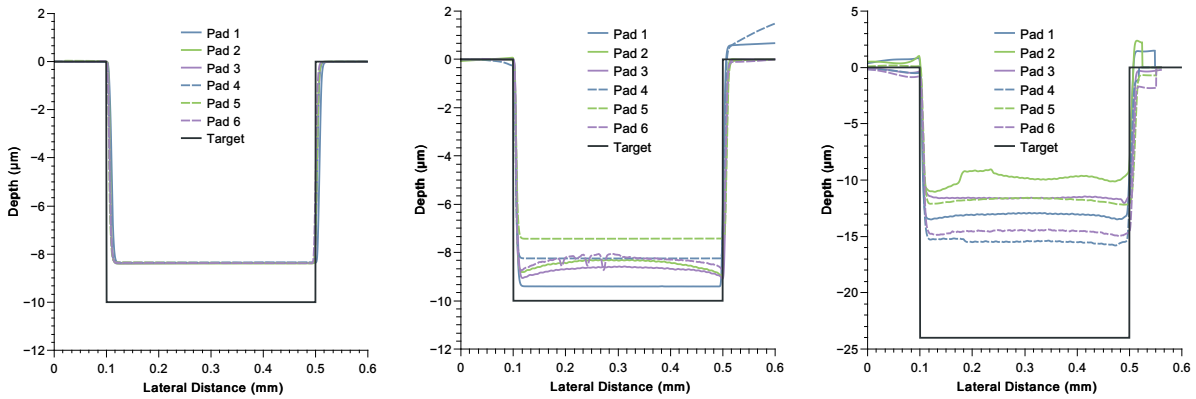

Figure 4.13: Profiler analysis of the AZ 9260 photoresist after development with fully developed 10 μm (left), under-developed 10 μm (center), and under-developed 24 μm target thickness (right). The thickness of the resist was less than the target thickness in all three case studies. Pad numbers correspond to Hall circuit labels in Figure 4.8.

individually measured and then averaged to provide a better sense of repeatability for each power level.

In the case of image reversal photoresists the laser exposes the negative space of the circuit design, this accounts for why there is coating removed from the square surrounding the designs in Figure 4.14(left). Increasing this buffer improves the odds of a proper lift-off but increases cycle time. Positive and positive bi-layer photoresists only have the laser raster across the circuit design itself which reduces the exposed area. These power studies, which focused on the adjustment of the laser lithography parameters were evaluated after the lift-off stage.

The circuit is constructed from a primary layer of Au. Unlike industrial ICs which are constructed with Cu, there is no encapsulation or similar method used to passivate the structures. For this reason, noble metals such as Au or Pt are preferred to prevent degradation of the sputtered structures. Electrical conductivity is also improved with less heating in the current lines which was beneficial at the low temperatures in which characterization was completed.

A proper undercut was found to be critical to the success of the lift-off. Figure 4.15(left) shows a correctly developed undercut prior to sputter deposition. The edges of the circuit appear somewhat brighter and out of focus due to the photoresist being viewed top-down, with the undercut observed through a portion of the photoresist. In contrast, designs that lacked a proper undercut have sidewalls

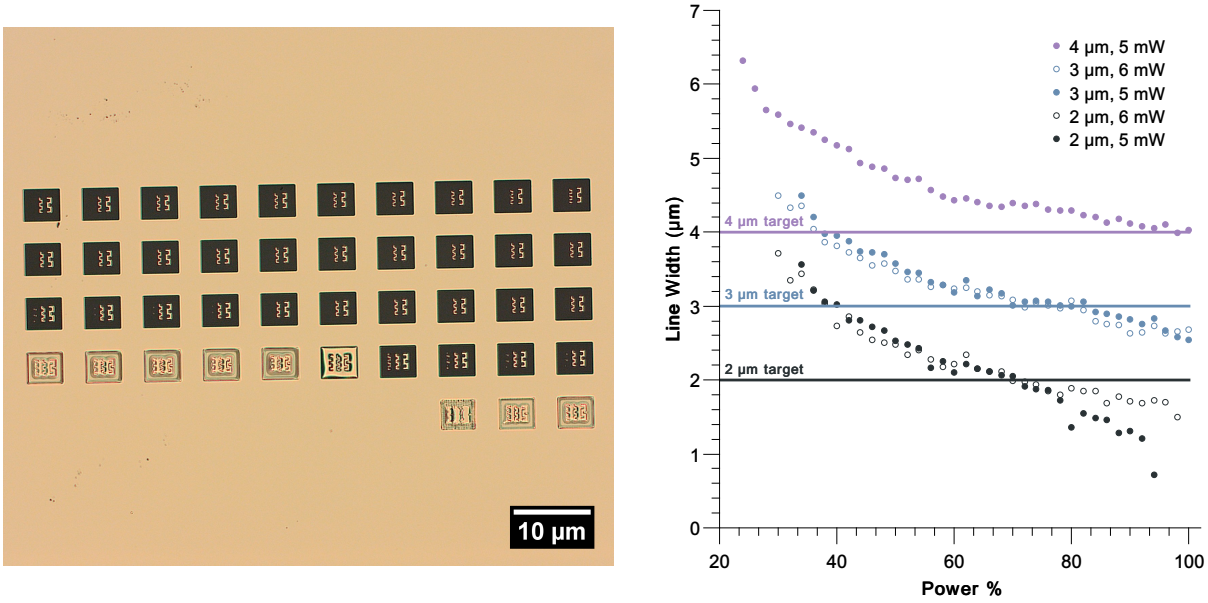

Figure 4.14: Example power study for laser powers 2-100% with 2% increments (left). Line width studies for power optimization with no ribbon for target thickness of 2, 3, and 4 μm line thicknesses. Slides were coated in Ti Prime and image reversed AZ 5214 E resist. Power percentage is for the laser, 1x1 pass, filter on, uni-directional and inverted with a buffer for image reversal (right).

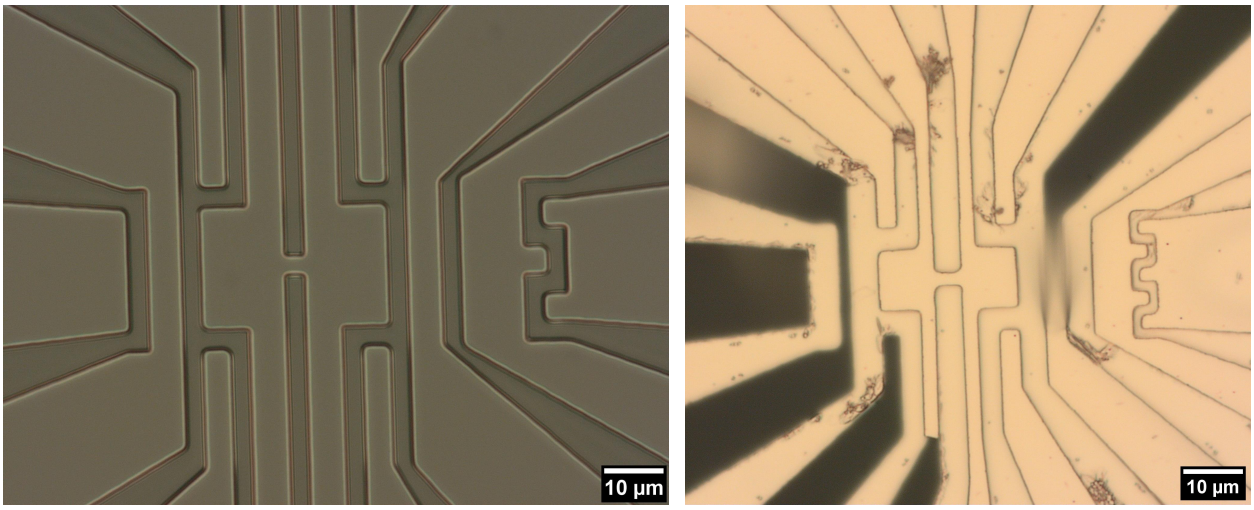

Figure 4.15: A Ti Prime + AZ 5214 E image reversal photoresist circuit with correct undercut after the development stage (left) compared to a poorly undercut LOR 3B + ma-P 1205 photoresist circuit that failed to lift-off correctly (right).

that appeared sharp and vertical. This led to lift-off issues as depicted in Figure 4.15(right). Here an insufficient undercut was produced by the LOR 3B and ma-P 1205 bi-layer photoresist. This circuit design was for a smaller sample which exacerbated lift-off issues by creating narrow coatings that required removal.

4.4.6 Sputter Deposition Evaluation

With a repeatable development and laser exposure process in place, the subsequent sputter deposition can be evaluated as shown in Figure 4.16. After the lift-off process the profiler was run across the deposited contact pads. The sputter deposition thickness target for this circuit was 250 μm with an adhesion layer of Cr accounting for approximately 50 μm. All measurements of these thicknesses were extremely accurate and consistent, confirming that the sputter deposition was reliable. The spikes in thickness on the edges of the pads shown in Figure 4.16(left) were largely due to the profiler needle itself, dragging and catching on portions of the applied coating during the measurement. This also accounts for some of the texture observed on the top of each pad as well. Some of these clean lift-off edges are shown in Figure 4.16(right).

4.4.7 Lift-off

Table 4.3: Lift-off temperatures and times for select photoresists.

Photoresists		Remover	Temperature (°C)	Time (minutes)
LOR 3B + ma-P 1205		NMP	60	20+
AZ 9260				
	10 μm	AZ 100	80	60-120
	24 μm	AZ 100	80	60-150
Ti Prime + AZ 5214 E				
	Standard	1165	80	40-95
	Image Reversal	1165	80	10

Lift-off times for the selected photoresists are listed in Table 4.3. Substrates were submerged in remover and placed on hot plates to accelerate the process. The substrate consists of a photoresist layer underneath the sputter deposition layers in positions where the coating was undesirable and

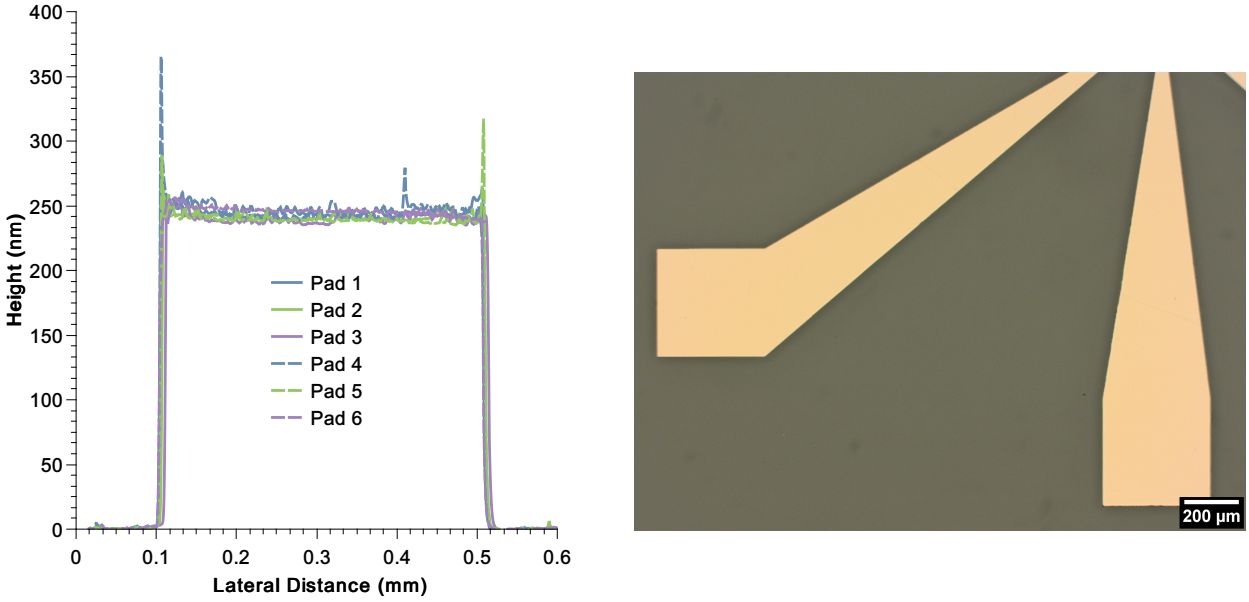

Figure 4.16: Successful lift-off of Ti Prime and AZ 5214 E photoresist. Profiler paths across the sputtered circuit pads after lift-off, measuring the thickness of the sputtered chromium and gold stack (left). Optical image of the pads leading to the Hall circuit at center (right). Pad numbers correspond to Hall circuit labels in Figure 4.8.

requires removal. Other areas that must be retained are simply the coating directly sputtered onto the glass substrate and micro-ribbon. Removers are unable to remove any of the sputter deposition coating but are able to breakdown the remaining photoresist. This process was accelerated by using tweezers to scratch portions of the slide that required removal, acting as points of initiation for the remover. A pipette was also used to flush remover across the surface removing debris in the process.

To remove unwanted photoresist from the LOR 3B and ma-P 1205 substrates an N-Methyl-2-pyrrolidone (NMP) bath, manufactured by MicroChemicals [267] was used. This process took a minimum of 20 minutes and in some instances did not produce an effective lift-off even when left overnight. This process was improved with optimized circuit design which maximized inter-sensors distances and removed unfavorable geometry that prevented portions of the metal from lifting off. Variability still existed, however, due to an insufficient undercut produced by LOR 3B. The LOR 3B seemed to have a higher sensitivity to changes in ambient temperature during processing which may have contributed to some of this variability. Long cycle times are detrimental to our process because portions of the micro-ribbon are exposed to the remover, etching or destroying the micro-ribbon.

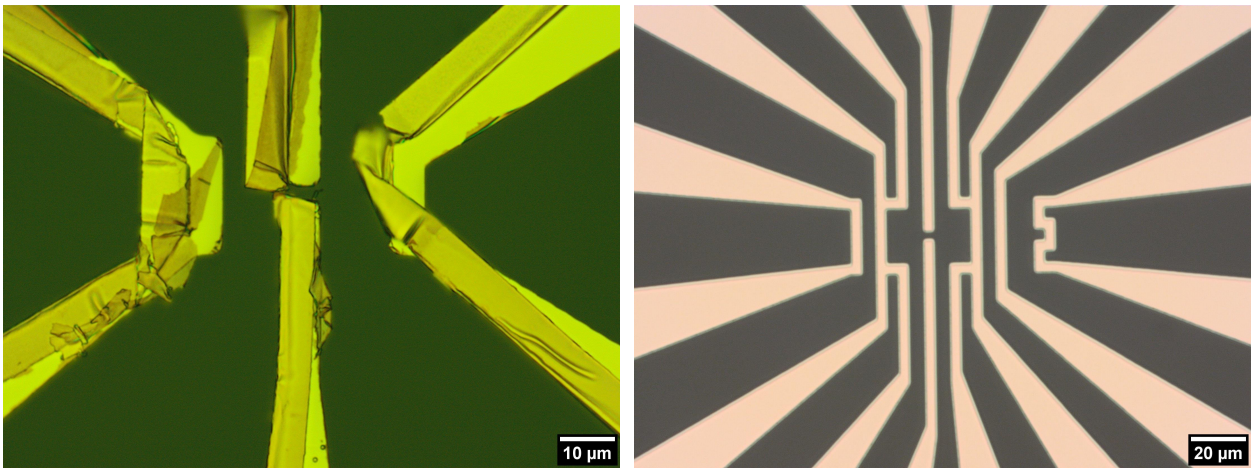

Figure 4.17: Poor lift-off of an AZ 9260 photoresist circuit with sidewall deposition adhering to substrate surface (left) compared to an optimized circuit design using Ti Prime + AZ 5214 E image reversal photoresist after successful lift-off (right).

The AZ 100 remover manufactured by MicroChemicals [268] was used for both target thicknesses of the AZ 9260 photoresist. Due to large variability in the photoresist thickness and no undercut to assist in detaching metal from the photoresist sidewalls, lift-off was poor as illustrated in Figure 4.17(left). Instead of rinsing away with the dissolved photoresist, gold adhered to the substrate surface where it was unable to be removed even in additional rinses. In contrast, an optimized design for a longer micro-ribbon is shown in Figure 4.17(right) using Ti Prime and AZ 5214 E image reversal photoresist. The laser is able to properly expose the negative space of the design and generate a sufficient undercut of the photoresist to allow for a repeatable lift-off.

Microposit remover 1165 manufactured by Dow Electronic Materials [269] was used for stripping the Ti Prime and AZ 5214 E photoresist. As noted in Table 4.3 when AZ 5214 E was used as a standard positive photoresist the time was longer to lift-off the finer features of the structure. This issue did not occur while using AZ 5214 E image reversal where processing times were kept to 10 minutes in all experiments, making it the shortest and most repeatable lift-off process. All subsequent optimizations were done using this image reversal photoresist.

4.4.8 Final Optimized Process

Positive, positive bi-layer, and image reversal photoresists were investigated and optimized to determine the most appropriate choice for our micro-ribbon lift-off application. Of these the AZ 5214 E image reversal photoresist with a Ti Prime adhesion layer was found to be the most effective and repeatable through the lift-off portion of the photolithography process.

Ti Prime was first applied to the substrate and spin coated at 6,000 RPM for 30 seconds followed by a soft bake on a hot plate at 120°C for 120 seconds. Next the AZ 5214 E photoresist was applied and spin coated at 3,500 RPM for 30 seconds. The process showed good results for the positive AZ 5214 E photoresist but improved lift-off properties in the image reversal configuration. This image reversal required an adjusted soft bake profile of 90°C for 240 seconds.

Once the photoresist application was complete, laser lithography was performed. Micro-ribbons were successfully processed with a laser power of 5 mW, 35% power (13% filter applied), 1×1, uni-directional, and inverted with a 1 mm buffer. Following the laser, a hard bake was performed on a hot plate at 120°C for 120 seconds, followed by a 120 second cool-down, and a 30 second flood exposure ($\lambda = 375$ nm). The image reversal photoresist was then developed in AZ MIF 726. As shown in Table 4.2, the development time was less than a minute.

After development, a Cr (50 μm) and Au layer (200 μm) were sputtered onto the substrate. The Au layer was increased from 150 μm due to the off-centered sputtering targets and the potential for the micro-ribbon to produce a shadow effect. The sputter deposition stage was also rotated to improve the uniformity of this conduction layer.

Lift-off provided the most variability between the different photoresists and thicknesses with results summarized in Table 4.3. Here AZ 5214 E in the image reversal configuration was the most repeatable, lifting off successfully for a variety of circuit designs in 10 minutes.

The final process with a $Ca_5In_2Sb_6$ micro-ribbon cut perpendicular to the c-direction is shown in Figure 4.18. Due to the high level of optimization, the circuit design was able to accommodate two thermometers, a heater, Hall probes and current lines. This allows the micro-ribbons to be fully characterized using the two configurations listed in Figure 4.18(right). While the PPMS puck

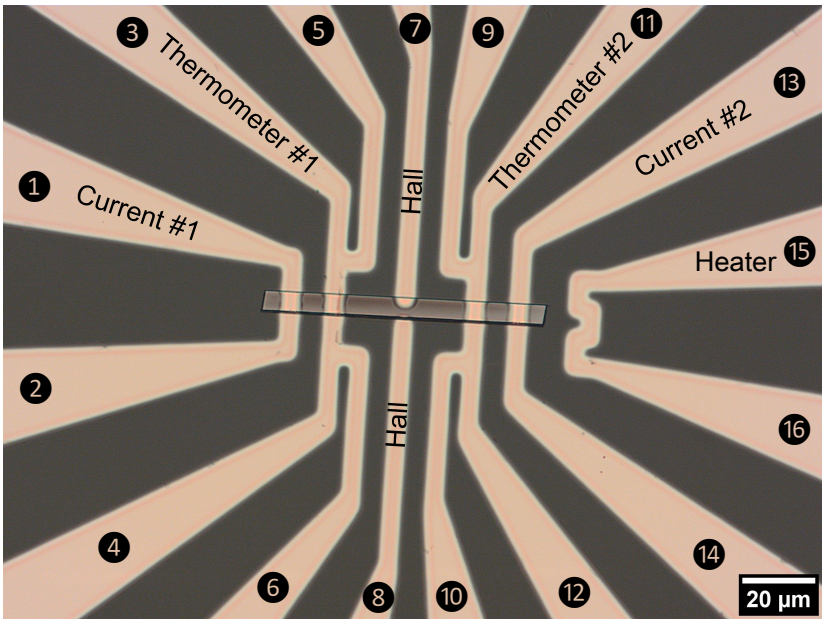

Configuration 1

Channel	Sensor	Input/Output	Node
1	Thermometer #1	I+	3
		I-	4
		V+	5
		V-	6
2	Thermometer #2	V-	9
		V+	10
		I-	11
		I+	12
3	Heater	I-	15
		I+	16

Configuration 2

1	Hall	V-	7
		V+	8
	Current 1	I+	1
	Current 2	I-	13

Figure 4.18: Successfully printed full characterization circuit over a $Ca_5In_2Sb_6$ micro-ribbon cut perpendicular to the c-direction. Sensors are labeled and enumerated, with the two characterization configurations listed at right.

was limited to three channels, the circuit could be bonded once and the probes swapped using an external switch box to switch between configurations even at low temperatures. Configuration 1 is capable of measuring Seebeck, electrical resistivity, and thermal conductivity. Configuration 2 is capable of measuring electrical resistivity, carrier concentration, and mobility. A second $Ca_5In_2Sb_6$ micro-ribbon, cut parallel to the c-direction was successfully processed and is shown in Figure 4.19 along with the successful bonding to a PPMS puck.

4.4.9 Transport Characterization

As illustrated above in Figure 4.6, out of 19 FIB-processed ribbons, only a single ribbon, cut perpendicular to the growth direction, was successfully characterized. Further, although the goal of the photolithography approach was to apply a circuit that would allow for complete characterization of the thermoelectric transport properties (Seebeck coefficient, thermal conductivity, and electrical conductivity), ultimately only a partial characterization of resistivity and carrier concentration was collected prior to the mirco-ribbon breaking apart.

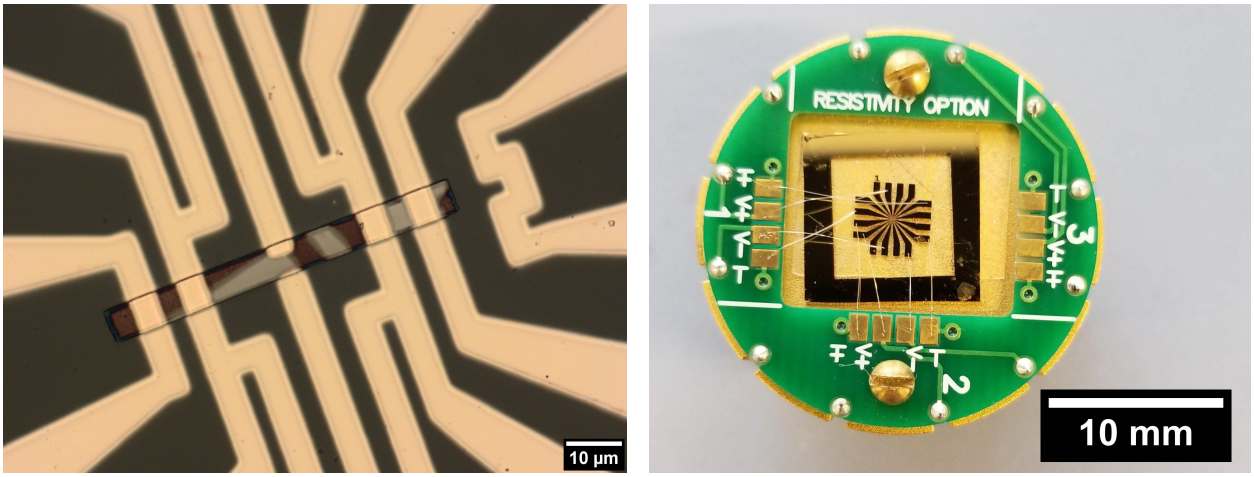

Figure 4.19: $Ca_5In_2Sb_6$ micro-ribbon cut parallel to the c-direction (left). Micro-circuit bonded successfully to surrounding PPMS puck (right).

Resistivity and Hall carrier concentration was collected on the successful $Ca_5In_2Sb_6$ micro-ribbon, cut perpendicular to the c-direction, in a limited temperature range from 220–300 K. Further data collection was not possible, as the sample was destroyed during testing, most likely due to excessive applied current. Several of the contacts were not sufficiently connected, but enough probes were found to be contacted to run a four-probe characterization on a sample cut perpendicular to the c-direction. Low resistance contacts allowed for a three-terminal measurement across an 11 μm segment of the sample. Measurements were unable to be repeated as the contacts had been destroyed. Other samples produced partial data sets before they too were destroyed due to either excess applied current or thermal load. Additionally, no reliable data was produced from the crystal cut parallel to the c-direction due to an attempted contact repair that destroyed the sample. Fortunately, the c-direction is the preferred growth direction of the crystal, so sufficiently large crystals ($\sim$ 5mm) could be characterized using a four-probe resistivity measurement by manually placing contacts, as shown in Figure 4.20.

Here four-terminal resistance measurements were collected whereby two leads pass a current through the sample while two other leads measure the potential drop across the sample. Ohm's Law, $R = V/I$, is used to calculate the sample resistance where R is the resistance of the material through which the current, I is passed through which exhibits a voltage V. The resistivity, ρ, is independent

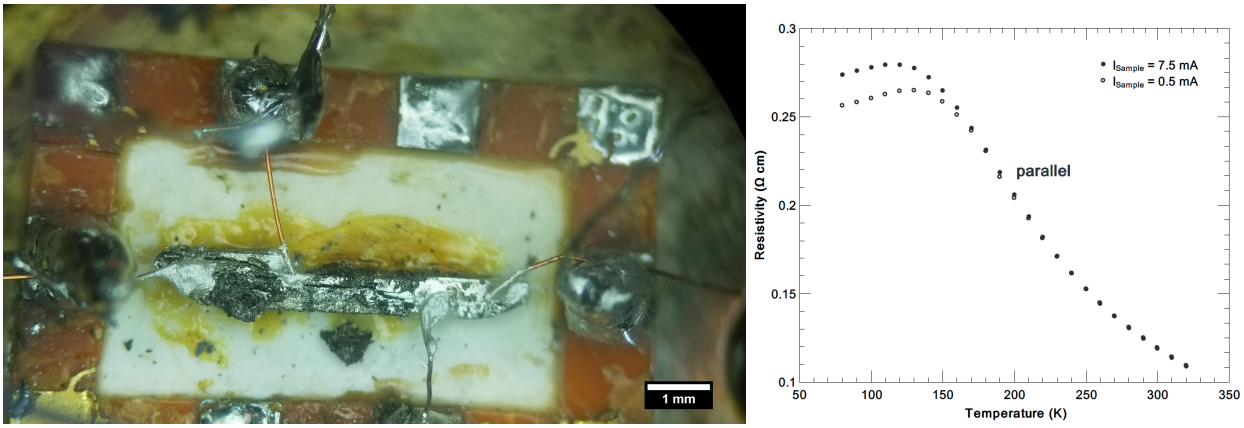

Figure 4.20: Four probe resistivity probes attached to single crystal $Ca_5In_2Sb_6$ parallel to the c-direction (left) with the resulting resistivity values for different input currents (right).

of sample dimensions and relates to R,

$$\rho = \frac{RA}{p}, \tag{4.1}$$

where p is the probe distance where the voltage is measured, and A is the cross-sectional area that is perpendicular to the direction of the current.

Electrical resistivity is measured in the sample by measuring the voltage difference between the two attached thermocouples, generated by the current supplied at $I_{\text{sample, in}}$ and expelled through $I_{\text{sample, out}}$. The current is then run in the opposite direction to eliminate the Peltier effect contribution. Electrical resistivity is defined in Equation 4.1 for the probe setup. In this manner the data is tested for repeatability, appropriate contact quality and sample uniformity. The measurements were carried out from 70K–320 K using liquid nitrogen to cool to chamber.

Resistivity values for the $Ca_5In_2Sb_6$ micro-ribbon cut perpendicular to the c-direction are compared with the measurements taken parallel to the c-direction on macroscopic crystals in Figure 4.21(upper left). The resistivity perpendicular to the c-direction was found to be a factor of 13-18 times higher than the parallel direction as depicted in Figure 4.21(upper right). The carrier concentration was measured only on the micro-ribbon, and was found to increase with increasing temperature, which indicates that the crystal is an intrinsic semiconductor, as shown in Figure 4.21(lower left). The magnitude of the carrier concentrations from the micro-ribbon is similar to

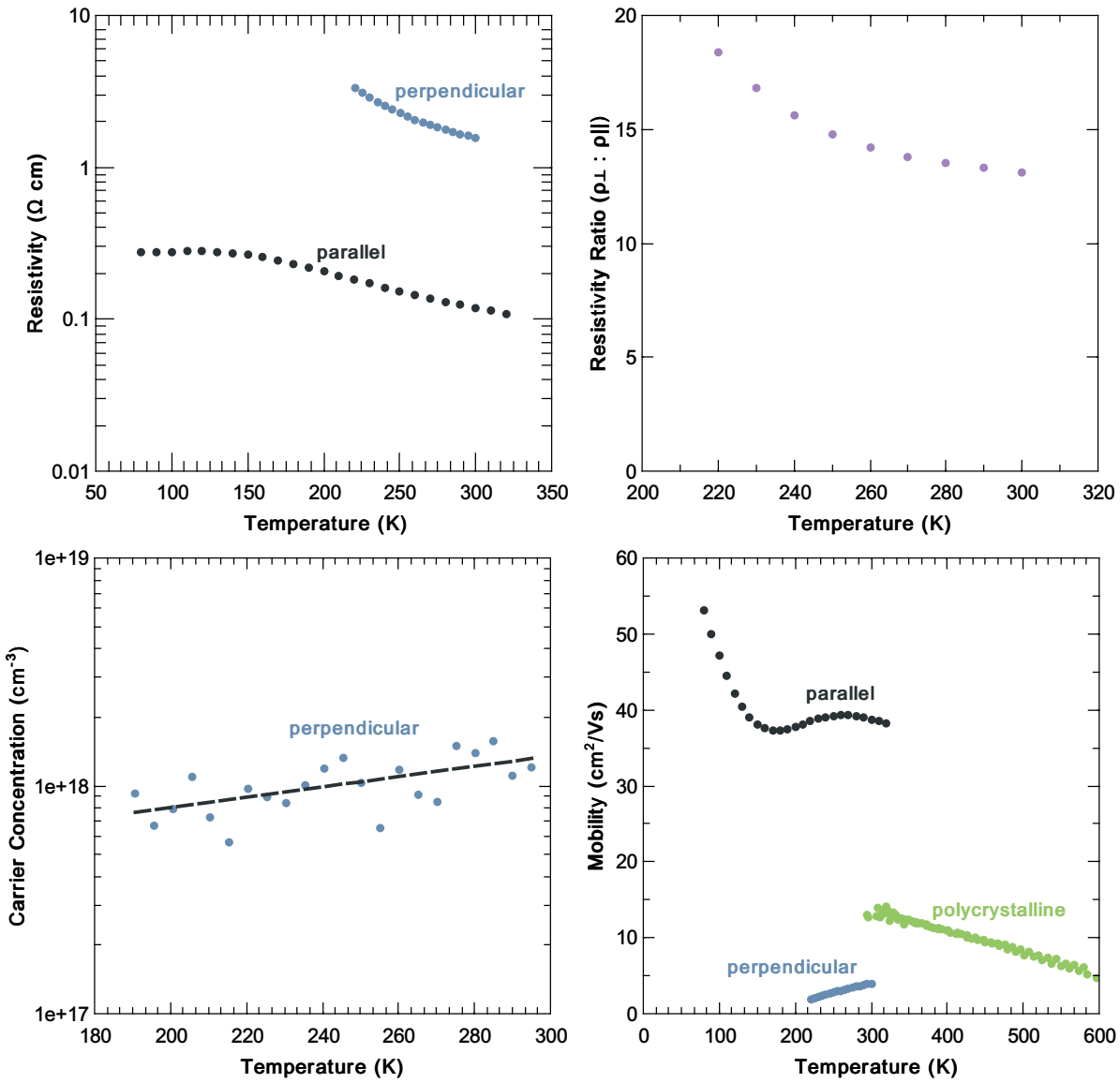

Figure 4.21: Resistivity, resistivity ratio, carrier concentration, and mobility of $Ca_5In_2Sb_6$ single crystal ribbon cut perpendicular to the c-direction compared to measured polycrystalline samples. Increased resistivity in the a-b plane is consistent with DFT predictions of anisotropic behavior in single crystals.

that of the previously reported polycrystalline $Ca_5In_2Sb_6$ [2], which is significant because it implies similar point defect densities and thus a narrow homogeneity range (*e.g.*, $Ca_5In_2Sb_6$ is a true line compound).

We are able to calculate mobility in both single crystal samples from $\sigma = ne\mu$ by assuming identical carrier concentrations in both of the characterized crystals. Note that carrier concentration

is not a function of crystallographic direction. Because the carrier concentration was only measured from 220-300K, data was extrapolated to low temperatures using an exponential fit. Mobility in the perpendicular and parallel directions are compared with the mobility of a polycrystalline sample in Figure 4.21(lower right). The polycrystalline data comes from the high temperature transport characterization carried out by Zevalkink et al. for the $Ca_5M_2Sb_6$ (M = Al, Ga, In) family [2]. Due to the small sample dimensions of the single crystal micro-ribbon, high-temperature measurements are not generally feasible (due to instrument geometry limitations), therefore single crystal data can only be compared to polycrystalline published values near room temperature. The comparison of single crystal and polycrystalline mobility 4.21(right) shows that the c-direction mobility is significantly higher, while the direction perpendicular to c is lower. This agrees with the calculated DFT results that predicted important anisotropy behavior, with increased resistivity in the a-b plane, and lower resistivity in the c-direction parallel to the covalent "ladder" polyanions.

Single crystal $Ca_5In_2Sb_6$ could potentially experience a significant thermoelectric performance increase if the c-direction is exploited. It is important to note, however, that the single crystals in this study are extremely resistive compared to the $Ca_5In_2Sb_6$ samples with the highest reported zT values. Thus, even if all of the thermoelectric transport properties were measured in the c-direction, a high zT is not expected. The electrical resistivity can be expected to decrease with increasing doping levels, which can have an important impact on the final figure-of-merit. Additionally, the $Ca_5In_2Sb_6$ micro-ribbons were evaluated for potential magnetoresistance between 0 and 14 T at 220 and 300 K. Data up to 5 T did not exceed the level of anticipated background noise, yielding no magnetoresistance behavior of note.

The resistivity anisotropy of $Ca_5In_2Sb_6$ is compared to other single crystal measurements from highly anisotropic materials in Table 4.4 at 220 and 300 K. Most of the compounds in Table 4.4 are layered compounds, in which case "parallel" refers to in-plane and "perpendicular" is out-of-plane. In the case of $Ca_5In_2Sb_6$ and $CsBi_4Te_6$, which both contain one-dimensional covalent chains, the data is parallel and perpendicular to the chain direction. It is observed that the resistivity of $Ca_5In_2Sb_6$ is more anisotropic than that of the tetradymite compounds (Bi_2Te_3 and Sb_2Te_3).

Table 4.4: Anisotropic thermoelectric properties at 220 and 300 K for selected one-dimensional (1D) compounds, van der Waals (vdW) compounds, and covalently bonded two-dimensional (Cov.-2D) compounds.

			220 K		300 K		
	Compound, direction		ρ (Ω cm)	$\rho_\perp/\rho_\parallel$	ρ (Ω cm)	$\rho_\perp/\rho_\parallel$	Ref.
1D	$Ca_5In_2Sb_6$	$\perp$	3.39E+00	18.6	1.56E+00	13.1	This work
		$\parallel$	1.82E-01		1.19E-01		
	$CsBi_4Te_6$	$\perp$	4.00E-02	126.9	3.96E-02	86.7	[66]
		$\parallel$	3.15E-04		4.57E-04		
vdW	Bi_2Te_3	$\perp$	–	–	4.84E-05	6.13	[270]
		$\parallel$	–		7.90E-06		
	$PbBi_4Te_7$(Cd)	$\perp$	1.30E-03	5.7	1.28E-03	4.3	[271]
		$\parallel$	2.26E-04		2.98E-04		
	$PbSb_2Te_4(SbI_3)$	$\perp$	3.49E-03	12.0	4.31E-03	10.1	[271]
		$\parallel$	2.91E-04		4.25E-04		
	Sb_2Te_3	$\perp$	–	–	4.27E-04	1.8	[272]
		$\parallel$	–		2.41E-04		
Cov.-2D	Mg_3Sb_2	$\perp$	1.39E+02	3.95	2.59E+00	0.49	[7]
		$\parallel$	3.52E+01		5.32E+00		
	SnSe	$\perp$	–	–	5.00E-01	5	[67]
		$\parallel$	–		1.00E-01		

The difference between the Zintl phases $Ca_5In_2Sb_6$ and Mg_3Sb_2 listed in Table 4.4, and the other layered materials is that κ_L is not expected to be highly anisotropic in the Zintl phases. A significant thermoelectric performance increase for $Ca_5In_2Sb_6$ is expected, while Mg_3Sb_2 behaves relatively isotropically as evidenced by its $\rho_\perp/\rho_\parallel < 1$ at 300 K. This analysis provides experimental confirmation of theorized anisotropy that can be exploited to dramatically increase zT values in single crystal $Ca_5M_2Sb_6$ (M = Al, Ga, In).

4.5 Concluding Remarks

Resistivity and carrier concentration values were collected on a single crystal micro-ribbon cut perpendicular to the c-direction. This coupled with resistivity values collected on a single crystal parallel to the c-direction yielded highly anisotropic electronic transport properties. This is the first experimental confirmation of this behavior in 5-2-6 Zintls, showing nearly a 20x increase in resistivity measurements in the perpendicular direction. It is anticipated that lattice thermal conductivity will remain isotropic, allowing for a significant thermoelectric performance boost

parallel to the c-direction.

While lacking a complete characterization across the low temperature regime this study proved that high quality micro-ribbons could be produced from larger single crystals using a FIB milling technique. A repeatable photolithography process has been established that is transferable to other micro-ribbon compounds and projects beyond just thermoelectric materials. The photolithography optimization is robust enough to allow for a number of sensors to be placed across samples.

CHAPTER 5

CRYSTAL GROWTH AND CHARACTERIZATION OF Mg_3Sb_2

The Zintl phase Mg_3Sb_2 has proven to be a promising new thermoelectric largely due to its excellent *n*-type performance. Electronic transport properties and the ability to dope *n*- or *p*-type have been shown to depend strongly on the Mg:Sb ratio present during synthesis. While Mg vacancies are suspected to be responsible for this behavior, the presence of vacancies has not been confirmed by direct experiments. In the present study, high quality single crystals have been successfully grown from Mg- and Sb-rich self-fluxes.

Refinement of SC-XRD revealed significant differences in the occupancy of the octahedrally-coordinated Mg(I) site. Further, the refinements reveal previously unknown interstitial sites. Despite differences in Mg occupancy, the Mg- and Sb-rich crystals are found to exhibit intrinsic semiconducting behavior, suggesting that the presence of grain boundaries might play a role in the highly *p*-type transport reported in previously studies.

5.1 Introduction

Thermoelectric materials offer the reversible conversion of heat and electricity. The maximum power and efficiency of a thermoelectric material is governed by its figure-of-merit, $zT = \alpha^2\sigma T/\kappa$, where α is the Seebeck coefficient, σ is the electrical conductivity, T is the absolute temperature, and κ is the thermal conductivity [59]. Extensive efforts have been made to discover materials that maximize zT, with high performance devices consisting of materials with zT exceeding unity [9].

Mg_3Sb_2 is an excellent *n*-type thermoelectric with a high $zT \approx 1.5$ [33]. Compared with state-of-the-art thermoelectric materials such as PbTe and Bi_2Te_3, it is lighter, less toxic and more earth abundant. Mg_3Sb_2 crystallizes in the trigonal, layered $CaAl_2Si_2$ structure, where Mg atoms occupy both the octahedrally-coordinated (Mg(I)) and tetrahedrally-coordinated (Mg(II)) cation sites [273]. It has a long history, beginning with its discovery in the 1930s [73, 274]. Initial studies of the thermoelectric transport in Mg_3Sb_2 characterized its undoped character [275] and a variety

of doping options on both the Mg (Zn[276, 277], Cd/Ag[278]) and Sb (Bi[279–283], Pb[284]) site, yielding *p*-type behavior.

These studies found persistent, but limited *p*-type thermoelectric performance below unity. A high figure-of-merit was only recently realized experimentally by Tamaki et al. [33] using Mg-rich growth conditions combined with Te doping on the Sb site ($Mg_{3.2}Sb_{1.5}Bi_{0.49}Te_{0.01}$). These results were confirmed under similar conditions in subsequent studies [5, 285, 286]. The superior performance of *n*-type Mg_3Sb_2 is due to a combination of higher band degeneracy and smaller effective mass [287, 288]. This results in a large thermoelectric quality factor, β, which is a metric of intrinsic material properties correlating to high performance thermoelectrics [285]. Consequently the *n*-type composition achieves a high performance of $zT \approx 1.5$ at 716 K [33] compared to the *p*-type performance below unity.

Intrinsic defects are understood to play a critical role in determining the dominant carrier type in Mg_3Sb_2. DFT calculations of defect energies show that Mg vacancies are responsible for the persistent *p*-type behavior in Sb-rich growths [5, 33, 289]. Mg-rich synthesis conditions are predicted by DFT to increase the formation energy of Mg vacancies and decrease the formation energy of Mg interstitials. This is thought to leads to an overall decrease in acceptor type defects [5, 33].

Although electronic transport properties and defect calculations both strongly support the theory that Mg-vacancies play a role in *n*- and *p*-type doping, the presence of Mg vacancies have not previously been directly observed in structural characterization of Mg_3Sb_2 samples. In the current study, single crystals of Mg_3Sb_2 were grown from Mg- and Sb-rich environments using a self-flux method. These crystals have been characterized and compared using SC-XRD and electronic transport measurements. This approach allows for direct assessment of the relationship between growth conditions and intrinsic defect concentrations.

5.2 Experimental Methods

5.2.1 Synthesis

Elemental Mg (granules, 99.8%), and Sb (shot, 99.999%) were weighed, mixed, and loaded into 2 ml capacity alumina Canfield crucible sets with 13 mm OD $\times$ 25 mm height [155]. Mg_3Sb_2 single crystals were grown using a self-flux method with either excess Mg (Mg_3Sb_2 + $Mg_{6.90}$) or Sb (Mg_3Sb_2 + $Sb_{3.56}$). Alumina crucibles were sealed in quartz ampules, 14/16 mm ID/OD. Mg-rich growths were double sealed using a larger quartz ampule, 17/19 mm ID/OD to safe guard against potential ruptures due to Mg vaporization losses reacting with the quartz. For Mg-rich growths, a large excess of Mg was needed as some of the elemental Mg was removed from the system due to formation of MgO with the Al_2O_3 crucibles, which produced a noticeable gray discoloration. Reactivity with the quartz ampules was more significant still, appearing black as the vaporized Mg reacted with the Si (2 Mg + Si $\rightarrow$ Mg_2Si) or O (2 Mg + SiO_2 $\rightarrow$ 2 MgO + Si) in the quartz. Tantalum tubes have been reported as an alternative to alumina crucibles. However, Ta reacts with Sb [290], forming a layer of $TaSb_2$ on the inner surface that acts as nucleation site for Mg_3Sb_2 crystals as described in Xin et al. [7].

The Sb-rich growths were heated to 800°C and then cooled to 675°C at a rate of 3°C/hr where they were extracted from the furnace, flipped, and centrifuged. The Mg-rich composition was heated to 800°C and cooled to 650°C at a rate of 3°C/hr where it was extracted from the furnace, flipped, and centrifuged. All growths were centrifuged for two minutes at 2500 RPMs separating the grown crystals from the remaining flux. No flux was removed for the Mg-rich growths as Mg reaction and vaporization losses were significant.

5.2.2 Structural Characterization and Metallography

Single crystal surfaces were observed using polarized light microscopy. Samples were also observed using a Zeiss Evo LS25 SEM with an attached EDAX Apollo X EDS. Data were collected and processed with the TEAM software suite to determine approximate chemical compositions. Electron

backscatter diffraction was carried out on a Tescan Mira 3XMH SEM equipped with an EDAX-TSL EBSD system. Microscopy revealed homogeneous main phase with only islands of elemental Sb metal. Thus, it may be concluded that the measured physical properties are reflecting the properties of the main Mg_3Sb_2 phase. Crystal structure and composition were evaluated with SC-XRD at the Max Planck Institute for Chemical Physics of Solids in Dresden, Germany.

5.2.3 Transport Characterization

Resistivity and Hall coefficients were measured on several crystals in the in-plane direction on a Physical Property Measurement System (PPMS) manufactured by Quantum Design. Resistivity was measured from 210 to 360 K with a standard four-point contacting method using Ag paint. Hall voltage was measured from 100 to 350 K as a function of magnetic field.

5.3 Results & Discussion

5.3.1 Crystal Growth and Morphology

The morphology of the grown Mg_3Sb_2 crystals can be described as large, flat platelets, measuring greater than 5 mm across, with size constrained mainly by the crucible diameter. Growth occurred preferentially along the a-b plane, confirmed by EBSD, in stacked layers parallel to the crucible bottom. No Mg flux drained from the Mg-rich growths as the excess Mg either reacted with the container or vaporized. Sb-rich growths benefited from Sb being a good flux [198] that does not readily wet to the surfaces of crystals, draining the liquid flux away from the crystals in the centrifuge process. While Sb has a higher melting temperature than most common fluxes [166] it possess a sufficiently low vapor pressure (1617°C, 1 atm.) and very low viscosity (1.22 mPa s) [291].

The surface morphology of Mg_3Sb_2 crystals was observed using SEM, shown in Figure 5.1. Here the hexagonal growth behavior is observed in plane as step-like growth terminations. While the transport properties are isotropic, the structure has a clear preferred growth direction that is

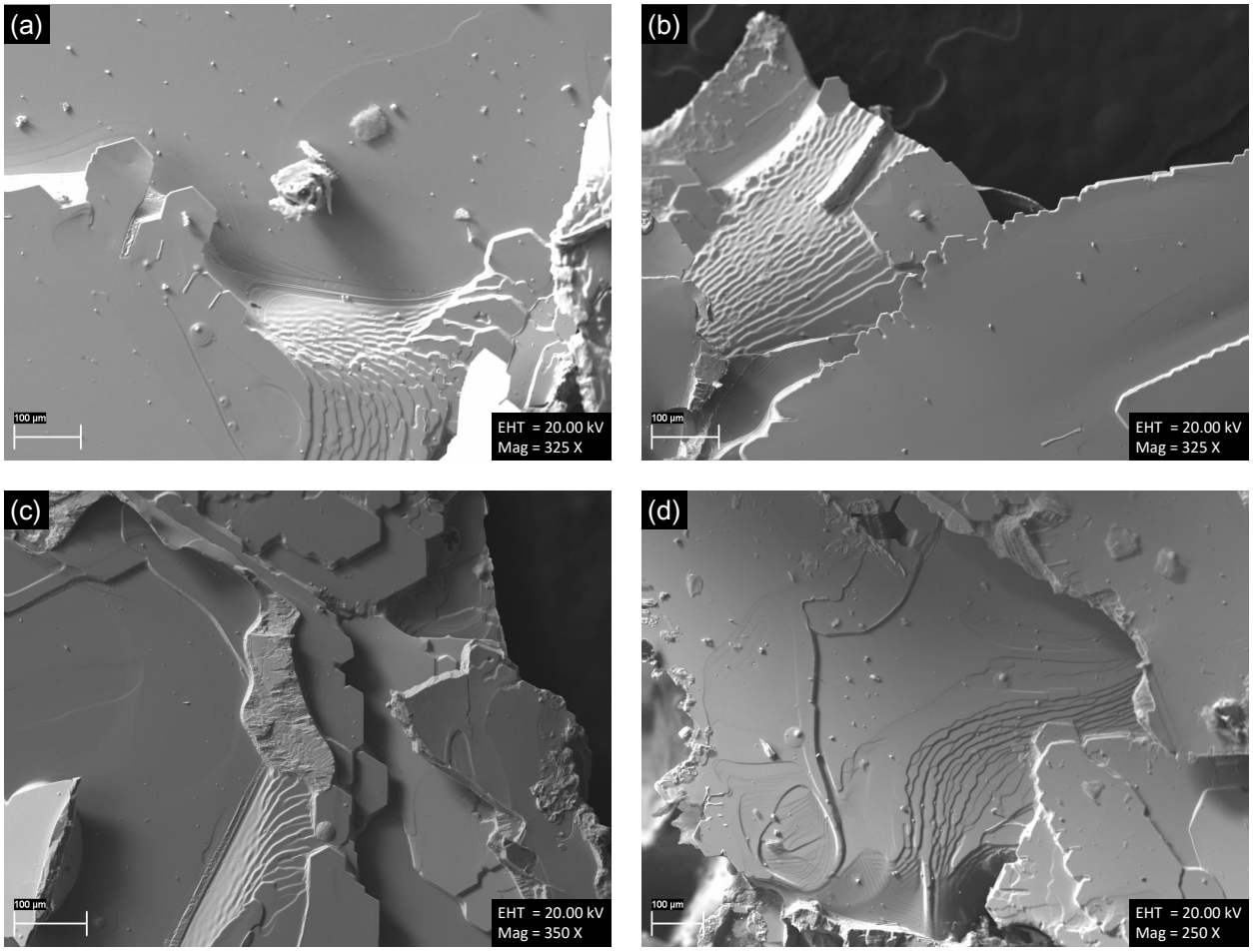

Figure 5.1: Scanning electron microscopy images of Mg_3Sb_2 single crystal platelets, note the hexagonal growth behavior. Crystal surfaces away from the growth perimeter were flat and smooth.

in-plane, suggesting that dangling in-plane bonds are more energetically costly than out-of-plane bonds. This growth behavior is consistent with that described in Xin et al. [7] for Mg_3Sb_2 single crystals. The orientation of the crystals was further confirmed using EBSD analysis.

5.3.2 Structure Description

The atomic positions and occupancies obtained from single crystal refinements are shown in Figure 5.2 with crystal data listed in Table 5.2. The most striking difference between the Mg- and Sb-rich crystals is in the occupancy of the octahedrally coordinated Mg(I) site. In Sb-rich growths, it was observed that the Mg(I) site was partially occupied at 87%, while in Mg-rich growths this site was

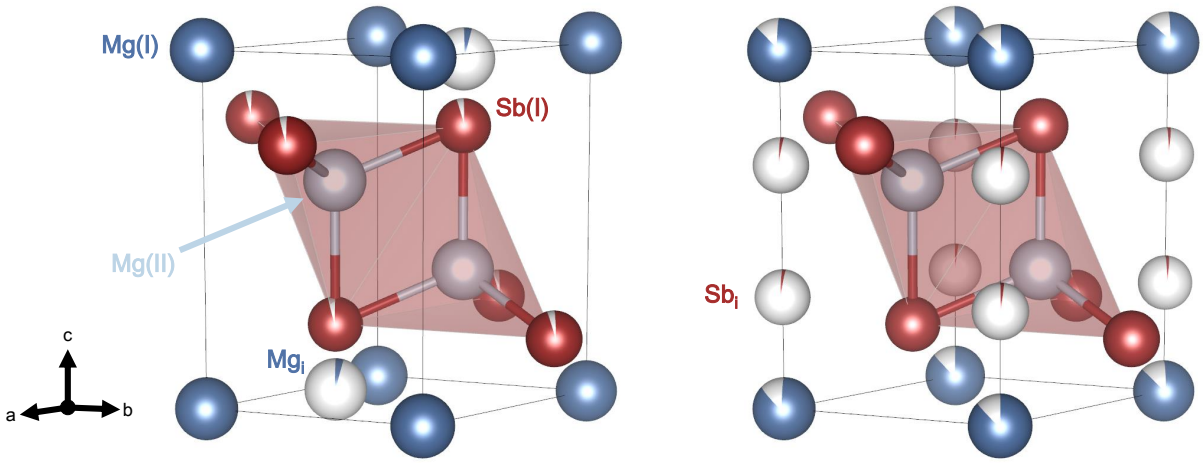

Figure 5.2: Crystal structure of Mg_3Sb_2 from Mg-rich growth conditions with Mg interstitial atoms and trace Sb(I) vacancies (left). Crystal structure from Sb-rich growth conditions with partial Mg(I) occupancy (right).

Table 5.1: Atomic positions and occupancy data for Mg_3Sb_2 single crystals grown from both Mg- and Sb-rich fluxes.

Atom	Site	x/a	y/b	z/c	B(is/eq)	occ.
Mg-rich						
Mg1	1a	0	0	0	3.6(5)*	1
Mg2	2d	2/3	1/3	0.634(2)	2.9(3)*	1
Mg3	2d	2/3	1/3	0.038(10)	2.531	0.035(10)
Sb1	2d	2/3	1/3	0.2281(4)	2.60(6)*	0.965(10)
Sb-rich						
Mg1	1a	0	0	0	1.74(8)*	0.87(1)
Mg2	2d	2/3	1/3	0.6350(4)	1.59(5)*	1
Sb1	2d	2/3	1/3	0.22836(6)	1.430(10)	1.00(1)
Sb2	2c	0	0	0.684(4)	1.4(5)*	0.014

fully occupied. This is largely consistent with DFT defect calculations [5, 33, 289] which have predicted low formation energies for Mg vacancies when Mg_3Sb_2 is in equilibrium with Sb. Past studies have also consistently indicated that vacancies on the octahedrally-coordinated Mg(I) site are lower in energy than vacancies on the tetrahedral Mg(II) site.

In addition to vacancies, DFT studies have considered a number of possible anti-site defects and a variety of interstitial defects. They consistently predict that the (0, 0, 0.5) position is the most stable site for a Mg interstitial, with a 2+ oxidation state. Indeed, the (0, 0, 0.5) site is the largest void in the Mg_3Sb_2 structure, so it seems like the most natural place for an extra atom. In contrast,

Table 5.2: Crystallographic data for Mg_3Sb_2 single crystals grown from both Mg- and Sb-rich fluxes.

	Mg-flux	Sb-flux
Space group	P -3 m 1	P -3 m 1
a (Å)	4.561(3)	4.5672(6)
c	7.250(6)	7.227(1)
Cell volume ($Å^3$)	130.6(3)	130.54(6)
F(000) (electrons)	138.0	138.1
Number of atoms in cell	5.0	4.9
Calculated density (g/cm^3)	4.023(9)	4.034(2)
Absorption coefficient (1/cm)	106.28	107.85
Radiation and wavelength	MoK 0.70930	MoK 0.70930
Mode of refinement	F(hkl)	F(hkl)
Number of atom sites	4	4
Two-theta and sinT/l (max)	66.40 0.772	85.84 0.960
Number of measured reflections	859	2733
Number of condit. reflections	859	2733
Number of unique reflections	221	405
Reflections used in refinement	152	385
R(sig), R(eq)	0.0510, 0.0678	0.0270, 0.0550
R(F), Rw	0.0756, 0.0757	0.0312, 0.0341
Goodness of fit	2.130	1.040
Scale factor	0.32(1) [8.688284]	0.269(3) [13.77765]
Number of free parameters	10	13

in the current study, there is no evidence of interstitial electron density at the predicted location of (0, 0, 0.5).

In the Mg-rich crystals, interstitial electron density is observed at (2/3, 1/3, 0.038) as shown in Figure 5.2(left). In Mg-rich growth conditions, the interstitials are more likely to be Mg than Sb. In either case, these interstitial sites are only physically reasonable if defect complexes form in this structure, such as a Frenkel pair. A recent DFT investigation [289] showed that a Mg vacancy next to a Mg-interstitial (Frenkel pair) returns to the original structure upon relaxation, which is contrary to our experimental results.

The refinement of Sb-rich crystals yielded interstitial positions at (0, 0, 0.684), shown in Figure 5.2(right), that have not been considered in previous defect calculations. The interstitial electron density cannot be unambiguously assigned to Mg or Sb. However, in Sb-rich growth conditions, Mg interstitials are unlikely. It is proposed here that Sb5+ to be a more likely possibility. Formation

of Mg(I) vacancies as acceptor type defects during growth in Sb-flux will push the Fermi level deep into the valence band. In response, this might stabilize high oxidation state interstitial ion such as a Sb5+. Considering the vacancies and presumed Sb interstitials, the overall composition of the Sb-rich crystals would be $Mg_{2.87}Sb_2$. The resulting Mg deficiency of 0.13 Mg per unit cell translates to a concentration of 1.0×10^{21} Mg/cm^{-3} or 2.0×10^{21} holes/cm^3. This should result in a degenerate *p*-type semiconductor. However, as discussed below, this is not consistent with the observed electronic transport behavior.

5.3.3 Electronic Transport Properties

The in-plane resistivity of Mg- and Sb-rich Mg_3Sb_2 crystals are shown in Figure 5.3. The magnitude and temperature-dependence of the resistivity suggest intrinsic semiconducting behavior under both growth conditions. The intrinsic behavior is consistent with reports from single crystals grown in Sb flux by Xin et al. [7], which are shown as the dashed curves. Note that the in-plane and out-of-plane resistivity reported by Xin et al. shows only a very small degree of anisotropy and that electronic transport is nearly isotropic, despite the highly-anisotropic crystal morphology.

The electrical resistivity of the Sb-rich samples was fit to the equation describing intrinsic behavior of the intrinsic semiconductor,

$$\rho = aT^{-3/2}e^{E_g/2k_BT}, \tag{5.1}$$

where a is a constant, T is temperature, E_g is the band gap, and k_B is the Boltzmann constant. This expression resulted in band gaps of 0.59 eV and 0.66 eV, consistent with previous reports. The resistivity of the crystallite from the Mg-rich batch does not show the typical exponential behavior of an intrinsic semiconductor. It seems that the doping level, which caused the leveling off of the Hall coefficient below 300 K, as shown in Figure 5.4, is also responsible for the leveling off of the resistivity with decreasing temperature.

Hall measurements were performed on several Mg- and Sb-rich crystals. The magnitude and temperature-dependence of the charge carrier concentration ($n_H = 1/R_He$) as measured by the

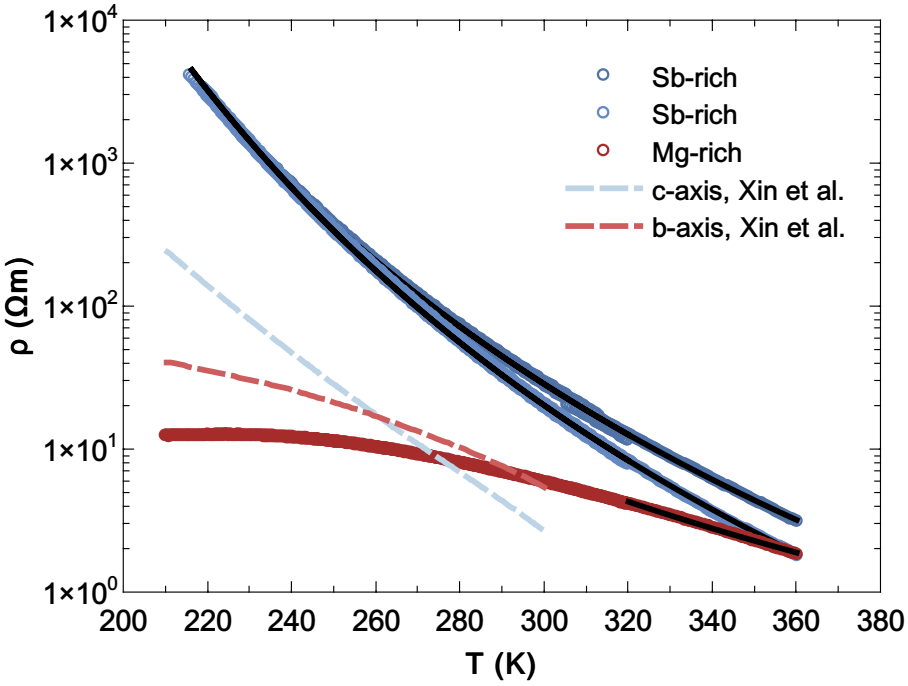

Figure 5.3: Resistivity values for select Mg_3Sb_2 single crystals from Sb- and Mg-rich growth conditions, compared to published values [7].

Hall effect suggests intrinsic semiconducting behavior for both sets of crystals. The most notable exception is the *p*-type temperature-independent behavior of some crystallites from the Mg-rich samples, with a very low charge carrier concentration corresponding to the concentration of Mg defects on the order of 10 ppm, which is well below the detection level of SC-XRD. One piece from the Mg-rich batch showed *n*-type charge carriers and follows the exponential temperature behavior of an intrinsic semiconductor but only at temperatures above 300 K. Below 300 K, the charge carrier concentration does not drop further, pointing to *n*-type defects with a concentration of approximately 10^{14} cm^{-3}. The Mg-rich sample batch reveals the difficulties of crystal growth from a flux.

The crystallites from the Sb-rich samples consistently show intrinsic carrier concentrations. This is surprising, given the large predicted Mg-deficiency which should lead to high p-type carrier concentrations. In light of the intrinsic semiconducting behavior of all samples, it is plausible that the Mg deficiencies may be compensated by additional Sb^{5+} interstitials in the vicinity of the Mg vacancies to achieve a charge balanced material.

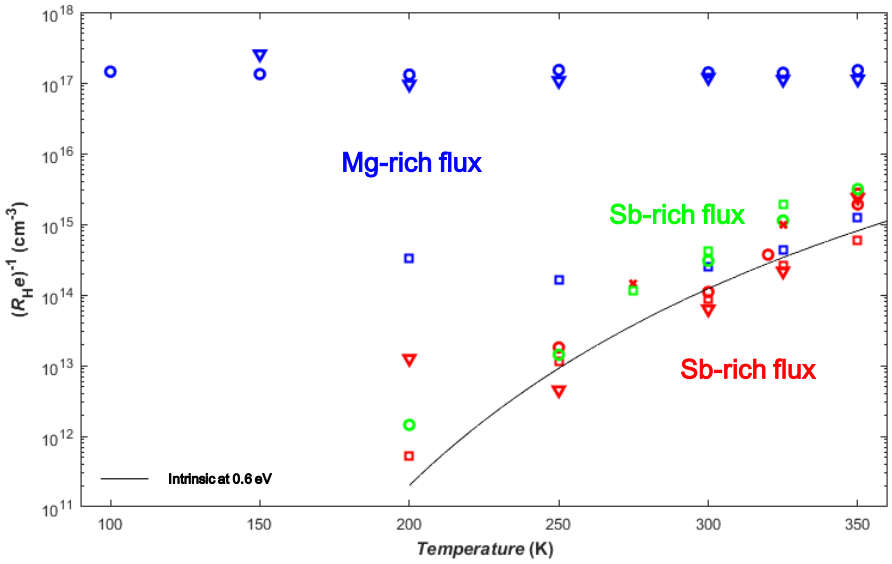

Figure 5.4: Inverse Hall coefficient of several Mg_3Sb_2 samples, measured across three batches.

The sign of the Hall effect for intrinsic semiconductors is determined by the mobility of the holes and electrons, typically resulting in *n*-type behavior due to electrons having larger mobility, expressed as,

$$R_H = \frac{p\mu_h^2 - n\mu_e^2}{e(p\mu_h + n\mu_e)^2} \xrightarrow{p=n=n_i} \frac{\mu_h - \mu_e}{en_i(\mu_h + \mu_e)}, \tag{5.2}$$

where p, n and n_i are the hole, electron and intrinsic charge carrier concentrations. The mobility $\mu_{h,e} = e\tau_{h,e}/m_{h,e}$ of the corresponding charge carriers is proportional to the transport scattering time $\tau_{h,e}$ and inversely proportional to the inertial or conductivity effective mass in each band $m_{h,e}$. The charge carrier concentration of an intrinsic semiconductor is given by [292],

$$n_i = \frac{1}{4}\left(\frac{2k_BT}{\pi\hbar^2}\right)^{3/2}(m_c m_v)^{3/4} e^{-E_g/2k_BT}, \tag{5.3}$$

where k_B is the Boltzmann constant, T is the temperature, and m_e is the mass of a free electron. In this case, the effective masses of the electrons and holes in the conduction and valence bands, m_c and m_v, are slightly different due to the geometrical averaging of the band anisotropy and multiplicity.

We estimate the expected temperature dependence of the charge carrier concentration by assuming a band gap of $E_g = 0.6$ eV. The DOS effective masses are provided by Zhang et al. and

account for the holes at the Γ point to 0.58 m_e, and for the electrons at the K point to 0.45 m_e [285]. For this estimation, electrons in the minimum of the ML band are not considered, with an effective mass of 1.05 m_e and lying only 0.02 eV above the minimum of the conduction band at the K point. The electrons around the K point and around the minimum of the ML conduction band have single valley effective masses of 0.28 m_e and 0.32 m_e but are greatly increased by the band multiplicities of two and six, respectively. The multiplicity of the hole pocket at the Γ point is one. The determining factor for the sign, and partially also for the size of the Hall effect (measured charge carrier concentration), are hole and electron mobilities. Zhang et al. estimated these to be 16 cm^2/V s and 84 cm^2/V s for holes and electrons, respectively [285]. The temperature dependence of the energy gap and mobilities were not included in the estimate. The estimate is presented as the black line in Figure 5.4, and is plot as $1/R_H e = n_i(\mu_h + \mu_e)/(\mu_h - \mu_e)$. This estimate correctly describes the order of magnitude and the temperature behavior of most of the data.

5.4 Concluding Remarks

Single crystals of Mg_3Sb_2 were successfully grown from both Mg- and Sb-rich environments with SC-XRD refinement revealing previously unreported interstitial positions for both conditions. Mg-rich growths had fully occupied Mg(I) sites and interstitial electron density at (2/3, 1/3, 0.038) where they are suspected to form a defect complex. Sb-rich growths revealed partial occupancy of the Mg(I) site, consistent with DFT results due to the low formation energy anticipated for Mg vacancies. While a number of anti-site and interstitial defects have been considered with DFT, interstitial position (0, 0, 0.684) is reported from this analysis where it is proposed that Sb5+ is a likely occupant. All measured crystals exhibited intrinsic semiconducting behavior, despite Mg vacancies.

CHAPTER 6

STRUCTURE AND ELECTRONIC PROPERTIES OF NEW ZINTL PHASE $\mathbf{Ca_9Zn_{3.1}In_{0.9}Sb_9}$

6.1 Introduction

Many new compound discoveries are occurring in the Zintl phase space [44, 127, 134, 144], often as an unintended consequence of attempts to dope or alloy known phases, which results in the discovery of novel compounds. This is often the result of flux growths, in which candidate elements are heated to form a homogeneous melt and slow cooled to produce crystals. Unlike exploratory powder synthesis, flux growths have a chance of yielding single-phase single crystals of a new compound or structure, if the overall melt composition happens to intersect the correct solid+liquid region of the phase diagram.

Previously, $Ca_5In_2Sb_6$ single crystals have been successfully grown from a self-flux of molten In and Sb. Earlier studies of polycrystalline samples have shown that $Ca_5In_2Sb_6$ is an intrinsic semiconductor with high resistivity, and therefore low zT. However, it has also been shown that $Ca_5In_2Sb_6$ can be doped with Zn^{2+} on the In^{3+} site, yielding a maximum $zT = 0.7$ at 950 K for $Ca_5In_{1.9}Zn_{0.1}Sb_6$ [1]. In this portion of the study, Ca-In-Zn-Sb elements are mixed in a flux growth. This quaternary phase space also includes the promising thermoelectric candidates Zn_4Sb_3 [29], $CaZn_2Sb_2$ [145], $Ca_{14}Zn_{1+x}Sb_{11}$ [293], and $Ca_9Zn_{4.5}Sb_9$ [35]. The Zintl phase $Ca_9Zn_{4.5}Sb_9$, in particular, has good thermoelectric properties due to the tunability of the Zn interstitial site.

From previous work, it is known that $Ca_5In_2Sb_6$ single crystals can be optimally grown in a $In_{73}Sb_{42}$ flux. Efforts to Zn-dope this compound began with the addition of small amounts of Zn to the same flux in hopes of producing $Ca_5In_{2-x}Zn_xSb_6$ single crystals. Doped single crystal growth is complicated by a large number of potential binary phases forming between Zn and any of the elements in the original Ca-In-Sb ternary system. These including the congruently melting $CaZn_2$ (T_m = 704°C), $CaZn_5$ (T_m = 695°C), and $CaZn_{11}$ (T_m = 724°C) [294]. Fortunately, no known

Zn-In binaries exist [295] and potential Zn-Sb binaries are not as concerning, due to solidification temperatures well below the flux growth extraction temperatures of 730°C [296]. Information on the ternary phase diagram is limited for the Ca-In-Sb system and even more so for the quaternary system with the addition of Zn.

Unlike In and Sb, Zn is not a preferred choice for flux growth due to its higher vapor pressure (907°C, 1 atm.). There are instances, however, of crystal growth using Zn as a flux [297, 298], motivated by its low melting temperature. Zn also has high viscosity, implying that Zn in excess may be hard to separate from grown crystals during centrifuging. The higher vapor pressure does allow for a secondary sintering process to remove excess Zn through evaporation if necessary [196]. This study treats Zn as a dopant and will be added to flux growths in small quantities and at temperatures where the vapor pressure is not yet a concern.

6.2 Experimental Methods

6.2.1 Synthesis

High purity elements were used in the synthesis including: Ca (Sigma-Aldrich: dendritic pieces, 99.9%), In (Alfa Aesar: Indium shot, 5mm & down, 99.9995%), Sb (Alfa Aesar: Antimony shot, 6mm & down, 99.999%), and Zn (Alfa Aesar: Zinc shot, 1-5mm, 99.999%). Elements were mixed in stainless steel ball mill jars under an argon atmosphere with two stainless steel balls (dia. = 12.7 mm) using a SPEX MixerMill 8000D. The mill was run for 60 minutes for each 5 gram sample processed. This process promotes thorough, homogeneous mixing of the constitutive powders, shot, and pellets.

A Dr. Sinter spark plasma sinter 211LX system was used to process powder samples using ultrafine grain graphite (POCO EDM-3) die sets with graphite foil spacers punched from sheets (Alfa Aesar, 0.13 mm thickness, 99.8% metals basis). These foils separate the sample from the graphite punches and promote a more uniform contact and conducting surface. Uniaxial pressure was applied to a pair of water-cooled steel platens that transferred this force through two conductive graphite pedestals. Both pressure and DC current were applied to samples simultaneously. Samples

were heated to 550°C in 5 minutes and held at temperature for 10 minutes to consolidate the powder into the desired phase. Temperatures were measured using a type-K thermocouple that was placed into a clearance hole on the side of the graphite die. All samples were processed under vacuum ($\approx 1 \times 10^{-2}$ torr). Samples routinely achieved density yields greater than 99% theoretical for $Ca_5In_2Sb_6$.

6.2.1.1 Flux Growth

Flux growth experiments were carried out in a Thermo Fisher Scientific 1100°C box furnace. Al_2O_3 Canfield crucible sets were loaded and sealed in quartz ampules at a vacuum of less than 1×10^{-4} torr. Flux growths were a mixture of elements: Ca 1.4 wt.%, Zn 1.7 wt.%, In 56.5 wt.%, and Sb 40.4 wt.% ($\approx Ca_5In_2Sb_6 + In_{68.4} + Sb_{41.5} + Zn_{3.7}$) with both In and Sb contributing as the major flux elements. Flux growths were heated from room temperature to 900°C in 12 hours, held at 900°C for two hours before slow cooling to 730°C at a rate of 3°C/hr, at which point growths were extracted and centrifuged at 2500 RPM for two minutes.

6.2.2 Structural and Thermal Characterization

SEM was performed on a Tescan Mira 3XMH while EDS was performed using an EDAX Apollo X module with an active area of 10 mm^2. Images were collected and processed with the Texture and Elemental Analytical Microscopy (TEAM) software suite to determine the approximate chemical composition of crystal and flux components. Single crystals were placed on conducting carbon tape to eliminate any potential charge build up. All samples evaluated were semiconducting or metallic in character.

Initial SC-XRD was performed at Michigan State University while the data used in the final structure analyses were collected at University of Delaware. Data was collected using a Bruker APEX II CCD-based diffractometer, using monochromated Mo Kα radiation ($\lambda = 0.71073$Å). The operating temperature was 200(2) K, maintained by a cold nitrogen stream. Crystals were selected under a microscope and cut to suitable sizes (ca. 0.1 mm in all dimensions). Many crystals

were tried and evaluated by rapid scans, before the best were chosen for full data collection. Data were acquired in batch runs at varied ω and θ and were integrated using the SAINT software [299], multi-scan absorption correction was performed using SADABS [2]. Crystal structures were solved with the ShelXT program using the intrinsic phasing solution method and were refined using full-matrix least squares minimization on F2 with the aid of ShelXL [300, 301]. Atomic coordinates were standardized using STRUCTURE TIDY [302].

Simultaneous thermogravimetry/differential scanning calorimetry measurements (TG/DSC) were conducted at University of Delaware on a TA Instruments SDT Q600 analyzer. The samples were loaded in capped alumina pans. After equilibration at 323 K, the temperature was increased to 1073 K at a rate of 20°/min. To prevent oxidation, the measurements were done under a constant flow of high-purity argon.

6.2.3 Resistivity Measurements

Electrical resistivity was measured on a custom-build cryostat system, with similar apparatus described in previous publications [303]. A four-terminal resistance measurement was conducted whereby two leads pass a current through the sample while two other leads measure the potential drop across the sample. Ohm's Law, $R = V/I$, was used to calculate the sample resistance where R is the resistance of the material through which the current, I, is passed through which exhibits a voltage V. The resistivity, ρ, is independent of sample dimensions and relates to R, $\rho = \frac{RA}{p}$, where p is the probe distance where the voltage is measured, and A is the cross-sectional area that is perpendicular to the direction of the current.

Single crystal samples were mounted on insulating chips using GE varnish. Electrical contacts were attached by hand with Pelco Colloidal silver liquid from Ted Pella using fine gauge insulated single strand copper wire, dia. 0.07 mm. A standard four probe resistivity measurement was completed with an applied current of 0.75 mA over a temperature range of 320–80 K.

6.3 Results & Discussion

6.3.1 Crystal Morphology and Composition

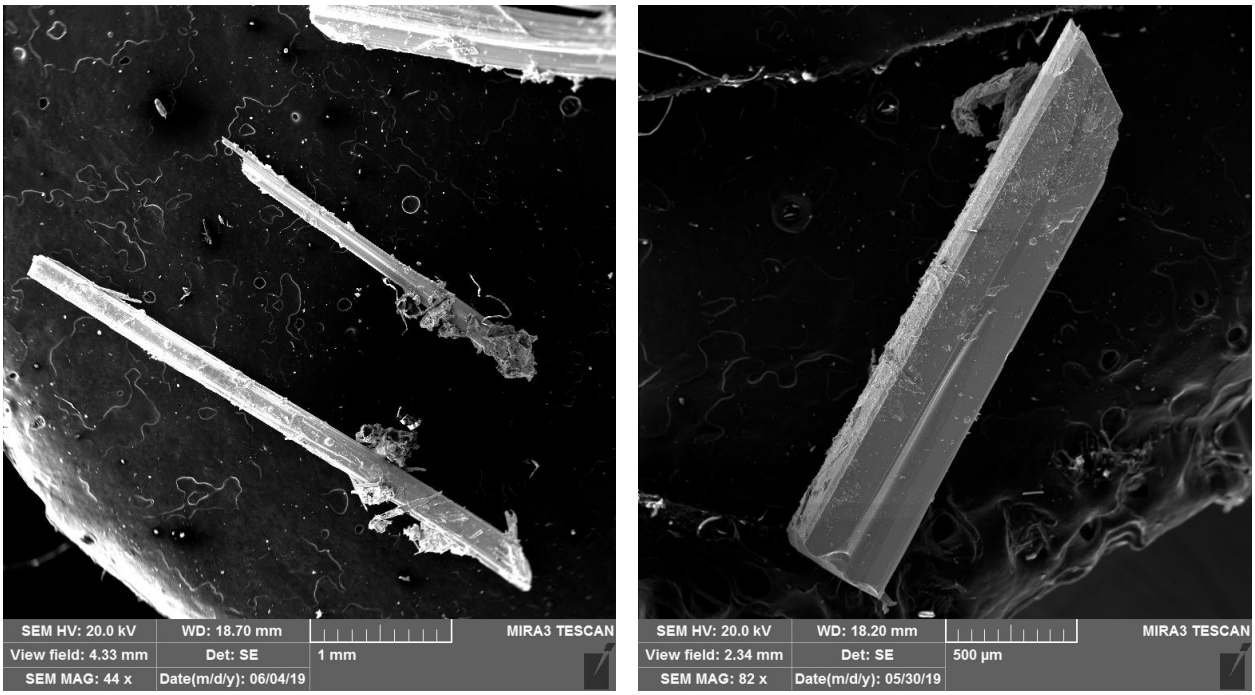

Figure 6.1: Representative SEM images of $Ca_9Zn_{3.1}In_{0.9}Sb_9$ single crystals.

Flux growths yielded crystals that appeared as long metallic ribbons with smooth reflective surfaces. The same growth conditions were repeated numerous times, producing large crystals greater than 4 mm in each run. Representative crystals are shown in Figure 6.1. EDS was used to check the composition of the crystals, with results shown in Figure 6.2. Despite the very high In:Zn ratio used in the flux, EDS clearly showed that the crystals contained more Zn than In. Since the solubility of Zn in $Ca_5In_{2-x}Zn_xSb_6$ is expected be $x < 0.2$ from prior literature, the high Zn:In ratio ($\approx 3:1$) of these crystals was the first indication that they may not have formed the intended $Ca_5In_2Sb_6$ structure type. The morphology of the crystals was also subtly different from what had been observed in the $Ca_5In_2Sb_6$ crystals with significantly longer crystals relative to the other growth directions and a different layering surface texture.

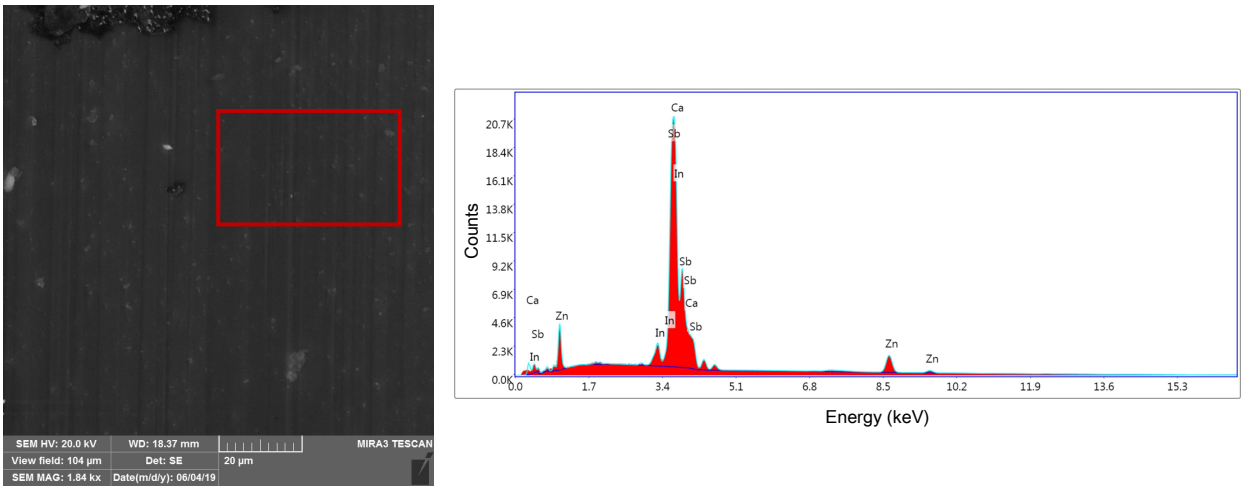

Figure 6.2: EDS analysis area of single crystal $Ca_9Zn_{3.1}In_{0.9}Sb_9$ (left). EDS spectra with unique and isolated Zn and In peaks near the prominent Ca and Sb emissions (right).

6.3.2 Thermal Analysis

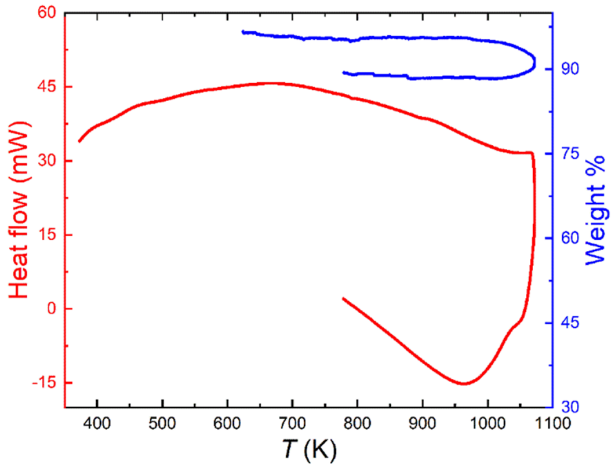

Figure 6.3: Combined TG/DSC analysis on the single crystals of $Ca_9Zn_{3.1}In_{0.9}Sb_9$. Weight % and specific heat flow are shown in blue and red, respectively. The heating sequence starts at 373K; the cooling sequence completes at 773 K.

DSC/TGA was performed at the University of Delaware to assess the stability of the crystals. After equilibration at 323 K, the temperature was increased to 1073 K at a rate of 20°/min. To prevent oxidation, the measurements were done under a constant flow of high-purity argon. DSC data do not indicate any intrinsic thermal events up to ca. 950 K. As the temperature approaches 1000 K, the sample began to display poor thermal stability, as demonstrated by the significant mass

loss shown in Figure 6.3. In the absence, of competing crystal growth phases it may be advantageous to further decrease the extraction temperature of the flux growth trials.

6.3.3 Structure Description

SC-XRD was used to investigate the crystal structure. From the initial analysis, it was immediately clear that the crystal structure was not the same as that of $Ca_5In_2Sb_6$, since the patterns could not be solved using the same orthorhombic space group. Initial analysis also ruled out any other known ternary phase in the Ca-In-Zn-Sb phase space, such as the $Ca_9Zn_{4.5}Sb_9$ structure. The most likely crystal system according to the initial refinement was hexagonal. However, all attempts to refine the atomic positions using a hexagonal lattice yielded what seemed to be unphysical structures with interatomic distances that were too short. For this reason, crystals were sent to the University of Delaware for additional SC-XRD measurements and structural analysis.

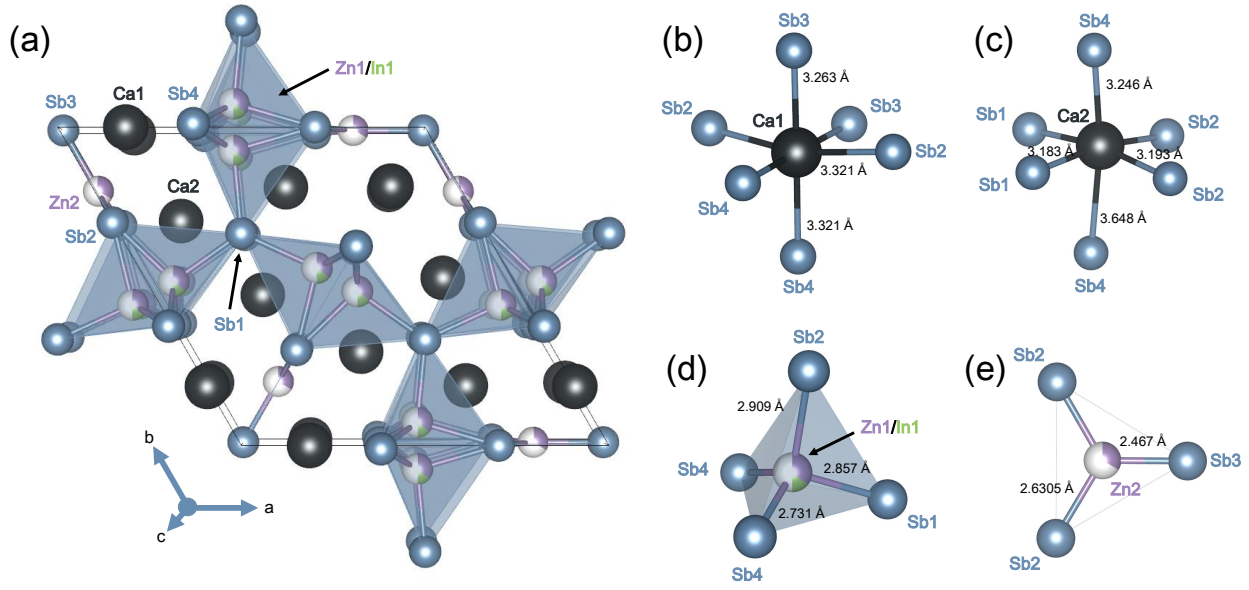

Figure 6.4: (a) Average crystal structure of $Ca_9Zn_{3.1}In_{0.9}Sb_9$. (b) Local coordination environment for Ca1. (c) Local coordination environment for Ca2. (d) Polyhedron coordination with mixed Zn1/In1 site. (e) Coordination for partially occupied Zn2 site.

The final average structure solution of the crystals is presented in Figure 6.4(a) along with details of the local coordination environment in 6.4(b-e). The overall composition was refined as $Ca_9Zn_{3.1}In_{0.9}Sb_9$. This is consistent with the EDS results, which show a more Zn-rich structure

compared to In. While the actual structure is heavily disordered, the averaged unit cell has been assigned to the hexagonal $P\bar{6}2m$ space group. Several superstructures with larger unit cells were considered, but in all cases, a significant amount of disorder remained that could not be readily resolved. In this work, attention is focused on the $P\bar{6}2m$ interpretation that was able to resolve atomic positions accurately but additional refinements were required to determine the partial occupancy of the Zn2 interstitial site.

Both Ca atoms, shown in Figure 6.4(b-c), are coordinated by six Sb atoms. The Zn1 and In1 atoms occupy two symmetry-equivalent sites bonded to four surrounding Sb atoms (shown in Figure 6.4(d)), forming a tetrahedral structure somewhat similar to what was observed in the $Ca_5M_2Sb_6$ (M = Al, Ga, In) system. These Zn1/In1 sites are only partially occupied with a combined occupancy of 50%. Further, since the neighboring Zn1/In1 sites are only 1.618(7) Å apart, they cannot be simultaneously occupied. The Zn2 atoms, shown in Figure 6.4(e), are situated in-plane with a triangle of Sb atoms that form chains parallel to the c-axis. Atomic coordinates and occupations reveals the partial occupation of both the Zn1/In1 (35.2% Zn and 14.8% In) and Zn2 (34.1%) sites.

6.3.4 Comparison with the $Ca_9Zn_{4.5}Sb_9$ Structure Type

The MSb_4 tetrahedra sub-structure is a common motif in pnictide-based Zintl phases, another example being the $Ca_5M_2Sb_6$ (M = Al, Ga, In) system discussed in previous chapters, which has anionic building blocks of M_2Sb_6. The anionic ribbons found in $Ca_9Zn_{4.5}Sb_9$ are similarly constructed from corner-sharing tetrahedra. While the novel structure reported here shares similarities to the interstitial-rich $Ca_9Zn_{4.5}Sb_9$ ($x \leq 0.8$) [35, 132], illustrated in Figure 6.5(left), it is significantly more complex. Other interstitially modified compounds include $Eu_9Zn_{4.5}Sb_9$ [131] and $Yb_9Zn_{4.5}Sb_9$ [132], which both belong to the *Pbam* space group, and $Ca_9Mn_{4.5}Sb_9$, belonging to the *Pnma* space group [131], illustrating how additional interstitial disorder, even with majority vacant interstitial sites can significantly alter the resulting structure.

The addition of a fourth element to these 9-4-9 type compounds is not without precedent, as has been recently shown in the synthesis of $AE_9Mn_{4-x}Al_xSb_9$ (AE= Ca, Yb, Eu) with Al

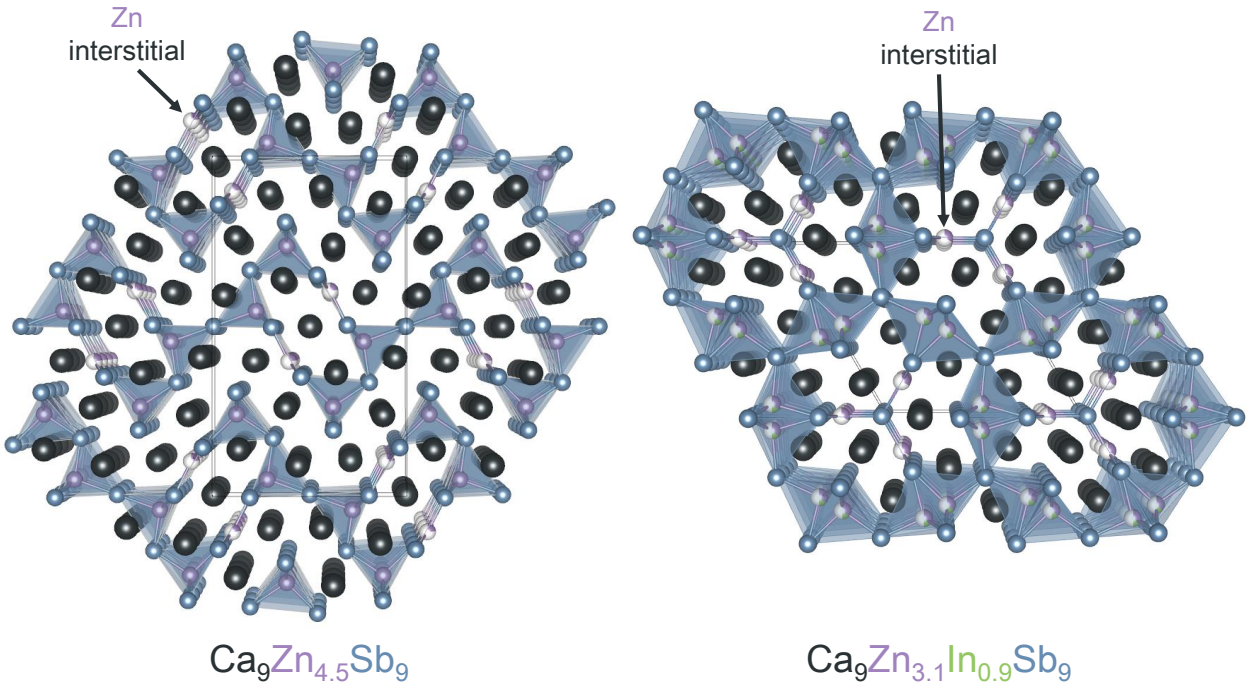

Figure 6.5: Comparison of $Ca_9Zn_{4.5}Sb_9$, orthorhombic space group *Pbam*, and $Ca_9Zn_{3.1}In_{0.9}Sb_9$, hexagonal space group $P\bar{6}2m$.

substitution [304], which are isostructural with $Ca_9Mn_4Bi_9$ [128], crystallizing in the orthorhombic space group *Pbam*. Substitution has also been performed on the cation site in the compositions $Ca_{9-x}RE_xMn_4Sb_9$ (RE = La-Nd, Sm; $x \approx 1$) which successfully electron-doped the structure with RE^{3+} on the Ca^{2+} site [305].

Unlike the $Ca_5M_2Sb_6$ (M = Al, Ga, In) system, the initially proposed $Ca_9Zn_4Sb_9$ structure is electron-deficient with respect to the ZKC counting scheme,

$$Ca_9Zn_4Sb_9 = (Ca^{2+})_9(Zn^{2+})_4(Sb^{3-})_9(h^+), \tag{6.1}$$

where h^+ represents an electron-hole. This electron-deficiency was resolved with the discovery of a partly occupied interstitial Zn site, leading to the formation of $Ca_9Zn_{4.5}Sb_9$ compounds,

$$Ca_9Zn_{4.5}Sb_9 = (Ca^{2+})_9(Zn^{2+})_{4.5}(Sb^{3-})_9. \tag{6.2}$$

The addition of Zn interstitials results in a valence-precise compound. Valence precision is resolved

in another manner for the $Ca_9Zn_{3.1}In_{0.9}Sb_9$ compound which can be approximated as,

$$Ca_9Zn_3InSb_9 = (Ca^{2+})_9(Zn^{2+})_3(In^{3+})(Sb^{3-})_9. \tag{6.3}$$

It is proposed that this is likely the long-range order solubility limit for the inclusion of In into the structure which is supported by the significantly In-rich single crystal growth conditions.

6.3.5 Electronic Transport Properties

Resistivity measurements on single crystals of $Ca_9Zn_{3.1}In_{0.9}Sb_9$ as shown in Figure 6.6 for two different single crystal samples. Results were very consistent between the two measured single crystals. Sample 1 had a probe separation of approximately 1.50 mm, a sample width of 0.46 mm, and thickness of 0.30 mm. Sample 2 had a probe separation of approximately 1.75 mm, a sample width of 1.14 mm, and was extremely thin with a thickness of only 0.07 mm.

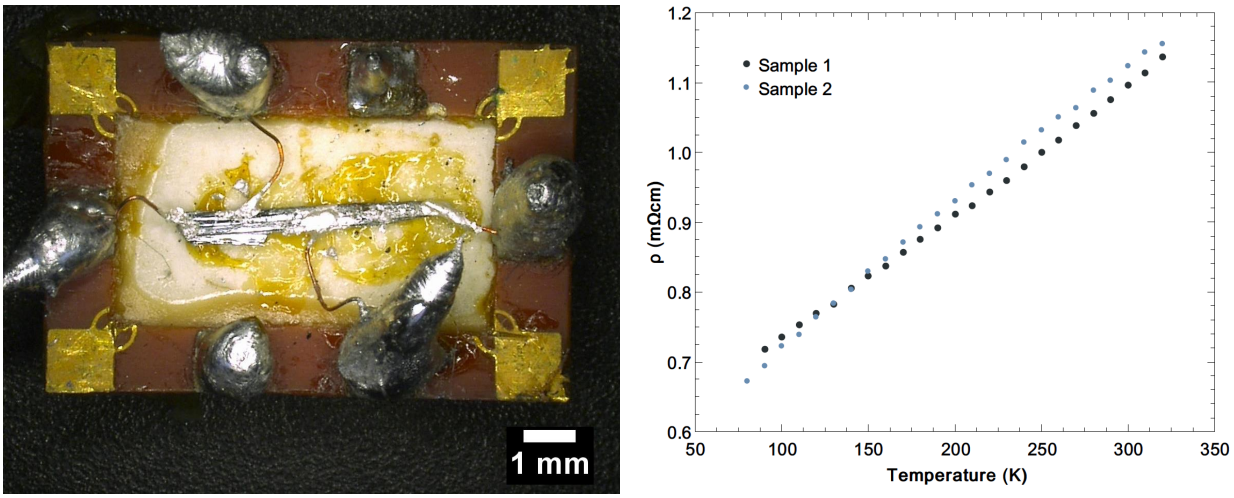

Figure 6.6: Four probe resistivity probes attached to single crystal $Ca_9Zn_{3.1}In_{0.9}Sb_9$, Sample 1 (left). Resulting resistivity values were consistent for two different crystals, showing low, linearly increasing resistivity (right).

Both single crystal samples exhibited linear metallic-like resistivity behavior over the measured temperature range of 80-320 K. The resistivity at room temperature of $\sim$1 mΩcm is comparable to the resistivity of many optimized thermoelectric materials, including $Ca_9Zn_{4.5}Sb_9$ [5]. Assuming that the current crystals are *p*-type (which is the most likely case for Zintl compounds) their low

resistivity suggests that their stoichiometry deviates somewhat from the valence-precise composition of $Ca_9Zn_3In_{0.9}Sb_9$. A slight deviation towards a Zn-rich composition (as suggested by EDS and SC-XRD refinements) would lead to a significant free hole concentration, and the observed metal-like resistivity.

6.4 Concluding Remarks

We report the discovery of novel quaternary Zintl phase, synthesized from an In- and Sb-rich flux. EDS and SC-XRD revealed a composition of $Ca_9Zn_{3.1}In_{0.9}Sb_9$ taking on a hexagonal structure type with extensive disorder due in part to the partial occupation of both the Zn1/In1 (35.2% Zn and 14.8% In) and Zn2 (34.1%) sites. This composition is very nearly valence precise, implying that this may be near the solubility limit of In in the structure. Temperature-dependent electrical resistivity measurements show low resistivity and metallic behavior over the temperature range of 80-320 K.

CHAPTER 7

CONCLUSIONS & FUTURE WORK

7.1 Conclusions

This work has focused on single crystal growth and characterization of select Zintl phase thermoelectrics. Single crystals of $Ca_5M_2Sb_6$ (M = Al, Ga, In; Pn = Sb, Bi) were grown from a molten metal flux. The $Ca_5M_2Sb_6$ compositions were all successfully grown from a $M_{73}Sb_{42}$ with $Ca_5Al_2Sb_6$ also grown from a Sb_{20} and Sn_{15} fluxes. $Ca_5Al_2Bi_6$ was grown from a Bi_{20} self-flux. Self-flux elements were preferred as they do not introduce an additional element that could form undesirable phases with or inadvertently dope. From these self-flux growths several useful tie lines have been added to the corresponding ternary phase diagrams where none existed before. This provides guidance to future crystal growth and synthesis studies.

In addition to the above listed compositions the first single crystal alloy of composition $Ca_5Ga_{2-x}In_xSb_6$ has been reported, synthesized from polycrystalline $Ca_5Ga_2Sb_6$ and $Ca_5In_2Sb_6$ with a mixed self-flux of $Ga_{37.5}In_{37.5}Sb_{42}$. The resolved composition was $Ca_5Ga_{1.12}In_{0.88}Sb_6$ with subsequent quick scans on other single crystals showing a slight preference for Ga on the M site. These results were further confirmed with EDS results on 30 individual crystals, all reporting more Ga than In. The alloyed composition maintains the *Pbam* space group within the orthorhombic crystal structure with the In and Ga atoms both partially occupying the center of the anionic polyhedral structures. The lattice dimensions obeyed Vegard's Law. The increase in lattice parameter with increasing In content is due to In being a larger atom than Ga with the crystal structure expanding to accommodate. This was likely the reason for the preference of Ga to occupy this site.

In addition to the structural characterization described above, electronic characterization was also conducted. The $Ca_5In_2Sb_6$ composition was characterized both perpendicular and parallel to the c-axis to investigate anisotropy. From the detailed structural characterization it is known that the preferred growth direction of the crystals is along the c-axis. Crystal growth perpendicular to

the c-axis was modest, measuring less than a millimeter. Due to such diminutive dimensions, the perpendicular measurement required FIB cutting and an optimized photolithography process to sputter sensors over the top of the sample for characterization. The photolithography process proved repeatable, allowing for the potential of a complete thermoelectric performance characterization (i.e., resistivity/conductivity, Seebeck coefficient, and thermal conductivity) to be performed. This photoresist stack and processing parameters can be transferred to other systems as well to characterize general micro-ribbon samples. Resistivity values collected on a single crystal parallel to the c-direction were accomplished with manually placed probes on a custom built cryostat system. These results combined to provide proof of highly anisotropic electronic transport properties with a nearly 20-fold increase in resistivity in the perpendicular direction. These results are in agreement with DFT calculations that predicted enhanced thermoelectric performance in the c-direction. It is predicted that lattice thermal conductivity will remain isotropic, allowing for a significant thermoelectric performance boost for crystals oriented parallel to the c-direction.

Aside from quantifying anisotropy, single crystals can also be used to study the defect chemistry of systems. In this work, single crystals of Mg_3Sb_2 were grown from both a Mg- and Sb-rich flux and the defect chemistry was explored through SC-XRD. This compound has been proven to be a promising *n*-type thermoelectric when synthesized in a Mg-rich environment. While Mg vacancies are suspected to be responsible for this, not experimental observations have been investigated.

In this work, Sb-rich growths revealed partial occupancy of the Mg(I) site, consistent with DFT calculations with Mg vacancies exhibiting a low formation energy to preferentially form. While a number of anti-site and interstitial defects have been considered with DFT, interstitial position (0, 0, 0.684) is reported where Sb5+ as a likely occupant. All measured crystals exhibited intrinsic semiconducting behavior, despite Mg vacancies.

This work has shown how single crystals can successfully characterize compound anisotropy and also describe the defect chemistry of a compound. A third use of single crystals is the use in exploratory growths. In this work, single crystal work continued with the discovery of Zintl phase $Ca_9Zn_{3.1}In_{0.9}Sb_9$ from an In- and Sb-rich self-flux. Structural characterization was completed

with EDS and SC-XRD where it was discovered that the average structure took on the hexagonal structure type with extensive disorder due in part to the partial occupation of both the Zn1/In1 and Zn2 sites. Low temperature electrical resistivity measurements show low resistivity and metallic behavior.

This work demonstrates the flexible utilization of single crystal growth and how it can be leveraged to produce results that are not possible in the synthesis and characterization of polycrystalline samples. The processes herein described can provide guidance for future characterization and exploratory efforts.

7.2 Future Work

The primary goals of this thesis were to use single crystal growth of Zintl phases to explore anisotropic transport properties, intrinsic point defects, and to discover new phases. While some exciting progress was made, this work also opened additional questions. Work in this study has provided a wide range of potential future work projects ranging from photolithography of different thermoelectric micro-ribbons to exploratory flux growths of novel compounds. Detailed below are projects that can build off of these successes.

7.2.1 Photolithography to Understand Anistropic Transport

At this point, countless questions remain regarding how bonding determines anisotropic electronic and thermal transport in Zintl phases. In the present study, anisotropy of electrical conductivity in one un-doped Zintl compound has been confirmed. Future work is to include a) characterize the remaining transport properties including the thermal conductivity and Seebeck coefficient, and b) characterize the same properties in samples with different alloying to vary the scattering mechanism, and c) different doping levels, including samples with optimized carrier concentration to confirm the high zT. Once the properties of this single compound are thoroughly understood, work will progress to other Zintl structure types.

To achieve in widening the scope of this research, it is necessary to further refine the pho-

tolithography process described in Chapter 4. The photolithography process allows for small single crystal micro-ribbons to be characterized, bypassing the need for larger single crystals which can be impractical to grow in some instances. In this work, a micro-ribbon of $Ca_5In_2Sb_6$ was characterized in the perpendicular to c-direction for resistivity and carrier concentration. The full suite of sensors were not leveraged due to the sample being destroyed in the process of testing, however, it was shown as a proof of concept that sensors could be placed on micro-ribbons repeatably using the optimized photolithography process outlined. This full suite of circuit sensors builds on the previous work of Gooth et al. [6] which used two thermometers and a resistive heater line. This work utilized similar sensors along with the addition of two isolated current lines and Hall sensors across the middle of the micro-ribbon, allowing for the characterization of the Hall effect, Seebeck coefficient, electrical and thermal conductivity.

In order to improve throughput of future projects, appropriate compositions must be selected. The first challenge is to find good candidate materials that can be processed using FIB cutting. Samples with heavier elements required reduced cutting speeds and low melting temperature elements were shown to violently vaporize when exposed to the beam. For this reason low melting temperature elements such as Ga are problematic. This issue was made worse due to Ga being used as a self-flux element in the growth of single crystal $Ca_5Ga_2Sb_6$ while also possessing poor wetting properties that allowed it to cling to crystal surfaces more readily. This knowledge can help filter out poor single crystal candidates for this process in advance, saving valuable time and labor.

Once micro-ribbons have been extracted from FIB cutting, a repeatable photolithography process has been developed that can be readily applied to any compound cut to the appropriate dimensions and surface quality. This allows for the characterization of any material along a specific growth direction, not limited to Zintl phases or even thermoelectrics, potentially useful for such fields as the development and characterization of scintillation materials where single crystals are often directly used in applications [204].

7.2.2 Flux Growths for Phase Diagram and New Compound Exploration

Flux growths are capable of producing high quality single crystals that provides an effective pathway to crystallizing incongruently melting compounds. This method is a useful tool in the alloying of compounds as was the case with the synthesis of single crystal $Ca_5Ga_{2-x}In_xSb_6$, and of discovering new ones, as was the case with $Ca_9Zn_{3.1}In_{0.9}Sb_9$. Growths can also assist in the describing the ternary phase space where no phase diagram exists. From knowledge gained in the crystal growth process, intelligent flux choices can be made in material systems for various purposes.

7.2.2.1 Solubility Study

In this work single crystals of $Ca_5Al_2Sb_6$ and $Ca_5Al_2Bi_6$ have been grown. Future work with these compositions can include a solubility study that will test the solubility limits of Sb and Bi in each structure type. It is important to remember that $Ca_5Al_2Bi_6$ is a different structure type compared to the $Ca_5M_2Sb_6$ (M = Al, Ga, In) class of compounds with the difference being how the polyanionic chains are packed into the structure.

Single crystals of $Ca_5Al_2Sb_6$ were grown using a Sb_{20} flux with an extraction temperature of 730°C while $Ca_5Al_2Bi_6$ single crystals were grown from a Bi_{20} flux with an extraction temperature of 470°C. The flux and extraction temperatures could be varied linearly between the two as shown in Figure 7.1 simply by mixing elements together. Additionally $Ca_5Al_2Bi_6$ single crystal growth could be attempted with an Sb flux at lower temperatures, avoiding the formation of $Ca_5Al_2Sb_6$.

7.2.2.2 Exploratory Growths

During the attempted synthesis of Zn-doped $Ca_5In_2Sb_6$, a new Zintl phase, $Ca_9Zn_{3.1}In_{0.9}Sb_9$, was discovered. This phase was grown repeatably and will encourage other exploratory growths of the same structure type. This compound has a unique valence-precision that can be generalized as

$$A_9T_3MPn_9 = (A^{2+})_9(T^{2+})_3(M^{3+})(Pn^{3-})_9, \tag{7.1}$$

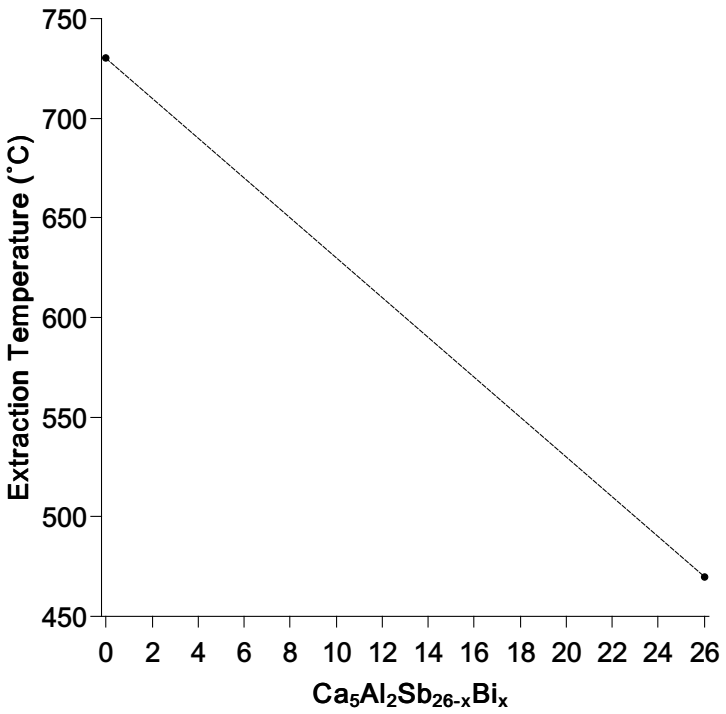

Figure 7.1: Proposed solubility study between the two stable compounds $Ca_5Al_2Sb_6$ and $Ca_5Al_2Bi_6$. Dashed line represents possible flux growth melt compositions with respect to extraction temperature.

where A could potentially be Ca, Sr, Yb, or Eu and T = Zn, Cd, or Mn, with M potentially occupied by Al or Ga, while Pn can be occupied by either Sb or Bi. This structure would accommodate these atoms at these sites, but further growths are needed to confirm their existence. This yields the potential for 72 possible combinations of the A/T/M/Pn elements which are listed in Table 7.1. From these, 24 total ternary phases in the form $A_9T_{4+x}Pn_9$ are theorized, with 16 of these already discovered and structurally characterized. Three quaternary compounds in the form $A_9(T_{1-x}M_x)_4Pn_9$ have been discovered [304] with this work producing the fourth of potentially 72 compositions. In addition to these compounds arsenic can also occupy the Pn site as is evidenced by the recent synthesis of $Ca_9Zn_{4.5}As_9$ [131], implying this table could be expanded further. Table 7.1 can act as a checklist for potentially new Zintl phase compounds with a shared valence counting and stoichiometry.

While some growths lead to the discovery of novel compounds, others can provide a more efficient pathway to the synthesis of known compounds. From our success of single crystal growth

Table 7.1: List of element combinations for potential quaternary compounds in the form $A_9(T_{1-x}M_x)_4Pn_9$. References are included for known $A_9T_{4+x}Pn_9$ ternaries and known quaternary compounds taking the form $A_9(T_{1-x}M_x)_4Pn_9$.

A	T	M	Pn	$A_9T_{4+x}Pn_9$	$A_9(T_{1-x}M_x)_4Pn_9$	A	T	M	Pn	$A_9T_{4+x}Pn_9$	$A_9(T_{1-x}M_x)_4Pn_9$
Ca	Zn	Al	Sb			Yb	Zn	Al	Sb		
Ca	Zn	Ga	Sb	[132]		Yb	Zn	Ga	Sb	[134]	
Ca	Zn	In	Sb		This work	Yb	Zn	In	Sb		
Ca	Zn	Al	Bi			Yb	Zn	Al	Bi		
Ca	Zn	Ga	Bi	[133]		Yb	Zn	Ga	Bi	[133]	
Ca	Zn	In	Bi			Yb	Zn	In	Bi		
Ca	Cd	Al	Sb			Yb	Cd	Al	Sb		
Ca	Cd	Ga	Sb			Yb	Cd	Ga	Sb		
Ca	Cd	In	Sb			Yb	Cd	In	Sb		
Ca	Cd	Al	Bi			Yb	Cd	Al	Bi		
Ca	Cd	Ga	Bi	[133]		Yb	Cd	Ga	Bi	[133]	
Ca	Cd	In	Bi			Yb	Cd	In	Bi		
Ca	Mn	Al	Sb		[304]	Yb	Mn	Al	Sb		[304]
Ca	Mn	Ga	Sb	[131]		Yb	Mn	Ga	Sb	[134]	
Ca	Mn	In	Sb			Yb	Mn	In	Sb		
Ca	Mn	Al	Bi			Yb	Mn	Al	Bi		
Ca	Mn	Ga	Bi	[134]		Yb	Mn	Ga	Bi	[134]	
Ca	Mn	In	Bi			Yb	Mn	In	Bi		
Sr	Zn	Al	Sb			Eu	Zn	Al	Sb		
Sr	Zn	Ga	Sb			Eu	Zn	Ga	Sb		
Sr	Zn	In	Sb			Eu	Zn	In	Sb		
Sr	Zn	Al	Bi			Eu	Zn	Al	Bi		
Sr	Zn	Ga	Bi	[133]		Eu	Zn	Ga	Bi	[133]	
Sr	Zn	In	Bi			Eu	Zn	In	Bi		
Sr	Cd	Al	Sb			Eu	Cd	Al	Sb		
Sr	Cd	Ga	Sb	[133]		Eu	Cd	Ga	Sb	[131]	
Sr	Cd	In	Sb			Eu	Cd	In	Sb		
Sr	Cd	Al	Bi			Eu	Cd	Al	Bi		
Sr	Cd	Ga	Bi	[133]		Eu	Cd	Ga	Bi	[133]	
Sr	Cd	In	Bi			Eu	Cd	In	Bi		
Sr	Mn	Al	Sb			Eu	Mn	Al	Sb		[304]
Sr	Mn	Ga	Sb			Eu	Mn	Ga	Sb		
Sr	Mn	In	Sb			Eu	Mn	In	Sb		
Sr	Mn	Al	Bi			Eu	Mn	Al	Bi		
Sr	Mn	Ga	Bi			Eu	Mn	Ga	Bi		
Sr	Mn	In	Bi			Eu	Mn	In	Bi		

of $Ca_5M_2Sb_6$ (M = Al, Ga, In) with a $M_{73}Sb_{42}$ flux it was theorized that the potentially analogous $Sr_5Ga_2Sb_6$ phase which, if it exists, could be synthesized. Both $Sr_5Al_2Sb_6$ and $Sr_5In_2Sb_6$ have been discovered and characterized, leading further to the possibility of a Ga analog. This work was unable to produce the theorized compound but did successfully synthesize single crystal $Sr_7Ga_8Sb_8$ from a $Ga_{73}Sb_{42}$ flux. The crystals took on a rectangular appearance but the yield was exceptionally low. This would provide a starting point at a minimum for future growths of these rather unique 7-8-8 compounds. This crystal structure was first reported in 2010 by Bobev et al. [306], so while compounds have been discovered recently, characterization is non-existent beyond a structural description. Such growths, coupled with electrical resistivity characterization, can be used as part of

a screening process for promising thermoelectrics and to better define ternary phase spaces.

APPENDIX

EDS: $Ca_5Ga_2Sb_6$ with $Ga_{73}Sb_{42}$ flux

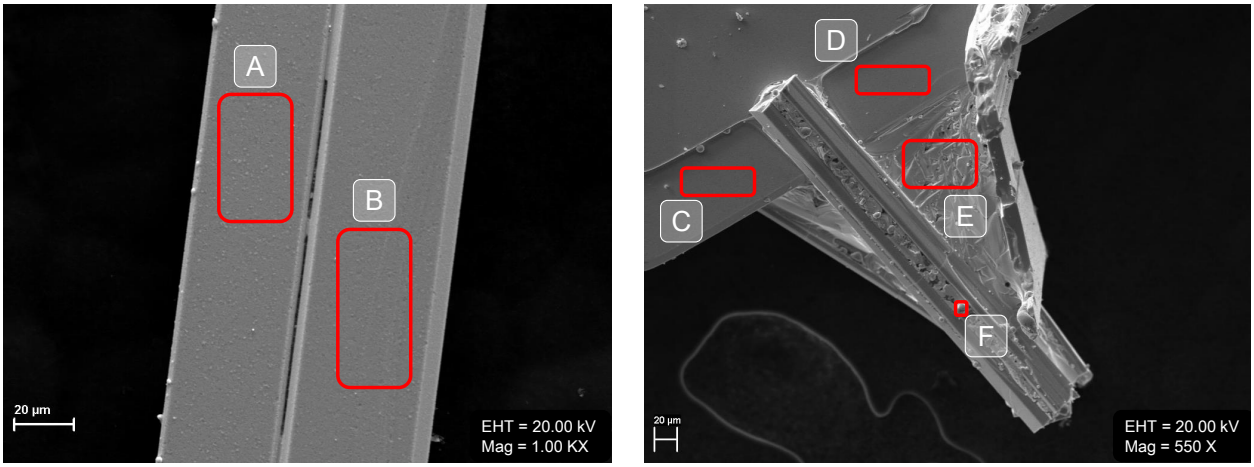

Figure A1: $Ca_5Ga_2Sb_6$ crystals from a $Ga_{73}Sb_{42}$ flux with superimposed EDS areas highlighted. Corresponding EDS data is shown in Figure A3 and Table A1.

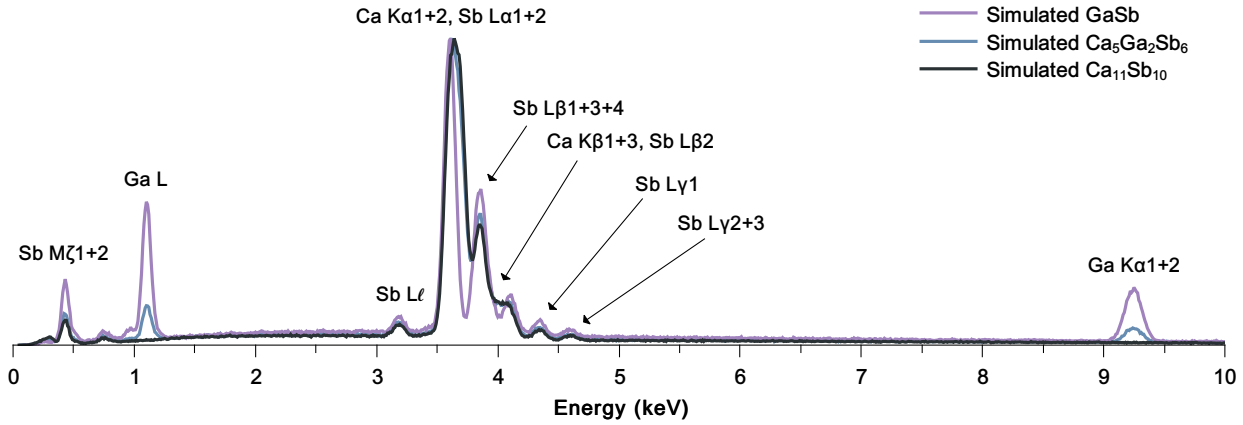

Figure A2: Simulated EDS patterns for potential crystal candidates grown from a Ca-Ga-Sb flux.

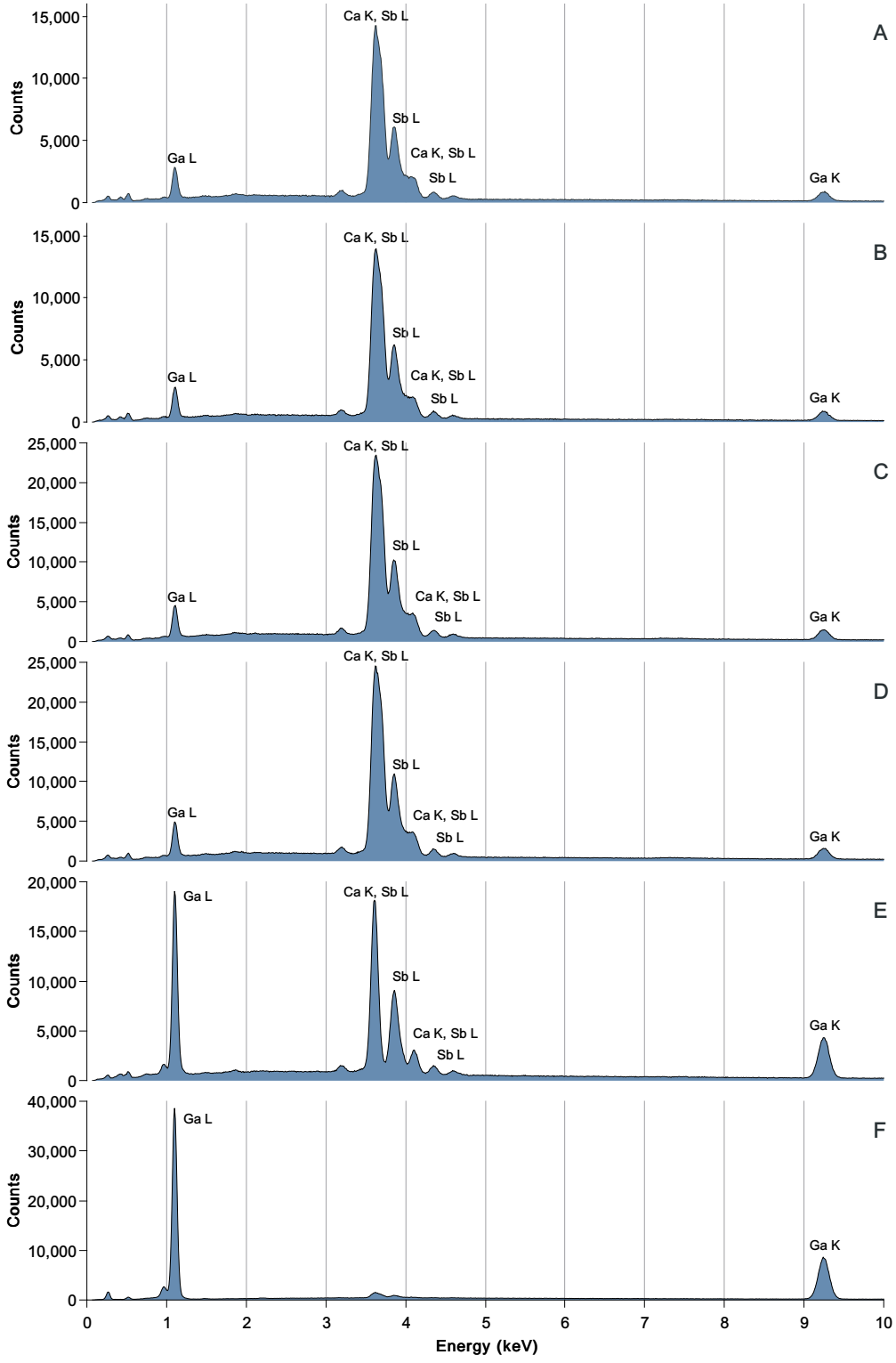

Figure A3: EDS spectra for $Ca_5Ga_2Sb_6$ with $Ga_{73}Sb_{42}$ flux, Areas A–F from Figure A1.

Table A1: Quantitative results: $Ca_5Ga_2Sb_6$ single crystals from a $Ga_{73}Sb_{42}$ flux, Areas A–F from Figure A1.

Area	Element	Weight %	Atomic %	Net Int.	Net Int. Error
A	Ca K	24.95	46.96	3615.82	0
	Ga K	14.12	15.28	410.61	0.03
	Sb L	60.93	37.76	4003.51	0
	$Ca_5Ga_{1.63}Sb_{4.02}$				
B	Ca K	24.95	46.96	3615.82	0
	Ga K	14.12	15.28	410.61	0.03
	Sb L	60.93	37.76	4003.51	0
	$Ca_5Ga_{1.67}Sb_{4.03}$				
C	Ca K	25.05	47.03	6123.36	0
	Ga K	14.46	15.61	697.47	0.02
	Sb L	60.48	37.36	6689.31	0
	$Ca_5Ga_{1.66}Sb_{3.97}$				
D	Ca K	24.87	46.69	6349.28	0
	Ga K	14.90	16.08	751.12	0.02
	Sb L	60.23	37.22	6959.81	0
	$Ca_5Ga_{1.72}Sb_{3.99}$				
E	Ca K	2.19	4.82	535.89	0.03
	Ga K	44.58	56.54	2271.39	0.01
	Sb L	53.23	38.64	6010.088	0
	Ga + Sb flux				
F	Ca K	0.93	1.63	215.31	0.05
	Ga K	95.92	96.56	4694.27	0
	Sb L	3.15	1.81	345.01	0.06
	Ga flux				

EDS: $Ca_5In_2Sb_6$ with $In_{73}Sb_{42}$ flux

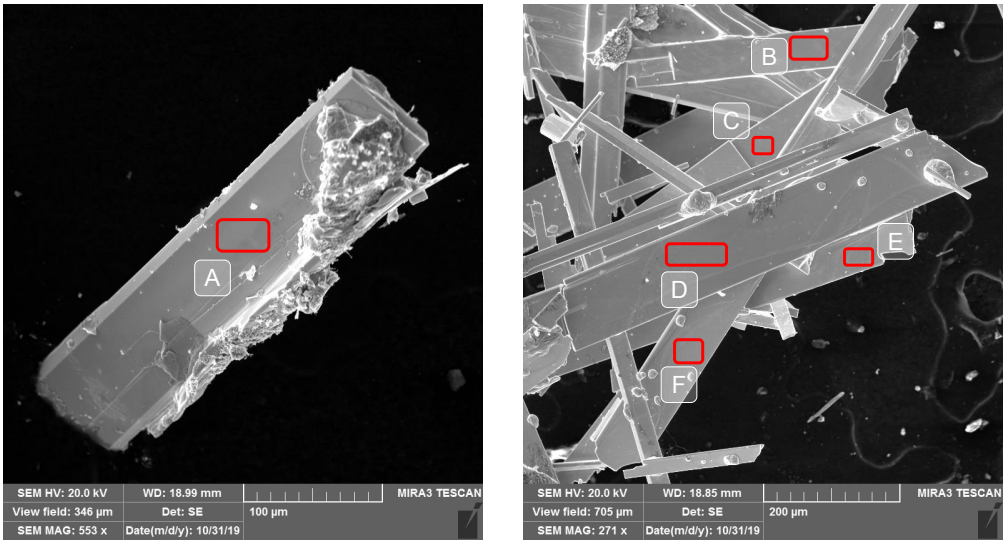

Figure A4: $Ca_5In_2Sb_6$ crystals from an $In_{73}Sb_{42}$ flux with superimposed EDS areas highlighted. Corresponding EDS data is shown in Figure A6 and Table A2.

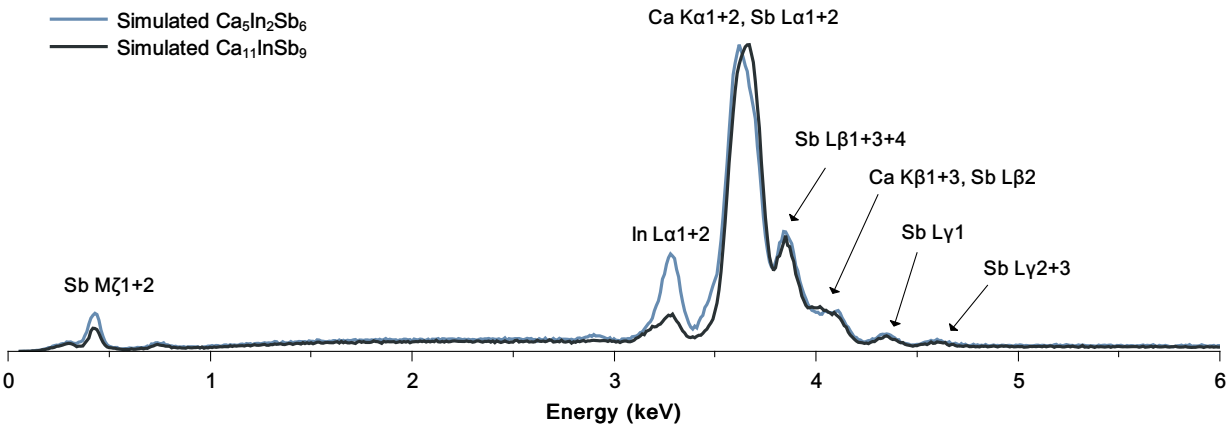

Figure A5: Simulated EDS patterns for potential crystal candidates grown from Ca-In-Sb flux.

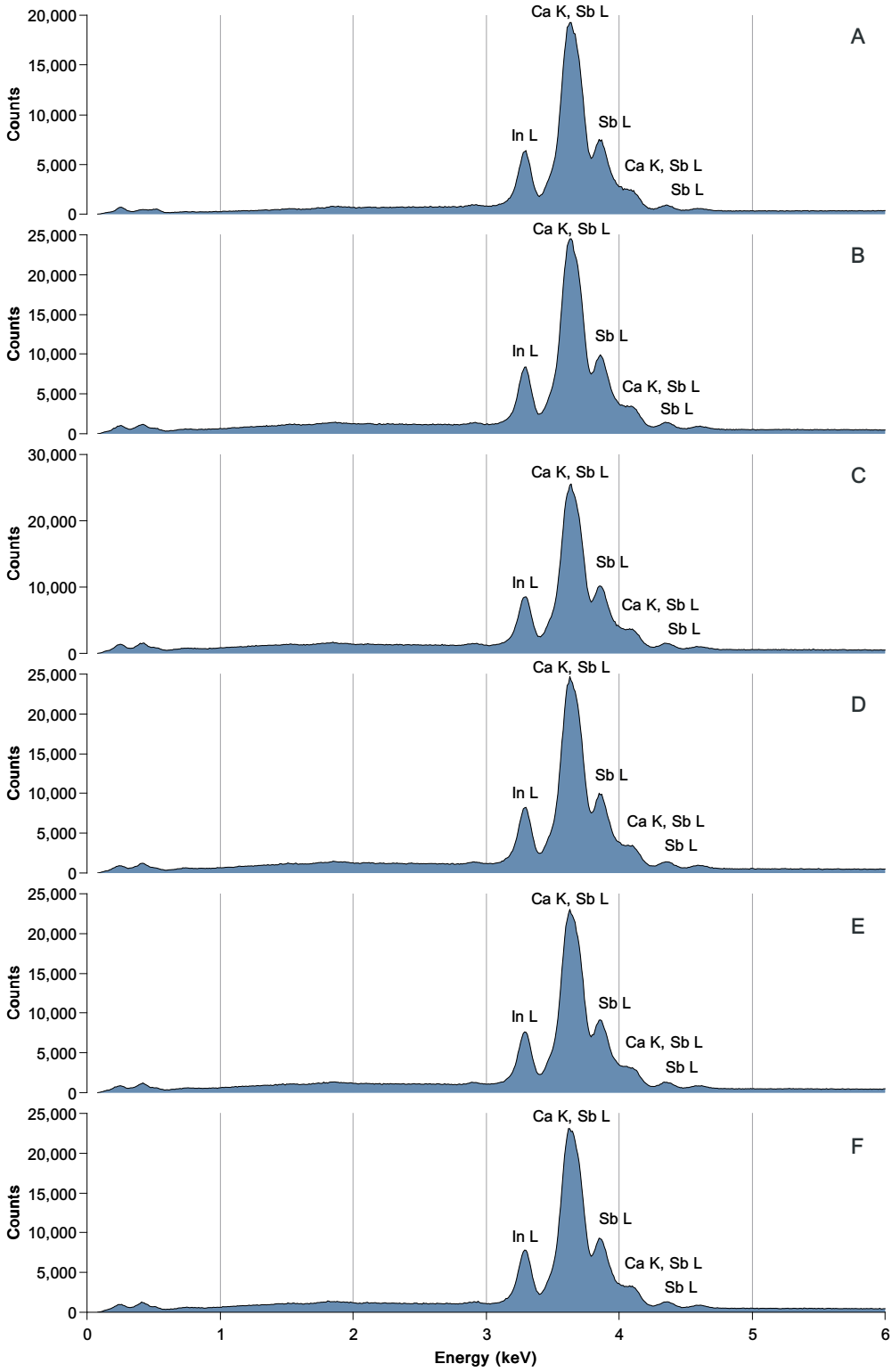

Figure A6: EDS spectra of $Ca_5In_2Sb_6$ single crystals from an $In_{73}Sb_{42}$ flux, Areas A–F from Figure A4.

Table A2: Quantitative results: $Ca_5In_2Sb_6$ single crystals from an $In_{73}Sb_{42}$ flux, Areas A–F from Figure A4.

Area	Element	Weight %	Atomic %	Net Int.	Net Int. Error
A	Ca K	23.09	47.34	5353.23	2.45
	In L	18.14	12.99	2280.57	1.95
	Sb L	58.77	39.67	5903.28	1.17
	$Ca_5In_{1.37}Sb_{4.19}$				
B	Ca K	22.67	46.74	6707.08	2.43
	In L	18.5	13.32	2967.94	1.84
	Sb L	58.83	39.94	7538.55	1.13
	$Ca_5In_{1.42}Sb_{4.27}$				
C	Ca K	22.87	47.03	6965.83	2.42
	In L	18.53	13.3	3058.69	1.88
	Sb L	58.6	39.67	7728.67	1.14
	$Ca_5In_{1.41}Sb_{4.22}$				
D	Ca K	22.74	46.85	6706.1	2.43
	In L	18.4	13.23	2940.68	1.83
	Sb L	58.86	39.92	7519.04	1.13
	$Ca_5In_{1.41}Sb_{4.26}$				
E	Ca K	22.83	46.98	6297.54	2.43
	In L	18.31	13.15	2736.97	1.86
	Sb L	58.86	39.87	7032.14	1.14
	$Ca_5In_{1.40}Sb_{4.24}$				
F	Ca K	22.77	46.89	6387.85	2.45
	In L	18.31	13.16	2784.23	1.95
	Sb L	58.92	39.94	7159.38	1.14
	$Ca_5In_{1.40}Sb_{4.26}$				

EDS: $Ca_5Ga_{2-x}In_xSb_6$ with $Ga_{37.5}In_{37.5}Sb_{42}$ flux

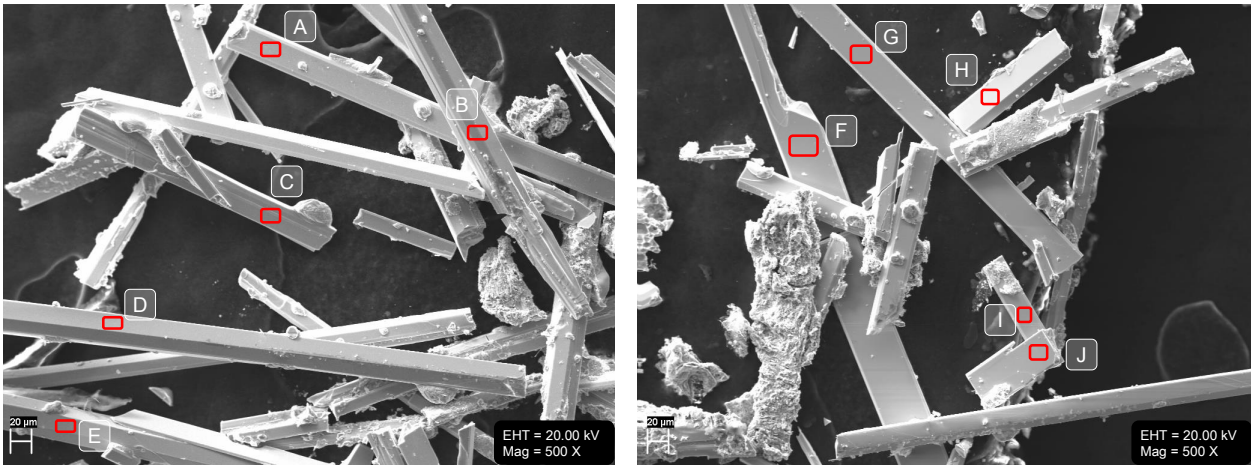

Figure A7: $Ca_5Ga_{2-x}In_xSb_6$ crystals from a $Ga_{37.5}In_{37.5}Sb_{42}$ flux with superimposed EDS areas highlighted. Corresponding EDS data is shown in Figures A8-A9 and Tables A3-A4.

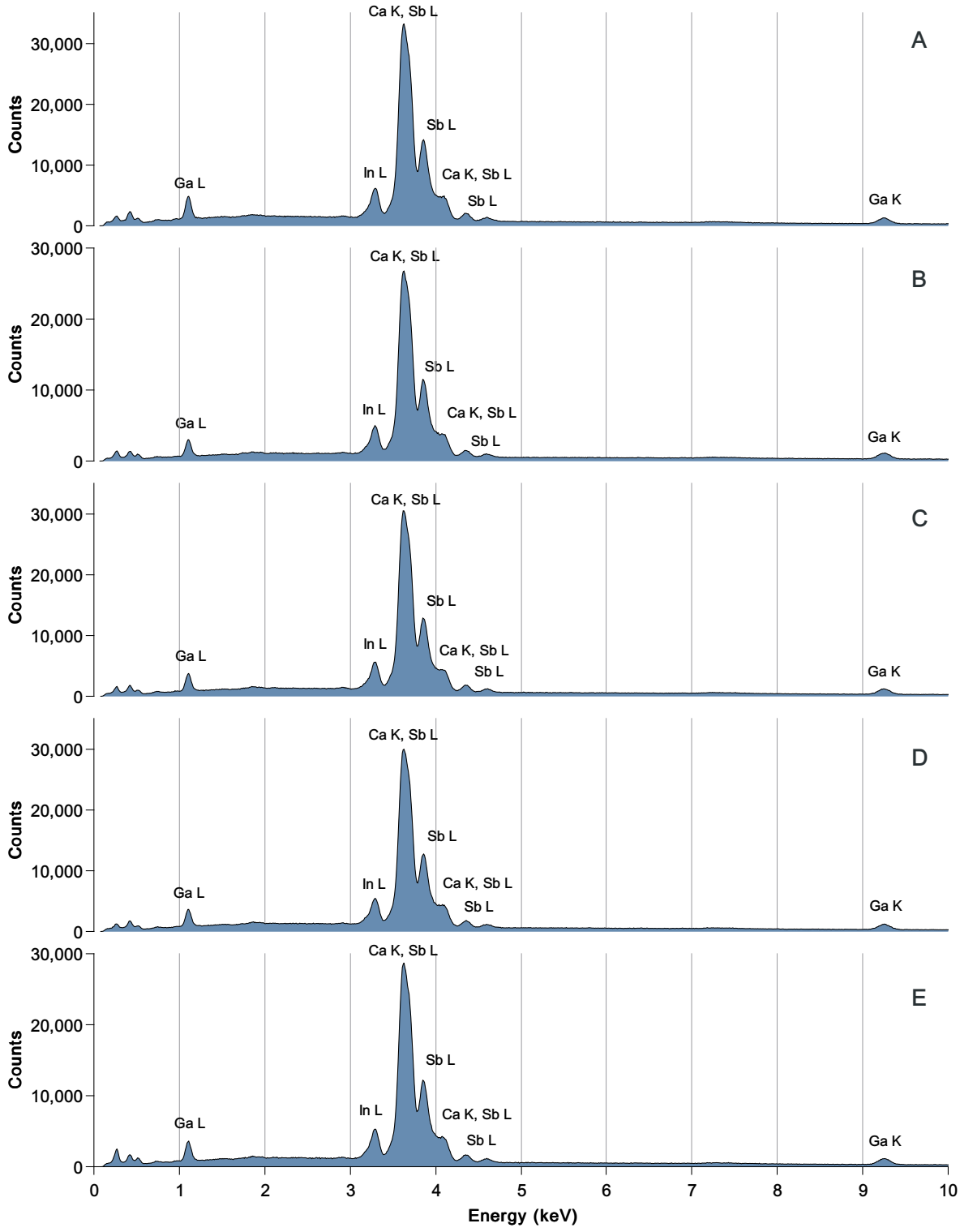

Figure A8: EDS spectra of $Ca_5Ga_{2-x}In_xSb_6$ single crystals from a $Ga_{37.5}In_{37.5}Sb_{42}$ flux, Areas A–E from Figure A7(left).

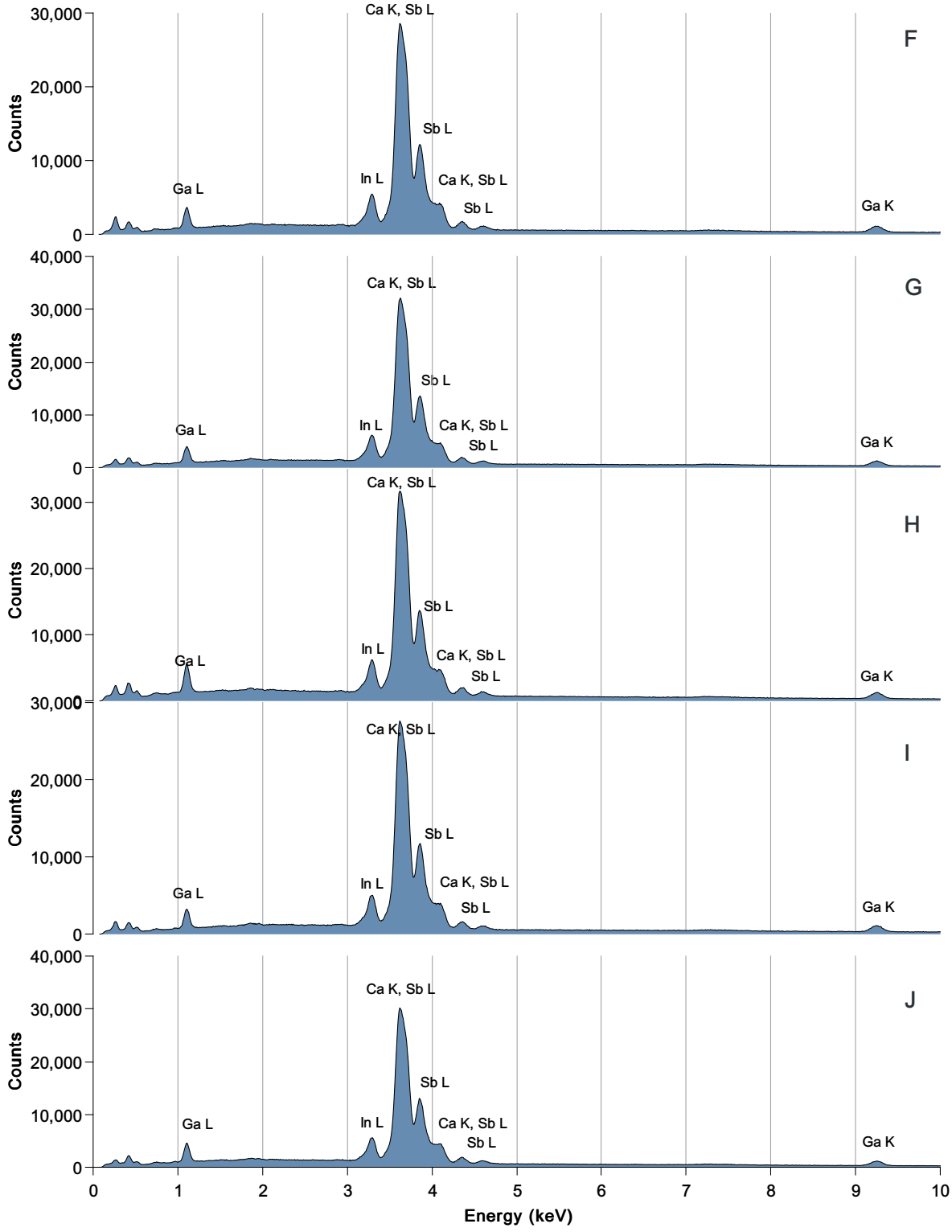

Figure A9: EDS spectra of $Ca_5Ga_{2-x}In_xSb_6$ single crystals from a $Ga_{37.5}In_{37.5}Sb_{42}$ flux, Areas F–J from Figure A7(right).

Table A3: Quantitative results: $Ca_5Ga_{2-x}In_xSb_6$ single crystals from a $Ga_{37.5}In_{37.5}Sb_{42}$ flux, Areas A–E from Figure A7(left).

Area	Element	Weight %	Atomic %	Net Int.	Net Int. Error
A	Ca K	24.19	47.38	8624.55	0.00
	Ga K	7.11	8.00	499.68	0.03
	In L	8.38	5.73	1721.06	0.02
	Sb L	60.31	38.89	9636.87	0.00
	$Ca_5Ga_{0.84}In_{0.60}Sb_{4.10}$				
B	Ca K	24.12	47.05	7110.61	0.00
	Ga K	8.14	9.12	473.11	0.03
	In L	8.61	5.86	1461.71	0.02
	Sb L	59.13	37.97	7817.09	0.00
	$Ca_5Ga_{0.97}In_{0.62}Sb_{4.04}$				
C	Ca K	24.16	47.26	7979.59	0.00
	Ga K	7.40	8.32	481.46	0.03
	In L	8.52	5.82	1622.57	0.02
	Sb L	59.93	38.59	8874.53	0.00
	$Ca_5Ga_{0.88}In_{0.62}Sb_{4.08}$				
D	Ca K	24.18	47.29	7880.12	0.00
	Ga K	7.45	8.38	478.95	0.03
	In L	8.43	5.75	1581.90	0.02
	Sb L	59.94	38.58	8756.67	0.00
	$Ca_5Ga_{0.89}In_{0.61}Sb_{4.08}$				
E	Ca K	24.08	47.12	7511.73	0.00
	Ga K	7.56	8.50	462.68	0.03
	In L	8.79	6.01	1581.05	0.02
	Sb L	59.57	38.36	8336.43	0.00
	$Ca_5Ga_{0.90}In_{0.64}Sb_{4.07}$				

Table A4: Quantitative results: $Ca_5Ga_{2-x}In_xSb_6$ single crystals from a $Ga_{37.5}In_{37.5}Sb_{42}$ flux, Areas F–J from Figure A7(right).

Area	Element	Weight %	Atomic %	Net Int.	Net Int. Error
F	Ca K	24.16	47.30	7459.85	0.00
	Ga K	7.22	8.14	438.34	0.03
	In L	8.61	5.88	1531.97	0.02
	Sb L	60.02	38.68	8312.45	0.00
	$Ca_5Ga_{0.86}In_{0.62}Sb_{4.09}$				
G	Ca K	24.07	47.24	8392.59	0.00
	Ga K	6.91	7.80	475.40	0.03
	In L	9.07	6.22	1823.96	0.02
	Sb L	59.95	38.74	9364.62	0.00
	$Ca_5Ga_{0.83}In_{0.66}Sb_{4.10}$				
H	Ca K	23.86	46.92	8246.97	0.00
	Ga K	7.15	8.08	485.62	0.03
	In L	8.67	5.95	1727.76	0.02
	Sb L	60.32	39.05	9353.86	0.00
	$Ca_5Ga_{0.86}In_{0.63}Sb_{4.16}$				
I	Ca K	24.01	47.05	7210.64	0.00
	Ga K	7.52	8.47	444.55	0.03
	In L	8.64	5.91	1496.17	0.02
	Sb L	59.83	38.58	8055.29	0.00
	$Ca_5Ga_{0.90}In_{0.63}Sb_{4.10}$				
J	Ca K	24.21	47.45	7905.85	0.00
	Ga K	6.95	7.83	446.90	0.04
	In L	8.21	5.61	1545.85	0.02
	Sb L	60.63	39.11	8875.99	0.00
	$Ca_5Ga_{0.82}In_{0.59}Sb_{4.12}$				

EDS: $Ca_5Al_2Sb_6$ with $Al_{73}Sb_{42}$ flux

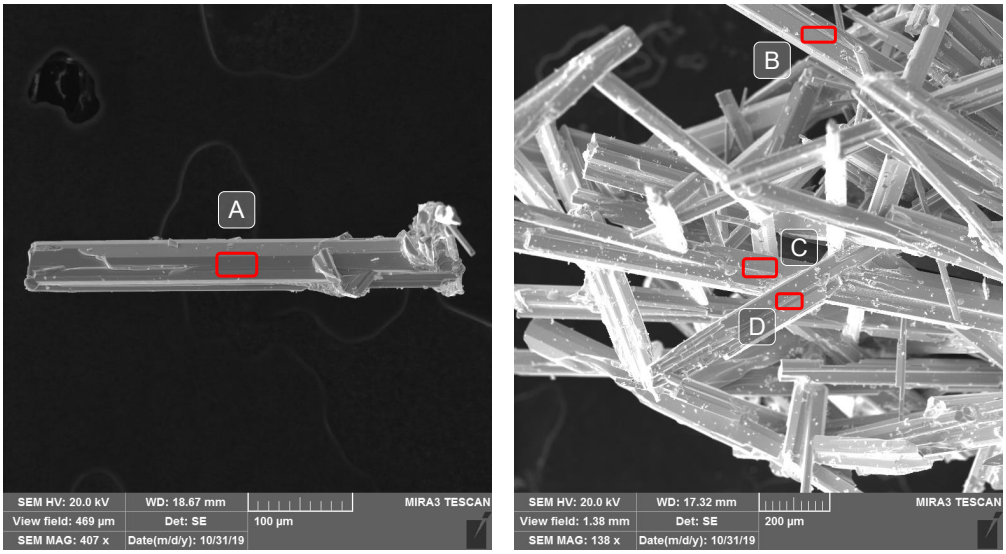

Figure A10: $Ca_5Al_2Sb_6$ crystals from a $Al_{73}Sb_{42}$ flux with superimposed EDS areas highlighted. Corresponding EDS data is shown in Figure A12 and Table A5.

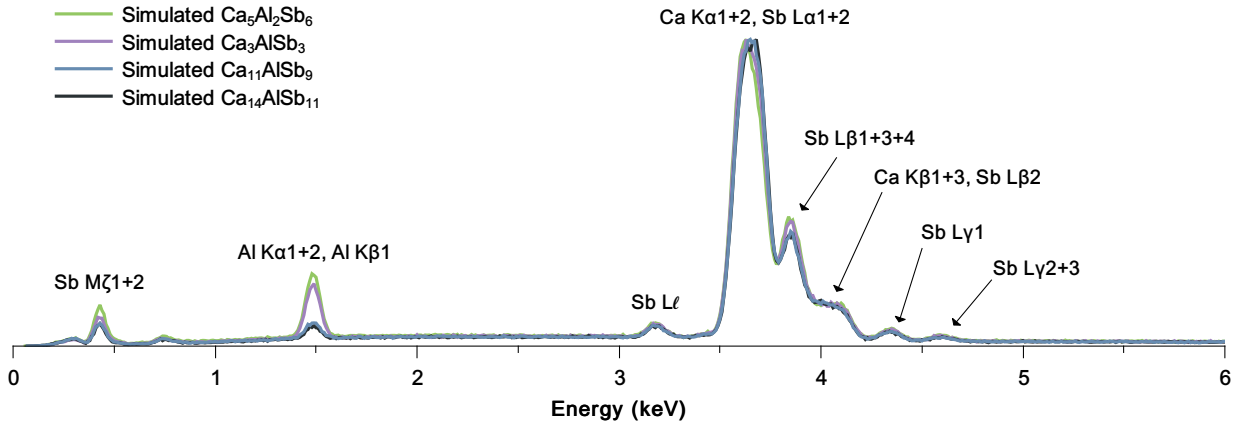

Figure A11: Simulated EDS patterns for known Ca-Al-Sb ternary phases.

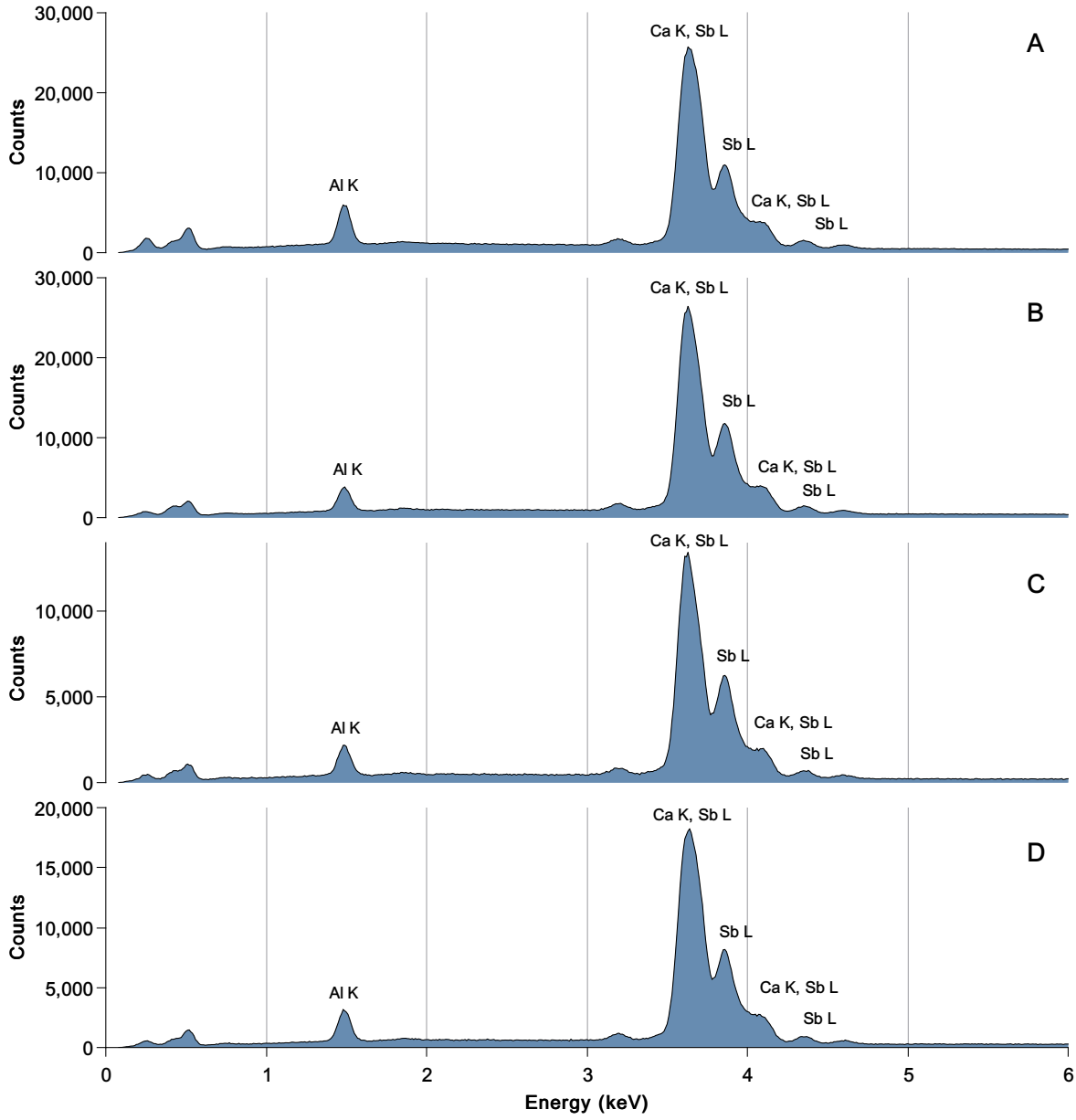

Figure A12: EDS spectra of $Ca_5Al_2Sb_6$ single crystals from a $Al_{73}Sb_{42}$ flux, Areas A-D from Figure A10.

Table A5: Quantitative results: $Ca_5Al_2Sb_6$ with $Al_{73}Sb_{42}$ flux, Areas A-D from Figure A10.

Area	Element	Weight %	Atomic %	Net Int.	Net Int. Error
A	Ca K	25.96	42.77	7188.52	2.38
	Al K	8.95	21.92	1577.16	8.3
	Sb L	65.09	35.31	7912.22	1.39
	$Ca_5Al_{2.56}Sb_{4.13}$				
B	Ca K	23.47	42.86	6427.13	2.43
	Al K	5.28	14.32	870.54	8.76
	Sb L	71.25	42.83	8544.4	1.34
	$Ca_5Al_{1.67}Sb_{5.00}$				
C	Ca K	21.67	39.53	3063.65	2.64
	Al K	6.37	17.25	542.91	9.03
	Sb L	71.96	43.22	4454.94	1.43
	$Ca_5Al_{2.18}Sb_{5.47}$				
D	Ca K	25.7	44.57	4972.62	2.42
	Al K	6.48	16.71	775.6	8.73
	Sb L	67.82	38.72	5754.27	1.43
	$Ca_5Al_{1.87}Sb_{4.34}$				

EDS: $Ca_5Al_2Sb_6$ with Sb_{20} flux

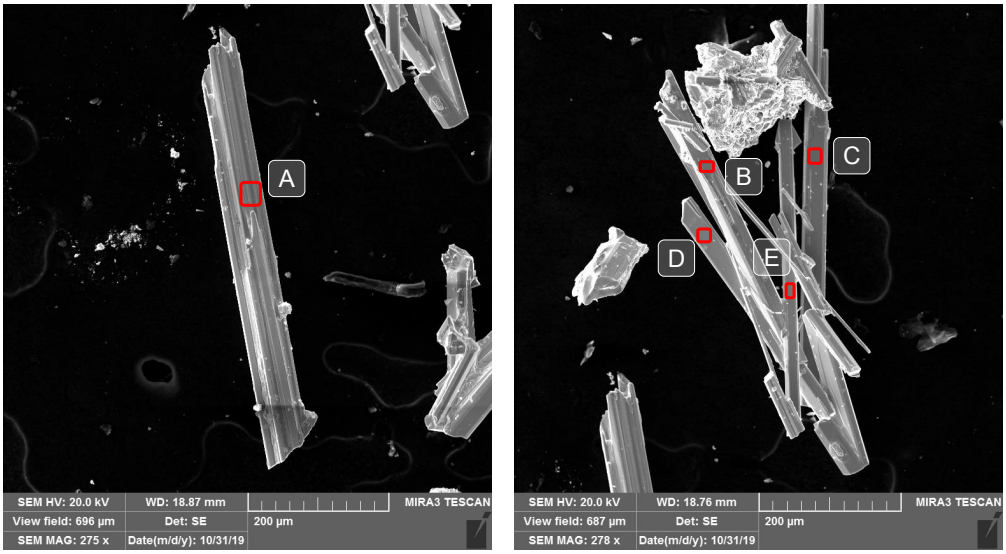

Figure A13: $Ca_5Al_2Sb_6$ crystals from a Sb_{20} flux with superimposed EDS areas highlighted. Corresponding EDS data is shown in Figure A14 and Table A6.

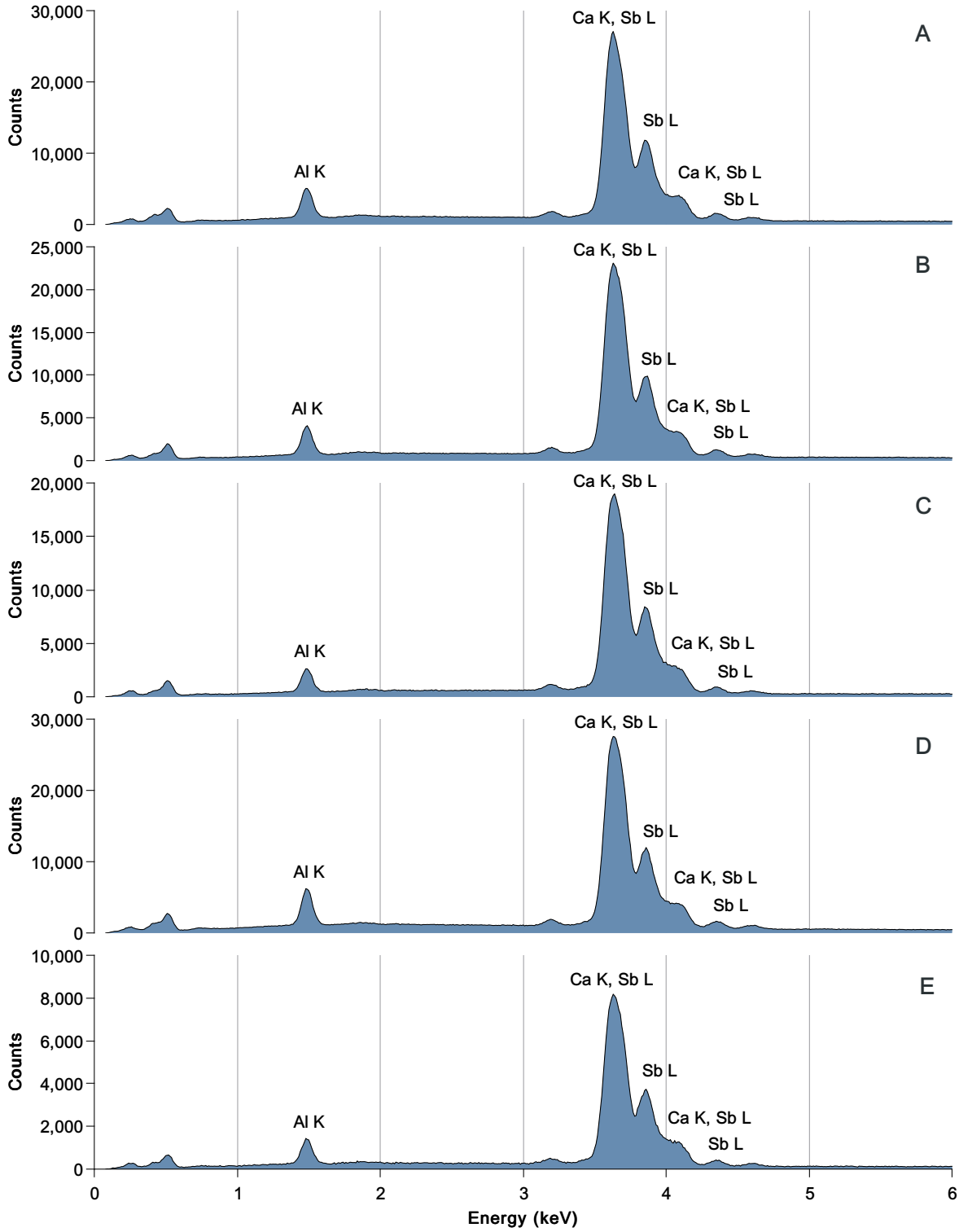

Figure A14: EDS spectra of $Ca_5Al_2Sb_6$ single crystals from a Sb_{20} flux, Areas A–G from Figure A13.

Table A6: Quantitative results: $Ca_5Al_2Sb_6$ with Sb_{20} flux, Areas A-E from Figure A13.

Area	Element	Weight %	Atomic %	Net Int.	Net Int. Error
A	Ca K	24.37	42.37	6899.49	2.41
	Al K	7.14	18.44	1248.88	8.48
	Sb L	68.49	39.2	8500.78	1.36
	$Ca_5Al_{2.18}Sb_{4.63}$				
B	Ca K	26.23	45.33	6369.67	2.38
	Al K	6.36	16.32	955.5	8.63
	Sb L	67.42	38.36	7179.57	1.42
	$Ca_5Al_{1.80}Sb_{4.23}$				
C	Ca K	26.42	46.77	5256.1	2.4
	Al K	5.05	13.28	613.51	9
	Sb L	68.54	39.95	5976.13	1.42
	$Ca_5Al_{1.42}Sb_{4.27}$				
D	Ca K	26.28	43.78	7720.93	2.36
	Al K	8.19	20.28	1521.45	8.34
	Sb L	65.53	35.94	8449.11	1.39
	$Ca_5Al_{2.32}Sb_{4.10}$				
E	Ca K	25.4	44.33	2227.8	2.63
	Al K	6.36	16.47	343.4	9.58
	Sb L	68.24	39.2	2623.69	1.6
	$Ca_5Al_{1.86}Sb_{4.42}$				

EDS: $Ca_5Al_2Sb_6$ with Sn_{15} flux

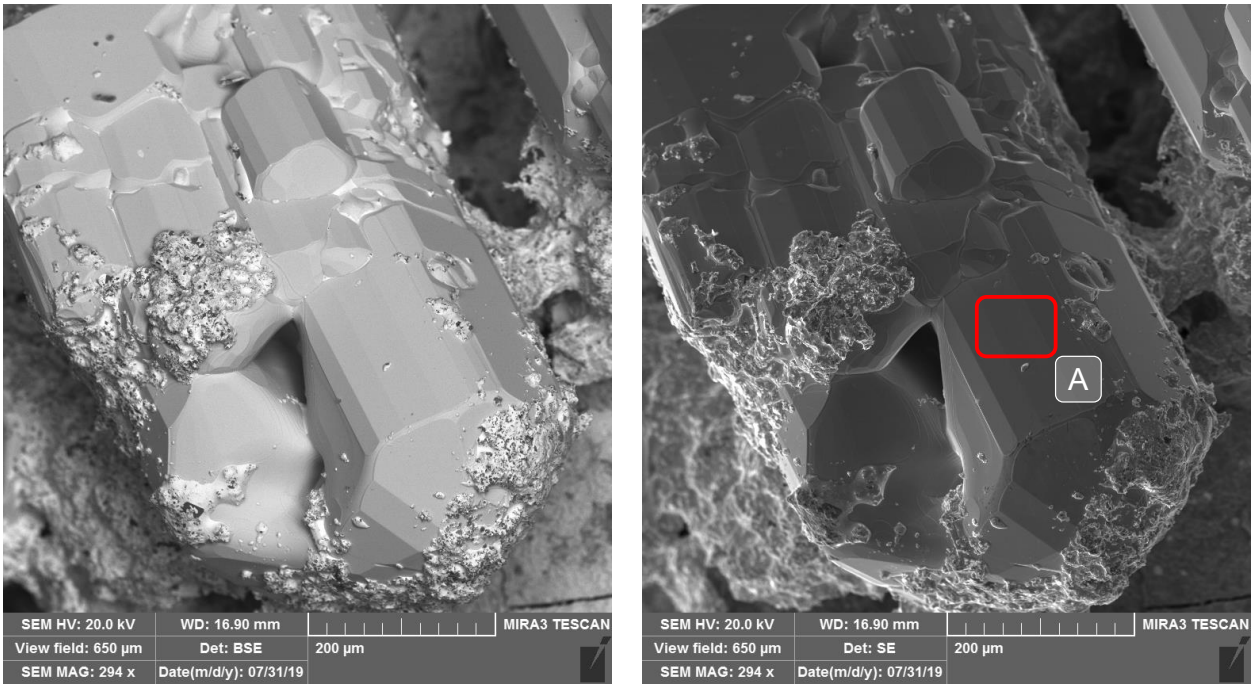

Figure A15: $Ca_5Al_2Sb_6$ crystals from a Sn_{15} flux imaged using backscattered electrons (left) to highlight flux coating the crystal. Superimposed EDS area highlighted (right) with corresponding EDS data shown in Figure A17 and Table A7.

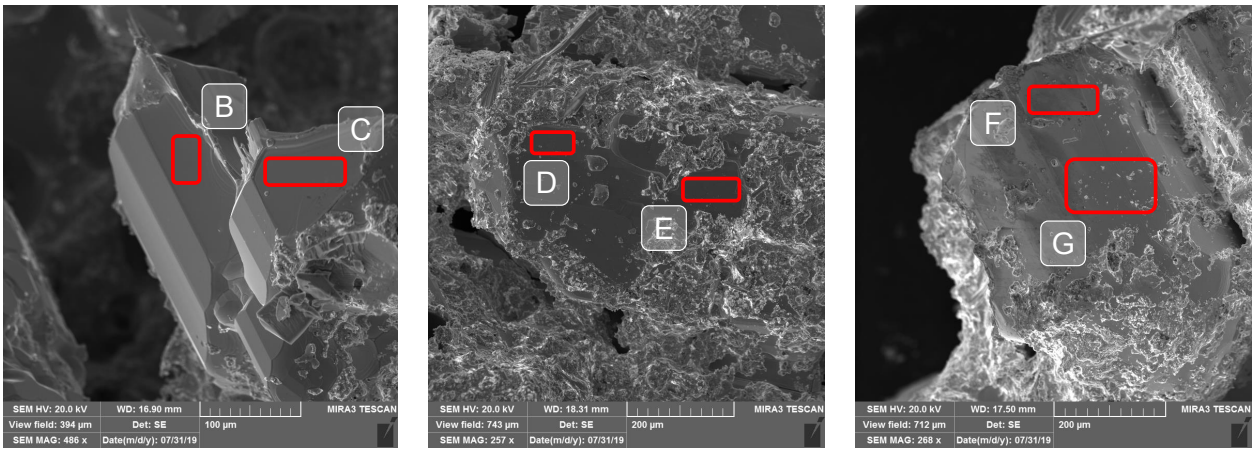

Figure A16: $Ca_5Al_2Sb_6$ crystals from a Sn_{15} flux with superimposed EDS areas highlighted. Corresponding EDS data is shown in Figure A17 and Table A7.

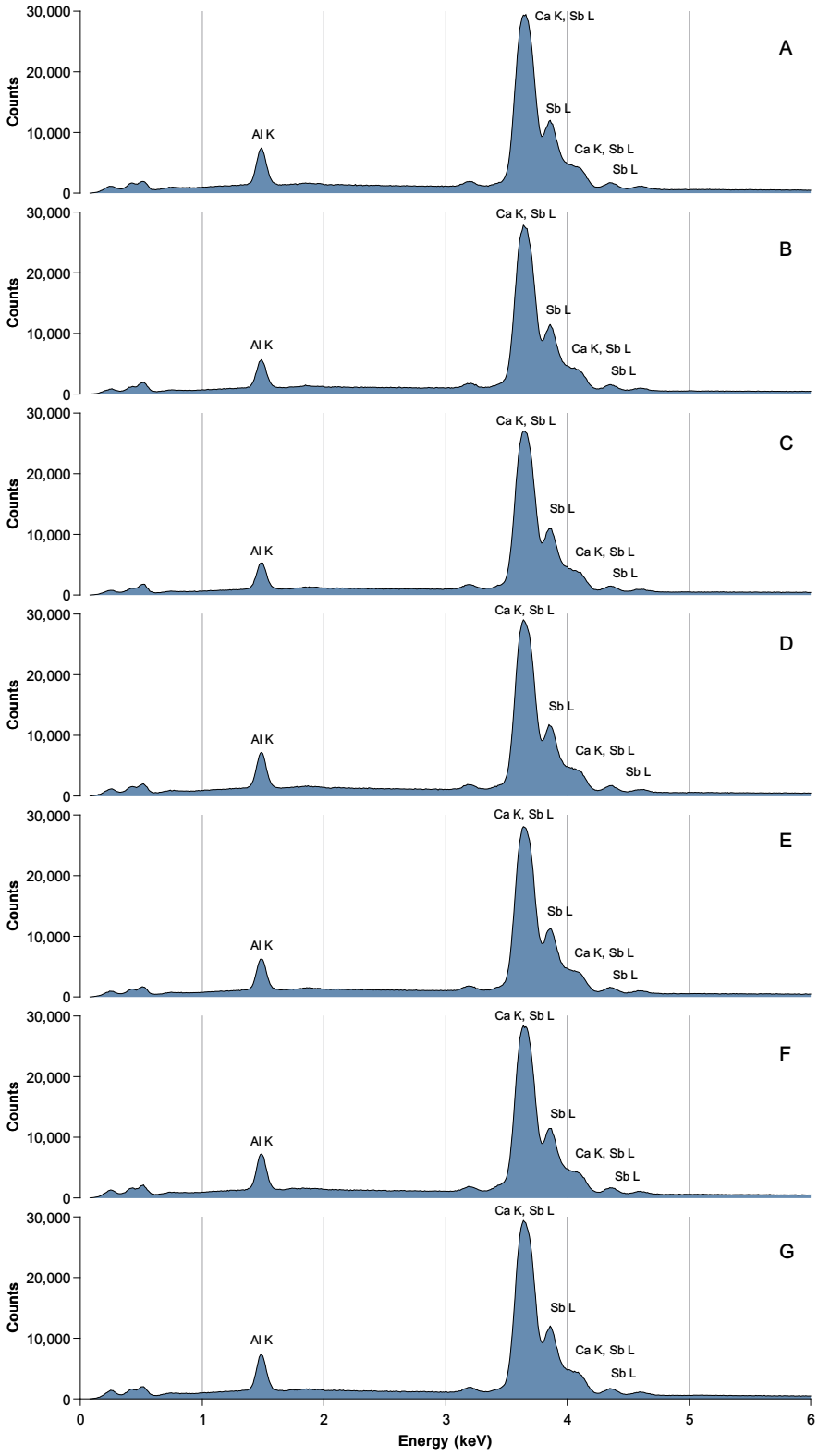

Figure A17: EDS spectra of $Ca_5Al_2Sb_6$ single crystals from a Sn_{15} flux, Areas A–G from Figure A15-A16.

Table A7: Quantitative results: $Ca_5Al_2Bi_6$ single crystals from a Sn_{15} flux, Areas A–G from Figure A15-A16.

Scan	Element	Weight %	Atomic %	Net Int.	Error %	Kratio	Z	A	F
A	CaK	29.32	45.89	9275.99	2.29	0.3094	1.1627	0.8912	1.0224
	AlK	9.78	22.74	2032.10	7.98	0.0392	1.1824	0.3383	1.0058
	SbL	60.91	31.38	8469.04	1.40	0.5595	0.8935	1.0333	0.9988
	$Ca_5Al_{2.48}Sb_{3.42}$								
B	CaK	30.76	51.45	8740.15	2.31	0.3157	1.1745	0.8881	1.018
	AlK	5.39	13.39	989.81	8.58	0.0207	1.194	0.3307	1.0049
	SbL	63.85	35.16	8001.90	1.38	0.5725	0.9025	1.0289	0.9989
	$Ca_5Al_{1.30}Sb_{3.42}$								
C	CaK	30.04	48.83	8560.23	2.26	0.3212	1.168	0.8951	1.0227
	AlK	7.31	17.64	1331.14	8.32	0.0289	1.1876	0.3308	1.006
	SbL	62.65	33.52	7837.03	1.45	0.5824	0.8976	1.0369	0.9988
	$Ca_5Al_{1.81}Sb_{3.43}$								
D	CaK	26.53	47.14	8835.26	2.27	0.3145	1.1654	0.8939	1.0226
	AlK	8.57	20.32	1657.54	8.23	0.0341	1.185	0.334	1.0059
	SbL	61.91	32.54	8135.8	1.44	0.5736	0.8955	1.0359	0.9988
	$Ca_5Al_{2.16}Sb_{3.45}$								
E	CaK	29.15	45.8	9048.39	2.28	0.3095	1.1629	0.893	1.0225
	AlK	9.66	22.55	1958.29	8.01	0.0387	1.1826	0.3371	1.0059
	SbL	61.19	31.65	8346.54	1.42	0.5654	0.8936	1.0352	0.9988
	$Ca_5Al_{2.46}Sb_{3.46}$								
F	CaK	29.61	45.86	8905.33	2.3	0.3096	1.1631	0.893	1.0226
	AlK	9.59	22.41	1911.88	8.18	0.0384	1.1828	0.3368	1.0059
	SbL	61.25	31.72	8220.31	1.43	0.5661	0.8937	1.0353	0.9988
	$Ca_5Al_{2.44}Sb_{3.46}$								
G	CaK	29.56	46.50	9232.37	2.14	0.2801	1.122	0.9072	1.0226
	AlK	9.36	21.88	1992.17	7.79	0.035	1.1415	0.3571	1.0059
	SbL	61.07	31.62	8391.94	1.6	0.5043	0.8621	1.0536	0.9988
	$Ca_5Al_{2.35}Sb_{3.40}$								

EDS: $Ca_5Al_2Bi_6$ with Bi_{20} flux

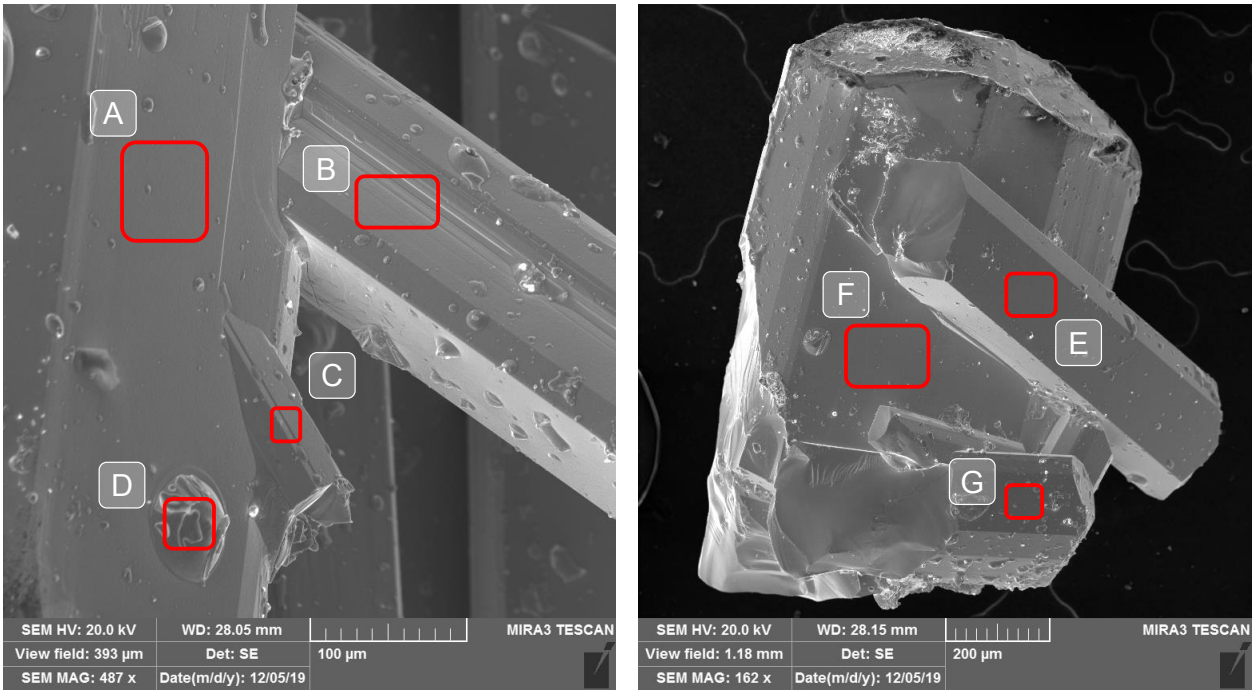

Figure A18: $Ca_5Al_2Bi_6$ crystals from a Bi_{20} flux with superimposed EDS areas highlighted. Corresponding EDS data is shown in Figure A19 and Table A8.

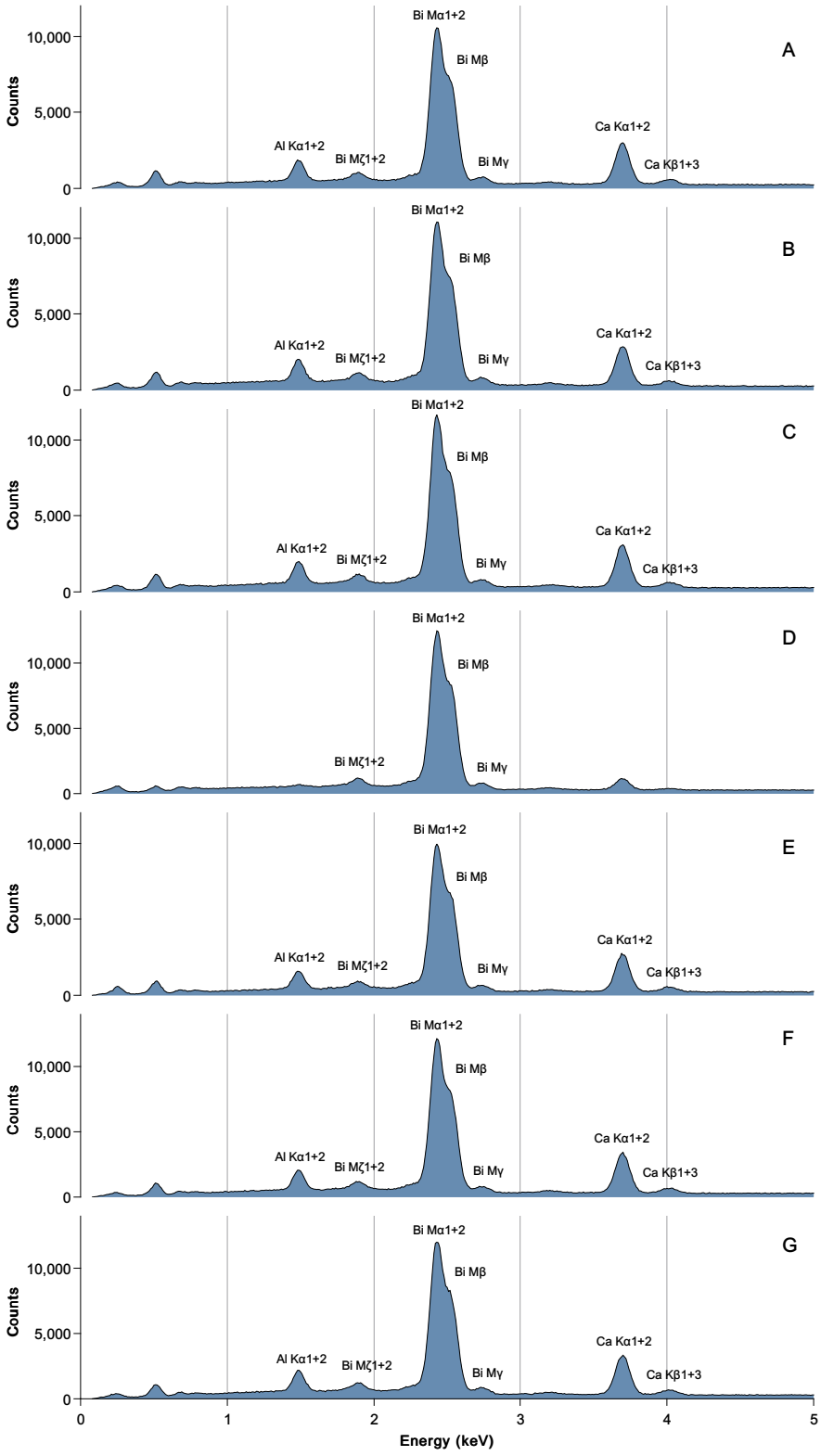

Figure A19: EDS spectra of $Ca_5Al_2Bi_6$ single crystals and flux components from a Bi_{20} flux, Areas A–G from Figure A18.

Table A8: Quantitative results: $Ca_5Al_2Bi_6$ single crystals and flux components from a Bi_{20} flux, Areas A–G from Figure A18.

Area	Element	Weight %	Atomic %	Net Int.	Net Int. Error
A	Ca K	23.77	49.60	1122.08	6.09
	Al K	7.37	22.84	428.85	8.47
	Bi L	68.86	27.56	386.52	8.75
	$Ca_5Al_{2.30}Bi_{2.78}$				
B	Ca K	22.11	46.21	1065.63	6.25
	Al K	8.35	25.92	497.5	8.11
	Bi L	69.54	27.87	402.19	8.64
	$Ca_5Al_{2.80}Bi_{3.02}$				
C	Ca K	22.78	47.9	1135.17	6.14
	Al K	7.7	24.06	472.67	8.3
	Bi L	69.52	28.04	415.37	8.46
	$Ca_5Al_{2.51}Bi_{2.93}$				
D	C K	15.12	51.22	242.51	7.38
	O K	13.73	34.93	189.37	11.44
	Bi L	71.14	13.85	512.93	8.05
	Bi flux				
E	Ca K	22.01	48.71	1011.03	6.26
	Al K	6.35	20.88	358.54	8.63
	Bi L	71.64	30.41	400.38	8.95
	$Ca_5Al_{2.14}Bi_{3.12}$				
F	Ca K	17.99	44.38	1268.1	6.24
	Al K	5.28	19.34	474.39	8.32
	Bi L	76.73	36.28	4012.31	1.89
	$Ca_5Al_{2.18}Bi_{4.09}$				
G	Ca K	17.35	42.62	1243.27	6.27
	Al K	5.81	21.18	529.71	8.38
	Bi L	76.84	36.19	4063.22	1.77
	$Ca_5Al_{2.48}Bi_{4.25}$				

BIBLIOGRAPHY

BIBLIOGRAPHY

[1] A. Zevalkink, J. Swallow, and G.J. Snyder. Thermoelectric properties of Zn-doped $Ca_5In_2Sb_6$. *Dalton Transactions*, 42(26):9713–9719, 2013.

[2] A. Zevalkink, G.S. Pomrehn, S. Johnson, J. Swallow, Z.M. Gibbs, and G.J. Snyder. Influence of the triel elements (M= Al, Ga, In) on the transport properties of $Ca_5M_2Sb_6$ Zintl compounds. *Chemistry of Materials*, 24(11):2091–2098, 2012.

[3] G. Thunis. Electronic transport properties of thermoelectric Zintl compounds $Ca_5Al_2Sb_6$ and Ca_3AlSb_3: an ab initio study. Master's thesis, Université catholique de Louvain, 2016.

[4] M. De Jong, W. Chen, T. Angsten, A. Jain, R. Notestine, A. Gamst, M. H. F. Sluiter, C. Krishna Ande, S. Van der Zwaag, J. J. Plata, C. Toher, S. Curtarolo, G. Ceder, K. A. Persson, and M. Asta. Charting the complete elastic properties of inorganic crystalline compounds. *Scientific Data, 2, 2015*, 2(1):150009, 2015.

[5] S. Ohno, K. Imasato, S. Anand, H. Tamaki, S.D. Kang, P. Gorai, H.K. Sato, E.S. Toberer, T. Kanno, and G.J. Snyder. Phase boundary mapping to obtain n-type Mg_3Sb_2-based thermoelectrics. *Joule 2*, pages 141–154, 2018.

[6] J. Gooth, A.C. Niemann, T. Meng, A.G. Grushin, K. Landsteiner, B. Gotsmann, F. Menges, M. Schmidt, C. Shekhar, V. Suss, R. Hune, B. Rellinghaus, C. Felser, B.H. Yan, and K. Nielsch. Experimental signatures of the mixed axial-gravitational anomaly in the Weyl semimetal NbP. *Nature*, 547(7663):324–327, 2017.

[7] J. Xin, G. Li, G. Auffermann, H. Borrmann, W. Schnelle, J. Gooth, X. Zhao, T. Zhu, C. Felser, and C. Fu. Growth and transport properties of Mg_3X_2 (X = Sb, Bi) single crystals. *Materials Today Physics*, 7:61–68, 2018.

[8] Lawrence Livermore National Laboratory. Estimated U.S. Energy Consumption. Online, April 2018.

[9] L.E. Bell. Cooling, heating, generating power, and recovering waste heat with thermoelectric systems. *Science*, 321(5895):1457–1461, 2008.

[10] A.F. Joffe. The revival of thermoelectricity. *Scientific American*, 199(5):31–37, 1958.

[11] D.M. Rowe. Thermoelectric generators. In S. Priya, A. Weidenkaff, and D.P. Norton, editors, *Advances in Electronic Ceramics II*, pages 107–123. John Wiley & Sons, Inc, Hoboken, NJ, USA, 2009.

[12] F.J. DiSalvo. Thermoelectric cooling and power generation. *Science*, 285(5428):703–706, 1999.

[13] T. Zhu, Y. Liu, C. Fu, J.P. Heremans, J.G. Snyder, and X. Zhao. Compromise and synergy in high-efficiency thermoelectric materials. *Advanced Materials*, 29(14):1605884, 2017.

[14] B. Poudel, Q. Hao, Y. Ma, Y. Lan, A. Minnich, B. Yu, X. Yan, D. Wang, A. Muto, D. Vashaee, X. Chen, J. Liu, M.S. Dresselhaus, G. Chen, and Z. Ren. High-thermoelectric performance of nanostructured bismuth antimony telluride bulk alloys. *Science*, 320(5876):634–638, 2008.

[15] L. Hu, H. Wu, T. Zhu, C. Fu, J. He, P. Ying, and X. Zhao. Tuning multiscale microstructures to enhance thermoelectric performance of n-type bismuth-telluride-based solid solutions. *Advanced Energy Materials*, 5(17):1500411, 2015.

[16] I.T. Witting, T.C. Chasapis, F. Ricci, M. Peters, N.A. Heinz, G. Hautier, and G.J. Snyder. The thermoelectric properties of bismuth telluride. *Advanced Electronic Materials*, 5(6):1800904, 2019.

[17] H. Zhao, J. Sui, Z. Tang, Y. Lan, Q. Jie, D. Kraemer, K. McEnaney, A. Guloy, G. Chen, and Z. Ren. High thermoelectric performance of MgAgSb-based materials. *Nano Energy*, 7: 97–103, 2014.

[18] P. Ying, X. Liu, C. Fu, X. Yue, H. Xie, X. Zhao, W. Zhang, and T. Zhu. High performance α-MgAgSb thermoelectric materials for low temperature power generation. *Chemistry of Materials*, 27(3):909–913, 2015.

[19] Y. Pei, J. Lensch-Falk, E.S. Toberer, D.L. Medlin, and G.J. Snyder. High thermoelectric performance in PbTe due to large nanoscale Ag_2Te precipitates and La doping. *Advanced Functional Materials*, 21(2):241–249, 2011.

[20] H. Wang, Y. Pei, A.D. LaLonde, and G.J. Snyder. Weak electron-phonon coupling contributing to high thermoelectric performance in n-type PbSe. *Proceedings of the National Academy of Sciences of the United States of America*, 109(25):9705–9709, 2012.

[21] K. Biswas, J. He, I.D. Blum, C.-I. Wu, T.P. Hogan, D.N. Seidman, V.P. Dravid, and M.G. Kanatzidis. High-performance bulk thermoelectrics with all-scale hierarchical architectures. *Nature*, 489(7416):414–418, 2012.

[22] H. Wang, Z.M. Gibbs, Y. Takagiwa, and G.J. Snyder. Tuning bands of PbSe for better thermoelectric efficiency. *Energy & Environmental Science*, 7(2):804–811, 2014.

[23] M. Zhou, J.-F. Li, H. Wang, T. Kita, L. Li, and Z. Chen. Nanostructure and high thermoelectric performance in nonstoichiometric AgPbSbTe compounds: the role of Ag. *Journal of Electronic Materials*, 40(5):862–866, 2011.

[24] S.H. Yang, T.J. Zhu, T. Sun, J. He, S.N. Zhang, and X.B. Zhao. Nanostructures in high-performance $(GeTe)_x(AgSbTe_2)_{100-x}$ thermoelectric materials. *Nanotechnology*, 19:245707, 2008.

[25] J. Ma, O. Delaire, A.F. May, C.E. Carlton, M.A. McGuire, L.H. VanBebber, D.L. Abernathy, G. Ehlers, T. Hong, A. Huq, W. Tian, V.M. Keppens, Y. Shao-Horn, and B.C. Sales. Glass-like phonon scattering from a spontaneous nanostructure in $AgSbTe_2$. *Nature Nanotechnology*, 8 (6):445–451, 2013.

[26] L.D. Zhao, G. Tan, S. Hao, J. He, Y. Pei, H. Chi, H. Wang, S. Gong, H. Xu, V.P. Dravid, C. Uher, G.J. Snyder, C. Wolverton, and M.G. Kanatzidis. Ultrahigh power factor and thermoelectric performance in hole-doped single-crystal SnSe. *Science*, 351(6269):141–144, 2016.

[27] R. Chetty, A. Bali, and R.C. Mallik. Tetrahedrites as thermoelectric materials: an overview. *Journal of Materials Chemistry C*, 3(48):12364–12378, 2015.

[28] T. Caillat, J. Fleurial, and A. Borshchevsky. Preparation and thermoelectric properties of semiconducting Zn_4Sb_3. *Journal of Physics and Chemistry of Solids*, 58(7):1119–1125, 1997.

[29] G.J. Snyder, M. Christensen, E. Nishibori, T. Caillat, and B.B. Iversen. Disordered zinc in Zn_4Sb_3 with phonon-glass and electron-crystal thermoelectric properties. *Nature Materials*, 3(7):458–463, 2004.

[30] J.-S. Rhyee, K.H. Lee, S.M. Lee, E. Cho, S.I. Kim, E. Lee, Y.S. Kwon, J.H. Shim, and G. Kotliar. Peierls distortion as a route to high thermoelectric performance in $In_4Se_{3-\delta}$ crystals. *Nature*, 459(7249):965–968, 2009.

[31] H. Liu, X. Shi, F. Xu, L. Zhang, W. Zhang, L. Chen, Q. Li, C. Uher, T. Day, and G.J. Snyder. Copper ion liquid-like thermoelectrics. *Nature Materials*, 11(5):422–425, 2012.

[32] Y. He, P. Lu, X. Shi, F. Xu, T. Zhang, G.J. Snyder, C. Uher, and L. Chen. Ultrahigh thermoelectric performance in mosaic crystals. *Advanced Materials*, 27(24):3639–3644, 2015.

[33] H. Tamaki, H. K. Sato, and T. Kanno. Isotropic conduction network and defect chemistry in $Mg_{3+\delta}Sb_2$-based layered Zintl compounds with high thermoelectric performance. *Advanced Materials*, 28(46):10182–10187, 2016.

[34] F. Gascoin, S. Ottensmann, D. Stark, S.M. Haïle, and G.J. Snyder. Zintl phases as thermoelectric materials: Tuned transport properties of the compounds $Ca_xYb_{1-x}Zn_2Sb_2$. *Advanced Functional Materials*, 15(11):1860–1864, 2005.

[35] S. Ohno, U. Aydemir, M. Amsler, J.-H. Pöhls, S. Chanakian, A. Zevalkink, M.A. White, S.K. Bux, C. Wolverton, and G.J. Snyder. Achieving $zT > 1$ in inexpensive Zintl phase $Ca_9Zn_{4+x}Sb_9$ by phase boundary mapping. *Advanced Functional Materials*, 27(20):1606361, 2017.

[36] J. Paik, E. Brandon, T. Caillat, R. Ewell, and Fleurial J.-P. Life testing of $Yb_{14}MnSb_{11}$ for high performance thermoelectric couples. In *Proceedings of Nuclear and Emerging Technologies for Space*, 2011.

[37] X.J. Wang, M.B. Tang, H.H. Chen, X.X. Yang, J.T. Zhao, U. Burkhardt, and Y. Grin. Synthesis and high thermoelectric efficiency of Zintl phase $YbCd_{2-x}Zn_xSb_2$. *Applied Physics Letters*, 94(9):92106, 2009.

[38] X. Yan, W. Liu, S. Chen, H. Wang, Q. Zhang, G. Chen, and Z. Ren. Thermoelectric property study of nanostructured p-type Half-Heuslers (Hf, Zr, Ti)$CoSb_{0.8}Sn_{0.2}$. *Advanced Energy Materials*, 3(9):1195–1200, 2013.

[39] Y. Liu, H. Xie, C. Fu, G.J. Snyder, X. Zhao, and T. Zhu. Demonstration of a phonon-glass electron-crystal strategy in (Hf,Zr)NiSn half-Heusler thermoelectric materials by alloying. *Journal of Materials Chemistry A*, 3(45):22716–22722, 2015.

[40] C. Fu, S. Bai, Y. Liu, Y. Tang, L. Chen, X. Zhao, and T. Zhu. Realizing high figure of merit in heavy-band p-type half-Heusler thermoelectric materials. *Nature Communications*, 6(1): 8144, 2015.

[41] G. Joshi, H. Lee, Y. Lan, X. Wang, G. Zhu, D. Wang, R.W. Gould, D.C. Cuff, M.Y. Tang, M.S. Dresselhaus, G. Chen, and Z. Ren. Enhanced thermoelectric figure-of-merit in nanostructured p-type silicon germanium bulk alloys. *Nano Letters*, 8(12):4670–4674, 2008.

[42] B. Yu, M. Zebarjadi, H. Wang, K. Lukas, H. Wang, D. Wang, C. Opeil, M. Dresselhaus, G. Chen, and Z. Ren. Enhancement of thermoelectric properties by modulation-doping in silicon germanium alloy nanocomposites. *Nano Letters*, 12(4):2077–2082, 2012.

[43] D. Champier. Thermoelectric generators: A review of applications. *Energy Conversion and Management*, 140:167–181, 2017.

[44] S.R. Brown, S.M. Kauzlarich, F. Gascoin, and G.J. Snyder. $Yb_{14}MnSb_{11}$: New high efficiency thermoelectric material for power generation. *Chemistry of Materials*, 18(7): 1873–1877, 2006.

[45] S.R. Brown, E.S. Toberer, T. Ikeda, C.A. Cox, F. Gascoin, S.M. Kauzlarich, and G.J. Snyder. Improved thermoelectric performance in $Yb_{14}Mn_{1-x}Zn_xSb_{11}$ by the reduction of spin-disorder scattering. *Chemistry of Materials*, 20(10):3412–3419, 2008.

[46] T.J. Seebeck. Ueber die magnetische polarisation der metalle und erze durch temperatur-differenz. *Annalen der Physik*, 82(1):1–20, 1826.

[47] J.C. Peltier. Nouvelles expériences sur la caloricité des courants électrique. *Annales de Chimie et de Physique*, 56:371–386, 1834.

[48] W. Thomson. On a mechanical theory of thermo-electric currents. *Proceedings of the Royal Society of Edinburgh*, 3:91–98, 1857.

[49] H.J. Goldsmid. *Introduction to Thermoelectricity*, volume 121. Springer Berlin Heidelberg, Berlin, Heidelberg, 2nd edition, 2016.

[50] C. Gayner and K.K. Kar. Recent advances in thermoelectric materials. *Progress in Materials Science*, 83:330–382, 2016.

[51] J.-B.-J. Fourier and A. Freeman. *The Analytical Theory of Heat*. London: The University Press, 1878. Print.

[52] R. Franz and G. Wiedemann. Ueber die wärme-leitungsfähigkeit der metalle. *Annalen der Physik und Chemie*, 165(8):497–531, 1853.

[53] J.M. Ziman. *Principles of the Theory of Solids.*, volume 2. Cambridge University Press, 1972.

[54] E.S. Toberer, A. Zevalkink, and G.J. Snyder. Phonon engineering through crystal chemistry. *Journal of Materials Chemistry*, 21(40):15843–15852, 2011.

[55] P. Debye. Zur theorie der spezifischen wärmen. *Annalen der Physik*, 344(14):789–839, 1912.

[56] V.I. Fistul. *Heavily doped semiconductors*. New York: Plenum Press, 1969.

[57] C.J. Vineis, A. Shakouri, A. Majumdar, and M.G. Kanatzidis. Nanostructured thermoelectrics: Big efficiency gains from small features. *Advanced Materials*, 22(36):3970–3980, 2010.

[58] D.M. Rowe. *Thermoelectrics handbook: macro to nano*. CRC/Taylor & Francis, Boca Raton, 2006.

[59] G.J. Snyder and E.S. Toberer. Complex thermoelectric materials. *Nature Materials*, 7(2): 105–114, 2008.

[60] J. Wang, S.-Q. Xia, and X.-T. Tao. $A_5Sn_2As_6$ (A = Sr, Eu). Synthesis, crystal and electronic structure, and thermoelectric properties. *Inorganic Chemistry*, 51(10):5771–5778, 2012.

[61] K. Koumoto and T. Mori. *Thermoelectric Nanomaterials: Materials Design and Applications*, volume 182. Springer, Berlin, Heidelberg, 2013 edition, 2013.

[62] L.P. Caywood and G.R. Miller. Anistropy of the constant-energy surfaces in *n*-type Bi_2Te_3 and Bi_2Se_3 from galvanomagnetic coefficients. *Physical Review B*, 2:3209–3220, Oct 1970.

[63] Y. Feutelais, B. Legendre, N. Rodier, and V. Agafonov. A study of the phases in the bismuth - tellurium system. *Materials Research Bulletin*, 28(6):591–596, 1993.

[64] K. Lee, S. Kamali, T. Ericsson, M. Bellard, and K. Kovnir. GeAs: Highly anisotropic van der Waals thermoelectric material. *Chemistry of Materials*, 28(8):2776, 2016.

[65] D. Chung, T. Hogan, P. Brazis, M. Rocci-Lane, C. Kannewurf, M. Bastea, C. Uher, and M.G. Kanatzidis. $CsBi_4Te_6$: A high-performance thermoelectric material for low-temperature applications. *Science*, 287(5455):1024–1027, 2000.

[66] D.-Y. Chung, S.D. Mahanti, W. Chen, C. Uher, and M.G. Kanatzidis. Anisotropy in thermoelectric properties of $CsBi_4Te_6$. *Materials Research Society Symposium - Proceedings*, 793: 141–148, 2004.

[67] L.D. Zhao, S.H. Lo, Y. Zhang, H. Sun, G. Tan, C. Uher, C. Wolverton, V.P. Dravid, and M.G. Kanatzidis. Ultralow thermal conductivity and high thermoelectric figure of merit in SnSe crystals. *Nature*, 508(7496):373–377, 2014.

[68] A.T. Duong, V.Q. Nguyen, G. Duvjir, V.T. Duong, S. Kwon, J.Y. Song, J.K. Lee, J.E. Lee, S.D. Park, T. Min, J. Lee, J. Kim, and S. Cho. Achieving ZT = 2.2 with Bi-doped n-type SnSe single crystals. *Nature Communications*, 7(1):13713, 2016.

[69] R. Nesper. The Zintl-Klemm concept – a historical survey. *Zeitschrift für anorganische und allgemeine Chemie*, 640(14):2639–2648, 2014.

[70] S.M. Kauzlarich, S.R. Brown, and G.J. Snyder. Zintl phases for thermoelectric devices. *Dalton Transactions*, pages 2099–2107, 2007.

[71] T.F. Fässler. *Zintl Phases: Principles and Recent Developments*, volume 139. Springer Berlin Heidelberg, Berlin/Heidelberg, 2011.

[72] E. Zintl and W. Dallenkopf. About the lattice structure of NaTl and its relationship to the structures of the type of β-brass. *Zeitschrift für Physikalische Chemie*, 16b(1):195–205, 1932.

[73] E. Zintl and G. Brauer. About the valence electron rule and the atomic radii of base metals in alloys. *Zeitschrift für Physikalische Chemie*, 20B(1):245–271, 1933.

[74] E. Zintl, A. Harder, and B. Dauth. Lattice structure of oxides, sulfides, selenides and tellurides of lithium, sodium and potassium. *Zeitschrift für Elektrochemie und angewandte physikalische Chemie*, 40(8):588–593, 1934.

[75] E. Zintl and A. Harder. Structure of the platinum - thallium alloys. *Zeitschrift für Elektrochemie und angewandte physikalische Chemie*, 41(11):767–771, 1935.

[76] E. Zintl. Intermetallic compounds. *Angewandte Chemie*, 52(1):1–6, 1939.

[77] R. Nesper. Structure and chemical bonding in Zintl-phases containing lithium. *Progress in Solid State Chemistry*, 20(1):1–45, 1990.

[78] S.M. Kauzlarich. *Chemistry, structure, and bonding of Zintl phases and ions*. The chemistry of metal clusters. VCH Publishers, 1996.

[79] S.C. Sevov. Zintl phases. In *Intermetallic Compounds - Principles and Practice*, chapter 6, pages 113–132. John Wiley & Sons, Ltd, 2002.

[80] A. Zevalkink, E.S. Toberer, W.G. Zeier, E. Flage-Larsen, and G.J. Snyder. Ca_3AlSb_3: an inexpensive, non-toxic thermoelectric material for waste heat recovery. *Energy & Environmental Science*, 4(2):510–518, 2010.

[81] W.G. Zeier, A. Zevalkink, E. Schechtel, W. Tremel, and G.J. Snyder. Thermoelectric properties of Zn-doped Ca_3AlSb_3. *Journal of Materials Chemistry*, 22(19):9826–9830, 2012.

[82] W. Mühlfordt. *20 years of the Wilhelm Klemm Foundation*. Shaker, Aachen, 2006.

[83] D. Santamaría-Pérez, Á. Vegas, and F. Liebau. The Zintl–Klemm concept applied to cations in oxides. II. The structures of silicates. *Structure and Bonding*, 118:121–177, 09 2005.

[84] G.N. Lewis. The atom and the molecule. *Journal of the American Chemical Society*, 38(4): 762–785, 1916.

[85] W.B. Pearson. The crystal structures of semiconductors and a general valence rule. *Acta Crystallographica*, 17(1):1–15, 1964.

[86] P. Alemany, M. Llunell, and E. Canadell. Roles of cations, electronegativity difference, and anionic interlayer interactions in the metallic versus nonmetallic character of Zintl phases related to arsenic. *Journal of Computational Chemistry*, 29(13):2144–2153, 2008.

[87] W. Hume-Rothery. The crystal structures of the elements of the B sub-groups and their connexion with the periodic table and atomic structures. *The London, Edinburgh, and Dublin Philosophical Magazine and Journal of Science*, 9(55):65–80, 1930.

[88] W. Hume-Rothery, C.W. Haworth, and R.E. Smallman. *The Structure of Metals and Alloys*. London: Institute of Metals and the Institution of Metallurgists, 1969.

[89] J.E. Inglesfield. Perturbation theory and chemical bonding in NaTl. *Journal of Physics C: Solid State Physics*, 4(9):1003–1012, 1971.

[90] Y. Grin, U. Schwarz, and W. Steurer. Crystal structure and chemical bonding. In *Alloy Physics*, chapter 2, pages 19–62. John Wiley & Sons, Ltd, 2007.

[91] M.B. McNeil, W.B. Pearson, L.H. Bennett, and R.E. Watson. Stabilization and chemical bonding in Zintl phases. *Journal of Physics C: Solid State Physics*, 6(1):1–10, 1973.

[92] H.B. Ozisik, H. Ozisik, K. Colakoglu, and G. Surucu. Structural and lattice dynamical properties of Zintl NaIn and NaTl compounds. *Computational Materials Science*, 50(3): 1070–1076, 2011.

[93] H. Bi, S. Zhang, S. Wei, J. Wang, D. Zhou, Q. Li, and Y. Ma. Globally stable structures of Li_xZn (x = 1-4) compounds at high pressures. *Physical Chemistry Chemical Physics*, 18: 4437–4443, 2016.

[94] L.H. Bennett. Nuclear magnetic resonance in Zintl intermediate phases LiCd and LiZn. *Physical Review*, 150:418–420, 1966.

[95] H. Ehrenberg, H. Pauly, M. Knapp, J. Gröbner, and D. Mirkovic. Tetragonal low-temperature structure of LiAl. *Journal of Solid State Chemistry*, 177(1):227–230, 2004.

[96] G.E. Jang, I.M. Curelaru, and M.P. Hentschel. Growth and characterization of large single crystals of the intermetallic compound Li-Ga (Zintl). *Journal of Crystal Growth*, 141(3): 399–403, 1994.

[97] J. Robertson. Electronic structure of Zintl compounds (NaTl) and alkali pnictides. *Solid State Communications*, 47(11):899–902, 1983.

[98] Z. Pawlowska, N. E. Christensen, S. Satpathy, and O. Jepsen. Calculated electron densities and sp^3-bonding character for binary and ternary Zintl phases. *Physical Review B*, 34: 7080–7088, 1986.

[99] G. Dmytriv, H. Pauly, H. Ehrenberg, V. Pavlyuk, and E. Vollmar. Homogeneity range of the NaTl-type Zintl phase in the ternary system Li–In–Ag. *Journal of Solid State Chemistry*, 178 (9):2825–2831, 2005.

[100] J. Köhler, S. Deng, C. Lee, and M.-H. Whangbo. On the origin of a band gap in compounds of diamond-like structures. *Inorganic chemistry*, 46(6):1957–1959, 2007.

[101] S.-M. Park, E. S. Choi, W. Kang, and S.-J. Kim. $Eu_5In_2Sb_6$, $Eu_5In_{2-x}Zn_xSb_6$: Rare earth Zintl phases with narrow band gaps. *Journal of Materials Chemistry*, 12(6):1839–1843, 2002.

[102] Z.-M. Sun, J.-G. Mao, and D.-C. Pan. Synthesis and crystal structure of a new Zintl phase $Sr_5In_2Bi_6$. *Journal of Alloys and Compounds*, 421(1-2):190–194, 2006.

[103] D.B. Luo, Y.X. Wang, Y.L. Yan, G. Yang, and J.M. Yang. The high thermopower of the Zintl compound $Sr_5Sn_2As_6$ over a wide temperature range: First-principles calculations. *Journal of Materials Chemistry A*, 2(36):15159–15167, 2014.

[104] I. Todorov, D. Y. Chung, L. Ye, A. J. Freeman, and M. G. Kanatzidis. Synthesis, structure and charge transport properties of $Yb_5Al_2Sb_6$: A Zintl phase with incomplete electron transfer. *Inorganic Chemistry*, 48(11):4768–4776, 2009.

[105] M.L. Fornasini and P. Manfrinetti. Crystal structure of ytterbium aluminium antimonide, $Yb_5Al_2Sb_6$. *Zeitschrift für Kristallographie - New Crystal Structures*, 224(3):345–346, 2009.

[106] U. Subbarao, S. Sarkar, V.K. Gudelli, V. Kanchana, G. Vaitheeswaran, and Sebastian C. Peter. $Yb_5Ga_2Sb_6$: A mixed valent and narrow-band gap material in the $RE_5M_2X_6$ family. *Inorganic Chemistry*, 52(23):13631, 2013.

[107] S.-J. Kim, J.R. Ireland, C.R. Kannewurf, and M.G. Kanatzidis. $Yb_5In_2Sb_6$: A new rare earth Zintl phase with a narrow band gap. *Journal of Solid State Chemistry*, 155(1):55–61, 2000.

[108] G. Cordier, E. Czech, M. Jakowski, and H. Schäfer. Zintlphasen mit komplexen anionen: zur kenntnis von $Ca_5Al_2Sb_6$ und $Ca_3Al_2As_4$. *Zeitschrift für Naturforschung*, 39(b):9–18, 1981.

[109] G. Cordier, H. Schäfer, and M. Stelter. Perantimonidogallate und -indate: Zur kenntnis von $Ca_5Ga_2Sb_6$, $Ca_5In_2Sb_6$ und $Sr_5In_2Sb_6$. *Zeitschrift für Naturforschung*, 40(b):5–8, 1985.

[110] S.I. Johnson, A. Zevalkink, and G.J. Snyder. Improved thermoelectric properties in Zn-doped $Ca_5Ga_2Sb_6$. *Journal of Materials Chemistry A*, 1(13):4244, 2013.

[111] E.S. Toberer, A. Zevalkink, N. Crisosto, and G.J. Snyder. The Zintl compound $Ca_5Al_2Sb_6$ for low-cost thermoelectric power generation. *Advanced Functional Materials*, 20(24): 4375–4380, 2010.

[112] C. Zheng and R. Hoffmann. Complementary local and extended views of bonding in the $ThCr_2Si_2$ and $CaAl_2Si_2$ structures. *Journal of Solid State Chemistry*, 72(1):58–71, 1988.

[113] J.K. Burdett and G.J. Miller. Fragment formalism in main-group solids: applications to aluminum boride (AlB_2), calcium aluminum silicide ($CaAl_2Si_2$), barium-aluminum ($BaAl_4$), and related materials. *Chemistry of Materials*, 2(1):12–26, 1990.

[114] P. Klüfers and A. Mewis. The crystal structure of $CaZn_2P_2$, $CaCd_2P_2$, $CaZn_2As_2$, and $CaCd_2As_2$. *Zeitschrift für Naturforschung*, 32(b):753–756, 1977.

[115] P. Klüfers and A. Mewis. The crystal structure of $BaZn_2P_2$ and $BaZn_2As_2$. *Zeitschrift für Naturforschung*, 33(b):151–155, 1978.

[116] P. Klüfers, A. Mewis, and H.-U. Schuster. Zur struktur von $ThCu_2P_2$, $YbZn_2P_2$ und $YbZnCuP_2$ sowie der verwandten verbindungen $YbCu_3P_2$ und $YbCu_2P_2$. *Zeitschrift für Kristallographie*, 149:211–226, 1979.

[117] P. Klüfers, H. Neumann, A. Mewis, and H.-U. Schuster. AB_2X_2 compounds with the $CaAl_2Si_2$ structure, VII I. *Zeitschrift für Naturforschung*, 35b:1317–1318, 1980.

[118] P. Klüfers and A. Mewis. AB_2X_2-Verbindungen mit $CaAl_2Si_2$-struktur. *Zeitschrift für Kristallographie*, 169(1-4):135–147, 1984.

[119] A. Mewis. The crystal structure of $CaZn_2Sb_2$, $CaCd_2Sb_2$, $SrZn_2Sb_2$ and $SrCd_2Sb_2$. *Zeitschrift für Naturforschung*, 88b:382–384, 1978.

[120] A. Mewis. The crystal structure of $CaMn_2P_2$, $CaMn_2As_2$, $SrMn_2P_2$ and $SrMn_2As_2$. *Zeitschrift für Naturforschung*, 88b:382–384, 1978.

[121] F. Wartenberg, C. Kranenberg, R. Pocha, D. Johrendt, A. Mewis, R.-D. Hoffmann, B.D. Mosel, and R. Pöttgen. New Pnictides with the $CaAl_2Si_2$ type structure and the stability range of this type. *Zeitschrift für Naturforschung B*, 57(11):1270–1276, 2002.

[122] O.Y. Zelinska, A.V. Tkachu, A.P. Grosvenor, and A. Mar. Structure and physical properties of ybzn2sb2 and ybcd2sb2. *Chemistry of Metals and Alloys*, 1:204–209, 2008.

[123] C. Yu, T.J. Zhu, S.N. Zhang, X.B. Zhao, J. He, Z. Su, and T.M. Tritt. Improved thermoelectric performance in the Zintl phase compounds $YbZn_{2-x}Mn_xSb_2$ via isoelectronic substitution in the anionic framework. *Journal of Applied Physics*, 104(1):13705, 2008.

[124] Q.-G. Cao, H. Zhang, M.-B. Tang, H.-H. Chen, X.-X. Yang, Y. Grin, and J.-T. Zhao. Zintl phase $Yb_{1-x}Ca_xCd_2Sb_2$ with tunable thermoelectric properties induced by cation substitution. *Journal of Applied Physics*, 107(5):53714, 2010.

[125] K. Guo, Q.-G. Cao, X.-J. Feng, M.-B. Tang, H.-H. Chen, X. Guo, L. Chen, Y. Grin, and J.-T. Zhao. Enhanced thermoelectric figure of merit of Zintl phase $YbCd_{2-x}Mn_xSb_2$ by chemical substitution. *European Journal of Inorganic Chemistry*, 2011(26):4043–4048, 2011.

[126] J. Shuai, H. Geng, Y. Lan, Z. Zhu, C. Wang, Z. Liu, J. Bao, C.-W. Chu, J. Sui, and Z. Ren. Higher thermoelectric performance of Zintl phases $(Eu_{0.5}Yb_{0.5})_{1-x}Ca_xMg_2Bi_2$ by band engineering and strain fluctuation. *Proceedings of the National Academy of Sciences of the United States of America*, 113(29):E4125–E4132, 2016.

[127] H. Zhang, J.-T. Zhao, Y. Grin, X.-J. Wang, M.-B. Tang, Z.-Y. Man, H.-H. Chen, and X.-X. Yang. A new type of thermoelectric material, $EuZn_2Sb_2$. *The Journal of Chemical Physics*, 129(16):164713, 2008.

[128] E. Brechtel, G. Cordier, and H Schäfer. Preparation and crystal structure of $Ca_9Mn_4Bi_9$ und $Ca_9Zn_4Bi_9$. *Zeitschrift für Naturforschung*, 34b:1229–1233, 1979.

[129] E. Brechtel, G. Cordier, and H Schäfer. New compounds with the $Ca_9Mn_4Bi_9$ structure: $Ca_9Cd_4Bi_9$, $Sr_9Cd_4Bi_9$, and $Ca_9Zn_4Sb_9$. *Zeitschrift für Naturforschung*, 36b:1099–1104, 1981.

[130] S.-J. Kim, J. Salvador, D. Bilc, S.D. Mahanti, and M.G. Kanatzidis. $Yb_9Zn_4Bi_9$: Extension of the Zintl concept to the mixed-valent spectator cations. *Journal of the American Chemical Society*, 123(50):12704–12705, 2001.

[131] X.C. Liu, Z. Wu, S.Q. Xia, X.T. Tao, and S. Bobev. Structural variability versus structural flexibility. a case study of $Eu_9Cd_{4+x}Sb_9$ and $Ca_9Mn_{4+x}Sb_9$ ($x \approx 1/2$). *Inorganic Chemistry*, 54(3):947–955, 2015.

[132] S. Bobev, J.D. Thompson, J.L. Sarrao, M.M. Olmstead, H. Hope, and S.M. Kauzlarich. Probing the limits of the Zintl concept: structure and bonding in rare-earth and alkaline-earth zinc-antimonides $Yb_9Zn_{4+x}Sb_9$ and $Ca_9Zn_{4.5}Sb_9$. *Inorganic Chemistry*, 43(16):5044, 2004.

[133] S.-Q. Xia and S. Bobev. Interplay between size and electronic effects in determining the homogeneity range of the $A_9Zn_{4+x}Pn_9$ and $A_9Cd_{4+x}Pn_9$ phases ($0 \leq x \leq 0.5$), A = Ca, Sr, Yb, Eu; Pn = Sb, Bi. *Journal of the American Chemical Society*, 129(32):10011, 2007.

[134] S.-Q. Xia and S. Bobev. New manganese-bearing antimonides and bismuthides with complex structures. synthesis, structural characterization, and electronic properties of $Yb_9Mn_{4+x}Pn_9$ (Pn= Sb or Bi). *Chemistry of Materials*, 22(3):840–850, 2010.

[135] S.K. Bux, A. Zevalkink, O. Janka, D. Uhl, S. Kauzlarich, J.G. Snyder, and J.-P. Fleurial. Glass-like lattice thermal conductivity and high thermoelectric efficiency in $Yb_9Mn_{4.2}Sb_9$. *Journal of Materials Chemistry A*, 2(1):215–220, 2014.

[136] S. Ohno, A. Zevalkink, Y. Takagiwa, S.K. Bux, and G.J. Snyder. Thermoelectric properties of the $Yb_9Mn_{4.2-x}Zn_xSb_9$ solid solutions. *Journal of Materials Chemistry A*, 2(20):7478, 2014.

[137] N. Kazem, J.V. Zaikina, S. Ohno, G.J. Snyder, and S.M. Kauzlarich. Coinage-metal-stuffed $Eu_9Cd_4Sb_9$: Metallic compounds with anomalous low thermal conductivities. *Chemistry of Materials*, 27(21):7508–7519, 2015.

[138] Z. Wu, J. Li, X. Li, M. Zhu, K.-C. Wu, X.-T. Tao, B.-B. Huang, and S.-Q. Xia. Tuning the thermoelectric properties of $Ca_9Zn_{4+x}Sb_9$ by controlled doping on the interstitial structure. *Chemistry of Materials*, 28(19):6917–6924, 2016.

[139] C. Chen, W. Xue, X. Li, Y. Lan, Z. Zhang, X. Wang, F. Zhang, H. Yao, S. Li, J. Sui, P. Han, X. Liu, F. Cao, Y. Wang, and Q. Zhang. Enhanced thermoelectric performance of Zintl phase $Ca_9Zn_{4+x}Sb_9$ by beneficial disorder on the selective cationic site. *ACS Applied Materials & Interfaces*, 11(41):37741–37747, 2019.

[140] Y.L. Yan, Y.X. Wang, and G.B. Zhang. A key factor improving the thermoelectric properties of Zintl compounds $A_5M_2Pn_6$ (A=Ca, Sr, Ba; M=Ga, Al, In; Pn=As, Sb). *Computational Materials Science*, 85:88–93, 2014.

[141] L. Ye, Y. X. Wang, J. Yang, Y. Yan, J. Zhang, L. Guo, and Z. Feng. Electronic structure and thermoelectric properties of the Zintl compounds $Sr_5Al_2Sb_6$ and $Ca_5Al_2Sb_6$: First-principles study. *RSC Advances*, 5(63):50720–50728, 2015.

[142] G. Yang, H. Cui, D. Ma, and C. He. The elastic and thermoelectric properties of the Zintl compound $Ca_5Al_2Sb_6$ under high pressure. *Journal of Applied Physics*, 116(22):223709, 2014.

[143] G. Dhanaraj. *Springer Handbook of Crystal Growth*. Springer-Verlag, 1st edition, 2010.

[144] A.B. Childs, S. Baranets, and S. Bobev. Five new ternary indium-arsenides discovered. synthesis and structural characterization of the Zintl phases $Sr_3In_2As_4$, $Ba_3In_2As_4$, $Eu_3In_2As_4$, $Sr_5In_2As_6$ and $Eu_5In_2As_6$. *Journal of Solid State Chemistry*, 278(C):120889, 2019.

[145] J.W. Zhang, L.R. Song, G.K.H. Madsen, K.F.F. Fischer, W.Q. Zhang, X. Shi, and B.B. Iversen. Designing high-performance layered thermoelectric materials through orbital engineering. *Nature Communications*, 7(1):10892, 2016.

[146] A. Zevalkink, E.S. Toberer, T. Bleith, E. Flage-Larsen, and G.J. Snyder. Improved carrier concentration control in Zn-doped $Ca_5Al_2Sb_6$. *Journal of Applied Physics*, 110(1):13721, 2011.

[147] A. Zevalkink, J. Swallow, and G.J. Snyder. Thermoelectric properties of Mn-doped $Ca_5Al_2Sb_6$. *Journal of Electronic Materials*, 41(5):813–818, 2012.

[148] G. Cordier, H. Schäfer, and M. Stelter. Ca_3AlSb_3 und $Ca_5Al_2Bi_6$, zwei neue zintlphasen mit kettenförmigen anionen. *Zeitschrift für Naturforschung*, 39(b):727–732, 1984.

[149] U. Aydemir, A. Zevalkink, A. Ormeci, H. Wang, S. Ohno, S. Bux, and G.J. Snyder. Thermoelectric properties of the Zintl phases $Yb_5M_2Sb_6$ (M = Al, Ga, In). *Dalton Transactions*, 44 (15):6767–6774, 2015.

[150] G. Cordier, H. Schäfer, and M. Stelter. Darstellung und struktur der verbindung $Ca_{14}AlSb_{11}$. *Zeitschrift für anorganische und allgemeine Chemie*, 519:183–188, 1984.

[151] G. Cordier and M. Stelter. $Sr_5Al_2Sb_6$ und $Ba_5In_2Sb_6$: Zwei neue Zintlphasen mit unterschiedlichen bänderanionen. *Zeitschrift für Naturforschung B*, 43(4):463–466, 1988.

[152] K. Byrappa and D. Y. Pushcharovsky. Crystal chemistry and its significance on the growth of technological materials: Part I; silicates, phosphates and their analogues. *Progress in Crystal Growth and Characterization of Materials*, 24(4):269–359, 1992.

[153] P. Cubillas and M.W. Anderson. Synthesis mechanism: Crystal growth and nucleation. In *Zeolites and Catalysis*, pages 1–55. Wiley-VCH Verlag GmbH & Co. KGaA, 2010.

[154] M. Tachibana. *Beginner's Guide to Flux Crystal Growth*. Springer, Tokyo, 2017.

[155] P.C. Canfield, T. Kong, U.S. Kaluarachchi, and N.H. Jo. Use of frit-disc crucibles for routine and exploratory solution growth of single crystalline samples. *Philosophical Magazine*, 96 (1):84–92, 2016.

[156] S.M. Koohpayeh. Single crystal growth by the travelling solvent technique: A review. *Progress in Crystal Growth and Characterization of Materials*, 62(4):22–34, 2016.

[157] K.K. Strelov and I.D. Kashcheev. Phase diagram of the system Al_2O_3-SiO_2. *Refractories*, 36(8):244–246, 1995.

[158] E.L. Kunz Wille, N.H. Jo, J.C. Fettinger, P.C. Canfield, and S.M. Kauzlarich. Single crystal growth and magnetic properties of the mixed valent Yb containing Zintl phase, $Yb_{14}MgSb_{11}$. *Chemical Communications*, 54(92):12946–12949, 2018.

[159] M. Wierzbicka-Wieczorek, P.K. Krug, and U. Kolitsch. High-temperature flux growth as a tool for the preparation of mixed-framework metal-y silicates: A systematic evaluation of the influence of experimental parameters. *Crystal Growth & Design*, 17(2):590–603, 2017.

[160] M.G. Kanatzidis, R. P ottgen, and W. Jeitschko. The metal flux: a preparative tool for the exploration of intermetallic compounds. *Angewandte Chemie (International ed. in English)*, 44(43):6996–7023, 2005.

[161] I. Higashi, Y. Takahashi, and T. Atoda. Crystal growth of borides and carbides of transition metals from molten aluminum solutions. *Journal of Crystal Growth*, 33(2):207–211, 1976.

[162] G.H. Olsen and A.V. Cafiero. Single-crystal growth of mixed (La, Eu, Y, Ce, Ba, Cs) hexaborides for thermionic emission. *Journal of Crystal Growth*, 44(3):287–290, 1978.

[163] S. Bobev, P.H. Tobash, V. Fritsch, J.D. Thompson, M.F. Hundley, J.L. Sarrao, and Z. Fisk. Ternary rare-earth alumo-silicides—single-crystal growth from Al flux, structural and physical properties. *Journal of Solid State Chemistry*, 178(6):2091–2103, 2005.

[164] N.P. Calta and M.G. Kanatzidis. Quaternary aluminum silicides grown in Al flux: $RE_5Mn_4Al_{23-x}Si_x$ (RE = Ho, Er, Yb) and $Er_{44}Mn_{55}(AlSi)_{237}$. *Inorganic Chemistry*, 52(17): 9931–9940, 2013.

[165] S. Okada, T. Mori, T. Yamasaki, G. Rogl, K. Kouzu, Q.S. Guo, P. Rogl, K. Yubuta, and T. Shishido. Crystal growth and some properties of $Tm(Al_{1-x}Mo_x)B_4$ synthesized by Al-flux. *Solid State Phenomena*, 289:65–70, 2019.

[166] P.C. Canfield and Z. Fisk. Growth of single crystals from metallic fluxes. *Philosophical Magazine B*, 65(6):1117–1123, 1992.

[167] S. Roberts and P.J. Dobson. Evidence for reaction at the al-sio2 interface. *Journal of Physics D: Applied Physics*, 14:L17, 1981.

[168] H. Zhu, K. Dong, J. Huang, J. Li, G. Wang, and Z. Xie. Reaction mechanism and mechanical properties of an aluminum-based composite fabricated in-situ from Al–SiO_2 system. *Materials Chemistry and Physics*, 145(3):334–341, 2014.

[169] R.S. Feigelson, R.K. Route, and H.W. Swarts. Solution growth of $CdGeAs_2$. *Journal of Crystal Growth*, 28(1):138–144, 1975.

[170] I. Miotkowski, S. Miotkowska, and A. Horak. Solution growth $CdGeP_2$ crystals and layers. *Journal of Crystal Growth*, 50(2):567–570, 1980.

[171] S. Fiechter and H.-M. Kühne. Crystal growth of RuX_2 (X = S, Se, Te) by chemical vapour transport and high temperature solution growth. *Journal of Crystal Growth*, 83(4):517–522, 1987.

[172] N. Matsumoto and S. Nagata. Single-crystal growth of sulphospinel $CuIr_2S_4$ from Bi solution. *Journal of Crystal Growth*, 210(4):772–776, 2000.

[173] Z. Henkie, P. Wiśniewski, and A Gukasov. U_3Bi_4 single crystal growth by the molten metal solution evaporation method. *Journal of Crystal Growth*, 172(3):459–465, 1997.

[174] G. Ryu, K. Son, and G. Sch utz. Growth and characterization of large weak topological insulator Bi_2TeI single crystal by bismuth self-flux method. *Journal of Crystal Growth*, 440: 26–30, 2016.

[175] J. Ye, H. Horiuchi, T. Shishido, N. Toyota, K. Ukei, T. Sasaki, and T. Fukuda. Growth and characterization of Va-Sn-Ga (Va = Ta, Nb, V) superconducting compounds. *Journal of Crystal Growth*, 99(1, Part 2):969–974, 1990.

[176] S. Okada, T. Shishido, M. Ogawa, F. Matsukawa, Y. Ishizawa, K. Nakajima, T. Fukuda, and T. Lundström. MnSi and $MnSi_{2-x}$ single crystals growth by Ga flux method and properties. *Journal of Crystal Growth*, 229(1-4):532–536, 2001.

[177] K.R. Thomas, J.Y. Cho, J.N. Millican, R.D. Hembree, M. Moldovan, A. Karki, D.P. Young, and J.Y. Chan. Crystal growth and physical properties of Ln_2MGa_{12} (Ln=Pr, Nd, and Sm; M=Ni, Cu). *Journal of Crystal Growth*, 312(8):1098–1103, 2010.

[178] J.R. Salvador, C. Malliakas, J.R. Gour, and M.G. Kanatzidis. $RE_5Co_4Si_{14}$ (RE = Ho, Er, Tm, Yb): Silicides grown from Ga flux showing exceptional resistance to chemical and thermal attack. *Chemistry of Materials*, 17(7):1636–1645, 2005.

[179] M.A. Kassem, Y. Tabata, T. Waki, and H. Nakamura. Single crystal growth and characterization of kagomé-lattice shandites $Co_3Sn_{2-x}In_xS_2$. *Journal of Crystal Growth*, 426:208–213, 2015.

[180] K. Sugiyama, A. Sawada, K. Ito, S. Iwasaki, and T. Endo. Crystal growth of $CuGaSe_2$ from In solutions. *Journal of Crystal Growth*, 84(4):673–675, 1987.

[181] K. Kliemt and C. Krellner. Single crystal growth and characterization of $gdrh_2si_2$. *Journal of Crystal Growth*, 419:37–41, 2015.

[182] H.J. Höbler, G. Kühn, and A. Tempel. Crystallization of $CuGaS_2$ from Pb and Sn solutions. *Journal of Crystal Growth*, 53(3):451–457, 1981.

[183] T. Klimczuk, C.H. Wang, Q. Xu, J. Lawrence, T. Durakiewicz, F. Ronning, A. Llobet, E.D. Bauer, Griveau J-C., W. Sadowski, H.W. Zandbergen, J.D. Thompson, and R.J. Cava. Crystal growth of CsCl-type $Yb_{0.24}Sn_{0.76}Ru$. *Journal of Crystal Growth*, 318(1):1005–1008, 2011.

[184] R. Eloirdi, J.-C. Griveau, E. Colineau, M. Ernstberger, R. Caciuffo, H.C. Walker, D. Le, and K.A. McEwen. Synthesis and characterization of large single crystals of $NpPd_3$ by flux method. *Journal of Crystal Growth*, 320(1):52–54, 2011.

[185] S. Okada, K. Kudou, T. Mori, K. Iizumi, T. Shishido, T. Tanaka, and P. Rogl. Crystal growth and some properties of $REMn_2Si_2$ (RE=Er, Tm, Yb, Lu) compounds. *Journal of Crystal Growth*, 244(3):267–273, 2002.

[186] B.-Z. Lee, C.-S. Oh, and D.N. Lee. A thermodynamic evaluation of the Ag-Pb-Sb system. *Journal of Alloys and Compounds*, 215(1):293–301, 1994.

[187] B. Sokolovskii, Y. Plevachuk, and V. Didoukh. Electroconductivity and liquid-liquid equilibrium in the Pb-Ga system. *Physica Status Solidi (a)*, 148(1):123–128, 1995.

[188] S.-K. Yu, F. Sommer, and B Predel. Isopiestic measurements and assessment of the Al-Pb system. *Zeitschrift für Metallkunde*, 87:574–580, 1996.

[189] A.J. McAlister. Al-Pb (aluminum-antimony). In T.B. Massalski, H. Okamoto, P.R. Subramanian, and L. Kacprzak, editors, *Binary Alloy Phase Diagrams*, pages 189–190. Materials Park, Ohio: ASM International, second edition, 1990.

[190] J.P. Nabot. In-Pb (indium-lead). In T.B. Massalski, H. Okamoto, P.R. Subramanian, and L. Kacprzak, editors, *Binary Alloy Phase Diagrams*, pages 2269–2271. Materials Park, Ohio: ASM International, second edition, 1990.

[191] P.R. Subramanian. Ca-Sn (calcium-tin). In T.B. Massalski, H. Okamoto, P.R. Subramanian, and L. Kacprzak, editors, *Binary Alloy Phase Diagrams*, pages 954–955. Materials Park, Ohio: ASM International, second edition, 1990.

[192] W.P. Allen and J.H. Perepezko. Solidification of undercooled sn-sb peritectic alloys: Part i. microstructural evolution. *Metallurgical Transactions A*, 22(3):753–764, 1991.

[193] T. Wadsten. On the preparation and properties of In_5S_4 obtained from molten tin. *Journal of Crystal Growth*, 52:673–678, 1981.

[194] C. Krellner and C. Geibel. Single crystal growth and anisotropy of cerupo. *Journal of Crystal Growth*, 310(7):1875–1880, 2008.

[195] J.B. Peng, G.L. Sun, and C.T. Lin. Investigation of thermal behavior and crystal growth of iron pnictides using Sn flux. *Journal of Crystal Growth*, 316(1):85–89, 2011.

[196] T. Wolf. Flux separation methods for flux-grown single crystals. *Philosophical Magazine*, 92(19-21):2458–2465, 2012.

[197] A.J. McAlister and D.J. Kahan. Al-Sn (aluminum-tin). In T.B. Massalski, H. Okamoto, P.R. Subramanian, and L. Kacprzak, editors, *Binary Alloy Phase Diagrams*, pages 215–216. Materials Park, Ohio: ASM International, second edition, 1990.

[198] W.K. Hofmann. Molybdenum and tungsten diselenide from high temperature solutions. *Journal of Crystal Growth*, 76(1):93–99, 1986.

[199] P.C. Canfield. Properties and applications of complex intermetallics. chapter Solution growth of intermetallic single crystals: A beginner's guide, pages 93–111. World Scientific Publishing, 2010.

[200] B.D. Ratner and D.G. Castner. *Electron Spectroscopy for Chemical Analysis*, chapter 3, pages 47–112. John Wiley & Sons, Ltd, 2009.

[201] G.M. Espallargas and L. Brammer. Diffraction studies in crystal engineering. In *Making Crystals by Design*, chapter 3.1, pages 241–265. John Wiley & Sons, Ltd, 2007.

[202] W. Massa. *The Geometry of X-Ray Diffraction*, pages 13–25. Springer Berlin Heidelberg, 2000.

[203] G. Rhodes. Collecting diffraction data. In G. Rhodes, editor, *Crystallography Made Crystal Clear*, Complementary Science, chapter 4, pages 49–89. Academic Press, Burlington, 3rd edition, 2006.

[204] D.M. Smiadak. Scintillator candidate compounds. Master's thesis, Michigan State University, 2015.

[205] T.W. Ni, M.A. Tofanelli, and C.J. Ackerson. Structure Determination by Single Crystal X-ray Crystallography. In T. Tsukuda and H. Häkkinen, editors, *Protected Metal Clusters*, volume 9 of *Frontiers of Nanoscience*, chapter 5, pages 103–125. Elsevier, 2015.

[206] SAINT, Software for Data Extraction and Reduction, Version 6.02, Bruker AXS Inc., Madison, WI, 2002.

[207] G.M. Sheldrick. A short history of SHELX. *Acta Crystallographica Section A*, 64(1): 112–122, 2008.

[208] O.V. Dolomanov, L.J. Bourhis, R.J. Gildea, J.A.K. Howard, and H. Puschmann. OLEX2: a complete structure solution, refinement and analysis program. *Journal of Applied Crystallography*, 42(2):339–341, 2009.

[209] J.D. Menczel, L. Judovits, R.B. Prime, H.E. Bair, M. Reading, and S. Swier. *Differential Scanning Calorimetry (DSC)*, chapter 2, pages 7–239. John Wiley & Sons, Ltd, 2008.

[210] W.M. Groenewoud. Thermogravimetry. In W.M. Groenewoud, editor, *Characterisation of Polymers by Thermal Analysis*, chapter 2, pages 61–76. Elsevier Science B.V., Amsterdam, 2001.

[211] T.L. Ngai and Chang Y.A. Ga-Sb (gallium-antimony). In T.B. Massalski, H. Okamoto, P.R. Subramanian, and L. Kacprzak, editors, *Binary Alloy Phase Diagrams*, pages 1849–1851. Materials Park, Ohio: ASM International, second edition, 1990.

[212] P.R. Subramanian. Ca-Sb (calcium-antimony). In T.B. Massalski, H. Okamoto, P.R. Subramanian, and L. Kacprzak, editors, *Binary Alloy Phase Diagrams*, pages 949–950. Materials Park, Ohio : ASM International, second edition, 1990.

[213] H. Okamoto. Ca-Ga (calcium-gallium). In T.B. Massalski, H. Okamoto, P.R. Subramanian, and L. Kacprzak, editors, *Binary Alloy Phase Diagrams*, pages 913–914. Materials Park, Ohio: ASM International, second edition, 1990.

[214] D.M. Young and S.M. Kauzlarich. Preparation, structure, and electronic properties of $Ca_{11}MSb_9$ (M = Al, Ga, In). *Chemistry of Materials*, 7(1):206–209, 1995.

[215] H. Okamoto and C.B. Alcock. Ca-In (calcium-indium). In T.B. Massalski, H. Okamoto, P.R. Subramanian, and L. Kacprzak, editors, *Binary Alloy Phase Diagrams*, pages 920–921. Materials Park, Ohio: ASM International, second edition, 1990.

[216] R.C. Sharma and Y.A. Chang. In-Sb (indium-antimony). In T.B. Massalski, H. Okamoto, P.R. Subramanian, and L. Kacprzak, editors, *Binary Alloy Phase Diagrams*, pages 2286–2288. Materials Park, Ohio: ASM International, second edition, 1990.

[217] G. Cordier, H. Schäfer, and M. Stelter. $Ca_{11}InSb_9$, eine Zintlphase mit diskreten $InSb_4^{9-}$ -anionen. *Zeitschrift für Naturforschung*, 40(b):868–871, 1985.

[218] V.P. Itkin, C.B. Alcock, P.J. van Ekeren, and H.A.J. Oonk. Al-Ca (aluminum-calcium). In T.B. Massalski, H. Okamoto, P.R. Subramanian, and L. Kacprzak, editors, *Binary Alloy Phase Diagrams*, pages 130–133. Materials Park, Ohio: ASM International, second edition, 1990.

[219] A. Zajaczkowski and J. Botor. Thermodynamics of the Al-Sb system determined by vapour pressure measurements. *Zeitschrift für Metallkunde*, 86:590–596, 1995.

[220] A.J. McAlister. Al-Sb (aluminum-antimony). In T.B. Massalski, H. Okamoto, P.R. Subramanian, and L. Kacprzak, editors, *Binary Alloy Phase Diagrams*, pages 206–208. Materials Park, Ohio: ASM International, second edition, 1990.

[221] A. Zevalkink, E.S. Toberer, W.G. Zeier, E. Flage-Larsen, and G.J. Snyder. Ca_3AlSb_3: an inexpensive, non-toxic thermoelectric material for waste heat recovery. *Energy & Environmental Science*, 4:510–518, 2011.

[222] J. Xu and H. Kleinke. Unusual Sb-Sb bonding in high temperature thermoelectric materials. *Journal of Computational Chemistry*, 29(13):2134–2143, 2008.

[223] G.A. Papoian and R. Hoffmann. Hypervalent bonding in one, two, and three dimensions: Extending the Zintl–Klemm Concept to nonclassical electron-rich networks. *Angewandte Chemie International Edition*, 39(14):2408–2448, 2000.

[224] K.-F. Liu and S.-Q. Xia. Recent progresses on thermoelectric Zintl phases: Structures, materials and optimization. *Journal of Solid State Chemistry*, 270:252–264, 2019.

[225] L. Vegard. Die konstitution der mischkristalle und die raumfüllung der atome. *Zeitschrift für Physik*, 5(1):17–26, 1921.

[226] A.R. Denton and N.W. Ashcroft. Vegard's law. *Physical Review A*, 43:3161–3164, 1991.

[227] N. Ritchie, J.M. Davis, and D.E. Newbury. DTSA-II: A new tool for simulating and quantifying EDS spectra - application to difficult overlaps. *Microscopy and Microanalysis*, 14(S2):1176–1177, 2008.

[228] N. Ritchie. Spectrum simulation in DTSA-II. *Microscopy and Microanalysis*, 15(5):454–468, 2009.

[229] J.D.H. Donnay and D. Harker. A new law of crystal morphology extending the Law of Bravais. *American Mineralogist*, 22(5):446–467, 1937.

[230] J. Prywer. Morphological importance of crystal faces in connection with growth rates and crystallographic structure of crystal. *Crystal Growth & Design*, 2(4):281–286, 2002.

[231] C.F. Macrae, I.J. Bruno, J.A. Chisholm, P.R. Edgington, P. McCabe, E. Pidcock, L. Rodriguez-Monge, R. Taylor, J. van de Streek, and P.A. Wood. Mercury CSD 2.0 – new features for the visualization and investigation of crystal structures. *Journal of Applied Crystallography*, 41 (2):466–470, 2008.

[232] M. Nespolo. The ash heap of crystallography: restoring forgotten basic knowledge. *Journal of Applied Crystallography*, 48(4):1290–1298, 2015.

[233] C.A. Volkert and A.M. Minor. Focused ion beam microscopy and micromachining. *MRS Bulletin*, 32(5):389–399, 2007.

[234] D.C. Cox. *Introduction to Focused Ion Beam Nanometrology*. Morgan & Claypool Publishers, 2015.

[235] L.A. Giannuzzi and F.A. Stevie. *Introduction to Focused Ion Beams: Instrumentation, Theory, Techniques, and Practice*. Springer, 2005.

[236] F.H. Dill, W.P. Hornberger, P.S. Hauge, and J.M. Shaw. Characterization of positive photoresist. *IEEE Transactions on Electron Devices*, 22(7):445–452, 1975.

[237] R.R. Dammel. *Diazonaphthoquinone-based Resists*, volume TT11. SPIE, 1993.

[238] H. Hiraoka. Functionally substituted novolak resins: Lithographic applications, radiation chemistry, and photooxidation. In *Materials for Microlithography*, chapter 17, pages 339–360. American Chemical Society, 1985.

[239] M.D. Rahman, R.R. Dammel, and D.L. Durham. Rearrangement of novolak resins. In *Advances in Resist Technology and Processing XI*, volume 2195. SPIE, 1994.

[240] H.-Y. Shih, T.-F. Yeh, A. Reiser, R.R. Dammel, H.J. Merrem, and G. Pawlowski. A percolation view of novolak dissolution. 3. dissolution inhibition. *Macromolecules*, 27(12): 3330–3336, 1994.

[241] C.L. Henderson, C.G. Willson, R.R. Dammel, and R.A. Synowicki. Bleaching-induced changes in the dispersion curves of DNQ photoresists. In *Advances in Resist Technology and Processing XIV*, volume 3049, 1997.

[242] C.L. Henderson, S.A. Scheer, P.C. Tsiartas, B.M. Rathsack, J.P. Sagan, R.R. Dammel, A. Erdmann, and C.G. Willson. Modeling parameter extraction for DNQ-novolak thick film resists. In *Advances in Resist Technology and Processing XV*, volume 3333, 1998.

[243] O.P. Lehar, M.A. Spak, S. Meyer, R.R. Dammel, C.J. Brodsky, and C.G. Willson. Resist rehydration during thick film processing. In *Advances in Resist Technology and Processing XVIII*, volume 4345. SPIE, 2001.

[244] A. Reiser, J.P. Huang, X. He, T.F. Yeh, S. Jha, H.Y. Shih, M.S. Kim, Y.K. Han, and K. Yan. The molecular mechanism of novolak–diazonaphthoquinone resists. *European Polymer Journal*, 38(4):619–629, 2002.

[245] M. Borzo, J.J. Rafalko, and R.R. Dammel. Molecular bases for the interaction between novolaks and diazonaphthoquinone photoactive compounds. In *Advances in Resist Technology and Processing XI*, volume 2195, pages 673–684. SPIE, 1994.

[246] G. Tam. PMGI bi-layer lift-off process, 1989. US Patent 4,814,258.

[247] Microchemicals. AZ 9200-series, thick resists for high resolution. https://www.microchemicals.com/products/photoresists/az_9260.html, 2019.

[248] O.P. Lehar, J.P. Sagan, L. Zhang, and R.R. Dammel. Solvent content of thick photoresist films. In *Advances in Resist Technology and Processing XVII*, volume 3999. SPIE, 2000.

[249] Microchemicals. AZ 5214 E image reversal resist for high resolution. https://www.microchemicals.com/products/photoresists/az_5214_e.html, 2019.

[250] M.E. Reuhman-Huisken, C.M.J. Mutsaers, F.A. Vollenbroek, and J.A.H.M. Moonen. Towards an optimized image reversal process for half micron lithography. *Microelectronic Engineering*, 9(1):551–556, 1989.

[251] W. Yin, W. Fillmore, and K.J. Dempsey. Optimization of the lithographic performance for lift-off processing. In *Advances in Resist Technology and Processing XVI*, volume 3678. SPIE, 1999.

[252] Kayaku Advanced Materials Inc. PMGI & LOR lift-off resists. https://kayakuam.com/products/pmgi-lor-lift-off-resists, 2019.

[253] Kayaku Advanced Materials Inc. ma-P 1200 photoresist series. https://kayakuam.com/products/ma-p-1200, 2019.

[254] L.E. Scriven. Physics and applications of DIP coating and spin coating. *MRS Proceedings*, 121:717, 1988.

[255] L.F. Thompson and M.J. Bowden. *Resist Processing*, chapter 4, pages 161–214. American Chemical Society, 1983.

[256] D.J.T. Hill, J.H. O'Donnell, and P.J. Pomery. Fundamental aspects of polymer degradation by high-energy radiation. In *Materials for Microlithography*, chapter 4, pages 125–149. American Chemical Society, 1985.

[257] A. Jouve, M. May, I. Servin, and J. Simon. *Lithography Resists*, chapter 6, pages 275–367. Wiley, Somerset, 1st edition, 2013.

[258] C.A. Mack and R.T. Carback. Modeling the effects of prebake on positive resist processing. In *Kodak Microelectronics Seminar*, pages 155–158. Interface '85, Proc., 1985.

[259] T.E. Everhart. Fundamental limits of lithography. In *Materials for Microlithography*, chapter 1, pages 5–9. American Chemical Society, 1985.

[260] S.S.S. Boon, S.S. Ann, K.J. Chui, and M. Yu. Impact of different developer concentrations for advanced packaging photolithography. In *2015 IEEE 17th Electronics Packaging and Technology Conference (EPTC)*, pages 1–4, 2015.

[261] H. Kikyuama, N. Miki, K. Saka, J. Takano, I. Kawanabe, M. Miyashita, and T. Ohmi. Principles of wet chemical processing in ULSI microfabrication. *IEEE Transactions on Semiconductor Manufacturing*, 4(1):26–35, 1991.

[262] H. Shimada, M. Onodera, T. Nonaka, K. Hirose, and T. Ohmi. Advanced development process for ultra fine photoresist patterns. *IEEE Transactions on Semiconductor Manufacturing*, 6(3): 269–273, 1993.

[263] J.I. Goldstein, D.E. Newbury, J.R. Michael, N.W.M. Ritchie, J.H.J. Scott, and D.C. Joy. *Scanning Electron Microscopy and X-Ray Microanalysis*. Springer, New York, NY, fourth edition, 2018.

[264] R. Hellborg, H.J. Whitlow, and Y. Zhang. *Ion Beams in Nanoscience and Technology*. Springer, Berlin, Heidelberg, 2010.

[265] Lasi - integrated circuit design for windows. https://lasihomesite.com/index.htm, 2004–2018.

[266] R.J. Baker. *CMOS: Circuit Design, Layout, and Simulation*. Wiley-IEEE Press, third edition, 2010.

[267] MicroChemicals. NMP 1-methyl-2-pyrrolidone. https://www.microchemicals.com/products/remover_stripper/nmp.html, 2019.

[268] MicroChemicals. AZ 100 remover, universal photoresist stripper. https://www.microchemicals.com/products/remover_stripper/az_100_remover.html, 2019.

[269] Dow Electronic Materials. Microposit remover 1165 for post-etch applications. https://kayakuam.com/wp-content/uploads/2019/09/Remover-1165-Data-Sheet-RH.pdf, 2019.

[270] Y. Zhang, T. Day, M.L. Snedaker, H. Wang, S. Krämer, C.S. Birkel, X. Ji, D. Liu, G.J. Snyder, and G.D. Stucky. A mesoporous anisotropic n-type Bi_2Te_3 monolith with low thermal conductivity as an efficient thermoelectric material. *Advanced Materials*, 24(37):5065–5070, 2012.

[271] L. Shelimova, T. Svechnikova, P. Konstantinov, O. Karpinskii, E. Avilov, M. Kretova, and V. Zemskov. Anisotropic thermoelectric properties of the layered compounds $PbSb_2Te_4$ and $PbBi_4Te_7$. *Inorganic Materials*, 43(2):125–131, 2007.

[272] L.D. Ivanova, Y.V. Granatkina, and Y.A. Sidorov. Electrical properties of antimony telluride single crystals doped with selenium and bismuth. *Neorganicheskie Materialy*, 35:44–52, 1999.

[273] C. Zheng, R. Hoffmann, R. Nesper, and H.G. Von Schnering. Site preferences and bond length differences in $CaAl_2Si_2$-type Zintl compounds. *Journal of the American Chemical Society*, 108(8):1876–1884, 1986.

[274] J.H. Bredt and L.F. Kendall. Magnesium antimonide and magnesium bismuthide as potential materials for power generating thermocouples. In *Proceedings-IEEE/AIAA*, 1966.

[275] C.L. Condron, S.M. Kauzlarich, F. Gascoin, and G.J. Snyder. Thermoelectric properties and microstructure of Mg_3Sb_2. *Journal of Solid State Chemistry*, 179(8):2252–2257, 2006.

[276] A. Bhardwaj, N.S. Chauhan, S. Goel, V. Singh, J.J. Pulikkotil, T. D. Senguttuvan, and D.K. Misra. Tuning the carrier concentration using Zintl chemistry in Mg_3Sb_2, and its implications for thermoelectric figure-of-merit. *Physical Chemistry Chemical Physics*, 18(8):6191–6200, 2016.

[277] H.X. Xin, X.Y. Qin, J.H. Jia, C.J. Song, K.X. Zhang, and J. Zhang. Thermoelectric properties of nanocrystalline $(Mg_{1-x}Zn_x)_3Sb_2$ isostructural solid solutions fabricated by mechanical alloying. *Journal of Physics D: Applied Physics*, 42:165403, 2009.

[278] K.X. Zhang, X.Y. Qin, H.X. Xin, H.J. Li, and J. Zhang. Transport and thermoelectric properties of nanocrystal substitutional semiconductor alloys $(Mg_{1-x}Cd_x)_3Sb_2$ doped with Ag. *Journal of Alloys and Compounds*, 484(1):498–504, 2009.

[279] H.X. Xin and X.Y. Qin. Electrical and thermoelectric properties of nanocrystal substitutional semiconductor alloys $Mg_3(Bi_xSb_{1-x})_2$ prepared by mechanical alloying. *Journal of Physics D: Applied Physics*, 39:5331, 2006.

[280] V. Ponnambalam and D.T. Morelli. On the thermoelectric properties of Zintl compounds $Mg_3Bi_{2-x}Pn_x$ (Pn = P and Sb). *Journal of Electronic Materials*, 42(7):1307–1312, 2013.

[281] A. Bhardwaj, A. Rajput, A.K. Shukla, J.J. Pulikkotil, A.K. Srivastava, A. Dhar, G. Gupta, S. Auluck, D.K. Misra, and R.C. Budhani. Mg_3Sb_2-based Zintl compound: A non-toxic, inexpensive and abundant thermoelectric material for power generation. *RSC Advances*, 3 (22):8504, 2013.

[282] S.H. Kim, C.M. Kim, Y.K. Hong, K.I. Sim, J.H. Kim, T. Onimaru, T. Takabatake, and M.-H. Jung. Thermoelectric properties of $Mg_3Sb_{2-x}Bi_x$ single crystals grown by Bridgman method. *Materials Research Express*, 2(5):055903, 2015.

[283] K. Imasato, S.D. Kang, S. Ohno, and G.J. Snyder. Band engineering in Mg_3Sb_2 by alloying with Mg_3Bi_2 for enhanced thermoelectric performance. *Materials Horizons*, 5(1):59–64, 2018.

[284] A. Bhardwaj and D.K. Misra. Enhancing thermoelectric properties of a p-type Mg_3Sb_2-based Zintl phase compound by Pb substitution in the anionic framework. *RSC Advances*, 4(65): 34552–34560, 2014.

[285] J. Zhang, L. Song, S.H. Pedersen, H. Yin, L.T. Hung, and B.B. Iversen. Discovery of high-performance low-cost n-type Mg_3Sb_2-based thermoelectric materials with multi-valley conduction bands. *Nature Communications*, 8:13901, 2017.

[286] J. Shuai, J. Mao, S. Song, Q. Zhang, G. Chen, and Z. Ren. Recent progress and future challenges on thermoelectric zintl materials. *Materials Today Physics*, 1(C):74–95, 2017.

[287] G.K.H. Madsen. Automated search for new thermoelectric materials: The case of LiZnSb. *Journal of the American Chemical Society*, 128(37):12140–12146, 2006.

[288] B.R. Ortiz, P. Gorai, L. Krishna, R. Mow, A. Lopez, R. McKinney, V. Stevanović, and E.S. Toberer. Potential for high thermoelectric performance in n-type Zintl compounds: a case study of Ba doped $KAlSb_4$. *Journal of Materials Chemistry A*, 5(8):4036–4046, 2017.

[289] P. Gorai and V. Stevanovic. Let's Uncomplicate: Mg complexes in Mg_3Sb_2, Oct 2019.

[290] F. Failamani, P. Broz, D. Macció, S. Puchegger, H. Müller, L. Salamakha, H. Michor, A. Grytsiv, A. Saccone, E. Bauer, G. Giester, and P. Rogl. Constitution of the systems {V,Nb,Ta}-Sb and physical properties of di-antimonides {V,Nb,$TaSb_2$}. *Intermetallics*, 65: 94–110, 2015.

[291] L. Battezzati and A.L. Greer. The viscosity of liquid metals and alloys. *Acta Metallurgica*, 37(7):1791–1802, 1989.

[292] N.W. Ashcroft and N.D. Mermin. *Solid state physics*. Holt, Rinehart and Winston, New York, 1976.

[293] S. Baranets and S. Bobev. From the ternary phase $Ca_{14}Zn_{1+\delta}Sb_{11}$ ($\delta \approx 0.4$) to the quaternary solid solutions $Ca_{14-x}RE_xZnSb_{11}$ (RE = La-Nd, Sm, Gd, $x \approx 0.9$). A tale of electron doping via rare-earth metal substitutions and the concomitant structural transformations. *Inorganic Chemistry*, 58(13):8506–8516, 2019.

[294] V.P. Itkin and C.B. Alcock. Ca-Zn (calcium-zinc). In T.B. Massalski, H. Okamoto, P.R. Subramanian, and L. Kacprzak, editors, *Binary Alloy Phase Diagrams*, pages 968–970. Materials Park, Ohio: ASM International, second edition, 1990.

[295] J. Dutkiewicz. In-Zn (indium-zinc). In T.B. Massalski, H. Okamoto, P.R. Subramanian, and L. Kacprzak, editors, *Binary Alloy Phase Diagrams*, pages 2316–2319. Materials Park, Ohio: ASM International, second edition, 1990.

[296] L.A. Zabdyr. Thermodynamics and phase equilibria in the Sb-Zn system. *Calphad*, 17(3): 269–280, 1993.

[297] H. Udono, S. Takaku, and I. Kikuma. Crystal growth of β-$FeSi_2$ by temperature gradient solution growth method using Zn solvent. *Journal of Crystal Growth*, 237:1971–1975, 2002.

[298] R. Hu, J. Hudis, C. Stock, C.L. Broholm, and C. Petrovic. Single crystal growth of $YbRh_2Si_2$ using Zn flux. *Journal of Crystal Growth*, 304(1):114–117, 2007.

[299] R. Saint-Martin, P. Berthet, and A. Revcolevschi. Single-crystal growth of Mg- and Ni-doped chain compound $SrCuO_2$ by the travelling-solvent floating-zone method and chain breaking effect induced by the dopants. *Journal of Crystal Growth*, 415:118–122, 2015.

[300] G.M. Sheldrick. *SHELXT* – integrated space-group and crystal-structure determination. *Acta Crystallographica Section A*, 71(1):3–8, Jan 2015. doi: 10.1107/S2053273314026370. URL https://doi.org/10.1107/S2053273314026370.

[301] G.M. Sheldrick. Crystal structure refinement with *SHELXL*. *Acta Crystallographica Section C*, 71(1):3–8, Jan 2015. doi: 10.1107/S2053229614024218. URL https://doi.org/10.1107/S2053229614024218.

[302] L.M. Gelato and E. Parthé. *STRUCTURE TIDY* – a computer program to standardize crystal structure data. *Journal of Applied Crystallography*, 20(2):139–143, Apr 1987. doi: 10.1107/S0021889887086965. URL https://doi.org/10.1107/S0021889887086965.

[303] E.H. Putley. *The Hall effect and semi-conductor physics*. Dover Publications, New York, 1968.

[304] X.-C. Liu, K.-F. Liu, Q.-Q. Wang, Y.-M. Wang, M.-Y. Pan, and S.-Q. Xia. Exploring new Zintl phases in the 9-4-9 family via Al substitution. Synthesis, structure, and physical properties of $Ae_9Mn_{4-x}Al_xSb_9$ (Ae = Ca, Yb, Eu). *Inorganic Chemistry*, 59(6):3709–3717, 2020.

[305] Y. Wang and S. Bobev. Rare-earth metal substitutions in $Ca_{9-x}RE_xMn_4Sb_9$ (RE = La-Nd, Sm; $x \approx 1$). Synthesis and characterization of a new series of narrow-gap semiconductors. *Chemistry of Materials*, 30(10):3518–3527, 2018.

[306] S. Bobev, J. Hullmann, T. Harmening, and R. Pottgen. Novel ternary alkaline-earth and rare-earth metal antimonides from gallium or indium flux. Synthesis, structural characterization and ^{121}Sb and ^{151}Eu Mössbauer spectroscopy of the series $A_7Ga_8Sb_8$ (A = Sr, Ba, Eu) and $Ba_7In_8Sb_8$. *Dalton Transactions*, 39(26):6049–6055, 2010.